

HIGH SENSITIVITY DNA DETECTION USING GOLD NANOPARTICLES AND CONDUCTING POLYMERS

Author

Elaine Spain B.Sc. (Hons.)

*A thesis presented at Dublin City University
for the Degree of Doctor of Philosophy*



Supervisors

Prof. Robert J. Forster

Prof. Tia E. Keyes

Dublin City University

Biomedical Diagnostics Institute

School of Chemical Science

June 2011

DECLARATION

I hereby certify that this material, which I now submit for assessment on the programme of study leading to the award of doctor of philosophy is entirely my own work, that I have exercised reasonable care to ensure that the work is original, and does not to the best of my knowledge breach any law of copyright, and has not been taken from the work of others save and to the extent that such work has been cited and acknowledged within the text of my work.

Signed: _____ ID No.: _____ Date: _____

ACKNOWLEDGEMENTS

Spending the past eight years at DCU in pursuing the Bachelor and Doctor of Philosophy degrees has been the best years of my life. The research project I have been working on is very interesting while most of the time, challenging. Therefore, there are complex and difficult tasks that I could not have completed alone. Herein, I would like to convey my heartfelt gratitude to a number of people who have contributed to the development of this thesis and to my overall experience as a graduate student at DCU.

Firstly, I would sincerely like to thank my supervisor Professor Robert Forster for giving me the opportunity to work on such an exciting project. Since joining the research group in September 2007, he has spent tremendous effort not only in leading the project but also in improving my technical writing and presentation skills. Your knowledge and expertise, creative ideas, easy going personality and passion for science have all made this experience fantastic. I would also like to thank my co-supervisor, Professor Tia Keyes for her guidance and support in my research work.

My appreciation also extends to the past and present members of my lab, especially Anita, Anitha, Claudio, Brian, Emmet, Colm, Aaron, Steven, Bincy and “The king”, who always provided a level head or coffee when I was threatening to throw numerous potentiostats out of the window. Special thanks are given to Dr. Jennifer Breannan (now Beirne), who trained me to use the instruments, and also shared her experience and knowledge in the biosensor research as well as her friendship. I have made some excellent friends and colleagues in my research group and I wish them every success in their forthcoming research and wherever they find themselves in the future! I would also thank all academics and technical staffs of the School of Chemical Sciences, DCU for their advice and help.

Now I would like to thank the people who have really made me come in everyday and allow me to leave with a smile on my face. I have been fortunate

over the course of these four years to meet and work with a great deal of talented and bright individuals. Lunch time is always the highlight of my day and I really love all of you guys (I don't love anyone more than the other Harvey!) and I know that we will be "real" friends forever. I really don't know where to start...there have been so many memories and fun times that nothing sticks out as my favourite. Nikki, Emma, Jen, Kelly and Susan have been the best friends (and wifey no. 2) that a girl could ever have. No problem is too small to moan about or dropping your work to go for a pint in the hub. Once the DCU bubble ends, I know that I will have you guys forever in my life whether it's for the gossip or a responsible night out on the lock ☺. The "honoury girls"...Dolan and zoe, ahhh what can I say! Fair dues to you lads, you were always outnumbered when it came to the slagging but you took it well most of the time. Thanks guys for giving me plenty to laugh over for the last 4 years and we will see how we get on after the "expiry date" ☺ but you are not going to get rid of me that easily (especially since ill always need a dogsitter).

I am very grateful to my mam, grandparents and my crazy siblings. They have taught me to be an optimistic person and not to take life too seriously. I would not be able to be anywhere without their unselfish love and support. Talking about crazy, I could not have gotten through the ordeal of writing my thesis without my mad hatter friend Fran. Your gossip and facebook stalking has really kept me going for 20 years now and I hope for another 20 more. Love you Ms. Freeman (sorry Read).

Finally, I want to thank my boyfriend and best friend Kieran. He has always been there for me and I love him from the bottom from my heart. As I said already, spending the past eight years at DCU has been the best years of my life and you are a major factor in that happiness. I hope we will always have our mini adventures and lots of fun times---"you know yourself, just to have something to tell the kids one day".

P.s. I would like to pat myself on the back. There has been many a time I wanted to quit and just leave with masters. Well I would like to thank that

stubborn Spain streak for making me finish this, especially when life threw hurdles at me and my motivation was completely out the window. Well Done!

APPENDIX: 1

GLOSSARY OF ACRONYMS

Acronym: Explanation

ACN	Acetonitrile
AFM:	Atomic force microscopy
Ag/AgCl	Silver / silver chloride
AgNO ₃	Silver nitrate
APS	Ammonium peroxydisulfate
ATR	Infrared attenuated total reflection
AuNPs	Gold nanoparticles
C ₁₂	Dodecanethiol
Ce(SO ₄) ₂	Cerium(IV) Sulfate
cdS	cadmium sulfide
ClO ₄	Perchlorate
CP	Conducting polymer
CV	Cyclic voltammetry
D _{CT}	Charge transfer diffusion coefficient
DNA	Deoxyribonucleic acid, either a single stand or a double strand
ds	Double stranded
EB	Emeraldine base
EDOT	3,4-Ethylenedioxythiophene

EDTA	Ethylenediaminetetraacetic acid
ELISA:	Enzyme linked immuno sorbent assay
EPR	Electron paramagnetic resonance
ES	Emeraldine salt
Et ₂ O	Diethyl ether
EtOAc	Ethyl acetate
FeCl ₃	Ferric chloride
FTIR	Fourier transform infrared spectroscopy
HAuCl ₄	Gold chloride acid
HCl	Hydrochloric acid
HNO ₃	Nitric acid
H ₂ O ₂	Hydrogen peroxide
H ₂ SO ₄	Sulphuric acid
HOMO	Highest occupied molecular orbital
HRP	Horse radish peroxidase
ITO:	Indium Tin Oxide
IUPAC	International union of pure and applied chemistry
KCl	Potassium chloride
KOH	Potassium hydroxide
LiClO ₄	Lithium perchlorate
LOD	Limit of detection

LUMO	Lowest unoccupied molecular orbital
MnO ₂	Manganese dioxide
N ₂	Nitrogen
NA	Nucleic acid
NaCl	sodium chloride
Na ₂ S ₂ O ₈	Sodium persulfate
NF	Nanofibres
NH ₃	Ammonium
NH ₄ OH	Ammonium hydroxide solution
PANI	Polyaniline
PBS	Phosphate buffered saline
PCR	Polymerase chain reaction
PEDOT	Poly(3,4-ethylenedioxythiophene)
PPy	Pyrrole
PS	Pernigraniline salt
PSS	Sodium poly(styrene sulfonate)
Pt	Platinum
PTh	Polythiophene
PVA	Poly(vinyl alcohol)
Redox	Reduction-oxidation reaction
RF	Roughness factor

RNA	Ribonucleic acid
S.aureus	Staphylococcus aureus
SAM:	Self assembled monolayer
S. epidermidis	Staphylococcus epidermidis
SEM:	Scanning electron microscope
SDS	sodium dodecyl sulphate
SPR	surface plasmon resonance
ss	single strand
TEM	Transmission electron microscopy
Tris-HCl	Tris-hydrochloric acid
UV:	Ultraviolet
vis:	Visible
VPP	Vapour phase polymerisation

Symbols

A	Area of the working electrode	cm ²
A _G	Geometric area	?
A _p	Area under the peak	cm ²
α	Transfer coefficient	-
C*	Bulk concentration	M
C _{dl}	Double layer capacitance	F
C _O *	Bulk concentration of the oxidised species	M

C_R^*	Bulk concentration of the reduced species	M
C	Capacitance	F
cm	Centimetre	-
D_{CT}	Diffusion coefficient	$\text{cm}^2 \text{s}^{-1}$
e^-	Electron	-
E	Electrochemical potential	V
$E_{1/2}$	Half wave potential	V
E°	Standard electrochemical potential	V
E_{DC}	Equilibrium DC potential	V
F	Faraday constant	C
g	g factor	-
G	Gauss	-
ΔG°	Gibbs free energy	eV
ΔH	Line width value	G
i	Current	A
j	Current density	Acm^{-2}
k_s	Standard heterogeneous electron transfer rate constant	$\text{cm}^2 \text{s}^{-1}$
M	Represents a metal	-
mA	Milliampere	-
mL	milliliter	-
mM	Millimoles per liter	-

μm	Micrometer	-
μM	Micro molar per liter	-
M_n	Number average molar mass	-
M_n^+	Metallic ion with positive charge of n	-
M_w	Molecular weight	g mol^{-1}
n	Number of electrons exchanged	-
nm	Nanometer	-
Ox	Oxidised species	-
Q	Charge passed in an electrochemical experiment	C
Γ	Surface coverage of self-assembled monolayer of alkanethiol on a substrate	mol cm^{-2}
R	Universal gas constant	$\text{J K}^{-1} \text{mol}^{-1}$
Red	Reduced species	-
R_{CT}	Charge transfer resistance	Ω
t	Time	s
T	Temperature	$^{\circ}\text{C}$
V	Volt	-
v	Scan rate in a cyclic voltammetry experiment	V s^{-1}

PUBLICATIONS AND PRESENTATIONS

Spain, E., Kojima, R., Kaner, R.B., Wallace, G.G., O'Grady, J., Lacey, K., Barry, T., Keyes, T.E., Forster, R.J., High Sensitivity DNA Detection Using Gold Nanoparticle Functionalized Polyaniline Nanofibres, *Biosensors and Bioelectronics* **26** (2011), pp. 2613-2618.

Spain, E., Brianna Miner, T.E., Forster, R.J., Gold Nanoparticle Suspensions Asymmetrically Functionalised with DNA, ***Submitted to Electrochemical Communications***

Spain, E., Dennany L., Wallace, G.G., O'Grady, J., Lacey, K., Barry, T., Keyes, T.E., Forster, R.J., "Highly Conductive DNA Detection using Electrochemical, Chemical and Vapour Phase Polymerisation of Polyaniline and Gold Nanoparticle Enhancement". **In preparation**

Posters:

Spain E., Brennan J.L., Keyes, T.E., Forster, R.J. "Electrochemical DNA biosensor using novel hydrogen peroxide sensor based on Au nanostructured modified gold electrode", 216th ECS Meeting, Vienna, October 2009

Spain E., Miner B. Keyes, T.E., Forster, R.J. "Electrochemically active AuNP for the detection of a biological species", Biomedical Diagnostic Institute Seminar, Dublin City University, Ireland, August 2010

Spain E., T.E., Forster, R.J "High Sensitivity DNA Detection Using Gold Nanoparticle Functionalized Polyaniline Nanofibres", Eirelec Meeting, Limerick, May 2011

Table of Contents

DECLARATION	ii
ACKNOWLEDGEMENTS	iii
APPENDIX: 1	vi
GLOSSARY OF ACRONYMS	vi
Symbols	ix
PUBLICATIONS AND PRESENTATIONS	xii
Posters:	xii

Chapter 1: THEORETICAL FRAMEWORK AND SURVEY OF LITERATURE

1.1 NUCLEIC ACID STRUCTURE	5
1.1.1 Primary structure.....	5
1.1.2 Secondary structure	8
1.2 DETERMINATION OF DNA HYBRIDISATION.....	13
1.2.1 Optical biosensors.....	13
1.2.2 Piezoelectric biosensors.....	17
1.3 ELECTROCHEMICAL DNA BIOSENSORS	19
1.4 ELECTROCHEMICAL DETECTION OF THE HYBRIDISATION EVENT	22
1.5 PROBE DNA IMMOBILISATION.....	26
1.6 NANOPARTICLE ENHANCEMENT OF THE HYBRIDISATION EVENT	28
1.6.1 Gold Nanoparticles.....	32
1.6.1.1 Background.....	32
1.6.1.2 Synthesis and Structure of AuNPs	32
1.6.1.3 Application of gold nanoparticles for DNA sensors	34
1.7 CONDUCTING POLYMERS	38
1.7.1 History of conducting polymers	38
1.7.2 Synthesis of conducting polymers	41
1.7.2.1 Electrochemical polymerisation of aniline	41
1.7.2.2 Electrochemical polymerisation of 5 membered heterocyclic thiophene ..	44
1.7.2.3 Chemical polymerisation of conducting polymers	46
1.7.2.3.1 Chemical polymerisation of aniline	46
1.7.2.3.1 Chemical polymerisation of PEDOT.....	48
1.7.2.4 Vapour polymerisation of conducting polymers	49

1.8 SELF ASSEMBLED MONOLAYERS OF ALKANETHIOLS ON METALS	50
1.8.1 Thiol tethered DNA.....	52
1.9 THEORITICAL BACKGROUND	54
1.9.1 Basic features of the electrochemical process.....	54
1.9.2. Cyclic voltammetry	54
1.9.2.1 CV of solution phase species	55
1.9.3 Potentiostatic techniques	59
1.10 CONCLUSION.....	60
1.11 REFERENCES	62

Chapter 2: SYNTHESIS AND CHARACTERISATION OF CONDUCTING POLYMERS, NANOPARTICLES AND NANOCOMPOSITES

2.1 INTRODUCTION.....	75
2.2 MATERIALS AND CHEMICALS.....	77
2.2.1 DNA	78
2.3 INSTRUMENTATION.....	78
2.3.1 Spectroscopic measurements	78
2.3.2 Microscopic measurements.....	79
2.4 EXPERIMENTAL PROCEDURES.....	81
2.4.1 Electrode fabrication and cleaning	81
2.4.2 Construction of nanogold working electrode.....	84
2.4.3 DNA capture strand immobilisation and hybridisation.....	86
2.4.4 Electrochemical detection of Staphylococcus aureus (S. aureus) single stranded DNA.....	87
2.5 SYNTHESIS OF POLYMERS.....	90
2.5.1 Electrochemical polymerisation.....	91
2.5.2 Vapour polymerisation	92
2.5.2.1 Polyaniline	92
2.5.2.2 PEDOT	93
2.5.3 Chemical polymerisation	94
2.5.3.1 Polyaniline	94
2.5.3.2 Chemical doping of emeraldine base nanofibres (PANI-NF)	94
2.5.3.2.1 AuNP incorporation after the chemical doping of PANI-NF.....	95

2.5.3.3	PEDOT	95
2.6	CONCLUSION	95
2.7	REFERENCES	97

Chapter 3: ELECTROCHEMICAL (MASTITIS PATHOGEN) DNA BIOSENSOR

3.1	INTRODUCTION.....	101
3.2	EXPERIMENTAL	104
3.2.1	Gold nanoparticle electrodeposition	104
3.2.2	Microscopic characterisation of gold nanoparticle electrodeposition.....	104
3.2.3	Voltammetric characterisation of an enzyme amplified DNA sensor	104
3.2.4	The influence of HRP labelled DNA hybridisation time	105
3.2.5	Species recognition ability (mismatch and non - pathogenic species)	105
3.2.5.1	Non-specific adsorption evaluation.....	105
3.2.5.2	1 and 3 base mismatch	106
3.2.6	Buffer identity	107
3.2.7	Alternative immobilisation / hybridisation procedures.....	107
3.3	RESULTS AND DISCUSSION	109
3.3.1	Electrochemical characterisation of gold nanoparticle electrodeposition	109
3.3.2	Scanning electron microscopy (SEM) of gold nanoparticle electrodeposition	112
3.3.3	Potentiodynamic study of an enzyme amplified DNA sensor	115
3.3.4	Potentiostatic study of an enzyme amplified DNA sensor.....	119
3.3.5	The influence of HRP labelled DNA hybridisation time on an enzyme amplified DNA sensor	124
3.3.6	Species recognition ability (mismatch and non- pathogenic species)	134
3.3.6.1	1 Base mismatch	134
3.3.6.2	3 Base mismatch (S. epidermidis discrimination)	134
3.3.7	Immobilisation buffer identity	136
3.3.8	1 step hybridisation of enzyme amplified DNA	141
3.4	CONCLUSION	144
3.5	REFERENCES	147

**Chapter 4: NANOPARTICLE FUNCTIONALISED POLYANILINE NANOFIBRES
FOR DNA SENSOR DEVELOPMENT**

4.1	INTRODUCTION.....	151
4.2	RESULTS AND DISCUSSION	152
4.2.1	Potentiodynamic polymerisation of PANI.....	152
4.2.2	Potentiostatic polymerisation of PANI.....	155
4.2.3	Voltammetric characterisation of PANI and PANI-AuNP.....	158
4.2.4	Microscopic characterisation of PANI-NF and PANI-NF-AuNP.....	162
4.2.5	UV - visible spectra of polyaniline.....	165
4.2.5.1	UV - vis of electropolymerised PANI film.	167
4.2.5.2	UV - vis of vapour polymerised PANI film.....	170
4.2.5.3	UV - vis of chemically polymerised PANI film.	173
4.2.5.4	UV-vis of chemically polymerised emeraldine base nanofibres.	176
4.2.6	RAMAN spectroscopy of polyaniline	179
4.2.6.1	Raman of electropolymerised PANI film.	182
4.2.6.2	Raman of vapour polymerised PANI film.....	185
4.2.6.3	Raman of chemically polymerised PANI film.	188
4.2.7	Electron paramagnetic resonance of polyaniline	194
4.2.7.1	EPR studies of electropolymerised PANI film.	195
4.2.7.2	EPR studies of chemically polymerised PANI film.	197
4.2.7.3	EPR studies of chemically polymerised emeraldine base nanofibres. ...	200
4.2.8	Detection of the hybridisation reaction.....	204
4.2.8.1	Electropolymerisation of aniline.....	204
4.2.8.2	Vapour polymerisation of aniline.	210
4.2.8.3	Chemical polymerisation of aniline	214
4.2.8.3.1	Chemically polymerised emeraldine base nanofibres.	218
4.3	CONCLUSION	222
4.4	REFERENCES	225

**Chapter 5: NANOPARTICLE FUNCTIONALISED PEDOT NANOFIBRES FOR DNA
SENSOR DEVELOPMENT**

5.1	INTRODUCTION.....	232
-----	-------------------	-----

5.2	RESULTS AND DISCUSSION	234
5.2.1	Potentiodynamic polymerisation of PEDOT	234
5.2.2	Potentiostatic polymerisation of PEDOT	236
5.2.3	Voltammetric characterisation of PEDOT and PEDOT-AuNP	239
5.2.4	Microscopic characterisation of PEDOT and PEDOT-AuNP	243
5.2.5	UV - visible spectra of PEDOT	247
5.2.5.1	UV - vis of electropolymerised PEDOT film	248
5.2.5.2	UV - vis of vapour polymerised PEDOT film	251
5.2.5.3	UV - vis of chemically polymerised PEDOT film	254
5.2.6	Raman spectroscopy of PEDOT	256
5.2.6.1	Raman of electropolymerised PEDOT film	259
5.2.6.2	Raman of vapour polymerised PEDOT film	262
5.2.6.2	Raman of chemically polymerised PEDOT film	265
5.2.7	Electron paramagnetic resonance of PEDOT	267
5.2.7.1	EPR studies of electrochemically polymerised PEDOT film	268
5.2.7.2	EPR studies of chemically polymerised PEDOT film	271
5.2.8	Detection of the hybridisation reaction	273
5.2.8.1	Electropolymerisation of EDOT	273
5.2.8.2	Vapour Polymerisation of EDOT	278
5.2.8.3	Chemical polymerisation of EDOT	282
5.3	CONCLUSION	286
5.4	REFERENCES	289

Chapter 6: CONCLUSIONS AND FUTURE WORK

6.1	Summary	295
-----	---------------	-----

DEDICATION

I would like to dedicate this thesis to Kieran, he knows the reason.

High Sensitivity DNA Detection using Gold Nanoparticles and Conducting Polymers

Elaine Spain

Abstract

The detection and quantitation of specific nucleic acid (NA) sequences continues to grow in importance driven by issues ranging from personalized medicine to companion diagnostics such as antibiotic selection for infectious diseases. In order to enhance the sensitivity of electrochemical detection of DNA, novel conducting polymer- metal nanoparticle composites have been created. An electrode modified with nanostructured gold (AuNP-elec) has been used to increase the surface of the electrode and therefore the amount of single strand DNA (ss-DNA) immobilised. This modification results in more capture strands being available to bind target strands thus improving the detection limit of the ssDNA biosensor. This sensor follows a three step procedure involving the immobilisation of a capture strand, its hybridisation with the target followed by complementary strand binding to a horse radish peroxidase, HRP, labelled oligo. By carefully selecting the immobilisation buffers as well as optimising the hybridisation times, a significantly improved current response was obtained. Electrochemical detection of both methods was carried out through a suitable substrate (H_2O_2) for the enzyme labelled duplex.

Polyaniline (PANI) has been synthesized by electrochemical, chemical and vapour oxidation methods. These PANI films have then been modified with electrochemically deposited chemically grown gold nanoparticles to give a nanocomposite material and deposited on gold electrodes. Single stranded capture DNA was then bound to the gold nanoparticles and the underlying gold

electrode and allowed to hybridise with a complementary target strand that is uniquely associated with the pathogen, *Staphylococcus aureus* (*S. aureus*), that causes mastitis. Significantly, cyclic voltammetry demonstrates that deposition of the gold nanoparticles increases the area available for DNA immobilisation by a factor of approximately 4. EPR reveals that the addition of the Au nanoparticles efficiently decreases the interactions between adjacent PANI chains and/or motional broadening. Finally, a horseradish peroxidase (HRP)-labelled DNA strand hybridises with the target allowing the concentration of the target DNA to be detected by monitoring the reduction of a hydroquinone mediator in solution. The sensors have a wide dynamic range, excellent ability to discriminate DNA mismatches and a high sensitivity. Semi-log plots of the pathogen DNA concentration vs. faradaic current were linear from 150 pM to 1 μ M and pM concentrations could be detected without the need for molecular, e.g., PCR or NASBA, amplification.

PEDOT films have been created by solution-casting an oxidant on the target substrate and then drying it followed by exposure to the monomer vapour. The dried substrate containing the oxidant is then placed over the liquid surface of the conjugated monomers in a closed chamber. The conjugated monomer liquid can easily volatilize and the substrate is fully exposed to the conjugated monomer vapour phase. The PEDOT films were also modified with AuNPs and compared to the electrochemical and chemical synthesis of PEDOT materials. Semi-log plots of the pathogen DNA concentration (150 pM to 1 μ M) vs. faradaic current were determined. The PEDOT biosensor after AuNP deposition showed a linear response over a wide dynamic range from 1 nM to 1 μ M with a detection limit of 3.8 fM. The implication of these findings and the possibility of extending such high sensitivity detection techniques for detecting other DNA molecules are discussed.



CHAPTER 1

THEORETICAL FRAMEWORK AND SURVEY OF LITERATURE

1.1 NUCLEIC ACID STRUCTURE

1.1.1 *Primary structure*

Nucleic acids are biological polymers. DNA is made up of monomer units called nucleotides, which are condensed together to form phosphodiester linkages between the monomers. Each nucleotide subunits consists of three components covalently bound together.¹

- A 5 carbon sugar molecule (ribose or deoxyribose),
- A phosphodiester,
- Nitrogen containing heterocyclic base attached to the sugar.

A phosphodiester bond is a group of strong covalent bonds between a phosphate group and two 5 carbon ring carbohydrates (pentoses) over two ester bonds. There are five different types of heterocyclic bases, differing only in the nitrogenous base. There are two purines (adenine and guanine) and three pyrimidines (cytosine, thymine and uracil) with adenine, cytosine and guanine being common to both DNA and RNA, and thymine and uracil being specific to DNA and RNA, respectively. The deoxyribose sugar of the DNA backbone has 5 carbons and 3 oxygens.¹ The carbon atoms in the deoxyribose, which is a sugar forming an important part of the backbone of the DNA molecule are numbered 1', 2', 3', 4', and 5' to distinguish from the numbering of the atoms of the purine and pyrimidine rings, as illustrated in Figure 1.1. A single-stranded non-circular DNA molecule has two non-identical ends, the 3' end and the 5' end (usually pronounced “three prime end” and “five prime end”). The chain like fashion of the DNA backbone is caused when the monomeric nucleotides are condensed together to form the phosphodiester linkage between the 3' hydroxyl of one ribose and the 5' hydroxyl of another ribose.

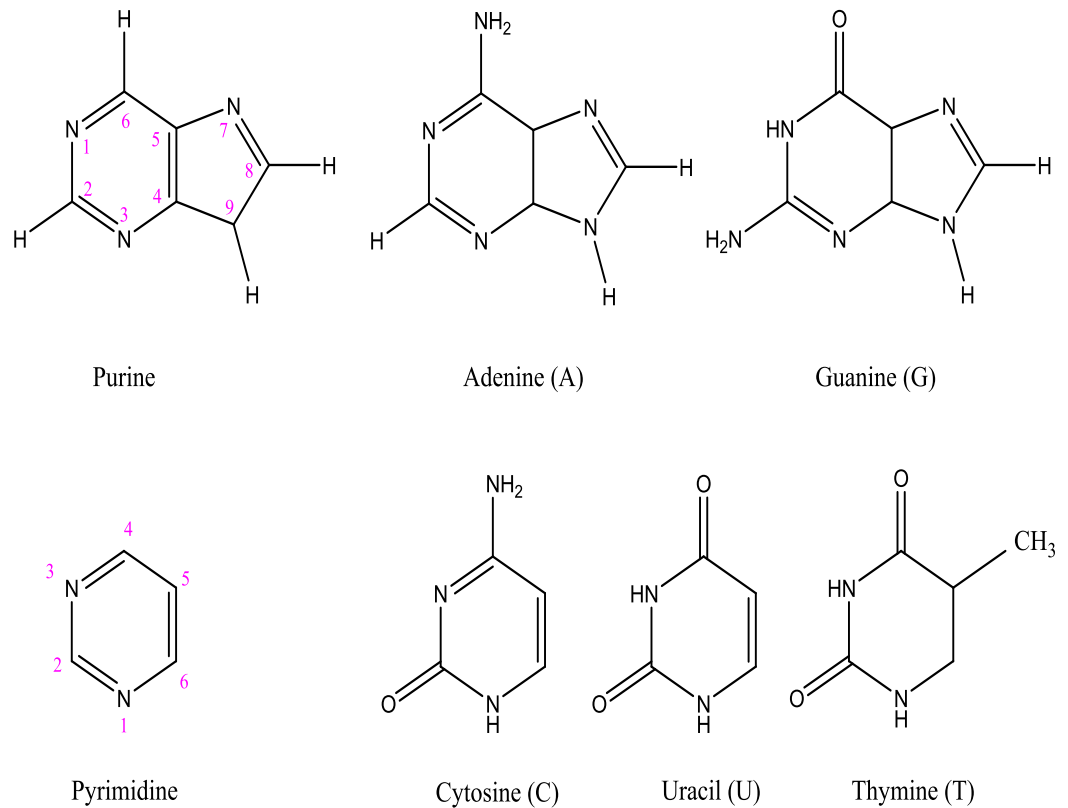


Figure 1.1 The five common heterocycles found in nucleic acids. Reproduced from Ref [2,3] Smith, E. L.; Hill, R. L.; Lehman, I. R.; Lefkowitz, R. J. *Principles of Biochemistry*, 7th edition, 1985, 652 and Nelson, D. L.; Cox, M. M. *Lehninger Principles of Biochemistry*, 4th Edition, 2004, 1200.

The deoxyribose sugar is shown in Figure 1.2. As a free sugar it can mutarotate under certain conditions, adopting furanose, acyclic and pyranose forms, but in DNA it is fixed as a furanoside. The heterocyclic bases are connected covalently by the N9 of purine or the N1 of pyrimidines to the C1 position of the deoxyribose, fixing the sugar into a five membered furanose configuration (β N-glycosidic bond).

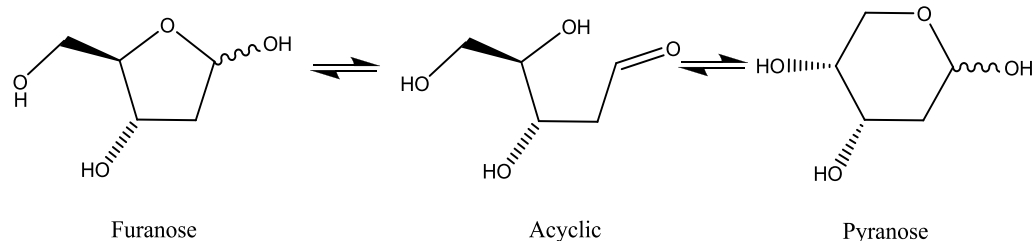


Figure 1.2 Muta-rotation of 2'-deoxy-D-ribose gives rise to furanose, acyclic and pyranose forms. Reproduced from Ref [4] Ghosh, A.; Bansal, M. *Acta Crystallographica Section D-Biological Crystallography* **2003**, 59, 620-626.

These phosphodiester bonds between the 3' carbon of one nucleotide and the 5' carbon of another nucleotide leads to the formation of the so-called "sugar-phosphate backbone", from which the bases project. This linkage provides the DNA chain with a 5' to 3' directionality. The 5' carbon of this deoxyribose is again linked to the 3' carbon of the next, and so forth. When a molecule of DNA is double stranded, as DNA usually is, the two strands run in opposite directions. Therefore, one end of the molecule will have the 3' end of strand 1 and the 5' end of strand 2, and vice versa in the other end.⁵

The heterocyclic base adopts an orientation above the furanose ring, typically on the same side as the base and the 5' hydroxyl group of the sugar. However, further possibilities can exist by rotation around the glycosylic bond, resulting in *syn* or *anti* configurations. The *anti* conformation is generally favoured, partly on steric grounds. The possible configurations for the purine and pyrimidine are illustrated in Figure 1.3

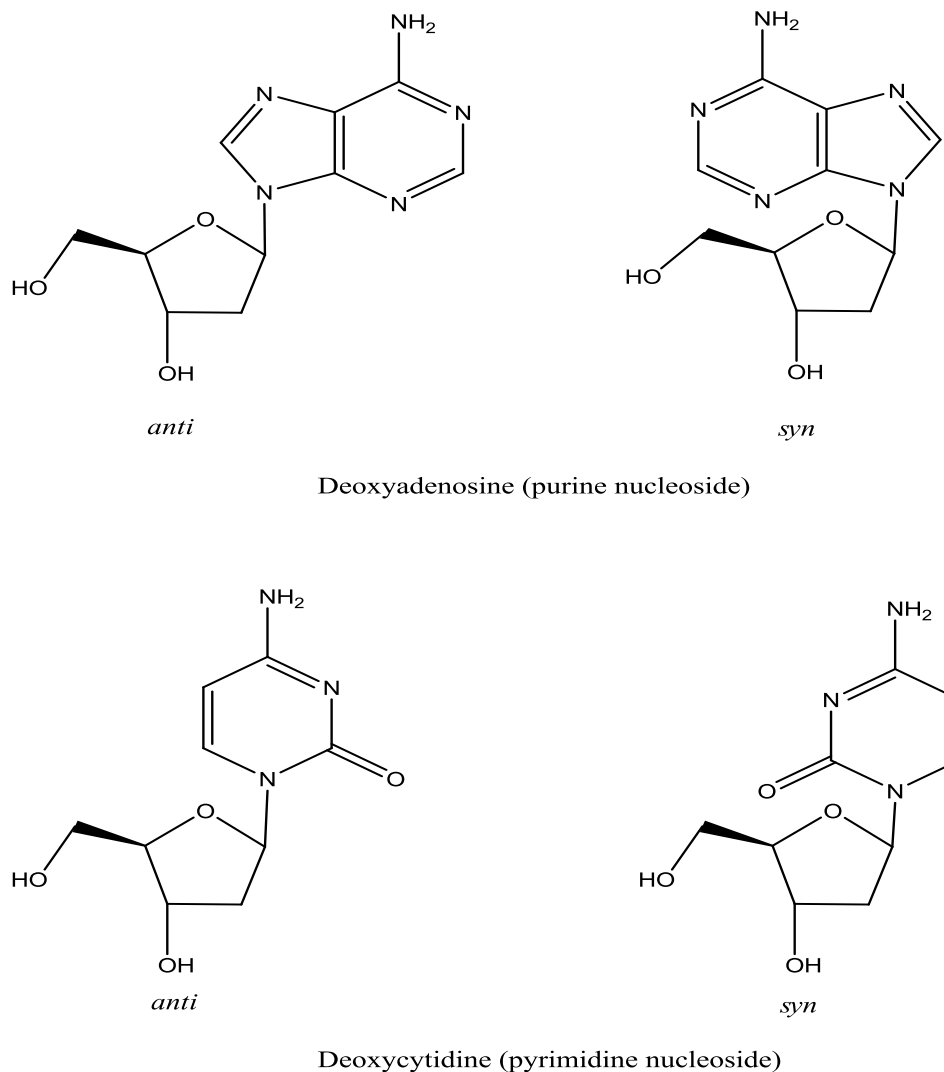


Figure 1.3 *Syn* and *anti* nucleoside conformations. Reproduced from Ref [5] Polsky, R.; Gill, R.; Kaganovsky, L.; Willner, I. *Analytical Chemistry*. **2006**, 78, 2268-2271.

1.1.2 Secondary structure

Biological functions such as genetic information cannot be obtained from the chemical structure of a single strand of DNA. However, the publication in the journal *Nature* in 1953 by James Watson and Francis Crick showed that DNA adopts a double stranded structure (duplex) and the mechanism of DNA replication became obvious. This work was dependant on the research of

Erwin Chargaff, who formulated a rule that molar ratio of purines to pyrimidines, is always 1:1.¹ Regardless of the sequence of nucleotides in the DNA strand, the number of moles of adenine in DNA was always equal to that of thymine and the same was true for guanine and cytosine.¹ This meant the formation of purine-pyrimidine pairs and A only pairs with T, and G with C (Figure 1.4).

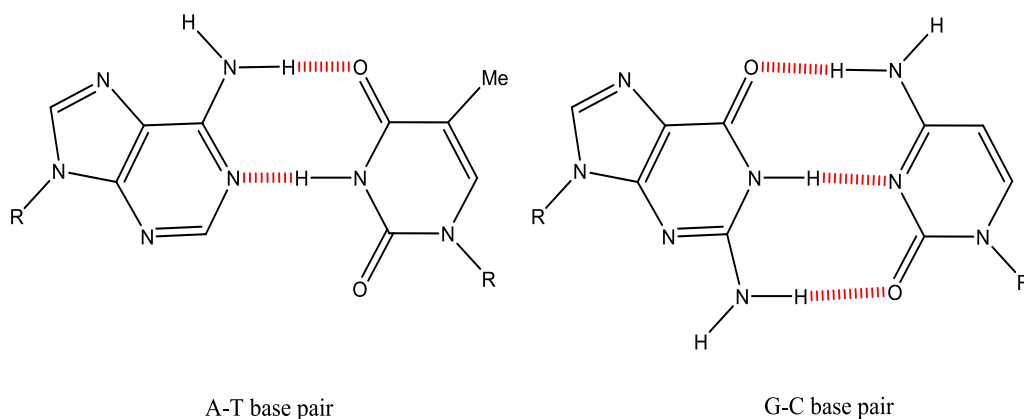


Figure 1.4 Hydrogen bonding between the Watson-Crick base pairs in DNA. Reproduced from Ref [5] Polsky, R.; Gill, R.; Kaganovsky, L.; Willner, I. *Analytical Chemistry*. **2006**, *78*, 2268-2271.

The formation of these base pairs provided evidence that the two strands of the double helix are complementary in sequence. Rosalind Franklin and Maurice Wilkins were able to provide further information on the structure of DNA. The double-helical structure was primarily elucidated from X-ray fibre diffraction data, demonstrating that the secondary structure of DNA is highly crystalline and helical in structure.⁵ They proposed the bases were found within the core of the helix and the negatively charged phosphodiester was the exposed backbone. Rosalind Franklin and Maurice Wilkins also discovered that the helical structure could be altered by varying the humidity. This allowed for the “A form” of the helix in low humidity and the “B form” under high humidity, to be determined.⁵ The model structures of the double helical structures are demonstrated in Figure 1.5

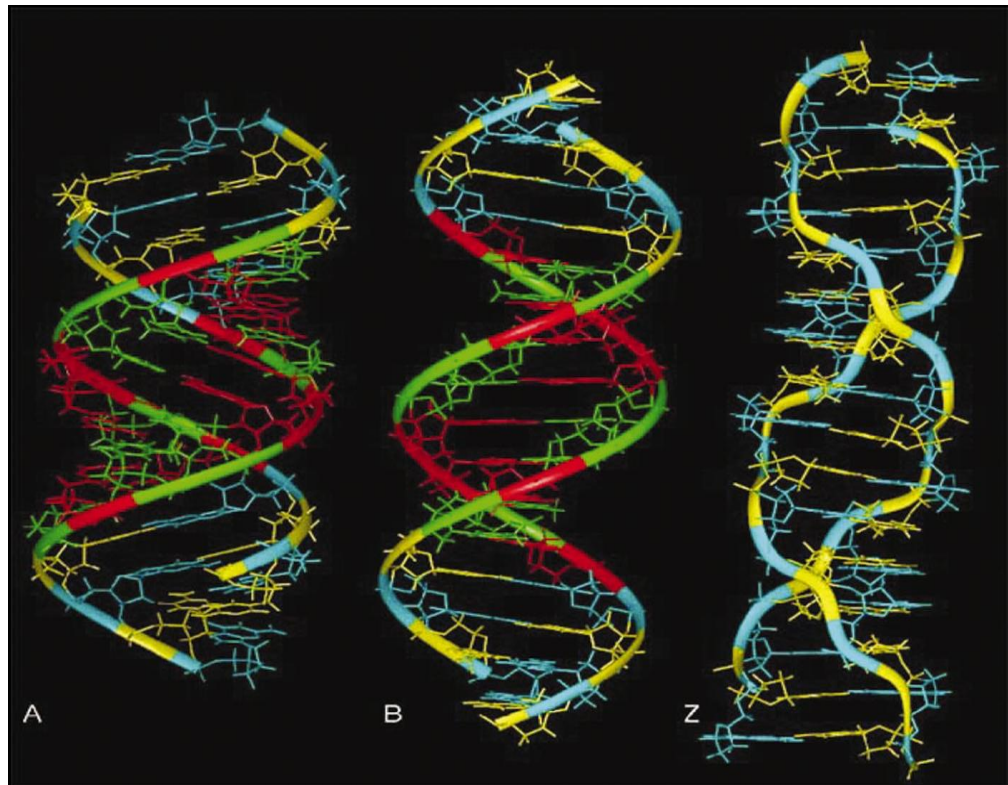


Figure 1.5: The currently accepted model structures for A-, B- and Z-DNA are shown here using the ball-and-stick representation. The nucleotides are colour-coded (cytosine in yellow, guanine in cyan, thymine in green and adenine in red) and a ribbon is superposed on the backbones connecting the P atoms. “A form” DNA and “B form” DNA are both right handed uniform double-helical structures; while “Z form”DNA is a left-handed double helix with a di-nucleotide repeat and the backbone follows a zigzag path. Reproduced from Ref [4] Ghosh, A.; Bansal, M. *Acta Crystallographica Section D-Biological Crystallography* **2003**, 59, 620-626.

From this research, Watson and Crick were able to deduce that the sequence of one strand of DNA precisely defines the sequence of the other; the two strands are said to be complementary. The two separate strands are antiparallel with the 5'-end of one strand next to the 3'-end of the other. They coil around each other to form a right-handed double helix. At the centre of the helix structure lays the hydrophobic base pairs and the sugars which are

planar and are stacked upon each other with the specific A-T and G-C base pairing. Hydrogen bonding links the two strands of the helix together, forming a right handed coil with 10 base pairs resulting in one complete turn of the helix (a full 360° turn of the double helix) in the most common “B form” DNA (the term "right-handed" indicates that the backbone at the front of the molecule facing the observer slopes down from top right to bottom left.). The planar heterocyclic bases stack one on another and the separation between successive base pairs along the helix axis is around 0.34 nm (Figure 1.6). Within the double helical structure, two grooves of unequal size are found. A minor groove of 0.6 nm and a major groove of 1.2 nm are found running around the helix along the entire length of the molecule. These grooves contain hydrogen bonding sites and interactions with proteins and the DNA can bind in these grooves (principally in the major groove) and some small drug molecules (e.g. netropsin, distamycin) can bind in the minor groove. The stability of the duplex is derived from both base stacking and hydrogen bonding.

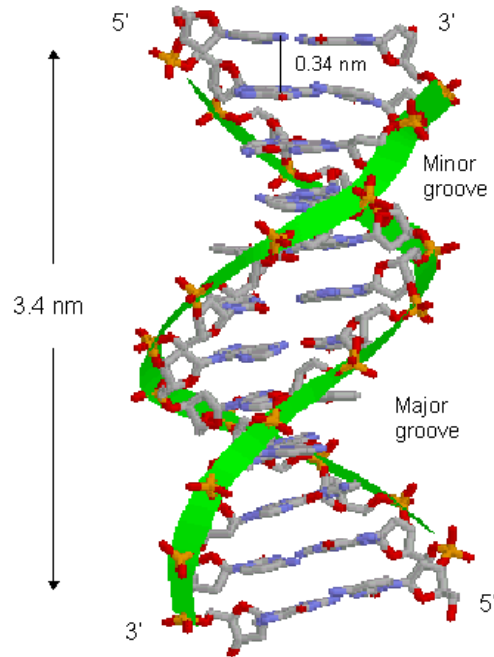


Figure 1.6 Structural dimensions of “B form” DNA duplex. Reproduced from Ref[4] Ghosh, A.; Bansal, M. *Acta Crystallographica Section D-Biological Crystallography* **2003**, 59, 620-626.

1.2 DETERMINATION OF DNA HYBRIDISATION

Micro scale DNA detection has been achieved through optical, microgravimetric and electrochemical methodologies for many years now. The most widely studied optical DNA detection is capillary electrophoresis (CE) with laser excited confocal fluorescence detection.⁶ This detection is typically used for PCR product sizing, DNA fragment analysis and sequence. CE devices can separate and detect DNA from tens to hundreds of base pairs in less than 10 minutes. However, CE analyses of PCR products do not provide sequence information which is vital in genetic assays of pathogen and disease diagnostics.

1.2.1 *Optical biosensors*

Optical biosensors are based on a number of different phenomena, including fluorescence, luminescence, absorption, evanescent wave and surface plasmon resonance, to convert biological information into a measurable optical signal. The basic principles of several major phenomena will be introduced briefly in this section

Nowadays, fluorescence is commonly used in optical biosensors. Fluorescence is widely used in chemical sensing not only because its sensitivity but also because of the availability of the diverse transduction schemes, which are based on changes in fluorescence intensity, fluorescence lifetime, and excitation or emission wavelength.⁷ Fluorescence works by the re-emission of a wavelength by molecules which have absorbed the radiation of a specific different wavelength. Fluorescence is a widely used characteristic tool, as each molecule has a specific spectrum and thus can be used to identify a particular molecule. In a fluorescence-based optical biosensor, a fluorescent-labelled antibody (sensing element) is attached to the end of an optical fiber, which is used to transmit the excitation light. The sensing is achieved by monitoring the fluorescence intensity, which is proportional to the

bonding between the antigens (analyte) with the antibody. Krull *et al*⁸ were the first to report an optical DNA biosensor. The assay was completely built up on an optical fiber. The transducer surface was first modified with long chain aliphatic spacers and then the capture probe was then synthesized in an automated solid phase synthesis technique. The detection of the dsDNA at the fiber surface was achieved by staining the DNA duplex with ethidium bromide, an intercalating dye. Other approaches for the direct fluorescence detection of DNA hybridisation relies on the incorporation of molecular beacons.⁹ Molecular beacons are single stranded oligonucleotides probes that are designed so that the bases at the two ends are complementary to one another. A loop is formed through self hybridisation and a fluorophore (F) and a quencher (Q) are coupled to both ends of each strand, as highlighted in Figure 1.7. This technique allows for both the fluorophores and quencher to be in close proximity to one another and therefore, the fluorescence of F is quenched by energy transfer (FRET). After the hybridisation of the complementary DNA, a rigid double helix was formed which opened the loop. This then caused the quencher and fluorophore to be separated, causing the restoration of the fluorescence of F. Sub-nanomolar concentration detection has been reported for the detection of dsDNA using this method.

Absorption is another simple phenomenon used in biosensing. Absorption is a process in which the energy of a photon is transformed to other forms of energy, such as heat. According to Beer-Lambert law, the absorbance of a molecule at a specific wavelength can be used to determine the concentration. Absorbance is typically measured directing a beam of radiation at the sample and detecting the intensity of the radiation that passes through it. Other absorption spectroscopy techniques such as ultraviolet-visible spectroscopy, infrared spectroscopy, and X-ray absorption spectroscopy have been developed to measure the absorption as a function of wavelength.

Chemiluminescence (CL) was first discovered by B. Radziszewski in 1877.¹⁰ The emission of light with limited emission of heat (luminescence) is known as CL. Peroxyoxalate chemiluminescence (POCL) is one of the most studied and resourceful CL processes available today.¹⁰ CL depends on the reaction

between aryl oxalates and an oxidant, usually hydrogen peroxide, to form a high-energy intermediate. The structure of the intermediate is yet to be

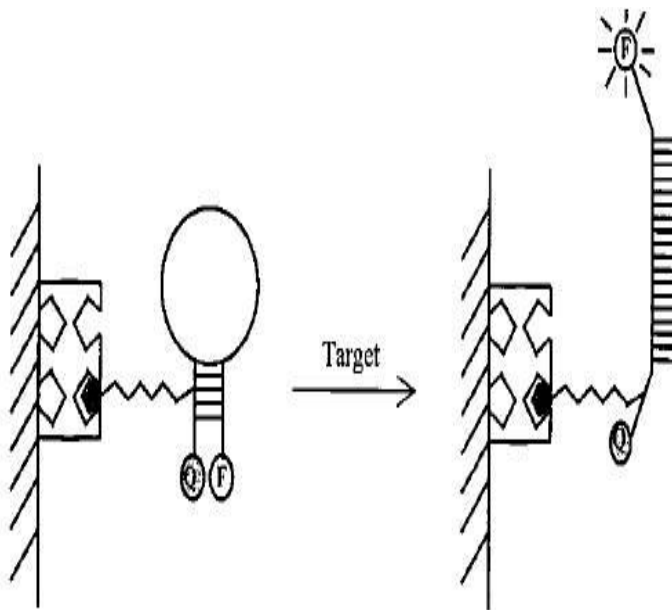


Figure 1.7 Schematic of the operation of a biotinylated MB immobilized on a solid surface. Biotin is added to the stem of the molecular beacon for surface immobilization with avidin. The MB is non fluorescent since the stem hybrid keeps the fluorophore (F) close to the quencher (Q). When the probe sequence in the loop hybridizes with its target, forming a rigid double helix, a conformational reorganization occurs that separates the quencher from the fluorophore, restoring the fluorescence of the fluorophore. Reproduced from Ref [9] Fang, X.; Liu, X.; Schuster, S.; Tan, W. *Journal of the American Chemical Society*. **1999**, 121, 2921-2922.

characterised, however, it is believed that a large number of fluorophores are excited.¹¹ This process is known as sensitization. The major advantage of CL is that the reaction is so rapid and the maximum intensity can be typically reached in less than one or two seconds. Therefore, CL detection systems are constructive for onsite analysis, and are suitable for assays which need a large sample throughput in a short period of time.¹² Comparing CL to other

techniques reveals another advantage. In CI, there is no requirement of irradiation of samples with electromagnetic radiation. This lack of source means that there is no noise caused by the light scattering, background emission and source instability.¹⁰ CL emission can be detected against a much darker background than fluorescence emission, resulting in a lower limit of detection.¹²

Enhanced chemiluminescence is commonly used in detection assays in biosensors. Horseradish peroxidase (HRP) is attached to a molecule of interest, which is catalysed by enhanced chemiluminescence to convert the substrate into a sensitized reagent in the vicinity of the molecule of interest. The determination of the molecule is caused by the further oxidation by hydrogen peroxide, producing a triplet carbonyl which emits light when it decays to the singlet carbonyl. Enhanced chemiluminescence allows for femtomolar concentrations of proteins to be detected.^{11,13}

Surface plasmon resonance (SPR) describes the optical excitation of surface plasmon which are surface electromagnetic waves that propagate on the boundary between a metal and an external dielectric (gas, liquid or solid).¹⁴⁻¹⁶ To realize the optical excitation of surface plasmons, a thin metal film will be evaporated onto a planar waveguide. When light propagating in the waveguide, evanescent waves penetrate the metal film, and plasmons will be excited on the outer side of the film. Since the metal absorbs the energy from the light in this process, there will be a narrow dip in the reflection spectrum. The measurements rely on monitoring changes in optical surface properties causing a shift in resonance angle. This causes a change in the refractive index upon binding of a molecule at the interface. Many configurations have been developed to realize SPR, such as the Kretschmann prism configuration and the grating scheme.¹⁷

Colourimetric detection is also commonly used in DNA detection. A one pit synthesis was reported by Storhoff *et al*¹⁸. They proposed that two different short capture probes were to be coupled to AuNPs at either the 5' or 3' end (Figure 1.8). In the presence of target DNA, the capture DNA hybridised in a

tail to tail like fashion causing a colour change in the solution. The colour change was attributed to the formation of the DNA linked to the 3D aggregates of AuNPs which resulted in red shift. The colour went from red to purple in the surface plasmon resonance. This purple colour is now exclusively reminiscent of a solution containing only complementary DNA at elevated temperatures. This technique allows the user to easily distinguish any sample containing a single base mismatch, due to the lack of colour change.

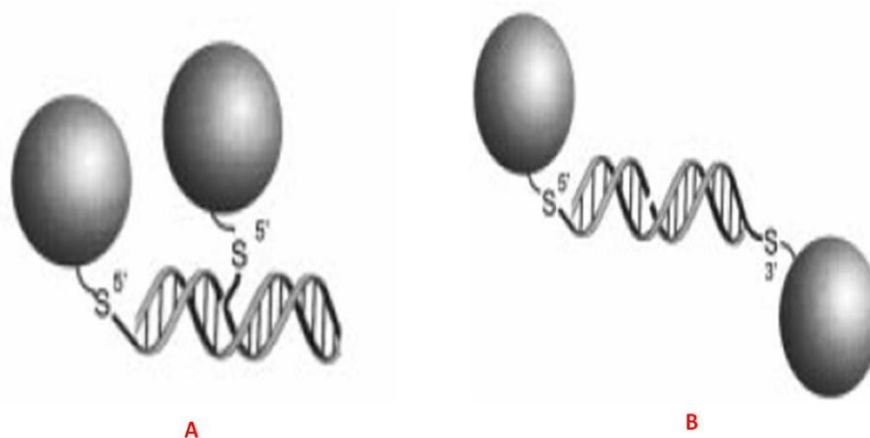


Figure 1.8 Representation of a nanoparticle based colorimetric detection of DNA. (A) The NPs are coupled to the capture probes at the 3' and 5' ends in a head to tail alignment. (B) After the hybridisation to the complementary strands, both capture probes are aligned in a tail to tail arrangement. Reproduced from Ref [18] Storhoff, J.; Elghanian, R.; Mucic, R.; Mirkin, C.; Letsinger, R. *Journal of the American Chemical Society* **1998**, *120*, 1959-1964.

1.2.2 Piezoelectric biosensors

Piezoelectric biosensors exploit the piezoelectric effect of some crystals, which have a physical deformation that is proportional to an applied electrical potential.¹⁹ Acoustic waves can be viewed as a standing wave which can propagate through the crystal. The piezoelectric properties of the crystal can then change the characteristic frequency of acoustic waves. The surface of the crystal can be coated with a biological recognition element and the reaction

between the analyte and the bio receptor is monitored by the change of the frequency of acoustic waves. Quartz is most common crystal type used in DNA hybridization, enzyme detections and gas phase biosensors.²⁰ Piezoelectric biosensors offer the possibility to monitor the hybridisation process in real time in response by monitoring the resonance frequency change in response to a weight increase on the quartz crystal.²⁰ However, piezoelectric sensors exhibit a lack of an exact correlation between mass addition and frequency change for solution phase sensing, and the sensitivity to environmental conditions.^{19,20} A comprehensive review of electrochemical DNA biosensors is described in full in a separate section (Section 1.3 and 1.4)

1.3 ELECTROCHEMICAL DNA BIOSENSORS

The term “biosensor” describes sensor devices that determine the concentration of a substance and other parameters of biological interest even if they do not utilize a biological recognition element directly.²¹ Alternatively, the probe or transducer incorporates the biological component (recognition function) as the key function element in the overall transducer element. The biological element and transducer can work collectively to relate the analytes concentration to a measurable electronic signal.²²

A biosensor consists of three parts:

1. Selective biological element which allows specific interactions to take place (e.g. tissue, micro organisms, organelles, cell receptors, enzymes, antibodies, nucleic acids);
2. The transducer which converts binding into a measurable signal;
3. The detector which converts the measurable signal into something that can be understood by users (works in a physicochemical way such as optical, piezoelectric, electrochemical, thermometric or magnetic).

According to the International Union of Pure and Applied Chemistry (IUPAC),²³ an electrochemical biosensor is defined as **“a self-contained integrated device, which is capable of providing specific quantitative or semi-quantitative analytical information using a biological recognition element (biochemical receptor) which is retained in direct spatial contact with an electrochemical transduction element.”** For example, the ideal characterisation of successful biosensors can be

- 1 Extremely specific, work in complex matrices, stable in storage and capable of use over a large number of assays;
- 2 Independent of physical parameters such as pH and temperature;
- 3 Precise, reproducible, accurate, high throughput and linear over a useful analytical range without dilution or concentration;
- 4 There must be minimal electrical noise;

- 5 Probe should preferably be physically small and biocompatible;
- 6 Rapid / real time analysis;
- 7 Biosensors as a whole should be cheap, small, reusable, flexible design and portable. It should have the capability to be used by semi skilled operators and the need for sample preparation should be minimal.^{24, 25}

A nucleic acid (NA) biosensor employs oligonucleotides as the sensing element, with a known sequence of bases, or a complex structure of DNA or RNA. Most NA biosensors are based upon highly specific hybridisation of complementary strands of DNA or RNA. DNA/RNA are the analytes and can be successfully detected through a hybridisation reaction. This type of biosensor is called a genosensor.²⁶

Genosensors result from integrations of a sequence – specific probes typically a short synthetic oligonucleotide and a signal transducer. A probe immobilised onto the transducer surface acts as a biorecognition molecule and recognises either the target DNA or RNA²⁷⁻³¹. The detection of DNA hybridisation on microarrays usually involves detecting the signal generated by the binding of a reporter probe (fluorescent, chemiluminescence, colorimetric) to the target DNA sequence. Typically, it takes about 20 hours or more to finish a traditional filter hybridisation procedure. Therefore, the detection of target biochemical molecules by means of traditional analytical methods can often be thought of as slow and time consuming.³²

However, DNA biosensors give results within an hour.³³⁻³⁵ The application of electrochemical methods provide significant advantages over optical biosensors.³⁶⁻³⁸ Specifically, the advantages of electrochemical biosensors include: low cost, reusability, speed,³⁹ as well as the relatively high stability and environmental insensitivity of electroactive labels; wide dynamic range and the wide range of available electrodes.³⁹

Furthermore, biosensors have been designed to exhibit high selectivity based on the inherent properties of the immobilised bio-components. The biological recognition element that is attached to the transducer surface selectively interacts with the analyte present in a complex sample matrix, thus eliminating

the requirement for separation and/or pre-concentration of the analyte. This means that DNA based biosensors can be simple and cost effective while providing fast results accurately.

1.4 ELECTROCHEMICAL DETECTION OF THE HYBRIDISATION EVENT

Before electrochemical sensing, gene chips were commonly used to create dense arrays of oligonucleotides. Gene chips are suitable when a large number of genes or sequences need to be simultaneously sampled.⁴⁰ Existing diagnostic tests such as Enzyme Linked Immunoassays (ELISA) are not sensitive enough for the detection of DNA at levels corresponding to early stages of diseases. Highly sensitive methods are essential to facilitate early detection of diseases and an adequate selection of treatment should be made available.^{41,42} Although traditional radioisotope-based DNA detection gives high sensitivity and selectivity, the labelling with radioactive reagents is challenging including the potential hazard to analysts as well as the environment and are time-consuming.⁴³ In order to overcome these limitations and fabricate an easy-to-use, inexpensive, miniaturized device for wide-scale genetic testing, a series of alternative non-radioactive DNA detection methods have been developed, such as fluorescence⁴⁴ chemiluminescence, electrochemical, and gravimetric DNA biosensors.⁴⁵ Electrochemical DNA biosensors has the advantages of being simple to operate, cheap, sensitive and selective.⁴⁶⁻⁴⁸

Nowadays, a simpler easier method can be employed to study DNA sequences. DNA biosensors are a promising tool for analyses as it converts DNA base pair recognition into a readable signal.^{47,49,50} DNA biosensors are based on the attachment of capture single stranded DNA probes onto a surface and the detection of surface hybridisation events with the complementary target sequence present in the sample as illustrated in Figure 1.9. The DNA duplex formed on the surface of the electrode (hybrid) is converted into an analytical signal by the transducer. Simply put, electrochemical biosensors convert the Watson-Crick base pairing recognition event (i.e. adenine pairing with thymine and guanine with cytosine)^{47,49,50} into a readable analytical signal.

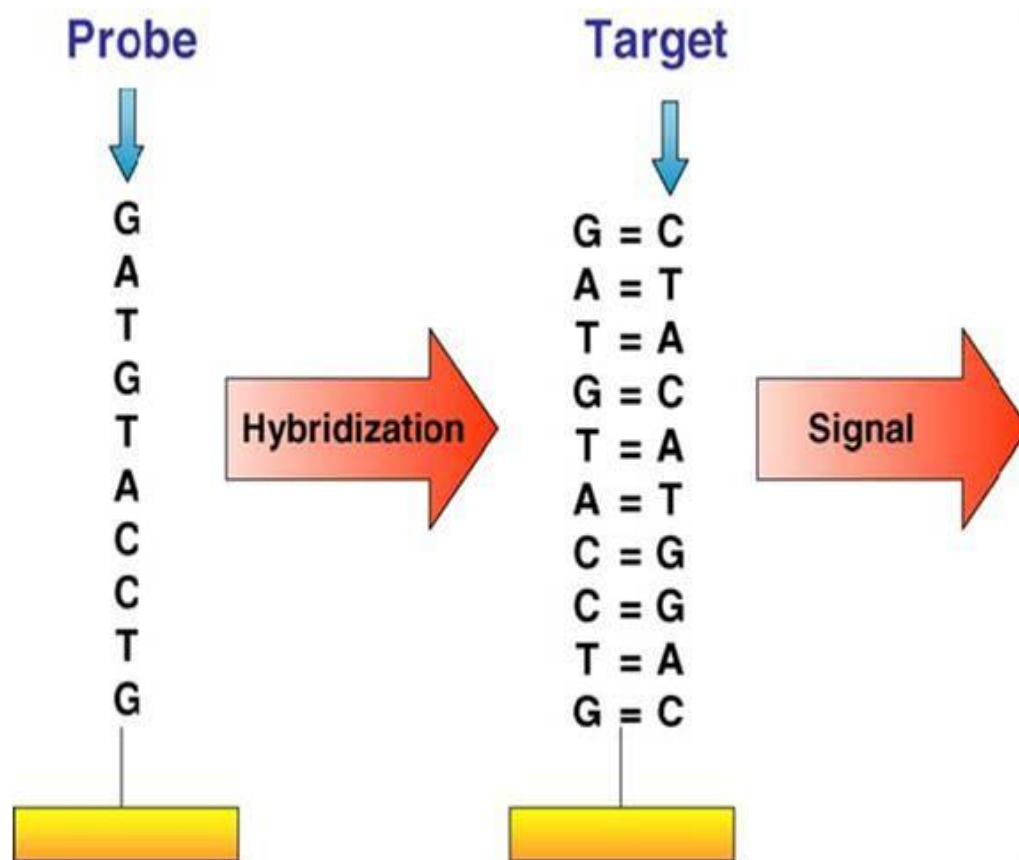


Figure 1.9 Steps involved in the detection of a specific DNA sequence using an electrochemical DNA hybridization biosensor. Reproduced from Ref [22] Wang J, *Analytical Chimica Acta*, **2002**, 469, 63-71.

Labels for electrochemical detection of hybridization can include anticancer agents (echinomycin [64] and epirubicin),⁵¹ organic dyes such as methylene blue,⁵²⁻⁵⁴ metal complexes (cobalt phenanthroline/ bipyridine and ruthenium bipyridine⁵⁵), enzymes or metal nanoparticles.⁵⁶ Efficient electrochemical detection of DNA hybridization has been achieved by labelling DNA with enzymes. Enzymes have been used to enhance assay sensitivity; due to their inherent amplification properties.⁵⁶

Horse radish peroxidase (HRP) is a commonly used enzyme. It has a high kinetic rate that maximises the enzymatic signal amplification.⁵⁷ By a simple conversion of HRP catalysed electron transfer to an amperometric signal, an

electrochemical sensor can measure the number of target oligonucleotides on the sensor surface. The current observed is proportional to the number of molecular targets in the sample. Zhang *et al*⁵⁸ reported HRP in the amplification of amperometric detection of DNA. The detection of DNA was as low as 3000 copies of a concentration of 0.5 fM. Pividore *et al*⁵⁹ reported a five step procedure for an enzyme based amperometric detection of hybridization.

1. DNA target immobilization was absorbed onto a nylon membrane.
2. Hybridisation occurred between DNA target and biotin DNA probe.
3. A complexation reaction occurred between the biotin DNA probe and HRP conjugate.
4. The modified membrane was integrated onto electrochemical transducer.
5. Amperometric detection using suitable substrate for enzyme labelled duplex.

E. Williams *et al*⁶⁰ used a biosensor that was amplified by an enzyme labelled antibody as illustrated in Figure 1.10. Hybridisation occurred between a target DNA to the capture probe and an antigen labelled DNA sequence. Electrochemical detection was achieved when the enzyme labelled antibody specific to the antigen is added. DNA hybridisation in this manner is favoured due to the high efficiency and specificity of the electrochemical biosensor in the presence of a mixture of many different, non-complementary, nucleic acids.^{27,48,61} Recent developments in the improvement of electrochemical DNA-hybridisation biosensors have been summarised.^{22,62,63}

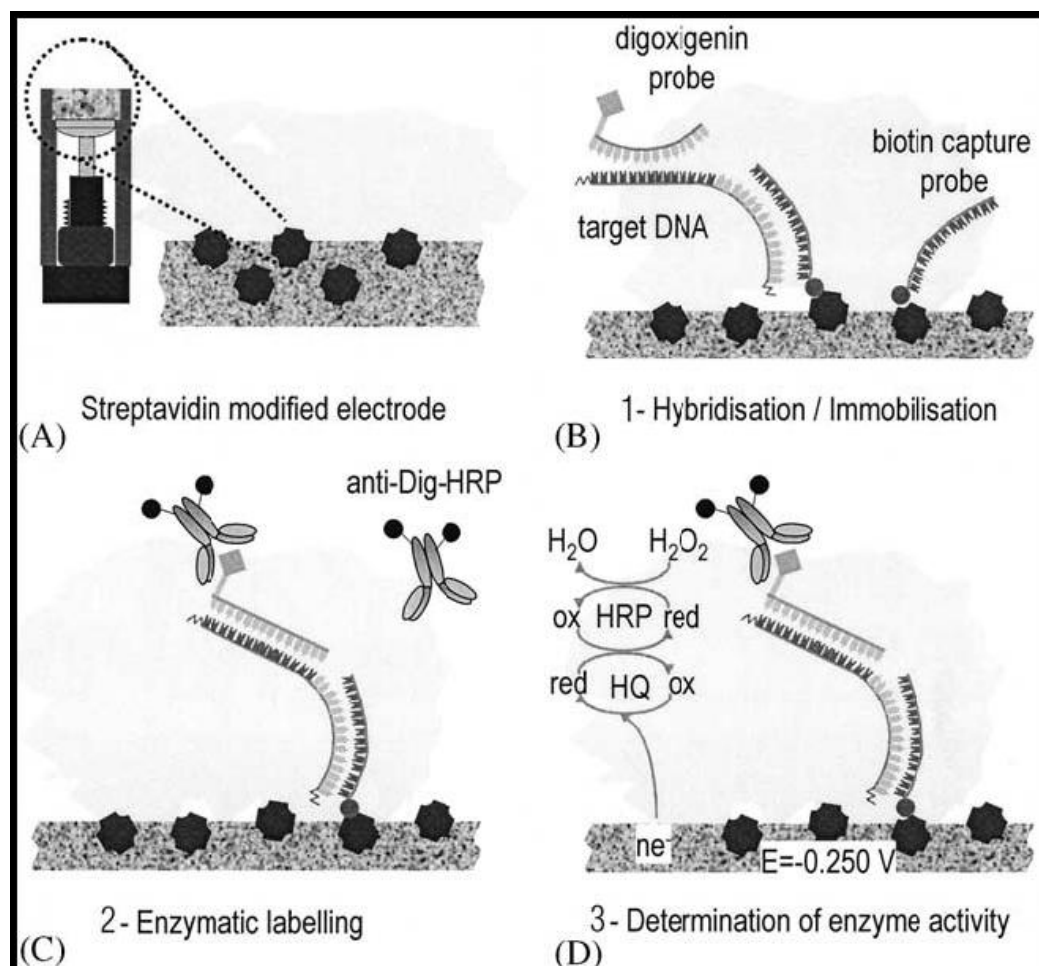


Figure 1.10 Schematic representation of the DNA analysis based on an electrochemical streptavidin carbon-polymer biocomposite. (A) Electrode modified with streptavidin (B) One step immobilisation/ hybridisation procedure: target-DNA is hybridised with the capture probe and with the digoxigenin modified probe. (C) Enzyme labelling based on the immunological reaction between the immobilised dsDNA-Dig with anti-Dig-HRP. (D) Electrochemical detection of the enzyme (HRP) labelled dsDNA. Reproduced from Ref [60] Williams, E.; Pividori, M. I.; Merkoçi, A.; Forster, R. J.; Alegret, S. *Biosensors and Bioelectronics*, **2003**, *19*, 165-175.

1.5 PROBE DNA IMMOBILISATION

The kinetics of nucleic acid hybridisation at solid surfaces is directly related to the accessibility of the DNA probe. For this reason, the covalent attachment of nucleic acids to the electrode surface through one of the ends of the DNA chain is most commonly used. An effective immobilisation of ssDNA on electrode surface is a critical factor in fabricating electrochemical DNA biosensors. An ideal immobilization method has to meet two requirements.⁶⁴

1. The electrode surface of the DNA biosensor must allow effective and specific binding of the ssDNA probe.
2. After the immobilisation of ssDNA, the electrode surface remains electro-active for detecting DNA hybridization.

The most common way of attaching DNA capture probes is to use thiol modified probe DNA that interacts with the gold surface through the sulphur atom of the thiol group. Almost 30 years ago, the self-assembly of sulphur-containing molecules was characterised by Nuzzo and Allara.⁶⁵ Disulphides, sulphides and thiols coordinate very strongly onto a variety of metals, e.g., gold, silver, platinum or copper. Nonetheless, gold is the most favoured, because it is reasonably inert. The assumed reaction between a thiolate compound and a gold substrate is:



The amount of probe DNA immobilisation on the electrode surface is an important factor because it directly influences the sensitivity of a DNA biosensor.⁶⁶ Self-assembly provides one of the most elegant approaches to obtain well defined and organised surfaces that can be an excellent platform for biosensor applications. General features of the direct chemisorption of self-assembled monolayers (SAMs) of thiol-modified DNA probes onto gold surfaces have been summarised in several papers and reviews^{63,67-70} and are briefly covered in the following section. Herne *et al.*⁷¹ gave a comprehensive

account of the structure of surface attached probes on gold disc electrodes and the impact of the probes distribution and orientation on the efficiency of hybridisation reactions. Their studies emphasised the following important points that are the basis of today's platform for sequence specific DNA biosensors.

- a) Random covalent binding of DNA to electrode surfaces, involving chemical modification of the bases, decreases the specificity of the recognition layer and therefore is not recommended.⁶³ The nonspecific adsorption of the probe on the substrate can be successfully blocked by immobilising a “back-filler” such as 6- mercaptohexanol, effectively forcing the DNA probes to be properly oriented for complementary DNA hybridisation.
- b) The buffer concentration has a substantial influence on the success of adsorption of thiolated probe on gold surface. It is found that a high buffer concentration, such as 1 M KH_2PO_4 , gives an improved coverage of the DNA as the high ionic strength is believed to suppress the intermolecular electrostatic repulsion between neighbouring strands.

The achievement of high sensitivity and selectivity requires maximisation of the hybridisation efficiency and minimisation of non-specific adsorption, respectively. In this work, gold disc electrodes modified with electrochemically deposited metal nanoparticles (gold) were used as a substrate for attachment of thiolated DNA.

1.6 NANOPARTICLE ENHANCEMENT OF THE HYBRIDISATION EVENT

Nanotechnology has become one of the most exciting fields in analytical chemistry for over the past decade. The term “Nanotechnology” involves the study, manipulation, formation and use of materials, devices and systems typically with dimensions smaller than 100 nm.⁷² The size range in which new, attractive properties different from bulk behaviour emerge depends on the material and the property of interest. Metal nanoparticles generally are reported to have diameters below 100 nm with current advances having a diameter range below 10 nm.⁷³ Because of the wide variety of nanomaterials of different sizes, shapes⁷⁴ and compositions commercially available, many applications have been discovered in today’s research for improved sensing devices.⁷⁵ The ability to modify the size and structure, and therefore the properties of the nanomaterials, has led to novel sensors and the enhanced performance of bio-analytical assays.⁷⁴

The advantage of nanomaterials is that they can be used widely in electroanalysis to dramatically increase the electrode area and hence increase the signal.⁷⁶ Figure 1.11 illustrates the dimensional compatibility of chemical and biological agents to the nanostructured materials commonly used methods of detection.⁷⁷ With DNA sensing, extremely small amounts of target analytes are used and therefore few hybridization events are observed.

Nanosized particles have the advantage that they have chemical and physical properties similar to small molecules and can be used for excellent chemical and biological sensing⁷⁸ and especially for specific electrochemical labels.^{79,80} New practices are based upon nanoparticles such as colloidal gold tags, semiconductor quantum dots, and polymeric amplification beads or magnetic beads. The power and wide scope of these nanoparticles can be greatly enhanced by coupling them with biological recognition reactions. They can provide a method for interfacing DNA recognition events with electrochemical

signal transduction and can quite successfully amplify the resulting electrical response.⁷⁶

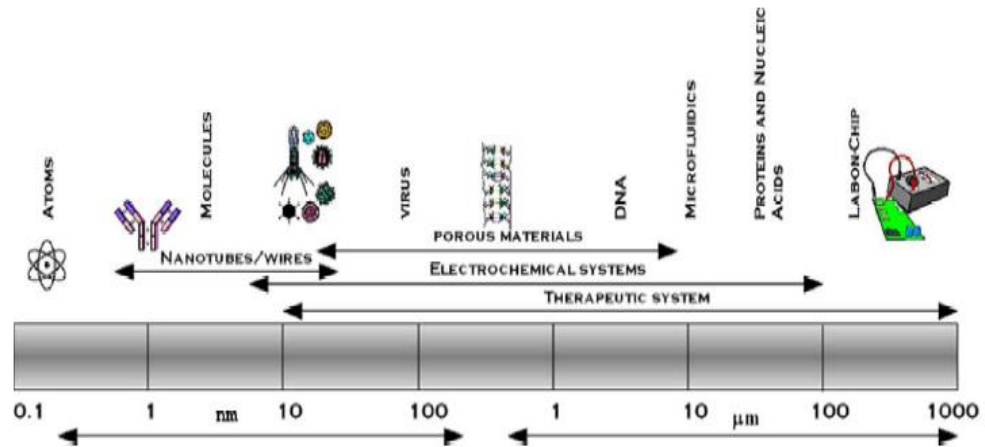


Figure 1.11 Size and compatibility. Reproduced from Ref[77]. Vaseashta, A.; Dimova-Malinovska, D. *Science and Technology of Advanced Materials*. **2005**, 6, 312-318.

Even though there are many types of nanoparticles- metals, oxides, semiconductors and composite, they all have the same basic applications in today's biosensors.⁷⁵

1. Immobilisation of biomolecules.
2. Catalysis of electrochemical reactions.
3. Enhancement of electron transfer.
4. Labelling biomolecules.
5. Acting as reactant.

In Table 1.1 a summary of different nanoparticles and their functions²⁴ is mentioned as well as their properties in electrochemical sensor system is provided. Biocatalysed production of insoluble products has also been used by Williner *et al.*⁷⁸ to sense DNA hybridization electrochemically at probe modified electrode. DNA probes are immobilized onto the electrode surface. Target DNA is pre-treated with an enzyme-modified probe, which binds to the 5' end of the target. The target-enzyme complex is hybridized to the probe,

and the bio catalyzed precipitation of product dimer provides amplification of the hybridization signal, which is detected as an increase in electron transfer resistance between the electrode and ferricyanide in solution.²⁴ Effective enhancement of electron transfer is dependent not only on conductivity of the nanoparticles but also of the arrangement between the nanoparticles and biomolecules. By creating a well defined and ordered arrangement between the nanoparticles, the construction of biosensors with greatly enhanced electron transfer properties provide promising approaches for the future.²⁴

Table 1.1 Properties of nanoparticles in electrochemical biosensors.
 Reproduced from Ref [24] Killard, A. J.; Smyth, M. R. *Surfactant Science Series* **2003**, 111, 451-497.

Function	Properties	Typical Nanoparticles	Sensor Advantages	Example
1	Bio - compatibility	Metal (Au,Ag) Oxide (SiO ₂ , TiO ₂)	Enhanced stability	Antibody is immobilized onto Au nanoparticles-stable for 100 days ^{75,81}
2	High surface energy.	Metal (Au, Pt)	Improved sensitivity and selectivity	H ₂ O ₂ sensor with Prussian Blue nanoparticle ^{75,82}
3	Conductivity of tiny dimensions	Metal (Au, Ag)	Direct electrochemistry of proteins, improved sensitivity	Electron transfer rate for glucose oxidase enhanced by Au nanoparticle ⁸³
4	Miniature size, modifiability	Semiconductor (CdS, PbS) Metal (Au, Ag)	Improved sensitivity, indirect detection	DNA sensor labelled with Ag nanoparticle ⁸⁴
5	Chemical activity	Oxide (MnO ₂)	New response mechanism	Lactate biosensor with MnO ₂ ⁷⁵

1.6.1 Gold Nanoparticles

1.6.1.1 Background

Nanotechnology, nanoscience, nanostructure, nanoparticles are now of the most widely used words in scientific literature. Nanoscale gold particles have been used for over two thousand years for both decorative and medical purposes before their unique properties were discovered.⁸⁵ The science of metal nanoparticles is thought to have started with Faraday's work in 1857.⁷³ Faraday reported a solution, deep red gold in colour when white phosphorous was used to reduce an aqueous solution of chloroaurate (AuCl_4^-). The colour of ruby glass was attributed to the minute size of gold nanoparticles.⁷³ Since then, the term colloid⁷³ was derived to describe dispersion of one substance in another and as result gold in solution. It is generally acknowledged that Norio Taniguchi⁸⁶ coined the term "nanoparticle" in 1974 and since then, colloidal gold, gold colloid or soluble gold was then referred to as gold nanoparticles or nano gold (AuNPs). The area has developed through the classical colloid science in the 1900s to today's chemical nanotechnology with precise synthesis methods, well-established structures, advanced characterisation methods and applications in the fields of catalysis, electronics and biology. More than a century after Faraday's discovery, Murray and Chen⁸⁷ showed possibility of attaching thiols to gold nanoparticles. This resulted in the preparation of stable gold nanoparticles with a precisely known molecular formula. AuNPs are the most studied of all metal nanoparticles due to their stability; furthest developed synthesis methods, biocompatibility, and attractive optical and electronic properties as well as their electrochemical response.⁷³

1.6.1.2 Synthesis and Structure of AuNPs

Nanoparticle syntheses in the liquid phase are routinely prepared by chemical reduction of a suitable metal salt such as AuCl_4^- , leading to nucleation and formation of nanoparticles. As already mentioned, Michael Faraday was the first to reduce an aqueous solution of AuCl_4^- with white phosphorous. Since

then there has been many routes reported to prepare Nanosized gold colloids using a number of different reducing agents. However, only two preparation methods have become well established.

In the preparation of nanoparticles, the particles need to be coated with a stabilising layer to terminate the growth and prevent aggregation. The reliable Turkevich⁸⁸ synthesis uses sodium citrate as both the reductant and stabiliser. Gold salt is boiled together with citrate and results in water soluble particles with diameters of 10 - 15 nm.⁸⁸ Citrate-stabilized particles are still widely employed due to their simple preparation method and outstanding visibility in microscopy images. However, they are not stable in dry form and their time for long-term stability in solution is limited.

One of the most widely used methods is the innovative 2 phase Brust - Schiffrin method. Self-assembled monolayers of thiols are well known to form a strong covalent bond on gold⁶⁵ and are therefore an excellent choice as stabilisers. Brust and Schiffrin⁸⁹ developed a synthesis method which combined Faraday's two phase reduction method with the self-assembly of thiols on gold. This experiment resulted in stable, thiolate-protected gold nanoparticles that can be isolated, re-dispersed, purified and can be analytically characterised. The two-phase reduction allows aqueous borohydride to reduce AuCl_4^- in toluene in the presence of stabilizing thiols.⁸⁹ The reduction and surface stabilization occurs simultaneously. Thiol was added to the separated toluene phase and the resulting polymer gold-thiol complex was reduced by slowly adding aqueous sodium borohydride under vigorous stirring. The reaction was then allowed to proceed for three hours. Thiolated ligands are attached to provide a strong interaction between the sulphur of the thiolate ligands and the gold, therefore facilitating the formation of a protective layer around the particle. This protective layer is responsible for the superior stability. The original Brust - Schiffrin method used dodecanethiolate as stabilizing ligand with equal molar amounts of gold and thiol and yielded particles with diameters in the range of 1-3 nm.⁸⁹

1.6.1.3 Application of gold nanoparticles for DNA sensors

Gold nanoparticles (AuNPs) are well-known low-dimensional functional materials with large surface-to-volume ratios and are biocompatible with biosystems.⁹⁰ The analysis of electrical DNA hybridization biosensors is usually based on the identification of the target gene by the formation of the a double stranded hybrid with its complementary nucleic acid DNA probe.⁹¹ Gold nanoparticles offer high sensitivity through amplified transduction of the oligonucleotide interaction. There has been much interest in the application of AuNPs and Merkoci *et al*^{91,92} has excellent reviews on the electrochemical sensing of DNA using AuNPs. Figure 1.12 is a schematic of the most important novel strategies for DNA detection systems based on AuNPs.⁹¹ These approaches consist of (A) the electrochemical recognition of AuNPs label by detecting the released gold ions after acidic dissolving; (B) direct detection by stripping voltammetry of the AuNPs anchored onto the surface of a conventional genosensor; (C) conductometric detection of silver enhancement; (D) enhancement of AuNPs anchored to conventional genosensor surface by using silver or gold; (E) AuNPs as carriers of other AuNPs; (F) using AuNPs as carriers for other electroactive labels.⁹¹

Crumbliss *et al*,³⁹ were the first to show the enzymatic activity on colloidal Au sols. This biomolecule nanoparticle conjugate was well retained when deposited onto conducting matrixes. As a result of these findings, AuNPs have been extensively used in the fabrication of HRP biosensors to detect hydrogen peroxide. Chen and co-workers,⁹³ were the first to attach gold nanoparticles onto gold electrodes. They investigated H₂O₂ reduction in the presence of catechol as a mediator using HRP-labelled Au colloids attached to a cysteamine monolayer on gold.

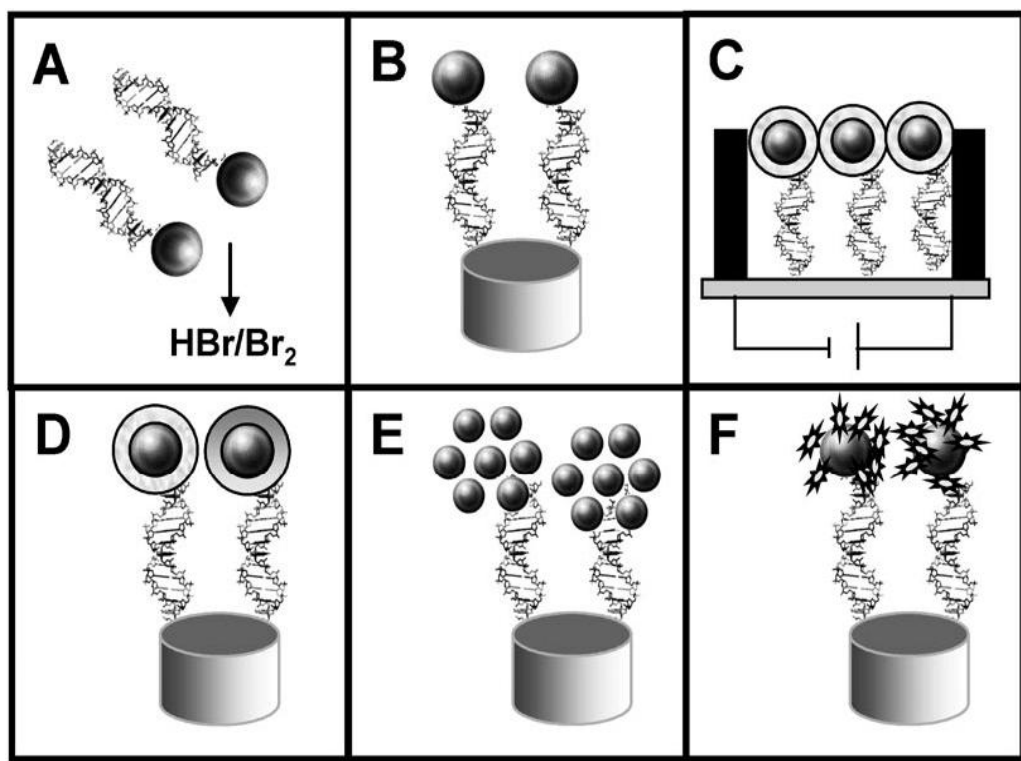


Figure 1.12 Schematic of the different approaches used for the integration of AuNPs into DNA biosensors: A) Previous dissolving of AuNP by using HBr/Br₂ mixture followed by Au(III) ions detection; B) direct detection of AuNPs anchored onto the surface of the genosensor; C) conductometric detection, D) enhancement with silver or gold followed by detection; E) AuNPs as carriers of other AuNPs; F) AuNPs as carriers of other electroactive labels. Reproduced from Ref [91] Castañeda, M. T.; Alegret, S.; Merkoçi, A. *Electroanalysis* **2007**, *19*, 743-753.

Wang⁹⁴ and Limoges⁹⁵ both reported the use of colloidal gold labels for the electrochemical detection of DNA hybridisation in **2001**. The AuNPs were captured to the hybridised target DNA, and anodic stripping was then performed to electrochemically measure the metal tracer. Picomolar detection was obtained from this highly sensitive technique. Wang then went on to report electrochemical genosensors based on AuNPs labels, which could be amplified by the catalytic electrodeposition of silver and its subsequent

stripping. The enhancement of the silver and the electrochemical potentiometric stripping detection proved to have a better detection limit (femtomolar range), based on the precipitation of silver on AuNPs tags and its dissolution (in HNO_3).^{96,97} However the HBr/Br_2 solution used in these experiments is highly toxic and therefore methods based on direct electrochemical detection of AuNPs tags, which replace the chemical oxidation agent, have been reported.

Enhancements by precipitation of silver or gold onto the AuNPs labels have been reported so as to achieve amplified signals and lower detection limits.⁹⁸ For instance, Fang *et al*,⁹⁹ demonstrated that an electrochemical detection method for analyzing sequence-specific DNA using AuNPs marked DNA probes could be made possible and subsequent signal amplification steps could be provided by silver enhancement. The assay relied on electrostatic adsorption of the immobilised oligonucleotides onto a glassy carbon electrode (GCE) with a mercaptohexyl group at the 5'-phosphate end onto a 16 nm diameter gold nanoparticle. After silver deposition onto the AuNPs, binding events between the capture and target DNA were monitored by the differential pulse voltammetry signal of the great number of silver atoms anchored onto the hybrids at the electrode surface. The self assembled cysteamine modified gold electrode showed that the detection of the single strand DNA was 10 times larger on this modified electrode than original bare gold electrode. A detection limit of 50 pM of complementary oligonucleotides was achieved.⁹⁸

Electrogenerated chemiluminescence (ECL) can also be employed to identify the signal amplification of electroactive molecules. Zhou and co-workers¹⁰⁰ have invented a DNA biosensor based on amplified voltammetric detection of DNA hybridization via oxidation of ferrocene caps on gold nanoparticle / streptavidin conjugate. The AuNPs/streptavidin conjugates were covered with 6-ferrocenylhexanethiol and then were attached onto a biotinylated DNA detection probe of a sandwich DNA complex. The DNA strands processes elasticity properties and therefore the ferrocene caps on AuNPs/streptavidin conjugates were positioned in close proximity to the DNA capture probe/hexanethiol modified electrode. Reversible electron transfer reactions

reported detection level as low as 2.0 pM for the oligodeoxynucleotide samples.¹⁰⁰ Fan⁹⁰ and Zhang¹⁰¹ have also fabricated some AuNPs-based electrochemical DNA sensors. The novel sensitive ECL method for the detection DNA hybridization based on AuNPs, carrying multiple ECL probes has reported a limit of detection of 5.0×10^{-12} mol L⁻¹ for target DNA.¹⁰¹ Abouzar *et al*¹⁰² have developed a label-free electrical detection of DNA hybridisation functionalised with AuNPs.

All these reports outline the recent developments of electrochemical deposition of AuNPs on a gold disc substrate to build novel HRP-based amperometric sensors. The deposition of AuNPs on gold disc electrodes have been used as a powerful procedure for construction of well defined chemical interface due to its simplicity, versatility, and convenience. In present work, we have fabricated an electrochemical DNA biosensor for detection of *Staphylococcus aureus* (S.aureus) sequence with the amplification of gold nanoparticles. The combination of the AuNPs and the enzymatic amplification of the electrochemical signal resulted in a highly sensitive detection of ss-DNA. AuNPs were firstly electrodeposited on the surface of the gold electrode to increase the electrode surface area increasing the amount of the capture strand DNA so as to enhance the hybridisation of the sequence specific target DNA. HRP labelled DNA was used to monitor the DNA hybridization event by measuring the current required to reduce hydroquinone oxidised during the regeneration of the HRP label. This DNA biosensor shows a higher sensitivity and selectivity.

1.7 CONDUCTING POLYMERS

A detection system for DNA using conducting polymers (CP) such as polyaniline (PANI) and PEDOT has been explored in this thesis.

1.7.1 History of conducting polymers

Polyacetylene is the simplest conjugated organic polymer and hence is used extensively to model mechanisms of electrical conduction for such systems.¹⁰³ Various models explain electrical properties of polymers in terms of delocalised charge carriers which are free to propagate along the polymer backbone, namely soliton pairs, polarons and bipolarons depending on the polymer as illustrated in Figure 1.13.¹⁰⁴

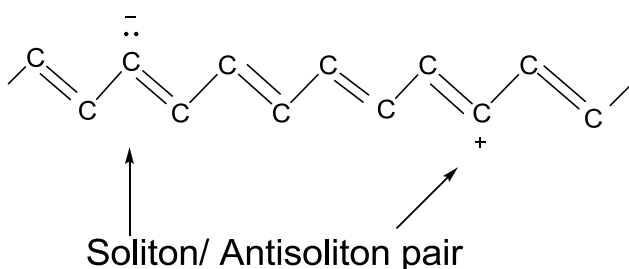
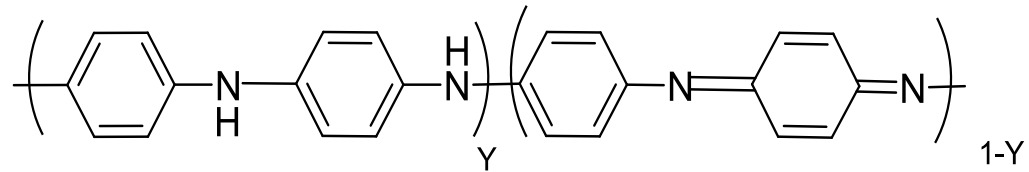


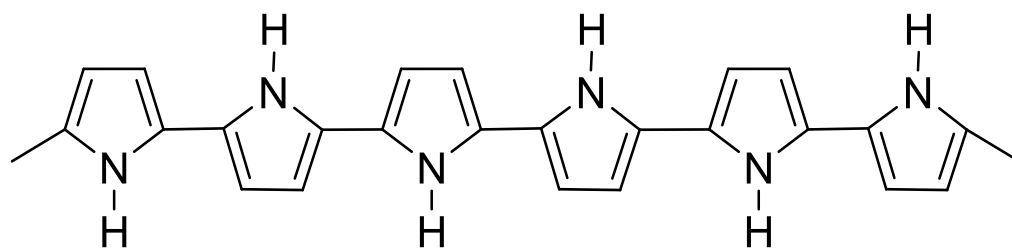
Figure 1.13 Schematic representation of the conduction mechanism in Polyacetylene. Reproduced from Ref [104] Kaiser, A. B.; Park, Y. W. *Current Applied Physics* **2002**, 2, 33-37.

After the discovery of polyacetylene there has been a great interest into the research of conducting polymers and many new polymers have been synthesised.¹⁰⁵ Many conjugated polymers with varying degrees of functionality have been produced with the most common being polyaniline (PANI),^{106,107} Polythiophene (PTh)¹⁰⁸ and Polyrrole (PPy).¹⁰⁵ These structures can be seen in Figure 1.14. These remarkable new materials exhibit the electrical and optical properties of metals or semiconductors whilst retaining the attractive mechanical properties and processing advantages of organic polymers. The essential structural characteristic of all conjugated polymers is

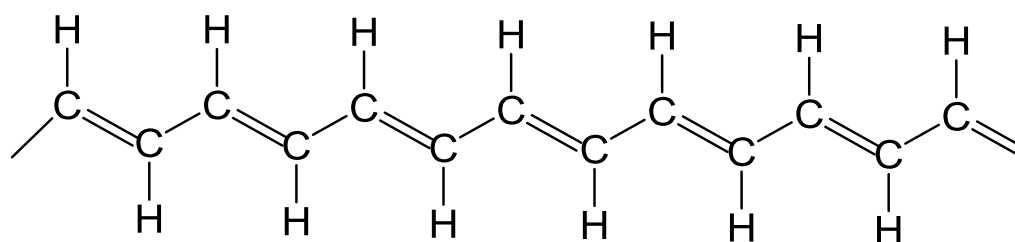
their quasi-infinite π system extending over a large number of recurring monomer units. This extended π – conjugated system of the conducting polymers have single and double bonds alternating along the polymer chain. This feature results in materials with a directional conductivity, which is strongest along the axis of the chain.¹⁰⁹ The resulting higher values of electrical conductivity of the organic polymers have led to the collective name “synthetic metals”.¹⁰⁸



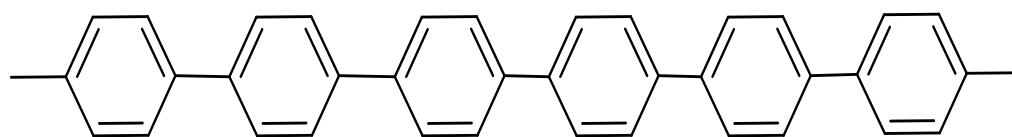
Polyaniline



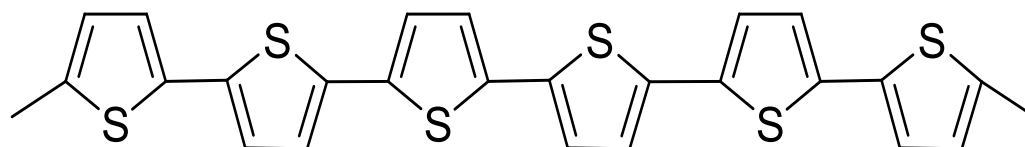
Polypyrrole



Polyacetylene



Polyphenylene



Polythiophene

Figure 1.14

Structures of some conducting polymers commonly used in biosensors. Reproduced from Ref [110] Wallace, G. G.; Spinks, G. M.; Kane-Maguire, *Conductive Electroactive Polymers: Intelligent Materials Systems, Second Edition* 2nd Edition. 2002, 224.

1.7.2 Synthesis of conducting polymers

Polymers can be synthesised in a number of ways including cationic, anionic, radical chain growth, co-ordination polymerisation, step growth polymerisation and electrochemical polymerisation.¹¹⁰ Electrochemical polymerisation includes suitable monomers being electrochemically oxidised to create active species which react to form a conjugated polymer backbone.¹⁰⁸

Typically, conducting polymers such as polypyrrole, polythiophene and polyaniline are prepared from oxidising a suitable monomer (Figure 1.15). Other reports have reviewed conducting polymer having photochemical or enzymatic oxidative polymerisations.¹⁰⁵

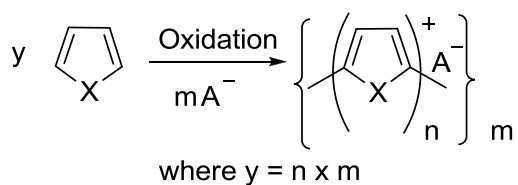


Figure 1.15 Oxidation of pyrrole to form polypyrrole (X = NH) or thiophene to form polythiophene (X = S). Reproduced from Ref [110] Wallace, G. G.; Spinks, G. M.; Kane-Maguire, *Conductive Electroactive Polymers: Intelligent Materials Systems, Second Edition* 2nd Edition. **2002**, 224.

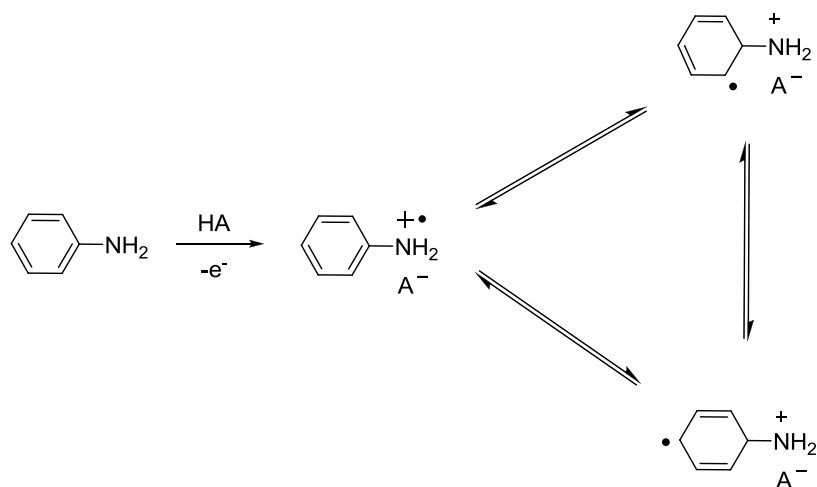
1.7.2.1 Electrochemical polymerisation of aniline

In this process, a film is deposited onto a working electrode. This method is beneficial as it provides greater control over the rate of polymerisation. The insertion of dopant anions is greatly enhanced as any anion present in the reaction can be easily incorporated into the polymer to maintain electrical neutrality. Polymerisation of conducting polymers is identified as a free radical propagation reaction and consists of a number of steps.

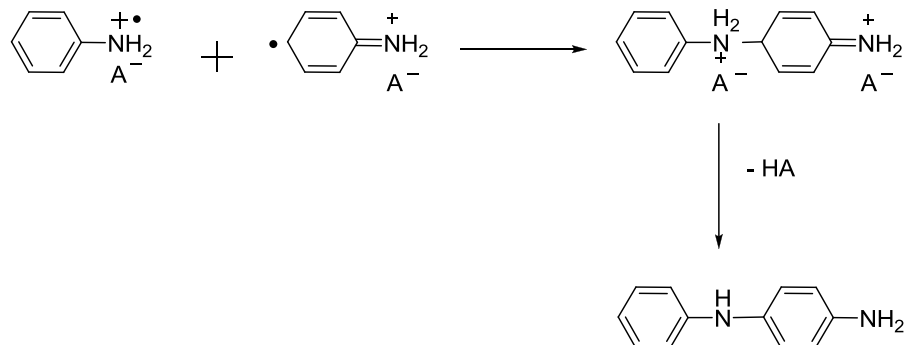
- Step 1: Monomer is oxidised. A radical cation is formed in three resonance forms.
- Step 2: The oxidised aniline species, with the radical cation centred on the nitrogen atom, couples with oxidised aniline which has an unpaired electron centred in the para position. This forms a dicationic species. Deprotonation of this species results in a neutral dimer.
- Step 3: This neutral dimer is then oxidised which results in a radical cation centred on the nitrogen atom. This then couples with oxidised aniline with an unpaired electron centred in the para- position which therefore results in chain propagation.¹⁰⁶

These steps are illustrated in Figure 1.16

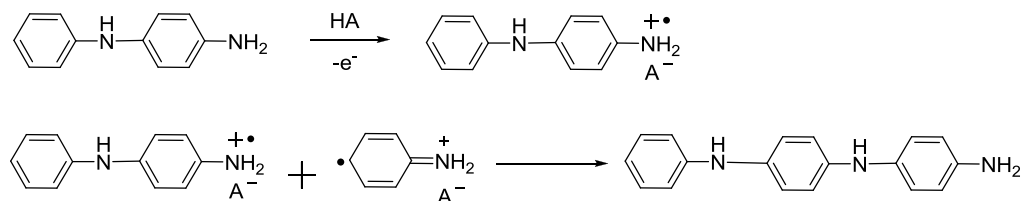
Step 1: Oxidation of Monomer



Step 2: Radical Coupling and Re-Aromatisation



Step 3: Chain Propagation



Step 4: Oxidation and Doping of the Polymer

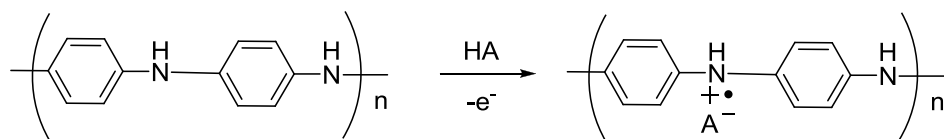


Figure 1.16 Mechanism for electropolymerisation of aniline forming polyaniline. Reproduced from Ref [110] Wallace, G. G.; Spinks, G. M.; Kane-Maguire, *Conductive Electroactive Polymers: Intelligent Materials Systems, Second Edition* 2nd Edition. 2002, 224.

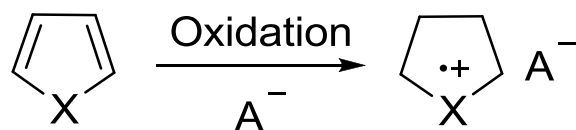
1.7.2.2 Electrochemical polymerisation of 5 membered heterocyclic thiophene

In this process, a film is deposited onto a working electrode. This method is beneficial as it provides greater control over the rate of polymerisation and has the advantage of reproducible product. The insertion of dopant anions is greatly enhanced as any anion present in the reaction can be easily incorporated into the polymer to maintain electrical neutrality. Polymerisation of conducting polymers (Figure 1.17) is identified as a free radical propagation reaction and consists of a number of steps.

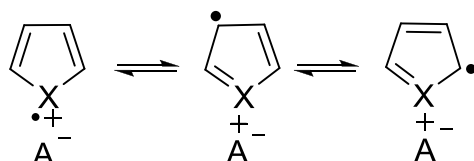
- Step 1: Monomer is oxidised. A radical cation is formed in three resonance forms.
- Step 2: The α - radical which is the most stable of this resonance form couple with another α - radical forming a dicationic dimer.
- Step 3: This dicationic dimer undergoes a deprotonation reaction which leaves a neutral dimer.
- Step 4: This neutral dimer is then oxidised to a radical cation. The dimer couples with other radical cations leading to chain propagation. When the chain reaches a certain length, the chain becomes insoluble and precipitates onto the electrode surface.

The generally accepted mechanism of polymerisation of PEDOT is similar to polypyrrole, which is shown above in Figure 1.17. However, unlike pyrrole, only the α - α coupling of the 3, 4-ethylenedioxythiophene is expected due to the blocked structure of the monomer.¹¹⁰

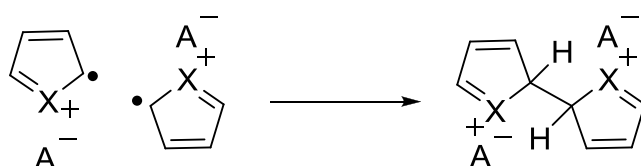
Step 1: Monomer Oxidation



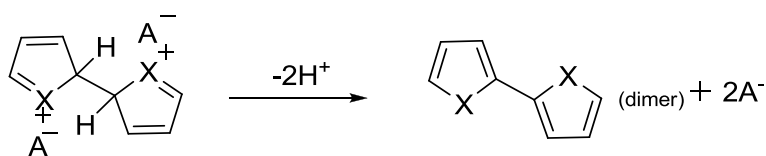
Resonance forms



Step 2: Radical-Radical Coupling



Step 3: Deprotonation / Re-Aromatization



Step 4: Chain Propagation

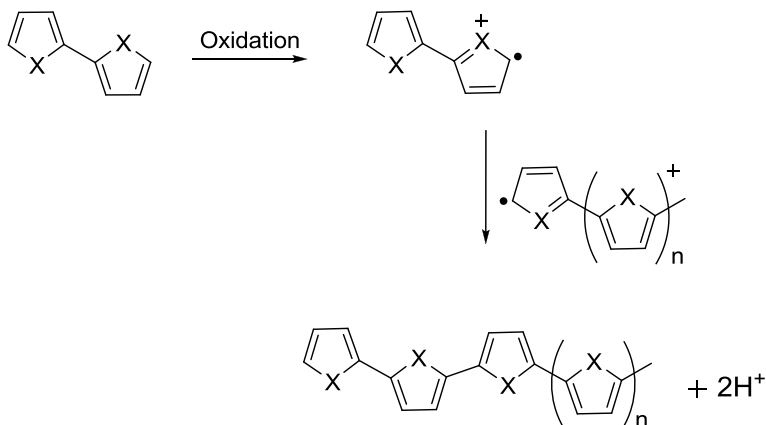


Figure 1.17

Mechanism of polymerisation of pyrrole (X=NH) and thiophene (X=S) forming polypyrrole and polythiophene. Reproduced from Ref [110] Wallace, G. G.; Spinks, G. M.; Kane-Maguire, *Conductive Electroactive Polymers: Intelligent Materials Systems, Second Edition* 2nd Edition. **2002**, 224.

1.7.2.3 Chemical polymerisation of conducting polymers

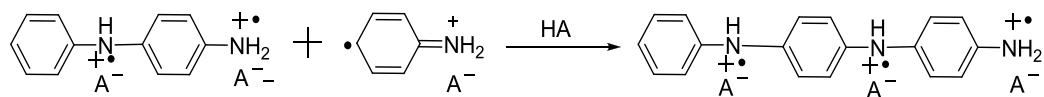
Chemically synthesised conjugated polymers start as insulators in the neutral state, and through oxidation or p-doping or, in a small number of cases n-doping, the required mobile charge carriers gives rise to the conducting form of the polymer.¹¹¹

Chemical oxidants such as FeCl_3 or $(\text{NH}_4)_2\text{S}_2\text{O}_8$ are used in chemical polymerisation to oxidise the monomer and provides the dopant anion. Chemical oxidation often results in the formation of conducting polymer powder. However, it can result in lower conductivity than electrochemically prepared conducting polymer. This approach is used in many areas of industry (DSM, Mitsubishi Rayon, Ormecon Chemie) but they are limited by the number of oxidants that they can use which will oxidise the monomer and provide a suitable dopant. Another disadvantage of this technique is that there is a lack of control over the potential within the reaction mixture, which can lead to over oxidation of the polymer and may give rise to poor doping control.^{105, 112}

1.7.2.3.1 Chemical polymerisation of aniline

For polyaniline, the chemical polymerisation mechanism is completely different to that of the electrochemical polymerisation. The difference is seen in the chain propagation and product formation steps and the initial product formed is pernigraniline salt.¹⁰⁶ This pernigraniline salt is reduced in a subsequent reaction with free aniline, which results in emeraldine salt and a radical cation of aniline.¹⁰⁶ The chemical polymerisation of aniline is shown in Figure 1.18.

Propagation of Chain



Reduction of Pernigraniline Salt to Emeraldine Salt

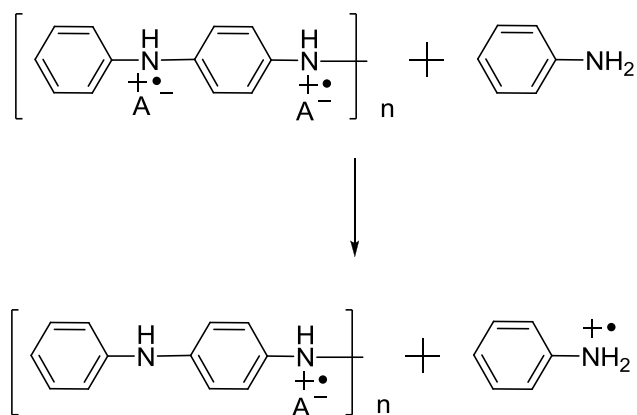


Figure 1.18 Mechanism for the chemical polymerisation of aniline forming polyaniline. Reproduced from Ref [110] Wallace, G. G.; Spinks, G. M.; Kane-Maguire, L. A. P. 2nd Edition. **2002**, 224.

1.7.2.3.1 Chemical polymerisation of PEDOT

Poly (3,4 – ethylenedioxythiophene) or PEDOT may also be synthesised chemically, though materials produced by electrochemical synthesis variants generally have superior conductivity and mechanical properties. PEDOT has a neutral backbone in the reduced state and is positively charged in the oxidised state. To obtain electro neutrality, counter anions are required to diffuse into the polymer layer during charging and also out of the polymer during neutralisation.¹¹¹ Significant changes in the polymer species can be characterised very easily. Chemical synthesis of PEDOT is typically favoured when a large amount is required.¹¹¹ Media such as H₂O, Et₂O, EtOAc, EtOH and MeCN as well as an oxidizing agent such as FeCl₃, Na₂S₂O₈, H₂O₂ and I₂ are used. Once polymerisation is complete, the oxidant must be washed away and the polymer is typically suspended in solution. For applications utilising soluble conducting polymers, the PEDOT is drop cast as a film and doped into and electrically conductive state.

Chemical oxidative polymerisation of the EDOT monomer has been carried out using several methods and oxidants. Corradi *et al*,¹¹³ have previously synthesised PEDOT by using FeCl₃ and Ce(SO₄)₂ as oxidants. They discovered that a large amount of FeCl₃ was required to find a reasonable yield with a high conductivity. The chemical synthesis of PEDOT has also been demonstrated by Yogesh *et al*,¹¹⁴ where FeCl₃ was used as the oxidant and the oxidising power of the reaction solution was changed by using solvent mixtures such as ammonium persulfate and or by adding FeCl₂. These approaches resulted in a highly conductive polymer (>50 S cm⁻¹). Leeuw and co workers¹¹⁵ used ferric tosylate at an elevated temperature (110 °C) in combination with imidazole as a base, and formed a black and insoluble PEDOT film that demonstrated conductivities of up to 550 S cm⁻¹.

1.7.2.4 Vapour polymerisation of conducting polymers

Several researchers¹¹⁶⁻¹¹⁸ have reported a method of polymerisation which involves simple vapour phase deposition. Vapour Phase Polymerisation (VPP) has been used for conducting polymers and was first described by Mohammadi *et al.*¹¹⁹ This had been used as a chamber vapour deposition (CVD) process using FeCl₃, H₂O₂ as oxidising agents for the polymerisation of pyrrole films. Since then it has been adapted for the distinct formation of surface patterns of polypyrrole using patterned copper converted to CuCl₂ as the oxidising agent.¹²⁰

Ueno *et al.*¹²¹ were the first to report VPP being used for *in situ* polymerisation of polypyrrole inside a number of different non-conducting polymers and rubbers. A conducting composite was made by exposing PVC blended with FeCl₃ to pyrrole vapours. Fu *et al.*¹²² showed that Fe(III) tosylate should be used as an oxidising agent for VPP for pyrrole in a polyurethane foam. Films with conductivities of approximately 70 S/cm were obtained using FeCl₃ as the oxidising agent.¹²³

This new technique has produced materials with higher conductivity, improved ordering, stability and controllable porosity at the nanoscale. Overall, these improved properties have enhanced the potential of these materials for electroanalytical applications.^{115,124-127}

1.8 SELF ASSEMBLED MONOLAYERS OF ALKANETHIOLS ON METALS

A self assembled monolayer (SAM) is a well organized monolayer formed by attachment of the head group of a molecule (e.g. the SH of an alkanethiol) as well as stabilising lateral interactions.⁶⁵ SAMs have become the focus of intensive investigation as they provide a facile means of defining the chemical composition and structure of a surface.¹²⁸ As a result, a number of reviews¹²⁹⁻¹³¹ and book chapters¹³² have been dedicated to the research of self-assembled monolayer formation, substrate preparation, surface characterisation and a wide area of applications (wetting, adhesion, biosensor, nanotechnology). A major objective is to develop new substrates for applications in DNA biosensors based on the formation of DNA containing SAMs on metal substrates.

As described in Section 1.3, self-assembly is an attractive choice for the immobilisation of thiolated probe DNA at surfaces. Most of the work on self-assembled monolayers has been focused on SAMs of alkanethiols on gold.¹²⁹ The high affinity of the sulphur head group for a metal substrate and the high strength of the interaction between the two is one of the reasons for the use of SAMs based on alkanethiols in biosensors. Self organisation is achieved when the alkyl chains align themselves by van der Waals forces and form a compact monolayer as illustrated in Figure 1.19.

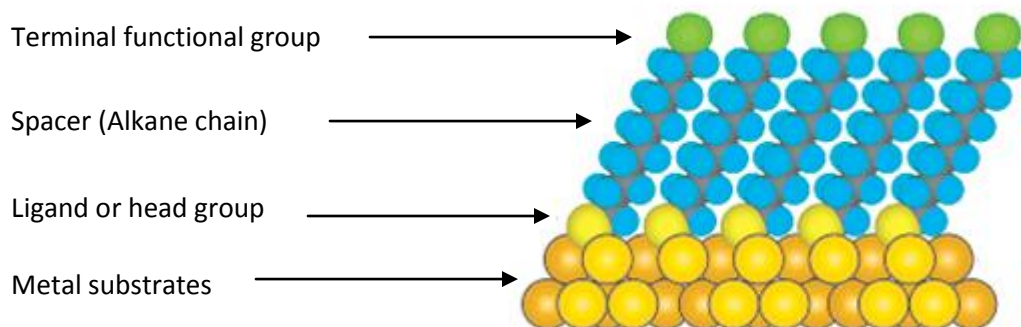


Figure 1.19 Schematic representation of self-assembled monolayer of alkanethiols on metal substrate. Reproduced from Ref [129] Love, J. C.; Estroff, L. A.; Kriebel, J. K.; Nuzzo, R. G.; Whitesides, G. M. *Chemical Reviews*. **2005**, *105*, 1103-1169.

Gold is the most widely used substrate for alkanethiol based SAMs. The first reports of SAMs formed on gold substrates were highly focused on the preparation of atomically flat, well-defined gold surfaces. Alkanethiol monolayers are readily formed on the gold surface in a stable, organized and densely packed manner. The adsorbed alkanethiol molecules lose their hydrogen atom from the thiol groups and form the new thiolate-gold bonds at an Au-S interface. By varying the chain length of the alkanethiols the well-defined thickness of the monolayer can be controlled. The chain acts as a physical barrier and alters electronic conductivity and local optical properties. Yokoyama¹³³ and co-workers have used co-adsorption of the alkane thiols to orientate DNA, so that it stands perpendicular to the metal surface. The main axes of each molecule are tilted by an angle of approximately 30° from the normal to the structure as shown in Figure 1.19. The formations of these SAM are based on the thiolate-gold bonds and the lateral interactions among the aliphatic chains of neighbouring alkanethiol molecules. These new bonds are thermodynamically favourable and each bond has been reported to release approximately 40-50 kcal/mol.⁶⁵ Gold is a metal that can be handled in air without the formation of an oxide surface layer, and can survive harsh chemical treatments such as those used to remove organic contaminants during cleaning.

1.8.1 Thiol tethered DNA

Gold surfaces have been used in biosensor applications for a number of years, since they can be easily modified with self assembled monolayers of ω functionalised thiols¹³⁴. Single or double stranded DNA (for certain lengths only) modified with a thiol is similar to long chain n-alkanethiols. They form uniform and closely packed monolayers on the gold electrode surface. Thiolation of ssDNA is most commonly used for the attachment of capture DNA followed by the packed self assembly onto surface such as gold, silver or copper.¹³⁵ The sulphur donor atoms strongly chemisorbs onto the gold (typical bond energy is 145-188 KJmol⁻¹) and the self assembly process then begins.¹³⁶ Each of the sulphur atoms is coordinative bound to three Au atoms (the sulphur is Sp³ hybridised). The thiol chain is therefore tilted with respect to the gold surface by approximately 20 to 4 degrees.¹³⁴

Previous reports¹³⁷ have discussed the effect of the length and the presence of an anchoring group on the assembly of DNA single strands on gold surfaces. The immobilisation of single-stranded oligonucleotides containing a 5'-hexanethiol anchoring group for lengths from 8 to 48 bases has been discussed. It has been shown that the oligonucleotide immobilisation is enhanced in the presence of a thiol group. However, the enhancement is reduced for longer DNA strand lengths.¹³⁷ The surface coverage begins to decrease with DNA strands longer than 24 bases, as a less ordered arrangement of the DNA is observed.

The great advantage of thiol tethered DNA is that the surface coverage of the immobilised DNA can be controlled by adjusting the immobilisation time and the concentration of the short chain alkyl thiols.¹³⁷ Typically, gold substrates with DNA monolayers are treated with a dilute "backfiller" i.e., 6-mercapto-1-hexanol (MCH) to improve the quality of the sensor. Co-immobilization of this OH-terminated thiol ensures the desired orientation of the immobilised ssDNA at the electrode surface, therefore increasing hybridisation efficiency. The strong affinity of the thiol group of the MCH for gold results in the displacement of less strongly, non-specifically adsorbed DNA bases. The negatively

charged DNA backbone is repelled by the net negative dipole of the alcohol terminus, thus assisting the DNA strands into the solution.¹³⁷

1.9 THEORITICAL BACKGROUND

1.9.1 *Basic features of the electrochemical process*

The electrochemical reaction rate is determined by a number of steps

1. Transport of electro active species to the electrode surface.
2. Charge Transfer at the surface.

Below is an example of an electrochemical reaction:



The conversion of the Oxidised form (Ox) to the Reduced form (Red) involves:

- a) The diffusion of Ox from the bulk solution to the electrode surface;
- b) Transfer of the electrons at the electrode surface to form Red;
- c) Diffusion of Red away from the electrode surface into the bulk solution.

The overall rate of the electrode reaction depends upon the slowest reaction involved in the above process i.e., the rate determining step.

1.9.2. *Cyclic voltammetry*

Cyclic voltammetry allows the oxidation and reduction processes at an electrode to be investigated by applying a triangular potential-time sweep with a given sweep rate to the working electrode. In this electrochemical technique, a potential region is scanned and the resulting current produced is measured. It is this voltammogram that is used for investigating analyte concentrations of redox properties.⁶⁴

Voltammetry is an important analytical technique due to the significant information it can supply about the thermodynamics and kinetics of electron transfer across the electrode / film interface.¹³⁸ As electron transfer steps are not purely thermodynamic processes, the current response is often influenced by kinetics. When the kinetics of the system are fast (reversible systems) the Nernst equation (Equation 1.2) describes the current response. However, when the kinetics are slower (irreversible systems) the current is dominated by the rate of electron transfer and it is necessary to interpret the response in terms of an electron transfer theory such as Butler-Volmer or Marcus theory. Diffusion of the electro-active species also influences the signal, although this parameter is removed upon surface confinement of the redox species.

$$E = E^{\circ} + \frac{RT}{nF} \ln \frac{C_O}{C_R} \quad \text{Equation 1.2}$$

A typical CV for a solution species is shown in Figure 1.20, together with the important analytical features. The CV was recorded using a gold working electrode in a quiescent solution. The potential of this working electrode is scanned with respect to a reference electrode, for example the Ag/AgCl (saturated KCl) electrode, using a potentiostat. Finally, an auxiliary electrode, typically a platinum wire, acts as a current source or sink. This prevents degradation of the reference electrode potential. Ohmic drop effects (the sum of the current and resistance between working and counter electrodes) can also be decreased by placing the auxiliary electrode near the working electrode.

1.9.2.1 CV of solution phase species

Consider a solution containing the oxidized form of the redox couple, Ox. As the electrode is scanned, initially no Faradic reaction takes place. When the potential approaches the redox potential of the species, a rapid increase in cathodic current develops due to the reduction of the redox couple. The sharp response is a result of the logarithmic characteristic of the Nernst equation (Eq. 1.2). At the formal potential, there exists a 50% oxidized and 50 % reduced

species at the electrode surface. As the layer grows, the flux of unreacted species to the electrode surface falls which results in the current decay as the diffusion layer extends farther away from the surface. When the potential is switched, the current remains cathodic, as the potential is still positive enough to reduce the redox couple. Once the potential becomes sufficiently negative so that reduction can no longer occur, the current goes to zero and then becomes anodic. The anodic current results from the oxidation of the reduced species within the depletion zone. The anodic current peaks and then decreases as this reduced species are consumed by the oxidation reaction.¹³⁹ Steady- state behaviour can be seen at microelectrodes as the diffusion to these small electrodes is extremely efficient. The potential is switched at a value beyond the redox potential and the solute is oxidised or reduced as in the first scan. The scan rate (v) can vary, typically from 50 mVs^{-1} to 100 Vs^{-1} .

The voltammogram in Figure 1.20 shows important parameters such as the anodic and cathodic peak potentials $E_{p,a}$ and $E_{p,c}$; the anodic and cathodic peak currents $i_{p,a}$ and $i_{p,c}$; and the half-peak potentials, which are the potentials $E_{1/2,a}$ and $E_{1/2,c}$, at which the cathodic and anodic currents reach half their peak values. E_{λ} is the potential at which redox switching takes place. These parameters provide all the significant information about the reaction that takes place at the electrode surface. The independent variables are voltage, scan rate and the range of potential over which the scan is made.¹⁴⁰

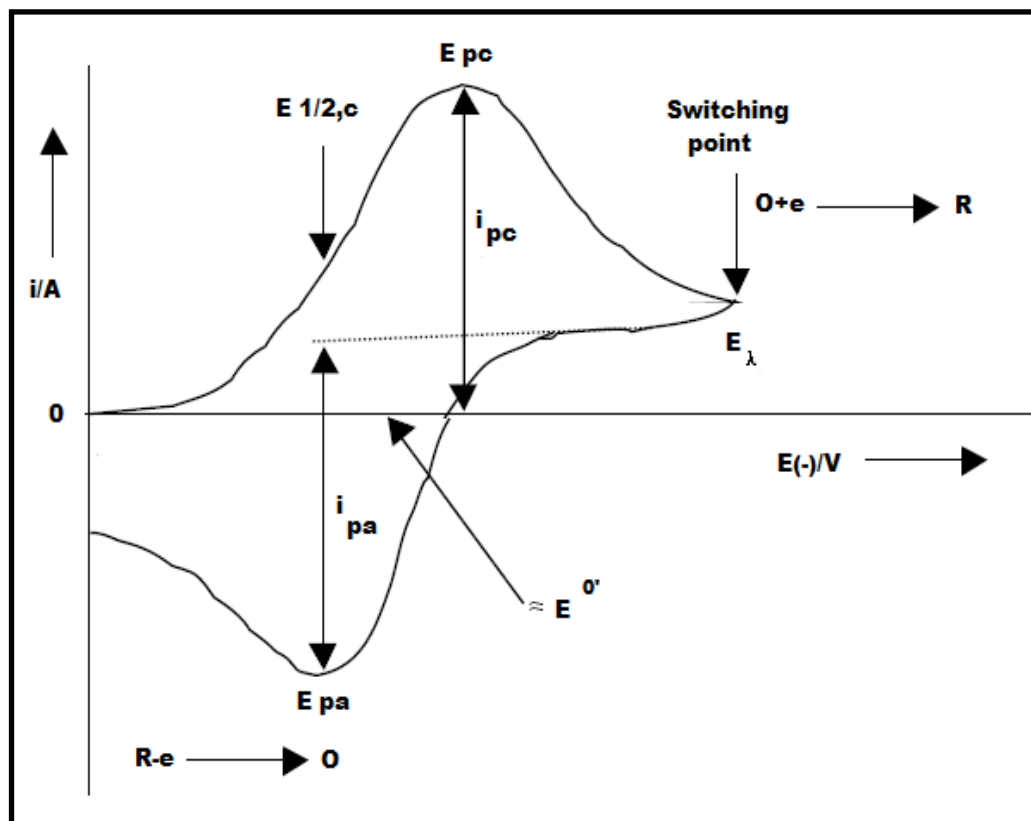


Figure 1.20 Diagnostic features of a cyclic voltammogram. E_{pa} , i_{pa} , E_{pc} , i_{pc} representing the anodic and cathodic peak potentials and currents respectively for a reversible reaction when a potential scan is applied to redox active species in solution phase. Reproduced from Ref [141] Edmonds, T. E.; Dean, J. R.; Latif, S. *Analytica Chimica Acta* **1988**, 212, 23-30.

A cyclic voltammogram offers a rapid means of determining the redox potentials of the electroactive species and is convenient for evaluating the effect of media upon redox process.¹⁴² The anodic (oxidation) or cathodic (reduction) peak area after subtracting the charging current baseline gives the charge for oxidation or reduction of the redox probe.

In many films, electrochemical charge transport occurs by electron self exchange reactions between neighbouring oxidized and reduced sites. The movement of charge compensating counter ions that are mobile within the

layer accompanies this electron hopping process. The effective diffusion coefficient, D_{CT} , corresponding to the diffusion of either electron or charge compensating counter ions, can be estimated using the Randles-Sevcik equation, which relates the scan rate to the peak current (i_p) as:

$$i_p = 0.4463nFAC \left(\frac{FvD}{RT} \right)^{1/2} \quad \text{Equation 1.3}$$

In this equation, n is the number of electrons appearing in half-reaction for the redox couple, v is the rate at which the potential is swept (V / sec), F is Faraday's constant (96485 C/mol), A is the electrode area (cm^2), R is the universal gas constant (8.314 J/mol K), T is the absolute temperature (K), and D is the analyte's diffusion coefficient (cm^2/sec). Note that if the temperature is assumed to be 25°C (298 K), the Randles-Sevcik can be written in a more concise form,

$$i_p = 2.69 \times 10^5 n^{3/2} A D^{1/2} v^{1/2} C \quad \text{Equation 1.4}$$

where the constant is understood to have units (i.e., $2.687 \times 10^5 \text{ C mol}^{-1} \text{ V}^{-1/2}$).

The peak potentials are not related to the scan rate for a reversible system but can be altered by the effects of ohmic (or iR) drop. The potential is related to the resistance (R) of the electrochemical cell and the current (i) passing through the cell by Ohm's law. The overall result is a potential that acts to weaken the applied potential by an amount iR . When working with low currents and highly conducting solutions this effect is minimised. If ohmic effects and slow electron transfer are absent and under semi infinite diffusion conditions, $\Delta E_p = \frac{0.059}{n}$ volts at 25°C and the ratio of the anodic and cathodic peak currents should be equal to one.

1.9.3 Potentiostatic techniques

In a potential step experiment, two responses can be recorded, whereby the potential of a working electrode is changed instantaneously and the current time (galvanostatic) or the charge time (potentiostatic) is found. In chronoamperometry, the potential is stepped so as to drive a Faradaic reaction. This potential is held while the current with time is monitored at the electrode (Figure 1.21).¹⁴³ At the initial potential, no significant current flows. At the final potential, the analyte is consumed at the electrode surface. There is a depletion of the concentration of the analyte near the electrode. The current response is shown by a rapid increase followed by decay as the analyte is exhausted and equilibrium is reached.¹⁴⁴ In this case, the charge for reduction is calculated by integrating the area under the current versus time curve within the limits of the initial to final deposition time.

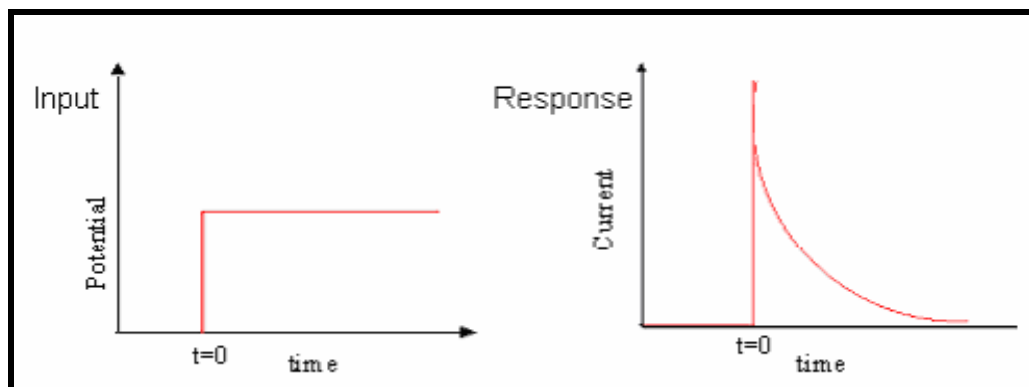


Figure 1.21 Variation of current with time in potentiostatic method. Reproduced from Ref [145] Soreta, T. R.; Strutwolf, J.; O'Sullivan, C. K. *Langmuir* **2007**, *23*, 10823-10830.

1.10 CONCLUSION

Novel materials and detection strategies have been opened up to a whole range of new possibilities for ultra sensitive and automated biological assays.¹⁴⁶ Traditional methods for detecting DNA hybridization methods for example gel electrophoresis and membrane blots, are much too slow and labour intensive.¹⁴⁷ Nucleic acids (NAs) are very small simple molecules, but what is challenging is detecting a particular sequence which contains useful information¹⁴⁷⁻¹⁴⁹ Wide scale genetic testing needs an easy to use, fast, inexpensive, miniaturized analytical device.^{72,150,151}

This thesis describes work on ultrasensitive, selective detection of DNA and this chapter has presented an introduction to the concepts of electrode modification with molecular layers. A brief review of electrochemical DNA biosensors is provided and the electrochemical detection of the hybridisation event has also been discussed. Some of these devices show great promise for obtaining sequence specific information in a quicker easy manner compared to traditional nucleic acid assays.

Electrochemistry offers innovative routes for interfacing the nucleic acid recognition system with the signal generating element and for amplifying electrical signals.¹⁵² Today biosensors offer faster, cheaper and simpler nucleic acid assays. They rely on the immobilization of a single stranded oligonucleotide probe onto a transducer surface to recognize by hybridization its complementary target sequence. This binding of the probe and the target strand is translated into an electrochemical signal.^{56,153,154}

The deposition of gold nanoparticles is described in Chapters 3-6 and an introduction to nanoparticles along with a review of nanoparticles used in the detection of DNA has been provided. The review shows that nanoparticles offer elegant ways for interfacing DNA recognition events with electrochemical signal transduction processes. The high sensitivity of the nanoparticles based

electrical systems gives the possibility of detecting DNA targets without the need for PCR amplification.

As conducting polymers are described in Chapter 4 and 5, a summary of the properties of polyaniline and PEDOT has been presented. The literature relating to the different ways to synthesis these conducting polymers has been reviewed.

1.11 REFERENCES

1. Watson, J. D.; Editor, *Discovering the Double Helix: History of Science; Biotechnology*. **2001**.
2. Smith, E. L.; Hill, R. L.; Lehman, I. R.; Lefkowitz, R. J. *Principles of Biochemistry*, 7th Edition, **1985**, 652.
3. Nelson, D. L.; Cox, M. M. **2004**, , 1200.
4. Ghosh, A.; Bansal, M. *Acta Crystallographica Section D-Biological Crystallography* **2003**, *59*, 620-626.
5. Polsky, R.; Gill, R.; Kaganovsky, L.; Willner, I. *Analytical Chemistry*. **2006**, *78*, 2268-2271.
6. HUANG, X.; QUESADA, M.; MATHIES, R. *Analytical Chemistry*. **1992**, *64*, 967-972.
7. Matveeva, E. G.; Shtoyko, T.; Gryczynski, I.; Akopova, I.; Gryczynski, Z. *Chemical Physics Letters* **2008**, *454*, 85-90.
8. PIUNNO, P.; KRULL, U.; HUDSON, R.; DAMHA, M.; COHEN, H. *Analytical Chemistry*. **1995**, *67*, 2635-2643.
9. Fang, X.; Liu, X.; Schuster, S.; Tan, W. *J. Am. Chem. Soc.* **1999**, *121*, 2921-2922.
10. Fletcher, P.; Andrew, K.; Calokerinos, A.; Forbes, S.; Worsfold, P. *Luminescence* **2001**, *16*, 1-23.
11. Devadoss, A.; Spehar-Deleze, A.; Tanner, D. A.; Bertoncillo, P.; Marthi, R.; Keyes, T. E.; Forster, R. J. *Langmuir* **2010**, *26*, 2130-2135.
12. Knight, A. *Trac-Trends in Analytical Chemistry* **1999**, *18*, 47-62.
13. Li, Z.; Liu, C.; Fan, Y.; Wang, Y.; Duan, X. *Analytical Biochemistry* **2006**, *359*, 247-252.

14. Thiel, A.; Frutos, A.; Jordan, C.; Corn, R.; Smith, L. *Analytical Chemistry*. **1997**, *69*, 4948-4956.
15. Heaton, R.; Peterson, A.; Georgiadis, R. *Proceedings of the National Academy of Sciences of the United States of America*. **2001**, *98*, 3701-3704.
16. Nelson, B.; Grimsrud, T.; Liles, M.; Goodman, R.; Corn, R. *Analytical Chemistry*. **2001**, *73*, 1-7.
17. RAETHER, H. *Springer Tracts in Modern Physics* **1988**, *111*, 1-133.
18. Storhoff, J.; Elghanian, R.; Mucic, R.; Mirkin, C.; Letsinger, R. *Journal of the American Chemical Society* **1998**, *120*, 1959-1964.
19. Polla, D. L.; Francis, L. F. *Annual Review of Materials Science* **1998**, *28*, 563-597.
20. Laenge, K.; Rapp, B. E.; Rapp, M. *Analytical and Bioanalytical Chemistry*. **2008**, *391*, 1509-1519.
21. Jianrong, C.; Yuqing, M.; Nongyue, H.; Xiaohua, W.; Sijiao, L. *Biotechnology Advances* **2004**, *22*, 505-518.
22. Wang, J. *Analytica Chimica Acta*, **2002**, *469*, 63-71.
23. Thevenot, D. R.; Toth, K.; Durst, R. A.; Wilson, G. S. *Pure and Applied Chemistry* **1999**, *71*, 2333-2348.
24. Killard, A. J.; Smyth, M. R. *Surfactant Science Series* **2003**, *111*, 451-497.
25. Pohanka, M.; Skladal, P. *Journal of Applied Biomedicine* . **2008**, *6*, 57-64.
26. Levicky, R.; Horgan, A. *Trends in Biotechnology* . **2005**, *23*, 143-149.

27. Lucarelli, F.; Marrazza, G.; Turner, A. P. F.; Mascini, M. *Biosensors and Bioelectronics* . **2004**, *19*, 515-530.
28. .Palecek, E. *Talanta* **2002**, *56*, 809-819.
29. Kerman, K.; Chikae, M.; Yamamura, S.; Tamiya, E. *Analytica Chimica Acta* **2007**, *588*, 26-33.
30. Drummond, T. G.; Hill, M. G.; Barton, J. K. *Nat. Biotechnology*. **2003**, *21*, 1192-1199.
31. Moeller, R.; Fritzsche, W. *IEE Proc.: Nanobiotechnology*. **2005**, *152*, 47-51.
32. Zhai, J.; Hong, C.; Yang, R. *Biotechnology. Adv.* **1997**, *15*, 43-58.
33. Piunno, P. A. E.; Krull, U. J.; Hudson, R. H. E.; Damha, M. J.; Cohen, H. *Analytical Chemistry*. **1995**, *67*, 2635-2643.
34. Hirschfeld, T. B. Patent Application Country: Application: DE; Patent Country: DE; Priority Application Country: US Patent 3708513, 1987.
35. Watts, H. J.; Yeung, D.; Parkes, H. *Analytical Chemistry*. **1995**, *67*, 4283-4289.
36. Teranishi, T.; Hosoe, M.; Miyake, M. *Advanced Materials* **1997**, *9*, 65-&.
37. Liu, Y.; Lei, J.; Ju, H. *Talanta* **2008**, *74*, 965-970.
38. Yang, Z. S.; Wu, W. L.; Chen, X.; Liu, Y. C. *Analytical Sciences* **2008**, *24*, 895-899.
39. Zhao, J. G.; Henkens, R. W.; Stonehuerner, J.; Odaly, J. P.; Crumbliss, A. L. *J Journal of Electroanalytical Chemistry* **1992**, *327*, 109-119.
40. Collins, A.; Morton, N. E. *Proceedings of the National Academy of Sciences of the United States of America*. **1994**, *91*, 6007-6011.

41. Wang, J.; Polsky, R.; Merkoci, A.; Turner, K. L. *Langmuir* **2003**, *19*, 989-991.
42. Wang, J.; Rivas, G.; Cai, X.; Palecek, E.; Nielsen, P.; Shiraishi, H.; Dontha, N.; Luo, D.; Parrado, C.; Chicharro, M.; Farias, P. A. M.; Valera, F. S.; Grant, D. H.; Ozsoz, M.; Flair, M. N. *Analytica Chimica Acta* **1997**, *347*, 1-8.
43. Magner, E. *Analyst* **1998**, *123*, 1967-1970.
44. Abad-Valle, P.; Fernández-Abedul, M. T.; Costa-García, A. *Biosensors and Bioelectronics*, **2005**, *20*, 2251-2260.
45. Liu, S.; Li, X.; Li, Y.; Li, Y.; Li, J.; Jiang, L. *Electrochimica Acta* **2005**, *51*, 427-431.
46. Liu, H.; Wang, G.; Chen, D.; Zhang, W.; Li, C.; Fang, B. *Sensors and Actuators B: Chemical* **2008**, *128*, 414-421.
47. Mascini, M.; Palchetti, I.; Marrazza, G. *Fresenius J. Analytical Chemistry*. **2001**, *369*, 15-22.
48. Babkina, S. S.; Budnikov, G. K. *Analytical Chemistry*. **2006**, *61*, 728-739.
49. Cai, H.; Cao, X.; Jiang, Y.; He, P.; Fang, Y. *Analytical and Bioanalytical Chemistry*. **2003**, *375*, 287-293.
50. He, P.; Xu, Y.; Fang, Y. *Microchimica Acta* **2006**, *152*, 175-186.
51. Erdem, A.; Ozsoz, M. *Analytica Chimica Acta* **2001**, *437*, 107-114.
52. Ozkan, D.; Kara, P.; Kerman, K.; Meric, B.; Erdem, A.; Jelen, F.; Nielsen, P. E.; Ozsoz, M. *Bioelectrochemistry* **2002**, *58*, 119-126.
53. Ozkan, D.; Erdem, A.; Kara, P.; Kerman, K.; Gooding, J. J.; Nielsen, P. E.; Ozsoz, M. *Electrochemistry Communications*. **2002**, *4*, 796-802.

54. Kara, P.; Kerman, K.; Ozkan, D.; Meric, B.; Erdem, A.; Ozkan, Z.; Ozsoz, M. *Electrochemistry Communications*. **2002**, *4*, 705-709.
55. Kerman, K.; Kobayashi, M.; Tamiya, E. *Measurement Science and Technology*. **2004**, *15*, R1-R11.
56. Gorton, L.; Lindgren, A.; Larsson, T.; Munteanu, F. D.; Ruzgas, T.; Gazaryan, I. *Analytica Chimica Acta* **1999**, *400*, 91-108.
57. Gau, V.; Ma, S.; Wang, H.; Tsukuda, J.; Kibler, J.; Haake, D. A. *Methods*, **2005**, *37*, 73-83.
58. Zhang, Y. C.; Kim, H. H.; Heller, A. *Analytical Chemistry*. **2003**, *75*, 3267-3269.
59. Pividori, M. I.; Merkoçi, A.; Alegret, S. *Biosensors and Bioelectronics* **2001**, *16*, 1133-1142.
60. Williams, E.; Pividori, M. I.; Merkoçi, A.; Forster, R. J.; Alegret, S. *Biosensors and Bioelectronics*, **2003**, *19*, 165-175.
61. Braguglia, C. M. *Chemical and Biochemical Engineering Quarterly* . **1998**, *12*, 183-190.
62. Pividori, M. I.; Merkoçi, A.; Alegret, S. *Biosensors and Bioelectronics*, **2000**, *15*, 291-303.
63. Palecek, E.; Fojta, M. *Analytical Chemistry*. **2001**, *73*, 74A-83A.
64. Bard, A. J. In *Electroanalytical Chemistry*; **1991**; .
65. Nuzzo, R. G.; Allara, D. L. *Journal of the American Chemical Society* **1983**, *105*, 4481-4483.
66. Peterson, A. W.; Heaton, R. J.; Georgiadis, R. M. *Nucleic Acids Research* . **2001**, *29*, 5163-5168.
67. Lei, C.; Hu, S.; Gao, N.; Shen, G.; Yu, R. *Bioelectrochemistry* **2004**, *65*, 33-39.

68. Venkatesh, A. G.; Herth, S.; Becker, A.; Reiss, G. *Nanotechnology* **2011**, *22*, 145301.
69. Zhang, H.; Lai, G.; Han, D.; Yu, A. *Analytical and Bioanalytical Chemistry* **2008**, *390*, 971-977.
70. Park, B. W.; Kim, D. S.; Yoon, D. Y. *Korean Journal of Chemical Engineering* **2011**, *28*, 64-70.
71. Herne, T. M.; Tarlov, M. J. *Journal of the American Chemical Society* **1997**, *119*, 8916-8920.
72. Chen, J.; Miao, Y.; He, N.; Wu, X.; Li, S. *Biotechnology. Adv.* **2004**, *22*, 505-518.
73. Murray, R. W. *Chemical Reviews* . **2008**, *108*, 2688-2720.
74. Wang, J. *Analyst (Cambridge, U.K.)* **2005**, *130*, 421-426.
75. Luo, X.; Morrin, A.; Killard, A. J.; Smyth, M. R. *Electroanalysis* **2006**, *18*, 319-326.
76. Wang, J. *Analytica Chimica Acta*, **2003**, *500*, 247-257.
77. Vaseashta, A.; Dimova-Malinovska, D. *Science and Technology of Advanced Materials*. **2005**, *6*, 312-318.
78. Willner, I.; Willner, B. *Pure and Applied Chemistry* . **2002**, *74*, 1773-1783.
79. Sole, S.; Merkoci, A.; Alegret, S. *Trends in Analytical Chemistry*. **2001**, *20*, 102-110.
80. Merkoci, A.; Alegret, S. *Trends in Analytical Chemistry*. **2002**, *21*, 717-725.
81. Zhuo, Y.; Yuan, R.; Chai, Y.; Tang, D.; Zhang, Y.; Wang, N.; Li, X.; Zhu, Q. *Electrochemistry Communications* **2005**, *7*, 355-360.

82. Fiorito, P. A.; Goncales, V. R.; Ponzio, E. A.; Cordoba de Torresi, S. I. *Chemical Communications* .(Cambridge, U.K.) **2005** , 366-368.
83. Xiao, Y.; Patolsky, F.; Katz, E.; Hainfeld, J. F.; Willner, I. *Science (Washington, DC, U.S.)* **2003**, 299, 1877-1881.
84. Cai, H.; Wang, Y.; He, P.; Fang, Y. *Analytica Chimica Acta*, **2002**, 469, 165-172.
85. Daniel, M.; Astruc, D. *Chemical Reviews* . **2004**, 104, 293-346.
86. Pandey, P.; Datta, M.; Malhotra, B. D. *Analytical Letters* . **2008**, 41, 159-209.
87. Chen, S. W.; Murray, R. W. *Langmuir* **1999**, 15, 682-689.
88. Enustun, B. V.; Turkevich, J. *Journal of the American Chemical Society* **1963**, 85, 3317-&.
89. Brust, M.; Walker, M.; Bethell, D.; Schiffrin, D. J.; Whyman, R. *Journal of the Chemical Society-Chemical Communications* **1994** , 801-802.
90. Lin, L.; Zhou, J.; Zhang, Y.; Lin, Z. *Electroanalysis* **2008**, 20, 1798-1804.
91. Castañeda, M. T.; Alegret, S.; Merkoçi, A. *Electroanalysis* **2007**, 19, 743-753.
92. Merkoci, A.; Aldavert, M.; Marin, S.; Alegret, S. *Trends in Analytical Chemistry*. **2005**, 24, 341-349.
93. Xiao, Y.; Ju, H.; Chen, H. *Analytica Chimica Acta* **1999**, 391, 73-82.
94. Wang, J.; Xu, D.; Kawde, A.; Polsky, R. *Analytical Chemistry*. **2001**, 73, 5576-5581.
95. Authier, L.; Grossiord, C.; Brossier, P.; Limoges, B. *Analytical Chemistry*. **2001**, 73, 4450-4456.

96. Wang, J.; Polsky, R.; Xu, D. *Langmuir* **2001**, *17*, 5739-5741.
97. Wang, J.; Xu, D.; Polsky, R. *Journal of the American Chemical Society* **2002**, *124*, 4208-4209.
98. Cai, H.; Wang, Y. Q.; He, P. G.; Fang, Y. H. *Analytica Chimica Acta* **2002**, *469*, 165-172.
99. Cai, H.; Xu, C.; He, P.; Fang, Y. *Journal of Electroanalytical Chemistry* **2001**, *510*, 78-85.
100. Wang, J.; Li, J. H.; Baca, A. J.; Hu, J. B.; Zhou, F. M.; Yan, W.; Pang, D. W. *Analytical Chemistry*. **2003**, *75*, 3941-3945.
101. Zhang, S.; Xia, J.; Li, X. *Analytical Chemistry*. **2008**, *80*, 8382-8388.
102. Abouzar, M. H.; Poghossian, A.; Pedraza, A. M.; Gandhi, D.; Ingebrandt, S.; Moritz, W.; Schöning, M. J. *Biosensors and Bioelectronics* **2011**, *26*, 3023-3028.
103. Thomas, H. R.; Salaneck, W. R.; Duke, C. B.; Plummer, E. W.; Heeger, A. J.; Macdiarmid, A. G. *Polymer* **1980**, *21*, 1238-1246.
104. Kaiser, A. B.; Park, Y. W. *Current Applied Physics* **2002**, *2*, 33-37.
105. Kanazawa, K. K.; Diaz, A. F.; Geiss, R. H.; Gill, W. D.; Kwak, J. F.; Logan, J. A.; Rabolt, J. F.; Street, G. B. *Journal of the Chemical Society-Chemical Communications* **1979**, , 854-855.
106. Diaz, A. F.; Lee, W. Y.; Logan, A.; Green, D. C. *J Journal of Electroanalytical Chemistry* **1980**, *108*, 377-380.
107. Diaz, A. F.; Logan, J. A. *J Journal of Electroanalytical Chemistry* **1980**, *111*, 111-114.
108. Diaz, A. F.; Castillo, J. I. *Journal of the Chemical Society-Chemical Communications* **1980**, , 397-398.

109. Buchner, W.; Garreau, R.; Roncali, J.; Lemaire, M. *Journal of Fluorine Chemistry* **1992**, *59*, 301-309.
110. Wallace, G. G.; Spinks, G. M.; Kane-Maguire, L. A. P. **2002**, 2nd Edition, 224.
111. Ateh, D. D.; Navsaria, H. A.; Vadgama, P. *Journal of the Royal Society Interface* **2006**, *3*, 741-752.
112. Kanazawa, K. K.; Diaz, A. F.; Gill, W. D.; Grant, P. M.; Street, G. B.; Gardini, G. P.; Kwak, J. F. *Synthetic Metals* **1980**, *1*, 329-336.
113. Corradi, R.; Armes, S. P. *Synthetic Metals*. **1997**, *84*, 453-454.
114. Ner, Y.; Invernale, M. A.; Grote, J. G.; Stuart, J. A.; Sotzing, G. A. *Synthetic Metals*. **2010**, *160*, 351-353.
115. de Leeuw, D. M.; Kraakman, P. A.; Bongaerts, P. F. G.; Mutsaers, C. M. J.; Klaassen, D. B. M. *Synthetic Metals* **1994**, *66*, 263-273.
116. Cheung, K. M.; Bloor, D.; Stevens, G. C. *Polymer* **1988**, *29*, 1709-1717.
117. Diaz, A. F.; Rubinson, J. F.; Mark, H. B. *Advances in Polymer Science* **1988**, *84*, 113-139.
118. Kaneko, M.; Wohrle, D. *Advances in Polymer Science* **1988**, *84*, 141-228.
119. Mohammadi, A.; Hasan, M. -.; Liedberg, B.; Lundström, I.; Salaneck, W. R. *Synthetic Metals* **1986**, *14*, 189-197.
120. Nannini, A.; Serra, G. *Journal of Molecular Electronics* **1990**, *6*, 81-88.
121. Ueno, T.; Arntz, H. D.; Flesch, S.; Bargon, J. *Journal of Macromolecular Science-Chemistry* **1988**, *A25*, 1557-1573.
122. Fu, Y. P.; Weiss, R. A.; Gan, P. P.; Bessette, M. D. *Polymer Engineering & Science*. **1998**, *38*, 857-862.

123. Kim, J.; Kim, E.; Won, Y.; Lee, H.; Suh, K. *Synthetic Metals* **2003**, *139*, 485-489.
124. Winther-Jensen, B.; Chen, J.; West, K.; Wallace, G. *Macromolecules* **2004**, *37*, 5930-5935.
125. Winther-Jensen, B.; Winther-Jensen, O.; Forsyth, M.; MacFarlane, D. R. *Science* **2008**, *321*, 671-674.
126. Winther-Jensen, B.; Forsyth, M.; West, K.; Andreasen, J. W.; Wallace, G.; MacFarlane, D. R. *Organic Electronics* **2007**, *8*, 796-800.
127. Winther-Jensen, B.; Forsyth, M.; West, K.; Andreasen, J. W.; Bayley, P.; Pas, S.; MacFarlane, D. R. *Polymer* **2008**, *49*, 481-487.
128. Krysinski, P.; Moncelli, M. R.; Tadini-Buoninsegni, F. *Electrochimica Acta* **2000**, *45*, 1885-1892.
129. Love, J. C.; Estroff, L. A.; Kriebel, J. K.; Nuzzo, R. G.; Whitesides, G. M. *Chemical Reviews* . **2005**, *105*, 1103-1169.
130. Schreiber, F. *Journal of Physics-Condensed Matter* **2004**, *16*, R881-R900.
131. Finklea, H. O. *Electroanalytical Chemistry: a Series of Advances, Vol 19* **1996**, *19*, 109-335.
132. Ulman, A. *Chemical Reviews*. **1996**, *96*, 1533-1554.
133. Arinaga, K.; Rant, U.; Tornow, M.; Fujita, S.; Abstreiter, G.; Yokoyama, N. *Langmuir* **2006**, *22*, 5560-5562.
134. Wackerbarth, H.; Grubb, M.; Zhang, J.; Hansen, A.; Ulstrup, J. *Langmuir* **2004**, *20*, 1647-1655.
135. Singhal, P.; Kuhr, W. G. *Analytical Chemistry*. **1997**, *69*, 4828-4832.

136. Hu, K.; Lan, D.; Li, X.; Zhang, S. *Analytical Chemistry*. **2008**, *80*, 9124-9130.
137. Steel, A. B.; Levicky, R. L.; Herne, T. M.; Tarlov, M. J. *Biophysical Journal* **2000**, *79*, 975-981.
138. Brown, A. P.; Anson, F. C. *Analytical Chemistry*. **1977**, *49*, 1589-1595.
139. Vanbenschoten, J. J.; Lewis, J. Y.; Heineman, W. R.; Roston, D. A.; Kissinger, P. T. *Journal of Chemical Education* . **1983**, *60*, 772-776.
140. Skoog, D. A.; West, D. M.; Holler, F. J. In *Fundamentals of analytical chemistry*; Saunders College Pub: Fort Worth, **1996**; .
141. Edmonds, T. E.; Dean, J. R.; Latif, S. *Analytica Chimica Acta* **1988**, *212*, 23-30.
142. Wang, J. *Biosensors for Environmental Monitoring*. **2000**, , 124-135.
143. Koryta, J.; Dvorak, J. In *Principles of electrochemistry*; Wiley: Chichester ; New York, 1987; .
144. Brett, C. M. A.; Brett, A. M. O. In *Electrochemistry: principles, methods, and applications*; Oxford University Press: Oxford ; New York, **1993**; .
145. Soreta, T. R.; Strutwolf, J.; O'Sullivan, C. K. *Langmuir* **2007**, *23*, 10823-10830.
146. Pumera, M.; Sánchez, S.; Ichinose, I.; Tang, J. *Sensors and Actuators B: Chemical*, **2007**, *123*, 1195-1205.
147. Wang, J. *Biosensors and Bioelectronics*, **2006**, *21*, 1887-1892.
148. Chen, J.; Zou, Y.; Li, Y.; Zhou, X.; Zhang, J.; Li, X.; Xiao, X.; Lin, Y. *Chemical Physics Letters* **2008**, *460*, 168-172.

149. Ko, Y.; Maeng, J.; Ahn, Y.; Hwang, S.; Cho, N. G.; Lee, S. *Sensors and Actuators B: Chemical* **2008**, *132*, 327-333.
150. Chen, H.; Dong, S. *Talanta* **2007**, *71*, 1752-1756.
151. Chen, J.; Tang, J.; Yan, F.; Ju, H. *Biomaterials* **2006**, *27*, 2313-2321.
152. Lee, T. M.; Hsing, I. *Analytica Chimica Acta*, **2006**, *556*, 26-37.
153. Garnier, F. In *Chemical and Biological Sensors from Conducting and Semiconducting Polymers* Encyclopedia of Materials: Science and Technology; Elsevier: Oxford, **2001**; pp 1150-1158.
154. Livache, T.; Roget, A.; Dejean, E.; Barthet, C.; Bidan, G.; Téoule, R. *Synthetic Metals* **1995**, *71*, 2143-2146.

CHAPTER 2

***SYNTHESIS AND
CHARACTERISATION OF
CONDUCTING POLYMERS,
NANOPARTICLES AND
NANOCOMPOSITES***

2.1 INTRODUCTION

The detection and quantitation of specific NA sequences continues to grow in importance driven by issues ranging from personalized medicine to companion diagnostics such as antibiotic selection for infectious diseases.^{1,2} Robust, low cost detection of low concentrations of NAs demands the development of novel highly sensitive detection strategies, for example, for some infectious disease and security applications, one may need to detect as few as a several thousand copies of NAs.^{1,2}

The use of AuNPs has been employed as a surface modification³⁻¹¹ to increase the surface area of the electrode and therefore the amount of single strand DNA (ss-DNA) immobilised. This results in more capture strands being available to detect target strands and hence improve the detection limit of the ss-DNA biosensor. The detection and electrochemical properties of a specific DNA sequence designed by gold nanoparticle functionalised gold electrodes (AuNP-elec) used in Chapter 3, is described here.

In order to directly detect low concentrations of DNA without PCR or NASBA based amplification, the optical or electrochemical signal-to-noise ratio associated with DNA hybridisation has to be maximised. Conducting polymers have important properties that facilitate the development of high sensitivity sensors.¹²⁻²⁴ For example, because of their relatively high conductivity, thick layers can be used and current generated throughout the three dimensional structure, thus increasing the overall response. Moreover, their ion-exchange properties can be tuned allowing interferences to be excluded.²⁵⁻²⁷ Conducting polymers have the advantage of a large specific surface area and fast electron transfer dynamics and its combination with gold particles produces sensors with high surface areas and conductivity.²⁸ For Chapter 4 and 5, the incorporation of AuNPs and conducting polymers to create nanocomposites with a very large surface area, good conductivity and excellent porosity leading to measurable currents even for low concentrations of DNA is reported. Two well studied polymers (polyaniline and PEDOT) were synthesised in their

conductive form by 3 key methods: chemical, electrochemical and vapour phase polymerisation. The fabrication of the electrodes, synthesis and characterisation of these polymers are described in this chapter.

2.2 MATERIALS AND CHEMICALS

Ethanol (99.5 %), tetrachloro gold aureate (HAuCl_4 , ≥ 99.99 %), sulphuric acid (H_2SO_4 , 99.99 %), hydroquinone (≥ 99 %) and hydrogen peroxide (H_2O_2 , 30 % (w/w) in H_2O) were all supplied by Sigma-Aldrich. Piranha solution (3:1 mixture of concentrated sulfuric acid and 30% hydrogen peroxide) was used to remove organic residues from substrates. Gold plating solution (HAuCl_4 , 3 mM) was obtained from Technic Inc. CA. The electrodes were polished using alpha alumina with a particle size of 0.3 μM (Buehler, USA) or fine diamond polish with a particle size of 1 μM (BASi).

Aniline (> 99.5 %) and 3, 4-ethylenedioxythiophene (97 %) were obtained from Merck and Sigma Aldrich. These monomers were fractionally distilled under a nitrogen atmosphere into a darkened vessel and the monomers were subsequently kept at -18°C in the dark, prior to use. A variety of inorganic / organic dopants were used to study the formation of polymer films including hydrochloric acid (HCl, 37 %), potassium chloride (KCl, ≥ 99 %) lithium perchlorate (LiClO_4 , 99.99 %), ammonium hydroxide solution (NH_4OH , 99.99 %), poly(vinyl alcohol) (PVA, 99 %), sodium dodecyl sulphate (SDS, 98.5 %), ammonium peroxydisulfate (APS, 98 %) and sodium poly(styrene sulfonate) (PSS) were supplied by Sigma-Aldrich and were used as received without further purification. Baytron CB40 otherwise known as ferric para-toluene sulfonate in 40 % 1 – butanol or ethanol (Fe (III) tosylate) and ferric chloride (Fe_3Cl , 97 %) was used as received from H.C. Starck. Dialysis tubing (MW, 12 K – 14 K) and a hot air blower (Fransen professional) were purchased from Fisher Scientific.

Buffer 1 (1.0 M sodium chloride (NaCl , ≥ 99.5 %), 10 mM Tris-hydrochloric acid (Tris-HCl, ≥ 99 %) and 1 mM ethylenediaminetetraacetic acid (EDTA, ≥ 98 %), pH 7.0) denoted as 1 M NaCl-TE was prepared in-house and used for solution phase DNA probe assembly. **Buffer 2** Denhardt's hybridisation solution (≥ 99.5 %) was used as received from Sigma Aldrich.

The quantity of enzyme labelled DNA present on modified electrode was measured in 0.1 M phosphate buffer saline (PBS), containing 0.1 M KCl and 1.81 mM hydroquinone. All chemicals were purchased from Sigma Aldrich and used as received unless otherwise stated. All the aqueous solutions were prepared from Milli-Q water (Millipore Core), 18 M Ω cm⁻¹.

2.2.1 DNA

The oligonucleotides were purchased from Eurogenec[®]™ (98 %). The base sequences are as follows:

Capture 5'- ACG-GCA-GTG-TTT-AGC-3' – SH

Target (Mastitis) 5'-TGA-TAA-ACA-CTG-CCG-TTT-GAA-GTC-TGT-TTA-GAA-GAA-ACT-TA-3'

Probe 5' Horseradish peroxisase– AAG-TTT-CTT-CTA-AAC-AGA-CT-3'

1 Base Mismatch 5'-TGC-TAA-ACA-CTG-CCG-TTT-GAA-GTC-TGT-TTA-AAA-GAA-ACT-TA-3'

3 Base Mismatch 5'-TGC-TAA-ACA-CTG-CCG-CTT-GAA-GTC-TGT-TTA-GAT-GAA- ATA-TA-3'

2.3 INSTRUMENTATION

2.3.1 Spectroscopic measurements

Thin films of the polymer were formed on ITO glass (1cm x 1 cm) using three methods: electrochemical, chemical and vapour oxidation. UV-vis, EPR and

Raman studies were carried out on these ITO substrates with / without the incorporation of gold nanoparticles.

Absorption spectra (300 to 1100 nm) of the polymer films supported on ITO-glass were measured using Shimadzu UV-1601 spectrophotometer. UV-visible spectroscopy of ss-DNA solutions was performed using a NanoDrop® ND-1000 UV-vis spectrophotometer.

A Bruker EMX EPR spectrometer was used to investigate the paramagnetic behavior of the polymers. Unless otherwise stated, the microwave frequency was 9.87 GHz, attenuator 20.0 dB, sweep width 70 G, modulation frequency 100 kHz and modulation amplitude 0.5 G. Samples consisted of the oxidised form of the polymer film on a platinum wire in contact with aqueous electrolyte in a microwave cavity cell that ensured identical cell geometry and reproducible cavity tuning.

Raman spectroscopy of polymer films were performed on a Jobin Yvon Horiba HR800 connected to a CCD detector. The laser beam (He – Ne laser) with 632.8 nm exciting radiation utilising a 300-line grating, was focused on the sample by a 100x lens. Baseline correction and smoothing were performed using Lab Spec software.

2.3.2 Microscopic measurements

Scanning Electron Microscopy (SEM) was used to investigate the surface morphology and micro/nanostructure of the conducting polymers. SEM images were taken using a Hitachi S3000N scanning electron microscope at an accelerating voltage of 20 kV. The polymer samples were electrochemically grown by applying a fixed oxidising potential to the working electrode, which involved both gold disc electrodes and 1 cm x 1 cm ITO coated glass. Prior to sample preparation, the ITO glass was washed with acetone and water for 2 minutes. The gold electrodes were cleaned as described in Section 2.3.1 and sonicated in acetone, ethanol and water for 15 min in each solvent to ensure

surface cleanliness. Samples were mounted on a high purity aluminium stub using either silver DAG conductive glue or conductive carbon tape.

Samples of emeraldine base nanofibres with / without AuNPs were dispersed in deionised water and were transferred to copper grids for transmission electron microscopy (TEM) measurements. Imaging was carried out on a Hitachi H8000 Scanning Transmission Electron Microscope at an accelerating voltage of 200 kV. Images were recorded using a Gatan Dual Vision 600t CCD camera attached to the microscope and were analysed using Gatan Digital Micrograph Version 3.11.1. The TEM was calibrated for diffraction and imaging mode using standard samples.

2.4 EXPERIMENTAL PROCEDURES

2.4.1 Electrode fabrication and cleaning

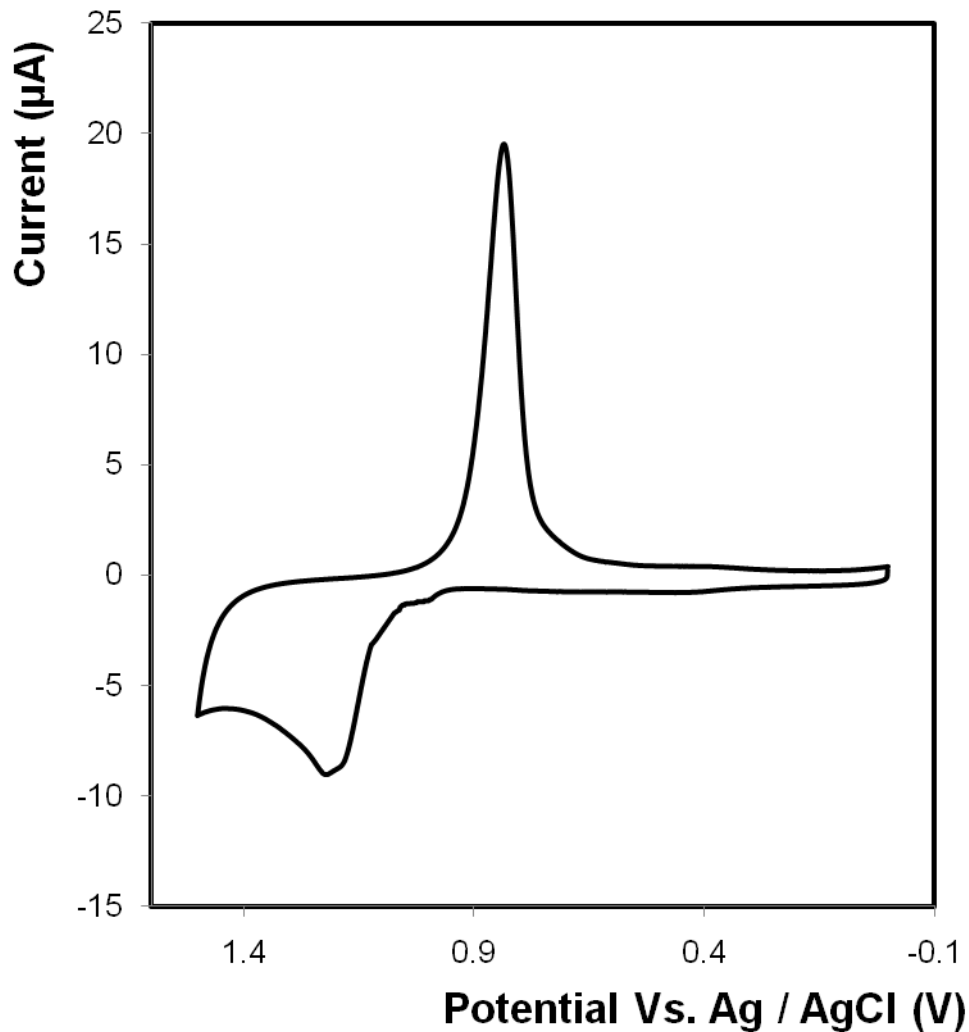


Figure 2.1 Cyclic voltammogram of a 2 mm diameter gold electrode in 0.1 M H₂SO₄ with a surface roughness factor of 1.1. The counter electrode was a platinum wire and the reference electrode was Ag/AgCl saturated in KCl. The scan rate is 100 mVs⁻¹. The sixth scan is presented.

Cyclic voltammetry was used as the principal electrochemical characterisation method for all mastitis based sensor analysis and was performed using a CH

Instruments Model 660 electrochemical workstation and a conventional three electrode cell. The working electrode was 2 mm diameter planar gold disc and the counter electrode was a large area coiled platinum wire. Potentials are quoted with respect to silver /silver chloride (Ag/AgCl) reference electrode (3 M KCl). All solutions were deoxygenated thoroughly using nitrogen prior to use and a blanket of nitrogen was maintained over the solution during all experiments. All experiments were carried out at room temperature (22 ± 3 °C). A 100 mVs^{-1} scan rate was used unless otherwise stated.

Initially, the surface of the gold disc working electrode was cycled in an electrolyte of 0.1 M KOH solution which was deoxygenated by purging with nitrogen for 15 min. A potential was applied from -400 mV to -1200 mV (vs. Ag / AgCl) with a scan rate of 100 mVs^{-1} to electrochemically clean the electrode. The electrode surface was then washed with deionised water and ethanol. The electrode was then polished with 0.3 μM alumina paste on a felt bed for at least 10 min. Voltammetry in acidic electrolyte (0.1 M H_2SO_4) was used to determine the microscopic area by cycling the electrode between 0 and 1.5 V, as shown in Figure 2.1. The gold oxide reduction peak (typically found at 0.8 V) was used to calculate the surface roughness factor (ratio of the microscopic to geometric areas) from the geometric area, 0.0314 cm^2 . A surface roughness factor less than 1.6 is desired. The calculation of electrochemical area and surface roughness factor is given below in Equation 1-3, where A_G is the geometric area, A is the electrochemical area, A_p is the area under the peak of interest and R.F. is the roughness factor. If the roughness exceeded 1.6, a second polishing procedure where manual abrasion of the electrode surface with 1 μm diamond polish on a nylon cloth was performed.

$$A_G = \pi r^2 \quad \text{Equation 2.1}$$

$$A = \frac{A_p}{390 \mu\text{Ccm}^{-2}} \quad \text{Equation 2.2}$$

$$R.F. = \frac{A_G}{A}$$

Equation 2.3

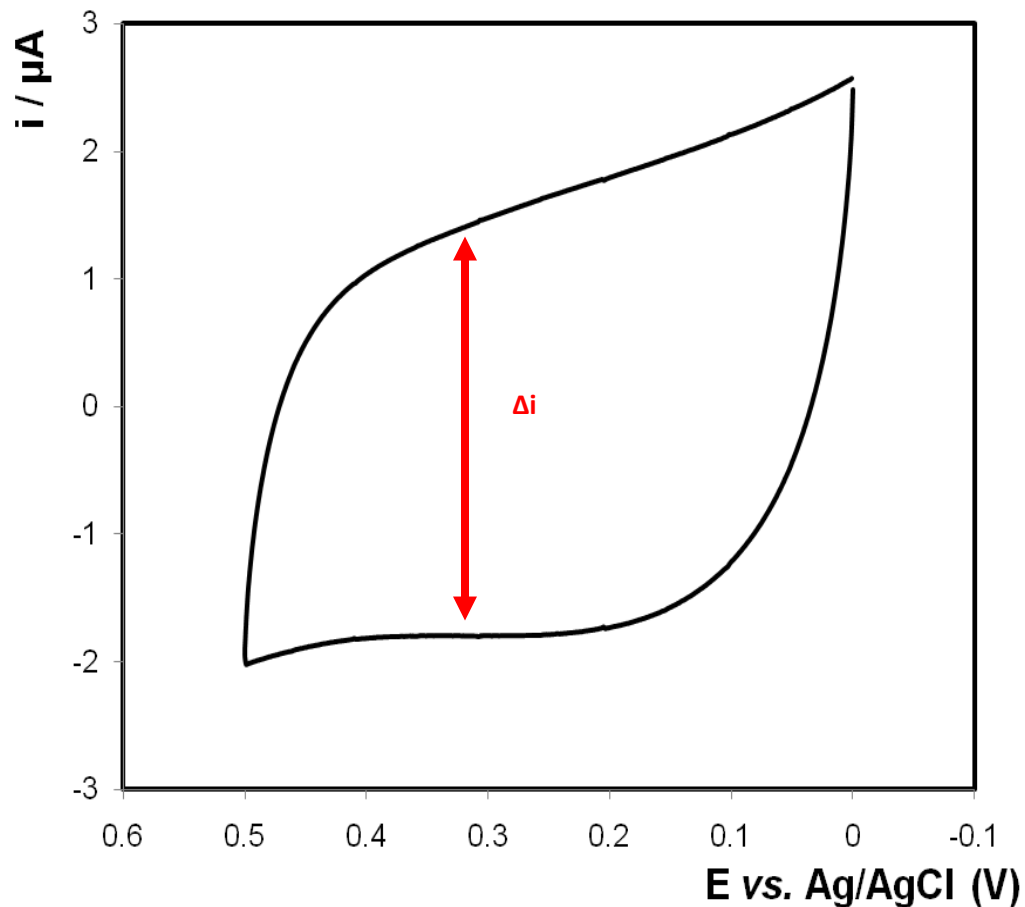


Figure 2.2 Cyclic voltammogram demonstrating capacitance of the bare gold electrodes in 0.1 M LiClO₄ in ACN. The potential was swept from 0 to 0.5 V with a scan rate of 100 mVs⁻¹.

The double layer capacitance was determined using cyclic voltammetry as illustrated in Figure 2.2. The current associated with the double layer charging is given by $\Delta i = 2 C_{dl} A v$.²⁹ A satisfactory value for capacitance for clean gold electrodes is 40 $\mu\text{F cm}^{-2}$.²⁹

2.4.2 Construction of nanogold working electrode

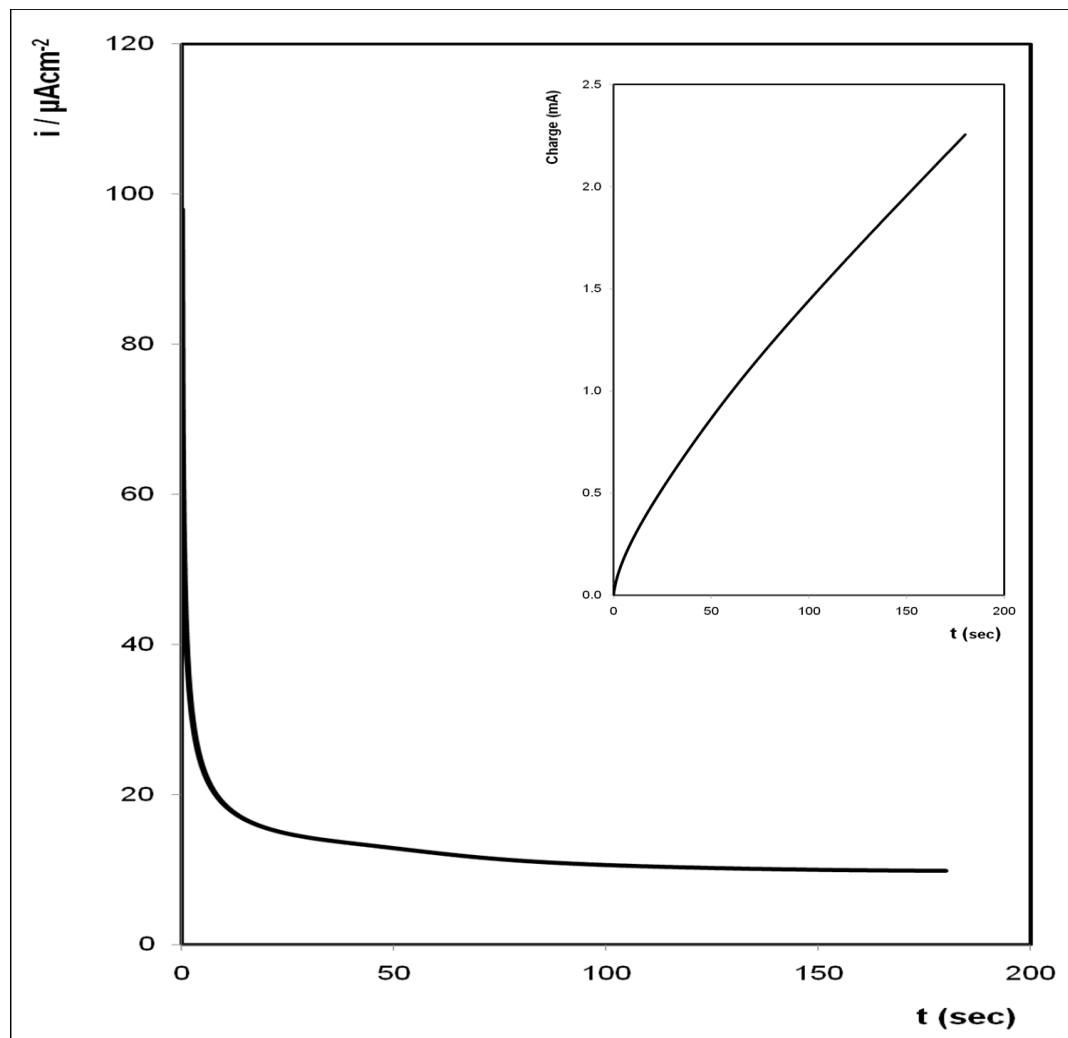


Figure 2.3 Current-time transient for growth of gold nanoparticles on a 2 mm diameter gold disc electrode. The potential (chosen from voltammetry) applied was -0.273 V at a scan rate of 100 mVs^{-1} . The inset illustrates the integrated curve of the current vs. time graph to provide information on the charge passed (the charge passed was 2.25×10^{-3} C).

Current-time transients were used for studying the nucleation and growth of gold nanoparticles onto a gold disc electrode. A 3 mM HAuCl_4 solution was used to deposit gold onto the working electrode by applying a fixed potential of

-0.273 V for 3 min at a scan rate of 100 mVs⁻¹. Figure 2.3 illustrates a typical transient for gold deposition on a gold disc electrode. At first, a current decay is observed for approximately 30 s and then a plateau with a current density of approximately 10 μA was observed for times up to 3 minutes. The initial current descend could be attributed to three processes, that is, a double-layer charging, a transient diffusion process prior to a steady-state on a gold disc electrode and a direct deposition of metal without nucleation.³⁰ At later stages the current decreases until it reaches a quasi-plateau. Such behaviour may result from a three-dimensional nucleation.³⁰ The current time curve that was recorded was then integrated to measure the charge passed. It was from this that the mass of gold deposited on the electrodes could be calculated using Faraday's law (Equation 5).

$$\text{Mass of Deposited Gold} = \frac{1}{F} \times \frac{Q \cdot M}{n} \quad \text{Equation 2.4}$$

Where F is faradays constant (96485 Cmol⁻¹), Q is the charge passed (C), M is the molecular weight of Au (gmol⁻¹) and n is the number of electrons passed (3).

A cyan free gold plating solution was used to deposit gold nanoparticles onto the electrode and polymer surfaces. A 10 mL of green 3 mM HAuCl₄ solution was heated to 60 °C until a gold yellow colour was observed. The working electrode coated with polymer was then modified by electrodeposition from this solution. After voltammetry experiments, a fixed potential of -1.5 V was applied to the working electrode and the charge passed was measured as a function of time (20, 30, 40, 50 seconds). The electrode was then rinsed with deionised water and dried under a hot air blower for approximately 20 s at approximately 40 °C. Electroplating by this method allows for 1.5 Coulombs (C) of Au segment to be electrodeposited on to the electrode with 30 s.

2.4.3 DNA capture strand immobilisation and hybridisation

A 150 μL of 1 μM solutions of both the capture and probe DNA were made up. The target DNA associated with the pathogen *Staphylococcus aureus* that causes mastitis, was made up to a volume of 150 μL with the concentrations ranging from 150 pM to 1 μM . The same concentration range was carried out for the 1 - 3 base mismatch target DNA strands. A volume of 150 μL was chosen purely because it corresponds to the minimum volume required to ensure that the electrode is fully immersed in the solution in an eppendorf.

Step 1: A monolayer of the capture oligo (3' thiolate) was deposited by immersing the working electrode in a 1 μM solution of the thiolated oligo prepared in 1M NaCl Buffer. After 5 h the electrode was thoroughly rinsed with deionised water to remove loosely bound material.

Step 2: Hybridization of the target oligo to the capture surface was performed at 37°C in hybridization buffer for 90 min. Following hybridization, the modified electrode was rinsed thoroughly with buffer. Concentrations ranged from 150 pM to 1 μM .

Step 3: The HRP-labelled probe oligo was hybridized to the target by immersing the modified electrode in a 1 μM solution of the enzyme labelled oligo for 90 min at 37 °C. Finally, it was thoroughly rinsed and dried in a nitrogen stream.

2.4.4 Electrochemical detection of *Staphylococcus aureus* (*S. aureus*) single stranded DNA

The quantity of the enzyme labelled DNA present on the surface was determined using a 1.8 mM hydroquinone redox probe in solution of phosphate buffer saline (0.1 M KCl). This solution was thoroughly deoxygenated using argon. Due to the sensitivity of the hydroquinone to photodegradation, the solution was prepared daily and the cell was wrapped in tinfoil to prevent any photochemical degradation.

Initially cyclic voltammetry experiments are carried out to establish the exact potential at which the reduction of hydroquinone to benzoquinone occurs on the modified gold disc electrodes, at a scan rate of 100 mVs^{-1} . An example of the CV carried out is highlighted in Figure 2.4. Chronoamperometry experiments were performed at an applied potential of approximately -0.40V vs. an Ag / AgCl reference electrode.

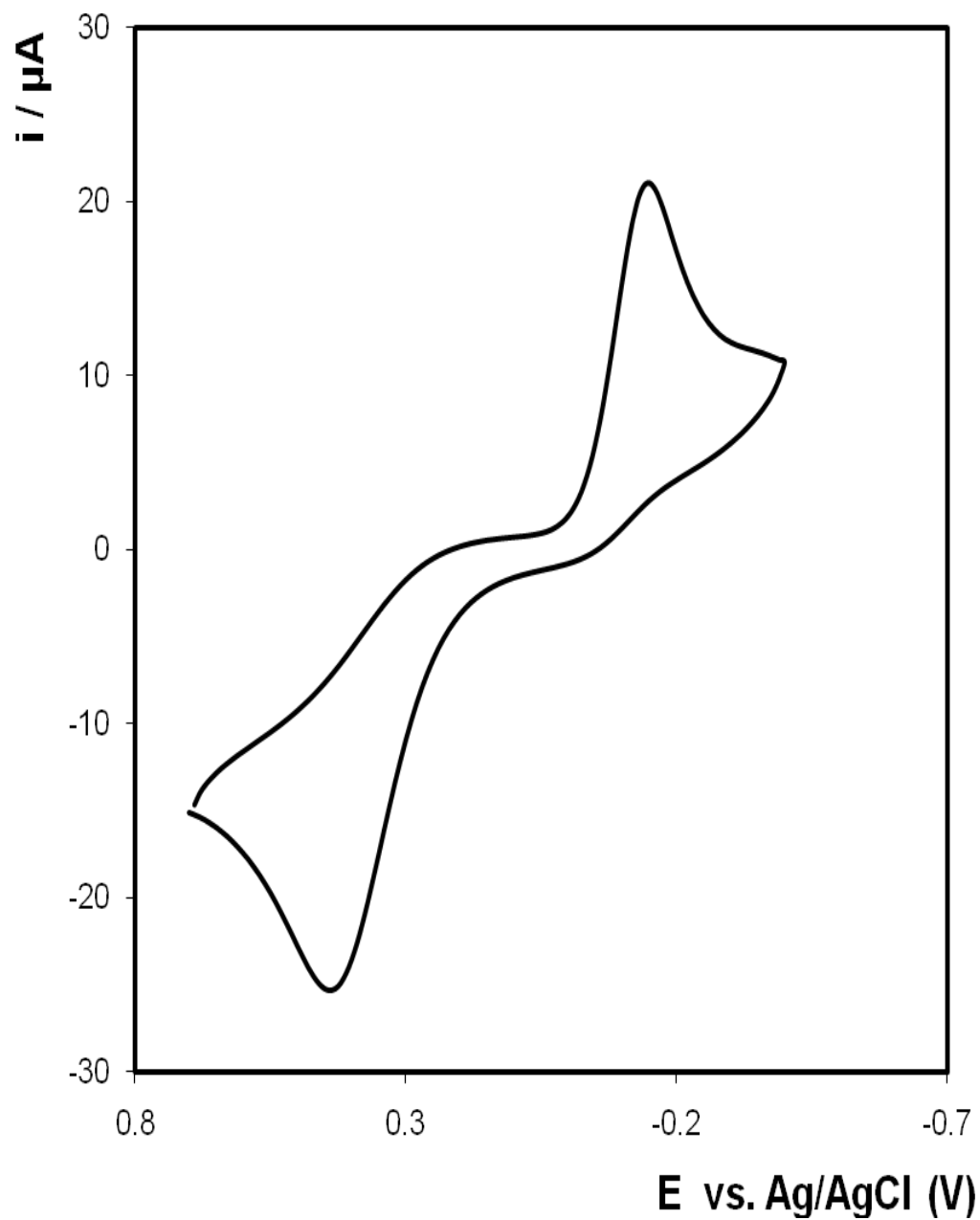
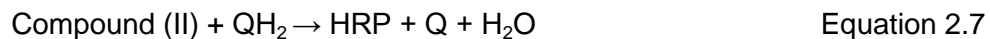
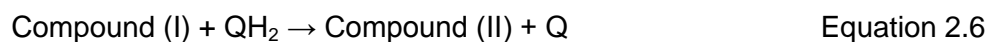


Figure 2.4 Cyclic voltammogram in phosphate buffered saline (PBS) and 0.1 M KCl and a concentration of 1.81 mM hydroquinone on a 2 mm diameter AuNP-elec (surface roughness 2.6 after AuNP depositions) functionalised with ss-DNA capture strand, target strand and probe HRP strand. Scan rate was 100 mVs^{-1} .

The hybridized target DNA can be conveniently detected by monitoring the reduction of hydroquinone to benzoquinone that mediates electron transfer to the bound HRP. The initial current in the absence of any deliberately added enzyme substrate was measured. Following addition of the enzyme substrate, 200 μM H_2O_2 , to the cell,³¹ the system was allowed to stabilise for approximately ten minutes before the current was measured. The electrode response³² is defined as the difference in current before and after the addition of H_2O_2 .

In the presence of HRP, hydroquinone is oxidised to benzoquinone resulting in a flow of electrons which may be measured using constant potential chronoamperometry. The hydrogen peroxide is a substrate of the HRP which catalyses the reaction. The H_2O_2 is broken down and the HRP is reduced. The hydroquinone allows this cycle to occur until it reaches a steady state current. The reactions associated with adding hydrogen peroxide³³ are shown below in Equation 2.5-2.8. Compounds I (oxidation state 5) and II (oxidation state 4) account for intermediates in the reactions and QH_2 and Q representing hydroquinone and its oxidized form (benzoquinone), respectively. Compound I was reduced to compound II, and then II to the original form of HRP by the redox mediator QH_2 . The benzoquinone is subsequently reduced back to hydroquinone by a rapid reaction involving the acceptance of two electrons from the electrode.



2.5 SYNTHESIS OF POLYMERS

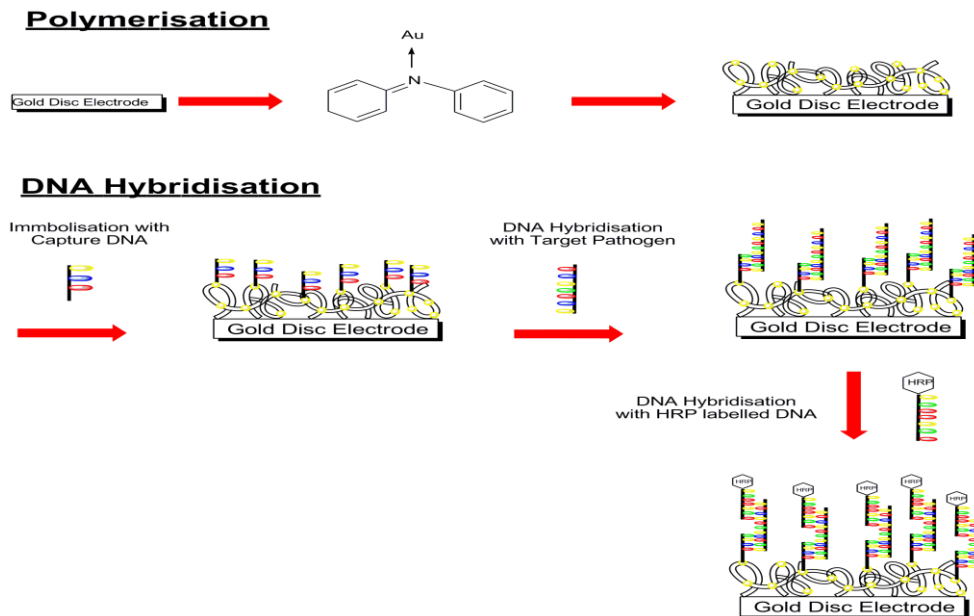


Figure 2.6

Systematic showing the stepwise creation of conducting polymers e.g. PANI, for a mastitis DNA pathogen detection system onto which gold nanoparticles have been chemically grown to give a nanocomposite material. **1.** After synthesis of polymer and incorporation of AuNPs onto a gold disc working electrode, the DNA was hybridised onto the modified electrode in 3 steps. **2.** Firstly, a monolayer of the capture oligo (3' thiolate) was prepared by immersing the working electrode in a 1 μ M oligo solution (1M NaCl Buffer) for 5 hours. **3.** Hybridization of target oligo to the capture surface was performed at 37 $^{\circ}$ C in hybridization buffer for 90 min. **4.** The HRP-labelled probe oligo was hybridized to the target by immersing the modified electrode in a 1 μ M solution of the enzyme labelled oligo for 90 min at 37 $^{\circ}$ C. **5.** The quantity of the enzyme labelled DNA present on the surface was determined potentiostatically using a hydroquinone redox probe solution.

Polymer films have been produced by electrochemical, chemical and vapour deposition. The polymers of interest are polyaniline, polypyrrole and PEDOT where electrochemical deposition of gold nanoparticles onto these polymers was then carried out. The overall scheme is portrayed in Figure 2.6. A platform for nanocomposites with a very large surface area, highly conductivity and excellent porosity leading to highly sensitive detection of DNA from pathogens has been created.

2.5.1 Electrochemical polymerisation

Electrochemical polymerisation can be divided into different type of approaches such as galvanostatic, potentiostatic and potentiodynamic utilizing a three-electrode configuration. Oxygen removal from the reaction medium is carried out by bubbling N₂ prior to electropolymerisation, whereas maintaining the cell oxygen-free during an experiment is accomplished by passing N₂ over the solution. Following electropolymerisation, the electrode was removed from the monomer solution and carefully rinsed with monomer-free electrolyte solution.

Polyaniline and PEDOT were first prepared potentiodynamically. An e-corder EA161 potentiostat was used to record cyclic voltammograms so as to measure the redox peaks at the working electrode as a function of applied potential. The parameters and polymerisation solution of each polymer are given below in Table 2.1.

Table 2.1 Summary of the different protonic acid media, potential sweep and scan rates used for the electrochemical oxidation of PANI, PPY and PEDOT.

POLYMER	[MONOMER]	ELECTROLYTE	POTENTIAL WINDOW vs. Ag/AgCl (V)	SCAN RATE (mVs ⁻¹)
PANI	40 mM	0.1 M HCl	- 0.5 → + 1.0	100
PEDOT	50 mM	0.1 M LiClO ₄	- 1.5 → + 1.5	100

CVs were carried out to provide information regarding the oxidation potential of the monomer. PANI and PEDOT were deposited electrochemically using a polymerisation cell as described above. These polymers were grown potentiostatically where a fixed potential is applied to the working electrode and the electrical charge passed is measured as a function of time. This allows for oxidised species to form and deposit on the electrode surface from the polymerisation solution preventing reduction or over oxidation of the polymer. From the oxidation peaks found in voltammetry experiments, the potential was fixed at +0.800 V for PANI and +0.500 V for PEDOT, where the time was set at 90 seconds and 120 s, respectively. Potentiostatic deposition onto ITO glass was also carried out for subsequent characterisation of the polymer films by UV-Vis, Raman and EPR.

2.5.2 Vapour polymerisation

Vapour phase polymerisation (VPP) consists of 3 key steps: oxidant deposition, monomer polymerisation and residual oxidant removal.³⁴ Fe (III) tosylate in a 40 % aqueous solution of butanol or ethanol was used as the oxidizing agent. Typically, an oxidant layer is deposited onto a substrate (generally glass or plastic) by spin coating. However, using gold disc electrodes, this process proved difficult and the catalyst was deposited by drop casting approximately 1 drop of the 0.85 M oxidant directly onto the electrode surface.

2.5.2.1 Polyaniline

The oxidant (0.85 M Fe (III) tosylate in 40 % aqueous solution of ethanol) was drop cast onto the gold working electrode and allowed to dry. When the coating was almost dry, but before the Fe (III) tosylate forms crystals, the samples were put in an oven at 120 °C for approximately 2 min until the solvent evaporated. This was indicated by the removal of the liquid and a dark yellow colour formed on the substrate.

A typical vapour polymerisation³⁵⁻³⁹ involved a glass reaction vessel containing approximately 5 mL of the monomer and the electrode. The electrode was exposed to the aniline monomer vapour for approximately 1 h at room temperature. Polymerisation occurs as the aniline monomer vapour comes into contact with the oxidant layer on the substrate forming a polyaniline film. The modified electrodes was then removed, washed in ethanol or methanol to remove any residual oxidant and allowed to dry quickly under a hot air blower (40 °C) for approximately 20 seconds. This was the allowed to cool to room temperature before any further modification or analysis.

2.5.2.2 PEDOT

The oxidising agent Fe (III) tosylate (40 % solution in butanol) was used in this procedure. The same method, except using EDOT as the monomer was carried out as described for PANI (Section 2.6.2.1). Table 2.2 summarizes the parameters and observation for VPP of PANI and PEDOT polymers.

Table 2.2 Summary of the polymerisation catalyst used, the exposure time to the vapour and the colour change observed after the vapour phase oxidative polymerisation of PANI and PEDOT.

Polymer	Oxidant	VPP Time (h)	Colour Change
PANI	Fe (III) tosylate 40 % in ethanol	1	Yellow/green to dark green
PEDOT	Fe (III) tosylate 40 % in butanol	1	Yellow / green to blue

2.5.3 Chemical polymerisation

PANI / APS, PPY / SDS and PEDOT / PSS were kindly provided by the University of Wollongong, IPRI, New South Wales, Australia. The emeraldine base nanofibres were provided by the Department of Chemistry & Biochemistry and California NanoSystems Institute, University of California, Los Angeles, California. The full synthetic procedures and characterisation of the samples, including UV-visible, EPR and Raman spectroscopy and electrochemical characterisation, have been previously reported.⁴⁰

2.5.3.1 Polyaniline

For the chemical polymerisation of aniline, the monomer (3.2 mM) was dissolved in 10 mL of carbon tetrachloride. This was carefully transferred to 10 mL of ammonium peroxydisulfate - APS (0.8 mM) dissolved in 1 M hydrochloric acid. Larger scale reactions were carried out using 200 mL of 1.6 M aniline in tetrachloride. This was then transferred to a 2 L beaker, where a solution of APS (0.4 M) was dissolved in 1 L of 1 M HCl. In all reactions, the aniline to ammonium peroxydisulfate molar ratio was kept at 4 to 1.

Purification: After 24 h, the dark-green precipitate was collected and purified by dialysis against deionised water. The purified material was then washed with 1 M $\text{NH}_3 \cdot \text{H}_2\text{O}$ until the filtrate became colorless. This ensured that all excess acid and by-products from polymerization were removed.⁴¹

2.5.3.2 Chemical doping of emeraldine base nanofibres (PANI-NF)

In a typical synthesis,²⁷ 0.205 g (2.2 mmol) of aniline was dissolved in 10 mL of 1 M HCl while 0.125 g (0.55 mmol) of ammonium peroxydisulfate (APS) was dissolved in 10 mL of 1 M HCl. The two solutions were then mixed, shaken for 1 minute and left to react overnight. The resulting emeraldine salt (ES) polyaniline nanofibres (PANI-NF) were then centrifuged and the supernatant discarded. The suspension was then reconstituted to 20 mL with a 1 M

solution of ammonium hydroxide solution (NH_4OH) to convert the material into the base form of the polymer. The solution was then purified via centrifugation ($3\times \text{H}_2\text{O}$) to yield a suspension of emeraldine base (EB) PANI-NF in H_2O .

2.5.3.2.1 *AuNP incorporation after the chemical doping of PANI-NF.*

A suspension of purified EB PANI-NF in H_2O was diluted to a 0.2 % w/v and combined in a 4:1 ratio with a 10 mM HAuCl_4 solution at 4 °C. The solution was left to react for 24 h at 4 °C, to yield the nanocomposite material, PANI-NF-AuNP.

2.5.3.3 **PEDOT**

To make up a 1:0.61 ratio of poly (3, 4 ethylenedioxythiophene) – poly (styrene sulfonate) (PEDOT / PSS) copolymer, a typical synthetic procedure^{42, 43} is as follows. 3.285 g (22.6 mmol) of PSS was dissolved in 100 mL of deionised water under ultrasonic stirring for 10 min. To this dissolved PSS, 5.3 g (37 mmol) of EDOT was added drop wise and then allowed to sit for 2-3 h to form a cloudy emulsion. This was then vacuum filtered and the “cloudy” filtrate went under ultrasonic stirring (30 – 45 min) until the mixture cleared. APS (11.8 g, 52 mmol) dissolved in 200 mL of deionised water was then added to 5 mg of ferrous ammonium sulphate which was dissolved in 10 mL of Milli – Q H_2O . This solution was added drop wise to the clear EDOT: PSS mixture where a darker colour was immediately observed. This solution was allowed to stir overnight and then polymerisation was allowed to proceed in a dialysis membrane for 24 hours at 40 °C. The precipitate was collected by filtration and washed with deionised water and methanol. Finally, it was dried under vacuum at room temperature for 24 h.

2.6 CONCLUSION

In this chapter, the production of the materials and chemicals used throughout this thesis are described. Also included are the specific details of the experimental procedures employed for the preparation of the mastitis DNA

biosensor. This chapter also outlines the fabrication and cleaning processes for several substrates that are used in the remaining sections of this thesis. These include gold disc electrodes, ITO glass and Tyndall gold.

2.7 REFERENCES

1. Sun, W.; Li, Y.; Yang, M.; Liu, S.; Jiao, K. *Electrochemistry Communications*, **2008**, *10*, 298-301.
2. Wang, J. *Biosensors and Bioelectronics*, **2006**, *21*, 1887-1892.
3. Ariga, K. *Journal for Nanoscience and Nanotechnology* . **2006**, *6*, 1.
4. Kerman, K.; Saito, M.; Tamiya, E.; Yamamura, S.; Takamura, Y. *Trends in Analytical Chemistry*. **2008**, *27*, 585-592.
5. Luo, X.; Morrin, A.; Killard, A. J.; Smyth, M. R. *Electroanalysis* **2006**, *18*, 319-326.
6. Tsung, C.; Hong, W.; Shi, Q.; Kou, X.; Yeung, M. H.; Wang, J.; Stucky, G. D. *Advanced Functional Materials*. **2006**, *16*, 2225-2230.
7. Willner, I.; Baron, R.; Willner, B. *Advanced Materials.(Weinheim, Ger.)* **2006**, *18*, 1109-1120.
8. dos Santos, D. S., Jr.; Alvarez-Puebla, R. A.; Oliveira, O. N., Jr.; Aroca, R. F. *Journal of Materials Chemistry*. **2005**, *15*, 3045-3049.
9. Merkoci, A.; Aldavert, M.; Marin, S.; Alegret, S. *Trends in Analytical Chemistry*. **2005**, *24*, 341-349.
10. Vaseashta, A.; Dimova-Malinovska, D. *Science and Technology of Advanced Materials*. **2005**, *6*, 312-318.
11. Wang, J. *Analyst (Cambridge, U.K.)* **2005**, *130*, 421-426.
12. Aleman, C.; Teixeira-Dias, B.; Zanuy, D.; Estrany, F.; Armelin, E.; del Valle, L. J. *Polymer* **2009**, *50*, 1965-1974.
13. Baltog, I.; Baibarac, M.; Lefrant, S.; Gomez-Romero, P. *Journal of Nanoscience and Nanotechnology* **2009**, *9*, 6204-6209.
14. Harish, S.; Mathiyarasu, J.; Phani, K. L. N. *Materials Research Bulletin* . **2009**, *44*, 1828-1833.

15. Feng, Y.; Yang, T.; Zhang, W.; Jiang, C.; Jiao, K. *Analytica Chimica Acta* **2008**, *616*, 144-151.
16. Lee, A. S.; Peteu, S. F.; Ly, J. V.; Requicha, A. A. G.; Thompson, M. E.; Zhou, C. *Nanotechnology* **2008**, *19*, 165501/1-165501/8.
17. Saheb, A.; Smith, J. A.; Josowicz, M.; Janata, J.; Baer, D. R.; Engelhard, M. H. *Journal of Electroanalytical Chemistry* **2008**, *621*, 238-244.
18. Zanardi, C.; Terzi, F.; Pigani, L.; Heras, A.; Colina, A.; Lopez-Palacios, J.; Seeber, R. *Electrochimica Acta* **2008**, *53*, 3916-3923.
19. Chen, W.; Li, C. M.; Chen, P.; Sun, C. Q. *Electrochimica Acta* **2007**, *52*, 2845-2849.
20. Kharat, H. J.; Kakde, K. P.; Savale, P. A.; Datta, K.; Ghosh, P.; Shirsat, M. D. *Polymers for Advanced Technologies* . **2007**, *18*, 397-402.
21. Selvaganesh, S. V.; Mathiyarasu, J.; Phani, K. L. N.; Yegnaraman, V. *Nanoscale Research Letters* **2007**, *2*, 546-549.
22. Venancio, E. C.; Wang, P.; MacDiarmid, A. G. *Synthetic Metals*, **2006**, *156*, 357-369.
23. Chiu, W. W.; Travas-Sejdic, J.; Cooney, R. P.; Bowmaker, G. A. *Synth. Met.* **2005**, *155*, 80-88.
24. Peng, H.; Soeller, C.; Vigar, N.; Kilmartin, P. A.; Cannell, M. B.; Bowmaker, G. A.; Cooney, R. P.; Travas-Sejdic, J. *Biosensors and Bioelectronics* **2005**, *20*, 1821-1828.
25. Koess, C.; Hamann, J. *Journal of Dairy Research* . **2008**, *75*, 225-232.
26. Arnold, F. E.; Arnold, F. E. *High Performance Polymers* **1994**, *117*, 257-295.
27. Zhang, K.; Jing, X. *Polymers for Advanced Technologies*. **2009**, *20*, 689-695.

28. Khan, A. A.; Alam, M. M.; Mohammad, F. *Electrochimica Acta*, **2003**, *48*, 2463-2472.
29. Bard, A. J.; Faulkner, L. R. **1980**, , 718.
30. Li, Y. G.; Lasia, A. *Journal of Applied Electrochemistry*. **1997**, *27*, 643-650.
31. Chetcuti, A. F.; Wong, D. K. Y.; Stuart, M. C. *Analytical Chemistry*. **1999**, *71*, 4088-4094.
32. Williams, E.; Pividori, M. I.; Merkoçi, A.; Forster, R. J.; Alegret, S. *Biosensors and Bioelectronics*, **2003**, *19*, 165-175.
33. Cao, Q.; Zhou, W. *Analytical Letters*. **2006**, *39*, 2725-2735.
34. Groenendaal, L.; Zotti, G.; Jonas, F. *Synthetic Metals* **2001**, *118*, 105-109.
35. Winther-Jensen, B.; Forsyth, M.; West, K.; Andreasen, J. W.; Bayley, P.; Pas, S.; MacFarlane, D. R. *Polymer* **2008**, *49*, 481-487.
36. Winther-Jensen, B.; Winther-Jensen, O.; Forsyth, M.; MacFarlane, D. R. *Science* **2008**, *321*, 671-674.
37. Winther-Jensen, B.; Forsyth, M.; West, K.; Andreasen, J. W.; Wallace, G.; MacFarlane, D. R. *Organic Electronics* **2007**, *8*, 796-800.
38. Winther-Jensen, B.; Chen, J.; West, K.; Wallace, G. *Macromolecules* **2004**, *37*, 5930-5935.
39. Winther-Jensen, B.; West, K. *Macromolecules* **2004**, *37*, 4538-4543.
40. Shedd, B.; Baker, C. O.; Heller, M. J.; Kaner, R. B.; Hahn, H. T. *Materials Science and Engineering: B* **2009**, *162*, 111-115.
41. Huang, J.; Kaner, R. B. *Journal of the American Chemical Society*. **2004**, *126*, 851-855.
42. Zhang, X. Y.; MacDiarmid, A. G.; Manohar, S. K. *Chemical Communications* **2005**, , 5328-5330.

43. Zhang, X. Y.; Lee, J. S.; Lee, G. S.; Cha, D. K.; Kim, M. J.; Yang, D. J.; Manohar, S. K. *Macromolecules* **2006**, *39*, 470-472.

3.1 INTRODUCTION

This chapter outlines the development of a sensitive electrochemical sensor for single stranded DNA (ss-DNA) detection. The ss-DNA of interest is from the mastitis causing pathogen *Staphylococcus aureus*. By creating an electrochemical detection platform, the problems often associated with culture based tests can be overcome. One of the challenges in bioanalytical chemistry is to amplify the detection of the biorecognition events, specifically DNA hybridisation.¹ Metal nanoparticles are widely used to amplify the biorecognition event and the hybridisation of enzymes such as HRP, are used as amplifying labels in developing bio electronic sensing devices.¹ Gold nanoparticles (AuNPs) have been reported to significantly increase the surface area of the electrode and therefore enhance the quantity of capture DNA available.²⁻⁴ Here, gold nanoparticles (AuNPs) and enzymatic amplification of the electrochemical signal are combined to yield a highly sensitive detection of ss-DNA.

The performance of this DNA sensor depends on the overall efficiency of the surface hybridisation event. Here, the capture DNA is immobilised onto the nanostructured electrode via the introduction of a thiol moiety at the 5' end of the DNA sequence to enable the formation of highly packed DNA. The target DNA exactly matches that of the probe (based on the complementary pairing of A with T and G with C) and a hybrid duplex DNA is formed on the electrode surface as illustrated in Figure 3.1.^{5,6} Formation of the DNA duplex (the hybridization event) is detected electrochemically by chronoamperometric detection of a HRP labelled DNA sequence. The use of the HRP enzyme as a label increases the assay sensitivity due to its inherent amplification.⁷ The current required to reduce hydroquinone oxidised during the regeneration of the HRP label (Figure 3.1) was measured. Nucleic acid testing in this way allows closely related organisms to be identified in a few hours.

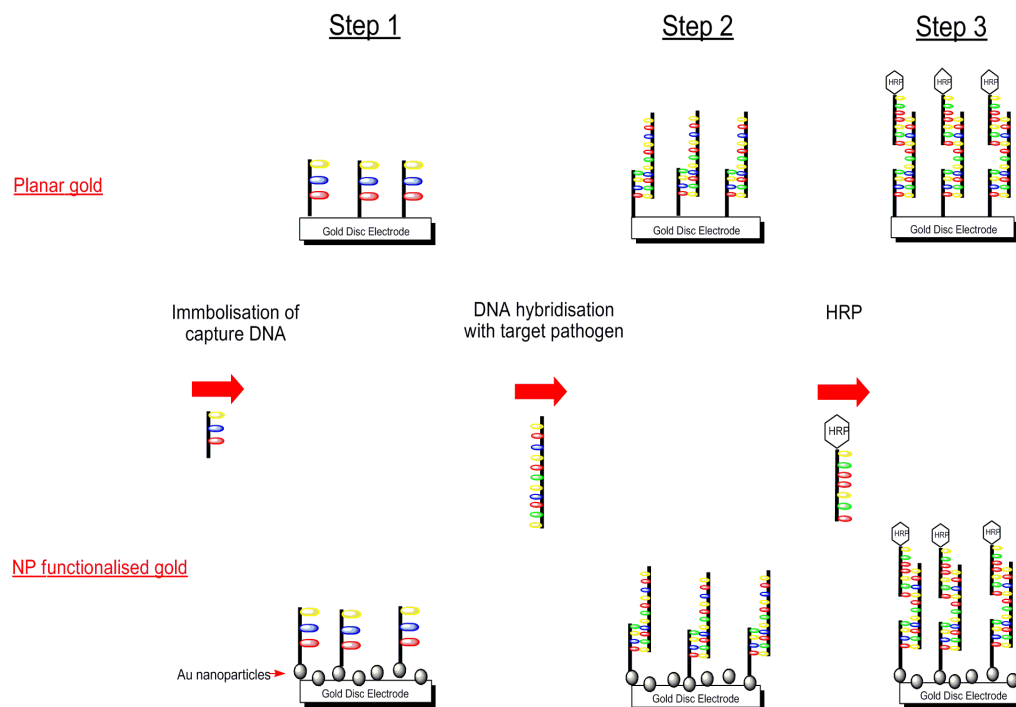


Figure 3.1 Schematic diagram of an enzyme linked DNA sensor, where each step is hybridised onto the electrode separately. This figure shows a three step procedure.

Controlling the surface density of the capture DNA as well as controlling their correct orientation is important for sensitive detection. In order to optimise the immobilisation and hybridisation processes, parameters such as immobilisation buffer and the HRP labelled DNA hybridisation time were investigated. A platform with a very high packing density of capture DNA may not be ideal for hybridisation, due to the lack of space between the immobilised capture DNA strands to allow hybridisation with the complementary target sequence.⁹ Steric hindrance as well as electrostatic interactions between capture molecules may also prevent target binding.¹⁰ On the other hand, a very low DNA density is also not constructive since it leads to small signals and higher signal to noise ratios (S/N).

The work reported within this chapter presents an approach to the fabrication of electrochemical DNA biosensors based on the formation of DNA sequences

on electrochemically deposited gold nanoparticles at the surface of gold disc electrodes. Scanning electron microscopy (SEM) was used to confirm the successful deposition as well as to measure the size and distribution of the deposited NPs. The anodic peak current signal recorded is enhanced for the nanostructured surfaces developed in this work. The influence of the immobilisation buffer chosen as well as the time required for HRP hybridisation was also optimised. A sensor platform has been provided that should be widely applicable for enhancing biosensor signals by purposely manipulating and structuring transducer surfaces at the nanoscale.

3.2 EXPERIMENTAL

3.2.1 *Gold nanoparticle electrodeposition*

Gold nanoparticles (AuNPs) were deposited onto polished and cleaned gold disc electrodes by electrochemical reduction of hydrogen tetrachloroaurate (3 mM HAuCl₄) in 0.1 M KCl on gold disc electrode. A potential of -0.273 V and a time of 3 min at a scan rate of 100 mVs⁻¹ were reported by Shu-feng *et al*¹¹ as being optimal for detection and their conditions were used here.

3.2.2 *Microscopic characterisation of gold nanoparticle electrodeposition*

Scanning electron microscopy (SEM) was used to characterise the surface of the gold disc electrode after gold electrochemical deposition. SEM images were carried out on a Hitachi S3000N scanning electron microscope at an accelerating voltage of 20 kV in a high vacuum mode. A full description of sample preparation is found in Section 2.3.2

3.2.3 *Voltammetric characterisation of an enzyme amplified DNA sensor*

The sequential construction of the sensor is depicted in Figure 3.1 in Section 3.1. The immobilisation and hybridisation of DNA onto the AuNP modified electrode was carried out as described in Section 2.4.3. However, it should be noted that in step 1 involving the immobilisation of the thiolated capture DNA strands to the AuNP modified electrode, 1 M NaCl-TE buffer was used. In steps 2 and 3 of DNA hybridisation involving the target and HRP attachment, Denhardt's hybridisation buffer was used. For the immobilisation buffer identity experiment, Denhardt's buffer was used.

3.2.4 *The influence of HRP labelled DNA hybridisation time*

Once the target DNA has been captured onto the sensor surface, the use of an enzyme such as HRP can be used as a label to convert a single hybridisation event into a chronoamperometric signal. The HRP-labelled probe oligo was hybridized to the target DNA by immersing the modified electrode in a 1 μM solution of the enzyme labelled oligo. The HRP labelled DNA hybridisation time was investigated in an attempt to lower the time necessary for the realisation of the assay. The time of exposure of 1 μM HRP labelled DNA was varied from 10 min to 3 h at regular intervals of 10 min. Chronoamperometric detection was then performed in 10 mls of deoxygenated phosphate buffered saline (PBS) and 0.1 M KCl and a concentration of 1.81 mM hydroquinone, at an applied potential of -0.4 V. After the signal stabilised, 200 μL of 3 mM H_2O_2 was injected. The current responses to reduce hydroquinone oxidised during the regeneration of the HRP label were then recorded and compared.

3.2.5 *Species recognition ability (mismatch and non - pathogenic species)*

3.2.5.1 *Non-specific adsorption evaluation*

The current required to reduce the oxidised hydroquinone during the regeneration of the HRP label depends directly on the amount of the HRP labelled DNA bound to the target DNA sites. However, physical adsorption of the HRP onto the electrode surface could also occur. In order to determine the extent of non specific adsorption, two control experiments were carried out. The immobilisation and hybridisation of each DNA step was carried out as stated in Section 2.4.3; however omitting (i) capture DNA and (ii) target DNA allowing the selectivity of the response to be ascertained. In both assays all electrode pre-treatment procedures stated in Section 2.4.1 were followed.

3.2.5.2 1 and 3 base mismatch

The purpose of this experiment is to ensure that this sensor can detect a desired DNA sequence of interest and is capable of distinguishing two DNA sequences which differ marginally in the base pairs. A new target strand with a single base mismatch (G was changed to A) is given below where the mismatch is highlighted in bold. This was used within the biosensor and all subsequent steps were carried out as normal to the last step which involves the electrochemical detection of *S. aureus* (Section 2.4.4).

5'-TGC-TAA-ACA-CTG-CCG-TTT-GAA-GTC-TGT-TTA-**AAA**-GAA-ACT-TA-3'

Also a three base mismatch (ACT changed to TTA) target strand named *Staphylococcus epidermidis* (*S. epidermidis*), can often be mistaken for *Staphylococcus aureus* (*S.aureus*) and its presence incorrectly associated with mastitis was used. Successful discrimination between the two sequences avoids any false results. Detection of the hybridisation of the desired DNA was achieved using the electrochemical procedure mentioned in Section 2.4.4.

5'-TGC-TAA-ACA-CTG-CCG-CTT-GAA-GTC-TGT-TTA-GAT-GAA-**ATA**-TA-3'

3.2.6 Buffer identity

Denhardt's buffer

The sensor as depicted in Figure 3.1 was produced. However, for the immobilisation step of the thiolated capture DNA to the Au modified electrode, Denhardt's buffer (Buffer 2) was used. The total target oligonucleotide concentration ranged from 150 pM to 1 μ M and the recommended¹² 90 min HRP labelled DNA hybridisation time remained constant.

3.2.7 Alternative immobilisation / hybridisation procedures

1 step hybridisation of enzyme amplified DNA

Bulk immobilisation¹² provides an alternative experiment to develop biosensors that require only a one step hybridisation / immobilisation procedure. The procedure is based on that reported by Williams *et al*,¹² but is considerably simplified here by using a directly-HRP-labelled probe oligonucleotide as depicted in Figure 3.2. This probe removes the cumbersome antibody-antigen-based HRP labelling step used in the William's method. The three oligonucleotides (capture, target and probe) were mixed to a final concentration of 1 μ M - 150 pM in 120 μ L Denhardt's buffer. After one hour of hybridisation at 37° C, the AuNP-electrode was immersed in the hybridised oligonucleotide mixture for five h to attach them to the electrode via the 3' thiolate group of the capture oligo.

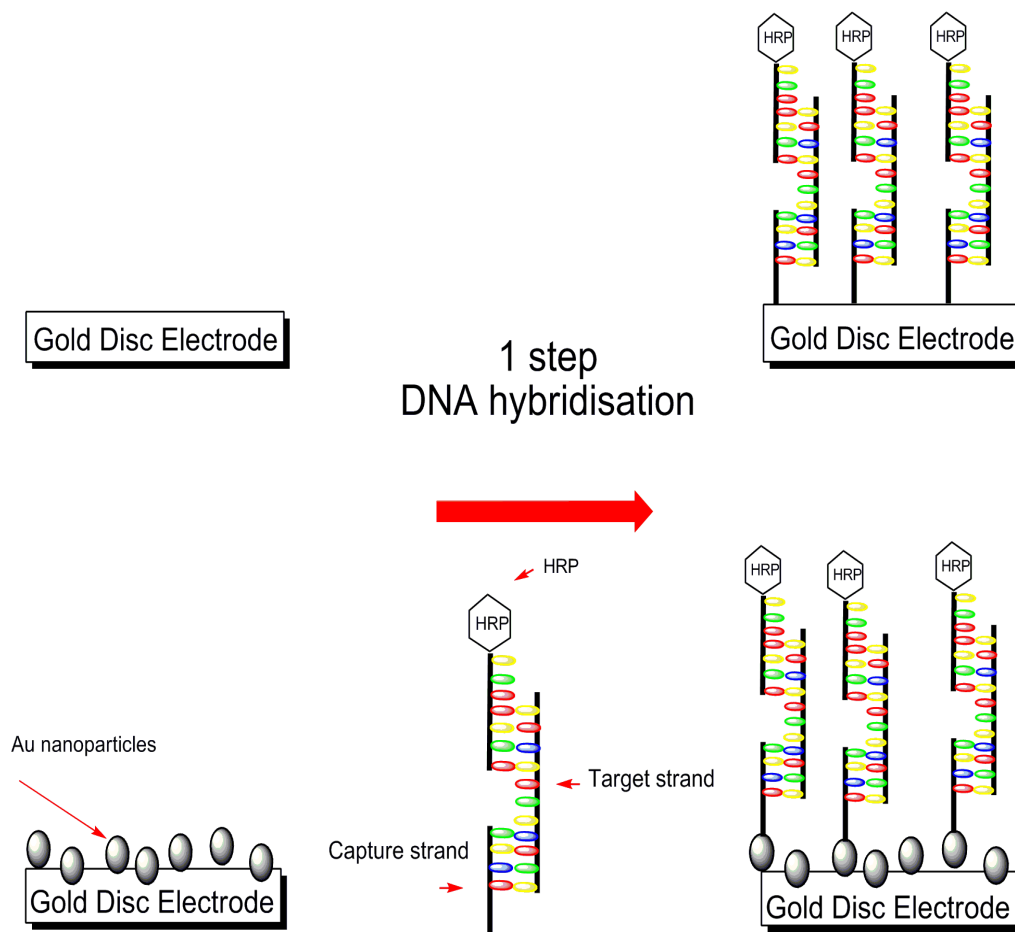


Figure 3.2 Schematic diagram of enzyme DNA sensor where all three DNA strands are allowed to intercalate in Denhardt's buffer before the hybridisation onto the unmodified / modified gold disc electrode. This shows a one step procedure for the DNA immobilisation.

3.3 RESULTS AND DISCUSSION

3.3.1 *Electrochemical characterisation of gold nanoparticle electrodeposition*

The DNA biosensor relies on the immobilisation amount and accessibility of the thiolated capture DNA.^{2,3,13,14} Gold nanoparticle modification has been reported to significantly increase the surface area of electrode and enhance the ability to capture DNA.^{2,15} The surface area of a gold electrode after modification can be estimated using cyclic voltammetry (CV).¹¹ The electrodes were immersed in a deoxygenated H₂SO₄ aqueous solution and the CV responses recorded. The surface areas could then be simply obtained from the coulombic integration of the reductive peak of the gold oxide.

Voltammetric determination of a gold electrodes real surface is based on the reducing a gold oxide monolayer described in Equation 3.1 - 3.3. The amount of surface oxide can be measured by integrating the gold oxide peak found in the cathodic scan. The charge passed during the reduction of the gold oxide monolayer is proportional to the real surface area of the gold nanoparticulate surface, with each cm² of gold surface consuming 390 μC.¹⁶ The roughness factor is defined as the ratio of the microscopic active surface area to the geometrical area.¹⁷



Unmodified gold electrodes were cycled in 0.1 M H₂SO₄ aqueous solutions and a stable gold oxide formation/reduction cyclic voltammogram was obtained. The pre-treated electrodes were then immersed into the 3 mM HAuCl₄ solution containing 0.1 M KCl as electrolyte, where electrochemical deposition was conducted at -273 mV for 3 min by single potential step.

The unmodified gold electrode (Figure 3.3, dashed line) is characterised by a sharp rise in the oxidation current at +1.2 V and a single oxide stripping peak near 0.8 V. These peaks are associated with the formation and subsequent re-reduction of a gold oxide monolayer on the underlying gold electrode. Any residue of organic contaminant left by the preceding cleaning treatments is removed during repeated oxidation and reduction of the gold.¹⁸ The surface of the planar gold electrode had an electrochemical area of 0.0392 cm² and a surface roughness factor of 1.25 which is close to the ideal factor of 1 of an electrode surface with no surface defects or contaminants.¹⁷

Figure 3.3 (thick line) also shows the CV after the potentiostatic deposition of 3 mM HAuCl₄, at a fixed potential of -0.273 mV for 3 min. The electrode was scanned in 0.1 M H₂SO₄ again to determine the new electrochemical area and surface roughness factor. It is apparent that depositing the gold nanoparticles significantly increases the charge passed during the formation of gold oxide. The formation of gold oxide was found at a more positive potential of 0.9 V (compared to 0.8 V for bare electrode). The charge passed during the reduction of a monolayer of gold oxide is 390 μC cm⁻² and by comparing the charge passed before and after nanoparticle deposition, the additional area available for DNA binding can be determined. The electrochemical area had increased from 0.0392 cm² to 0.0791 cm² in the presence of the AuNPs, i.e., deposition of the gold nanoparticles increases the gold surface area by a factor of approximately 8.

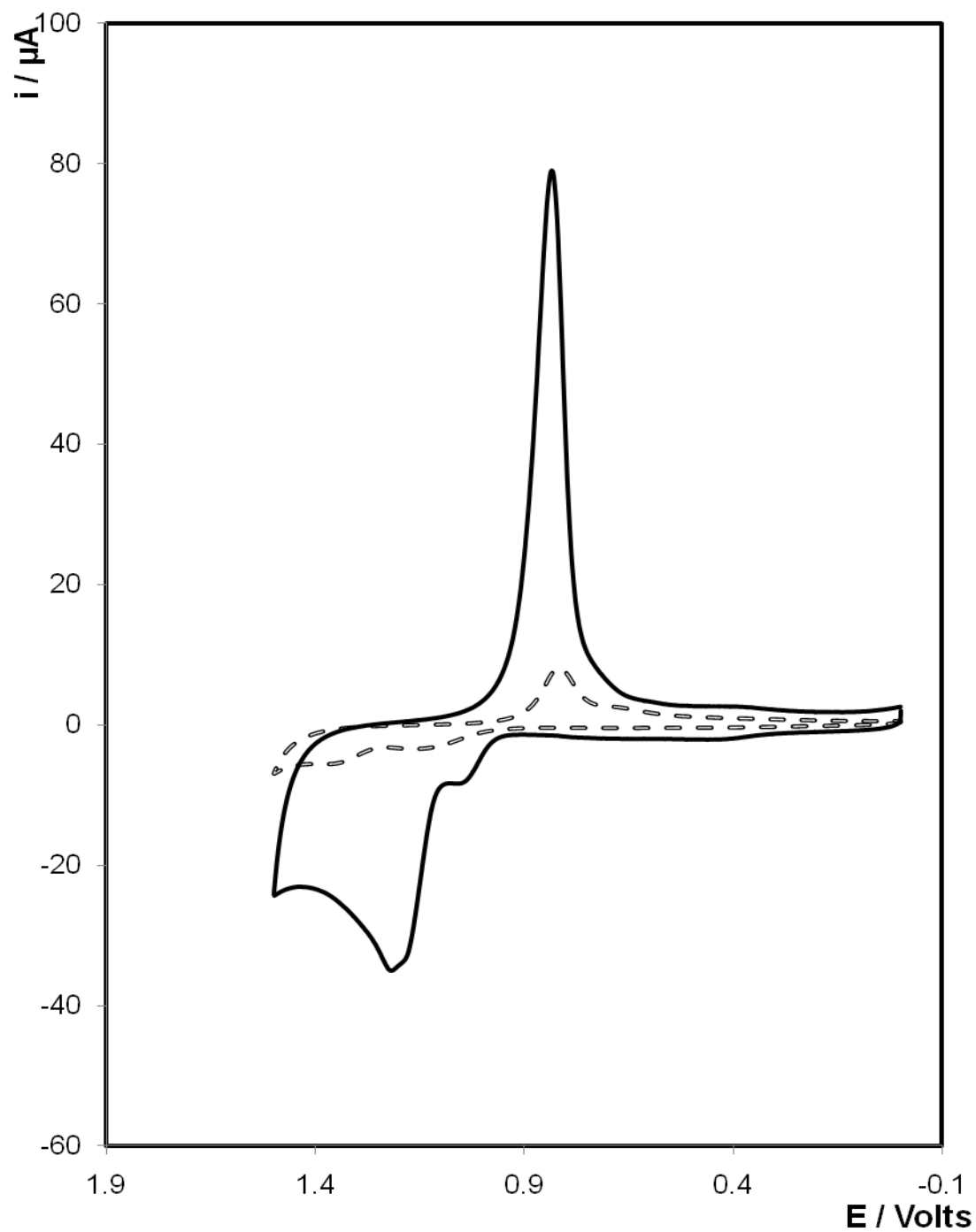


Figure 3.3 Cyclic voltammograms of a 2 mm diameter planar gold electrode in 0.1 M H_2SO_4 before (dashed line) and after modification with gold nanoparticles formed in 3 mM HAuCl_4 at an applied potential of -0.273 V vs. Ag/AgCl. The deposition time of the AuNPs was 3 min, and the supporting electrolyte was 0.1 M KCl (bold line).

3.3.2 Scanning electron microscopy (SEM) of gold nanoparticle electrodeposition

SEM is used for investigating the surface morphology and micro/nanostructures of the gold deposits.¹⁹ SEM was carried out on an unmodified gold electrode and the modified electrode following electrodeposition of gold NPs. The concentration of the gold salt solution was 3 mM and the deposition process lasted for 3 min

Figure 3.4 (row A) shows the SEM of a bare gold electrode. This figure shows that no gold nanostructures are observed on the electrode. The surface of the planar gold electrode had a surface roughness factor of 1.25 and is relatively smooth.

Figure 3.4 (row B) shows the SEM image where many small crystals, generally 260 nm in size, are present indicating that fractional gold deposition has occurred. This correlates to the surface roughness factor of 2.52 calculated in Section 3.3.1. After the electrochemical deposition of gold the surface area of the electrode increased by 49 %. These nanoparticles on the electrode allows for the amount of single strand DNA (ss-DNA) immobilised to also be increased. The creation of this additional area available for DNA binding ought to increase the overall sensitivity of the DNA detection. Discussed later on in Section 3.3.4, the system utilising the DNA on the nanoparticles modified electrode produced an enhancement in the hybridisation efficiency and the sensitivity limit by a factor of 4 compared to a conventional DNA immobilisation system on a planar surface

As it was hard to distinguish the gold nanoparticles from the gold disc electrodes, the electrodeposition was also carried out on ITO glass electrodes. Figure 3.4 (row C) shows the SEM images of the nanogold electrode obtained by the electrodepositing the potential of -0.273 V (vs. Ag/AgCl) in 3 mM HAuCl₄ for 3 min. The growth rate of the AuNPs was very rapid and multilayers of AuNPs could be observed. The electrode surface looked to be fully occupied

by many large nanogold aggregates. The smallest particles had a diameter of about 202 nm, where the bigger clusters had a diameter of approximately 340 nm. From the SEM images, it could be clearly seen that the nanogold electrode obtained after the electrodepositing for 3 min in 3 mM HAuCl_4 had a large apparent surface area, which was in agreement with the cyclic voltammogram in Figure 3.4. The SEM images consisted of clusters of gold nanoparticles and many voids between particles. This electrode modified by AuNPs provides a good environment for DNA immobilization and hybridization.

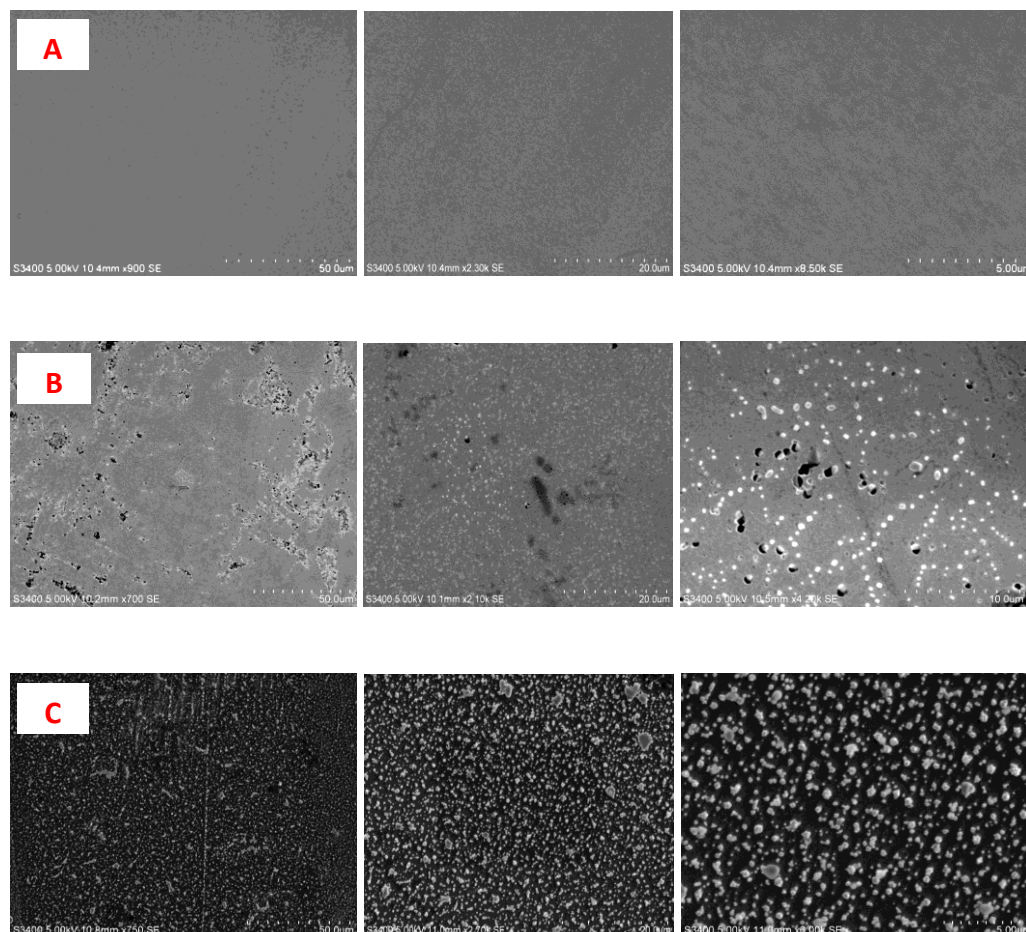


Figure 3.4 (A) Scanning electron micrograph image of a freshly electrochemically cycled 2 mm diameter gold disc electrode. (B) SEM of a gold disc electrode after the electrochemical deposition of AuNPs. (C) SEM of an ITO glass electrode after the electrochemical deposition of AuNPs showing 1.3 μg of AuNPs deposited. The deposition potential was held at -0.273 V vs. Ag/AgCl in a 3 mM HAuCl₄ solution, with a deposition time of 3 min, and the supporting electrolyte was 0.1 M KCl. The charge passed was 2.01×10^{-3} C. The accelerating voltage was set at 5 kV.

3.3.3 Potentiodynamic study of an enzyme amplified DNA sensor

The main objective is to detect the presence of the sequence specific DNA through the use of an enzyme labelled DNA strand, horseradish peroxidase (HRP) and an electron mediator hydroquinone. Cyclic voltammetry was used to determine the working potential.

The DNA capture probes are modified at the 5' end with thiol groups to immobilise the oligonucleotides to the electrodes gold surface allowing for a significant amount of hybridisation with target DNA.²⁰ It is well known that thiols adsorb rapidly onto the surface of the gold electrode through the sulphur atom resulting in a Au-S-(CH)_n bond.²⁰ The immobilisation buffer for the attachment of the capture DNA to the Au modified electrode was carried out in 1 M NaCl-TE buffer (buffer 1). Hybridisation, as described in Section 2.4.3, of the target and HRP labelled DNA was carried out in Denhardt's buffer.

HRP is a commonly used enzyme for the construction of hydrogen peroxide-based biosensors.²¹ The redox centers of HRP, like most enzymes, are electrically insulated by a protein shell. Consequently, direct electron transfer between HRP and the electrode is relatively slow and can be difficult to detect. Mediators such as hydroquinone are introduced to facilitate the electrical communication of HRP with the electrode surface.²¹ The electrocatalytic ability of the HRP electrode for the reduction of H₂O₂ was tested by using hydroquinone as electron mediator by cyclic voltammetry. The mediator concentration is a factor that affects the response of the biosensor. *Chetcuti et al*²² investigated the response of the enzyme electrode and found that it increased sharply as the concentration of hydroquinone increased, and attained a saturation value at 1.8 mM. A further increase of the hydroquinone concentration did not change the response current significantly, which is typical of a mediator-based sensor.²¹ At a low mediator concentration, the biosensor response is mediator-dependent. Only when the mediator concentration is high enough, the biosensor response becomes substrate-dependent. Thus, 1.8 mM hydroquinone was considered to be a suitable mediator concentration

for enhancing the electron transfer between the HRP and the electrode^{21,22} and was used in amperometric determination for all further research.

Figure 3.5 shows the cyclic voltammograms behaviour of HRP - AuNP modified electrode (roughness factor of 2.6) in an unstirred deoxygenated PBS solution (pH 7.4) containing 1.8 mM hydroquinone at a scan rate of 100 mV s^{-1} without any H_2O_2 . One couple of redox peaks, which correspond to the typical electrochemical behaviour of hydroquinone,²³ due to 2e^- , 2H^+ coupled redox reaction of HQ molecule were exhibited. The upper curve represents the reduction of hydroquinone to benzoquinone at approximately -0.05 V (Figure 3.5, bold line). At a potential of -0.40 V all of the hydroquinone was fully reduced to benzoquinone, where the direction of the potential is then reversed and the benzoquinone is then oxidised and the anodic peak occurs. The lower curve represents the oxidation of hydroquinone found at $+0.423 \text{ V}$.

In Figure 3.5 (dashed lines); the addition of $200 \mu\text{M}$ H_2O_2 to the solution resulted in a typical²⁴ enhancement in the reduction current peak and a decrease in the oxidative current peak. This demonstrates the electrocatalytic behavior of the HRP in response to the reduction of hydrogen peroxide.²⁵ When further adding another $200 \mu\text{M}$ of H_2O_2 to the cell, the cathodic peak further enhances and the anodic peak further reduces. The fact is indicative of HRP-dependent catalytic reduction of the H_2O_2 based on an electron mediator.²⁵ These phenomena evidently show that the HRP to the DNA sensor surface possessed excellently electrocatalytic ability for the H_2O_2 reduction and the hydroquinone could effectively communicate electrons from the redox center of HRP and the Au electrode.²⁶ This comparison of the voltammograms with and without H_2O_2 present, demonstrated that hydroquinone could effectively shuttle electrons between the redox center of HRP and the electrode surface.²⁷ In addition, as shown in Figure 3.5, upon addition of H_2O_2 to HQ/PBS, the reduction peak of HRP shifts slightly to negative, which has also been observed in the literature.²⁶ The peak separation of ca. 438 mV observed in Figure 3.5 (bold line) decreases down to 392 mV after the addition of H_2O_2 (figure 3.5, dashed line). The decrease in

the peak-to peak separation clearly indicates a faster heterogeneous electron transfer of HQ upon addition of H_2O_2 .²⁶

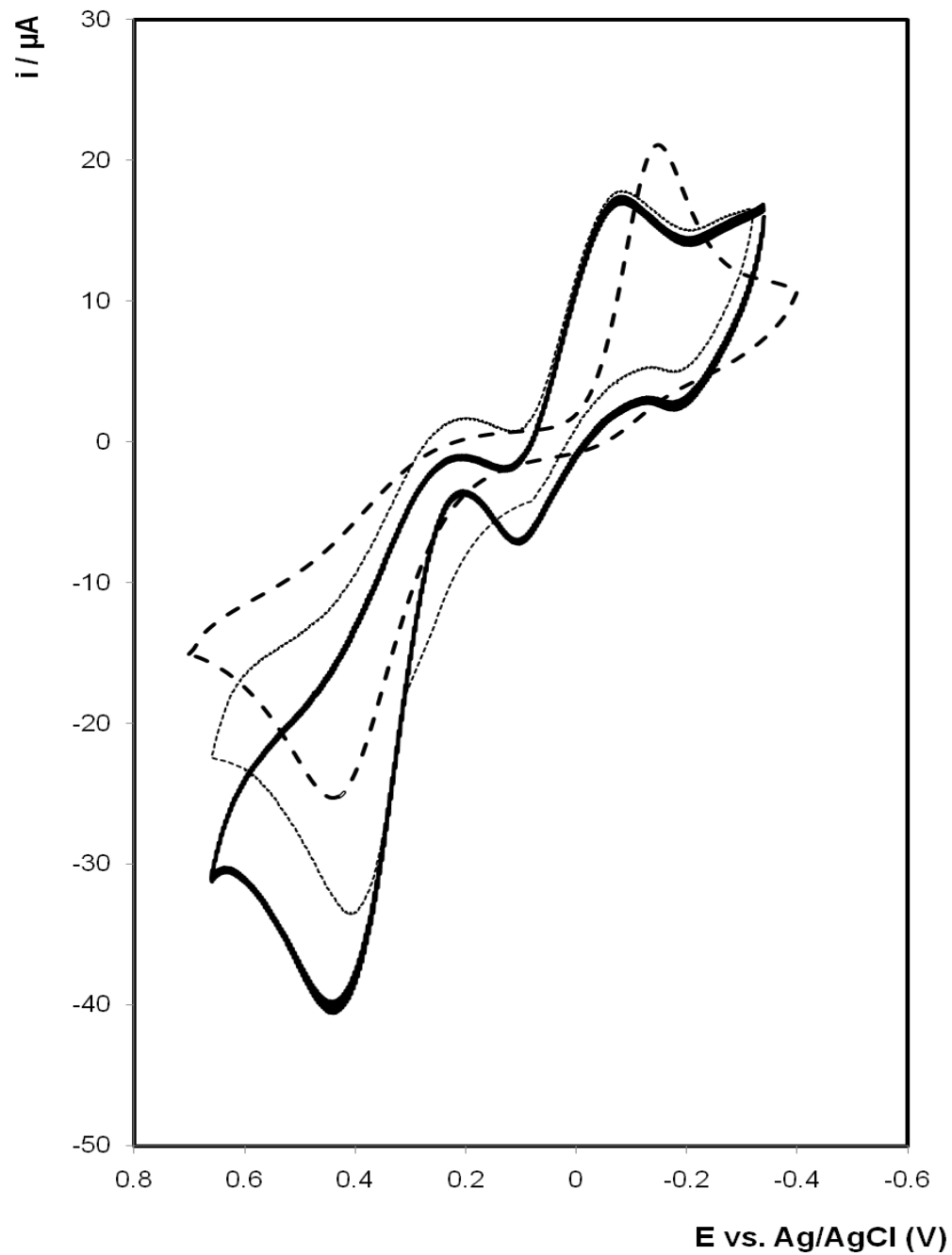


Figure 3.5 Cyclic voltammograms of the HRP/DNA/AuNP electrode in 0.1 M phosphate buffered saline (0.1 M KCl) containing 1.8 mM hydroquinone in the absence (bold line) and presence (dashed lines) of 200 μM H_2O_2 . Scan rate was 100 mVs^{-1} .

3.3.4 Potentiostatic study of an enzyme amplified DNA sensor

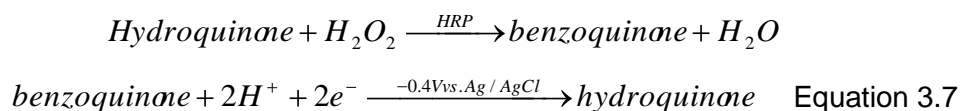
An enzyme biosensor relies on the reaction between enzymes and target analytes to produce a signal proportional to the target analyte concentration.²⁸ The quantity of the enzyme labelled DNA present on the surface is based on the electrochemical monitoring of the activity of horseradish peroxidase (HRP) through its catalysis of hydrogen peroxide (H_2O_2) in the presence of the mediator hydroquinone (HQ).²⁹ The amperometric response of the HRP - Au modified electrode to 200 μM hydrogen peroxide was investigated over the potential range of -0.1 to -0.6 V in a 1.8 mM hydroquinone solution prepared in phosphate buffer saline (0.1M KCl). The response increased sharply from -0.1 to -0.3 V and reached its peak value at -0.4 V, similar to the trend of the cyclic voltammetric response observed in Figure 3.5. A further increase of the negative potential gave very little change in current response, as the limiting potential had been achieved. Thus, -0.4 V was selected as the applied potential for amperometric detection of H_2O_2 .

The effect of the H_2O_2 concentration on the HRP/AuNP biosensor was studied in 0.1 M PBS (pH 7.4) containing 1.8 mM hydroquinone. The electrode response improved with increasing H_2O_2 concentration and the current response achieves a maximum value in the presence of 200 μM H_2O_2 , indicating that H_2O_2 concentration is very important in HRP reactions to produce good sensitivity. However, if the concentration of H_2O_2 was too high, it would cause all active centers to be occupied by H_2O_2 and inhibit the activity of HRP. When the concentration of H_2O_2 was lower than 0.25 μM , the electrochemical response generated by the enzyme electrode was so weak that the determination of target DNA was not accurately possible. Thus, 200 μM H_2O_2 was considered to be a suitable substrate concentration for the amperometric measurement.²⁶

As illustrated in Figure 3.6, the initial current (approximately 0.01 μA) in the absence of any deliberately added enzyme substrate (H_2O_2) was measured for

approximately 10 min. When the H₂O₂ (200 μM) was added to pH 7.4 PBS (0.1 M KCl) containing 1.8 mM HQ, the biosensor responded rapidly to the substrate increase.³⁰ The response current rises steeply to reach a stable response. The response time to reach 95% of the maximum current is within 5 s, which indicates a fast process. Such a fast response may be attributed to the desirable environment for HRP provided by the AuNPs as well as the fast diffusion of the mediator to the DNA labelled HRP.³¹

In the presence of HRP, hydroquinone is oxidised to benzoquinone (BQ) resulting in a flow of electrons. The hydrogen peroxide is a substrate of the HRP which catalyses the reduction of H₂O₂ coupled to the oxidation of HQ into BQ and causes the source of the current peak. The H₂O₂ is broken down and the HRP is reduced (Equation 3.7). The hydroquinone allows this cycle to occur until it reaches a steady state current (approximately 10 min) and the current is measured again. In the presence of HRP, production of BQ should be directly related to the amount of enzyme. The electrode response¹² is defined as the difference in current before and after the addition of H₂O₂, this is denoted throughout the thesis as the differential current (Δi).



To evaluate the sensitivity of this assay, target DNA was serially diluted to concentrations ranging from 1 μM to 150 pM. For comparison purposes, the absolute current measured for 150 pM to 1 μM target DNA, the slope of the calibration curve and the lower concentrations of the target that could be detected were considered. The effect of the surface modification on the electron transfer is also clearly shown in the calibration results. Figure 3.7 compares the two cases of (a) HRP immobilised on a bare electrode and (b) HRP immobilised on the Au surface modified electrode. As depicted in Figure 3.7 (■), for the unmodified gold electrode, a variation in signal with change in concentration (150 pM to 1 μM) was observed. The cyclic voltammetry peaks were well defined and proportional to the concentration of the corresponding

DNA targets and the resulting calibration plots are linear. The dynamic linear calibration range of the HRP modified electrode is 1 -100 nM with a correlation coefficient of 0.9505. The reproducibility is excellent even at low DNA concentrations, e.g., at 150 pM the signal-to-noise ratio is at least ten. The signal-to-noise ratio, often written S/N or SNR, is a measure of signal strength relative to background noise.

Figure 3.7 (♦) shows the calibration curve of a HRP/DNA/Au-NPs/electrode when the Au nanoparticles were deposited for 3 min. The HRP modified on AuNP / electrode shows faster and more sensitive current response to the addition of hydrogen peroxide when compared with the enzyme electrode not containing gold nanoparticles. In the presence of AuNPs, the slope of the current response of *S.aureus* was amplified 4.5 fold with increasing concentrations of target DNA hybridised under optimal experiment conditions. Significantly, after AuNP modification, a greater sensitivity in current response (slope of 199.6 nA^{-1}) was observed when compared to the current response in the absence of AuNP (slope of 43.9 nA^{-1}). The dynamic linear calibration range for the AuNP modified electrode is 150 pM and 10 nM with a calculated limit of detection (LOD) of 0.158 pM and a correlation coefficient of 0.9313. The LOD is the minimum concentration at which the analyte or measured and can be identified. The LOD of the AuNP-DNA assay has significantly improved than the DNA assay on the planar gold electrode (LOD = 0.645 pM). This verified that the AuNP nanostructured surfaces showed better analytical performance than the planar gold electrode, in correlation with a 4.5 fold enhancement in sensitivity (slope) as compared to the unmodified gold electrode. The enhancement in signal was attributed to the improved condition for effective hybridisation between the capture DNA and the target as a result of the surface modification. The fabrication repeatability of four HRP electrodes, prepared independently, shows an acceptable reproducibility, with a standard deviation (RSD) of 4.8% for the response to the same concentration of $200 \mu\text{M H}_2\text{O}_2$.

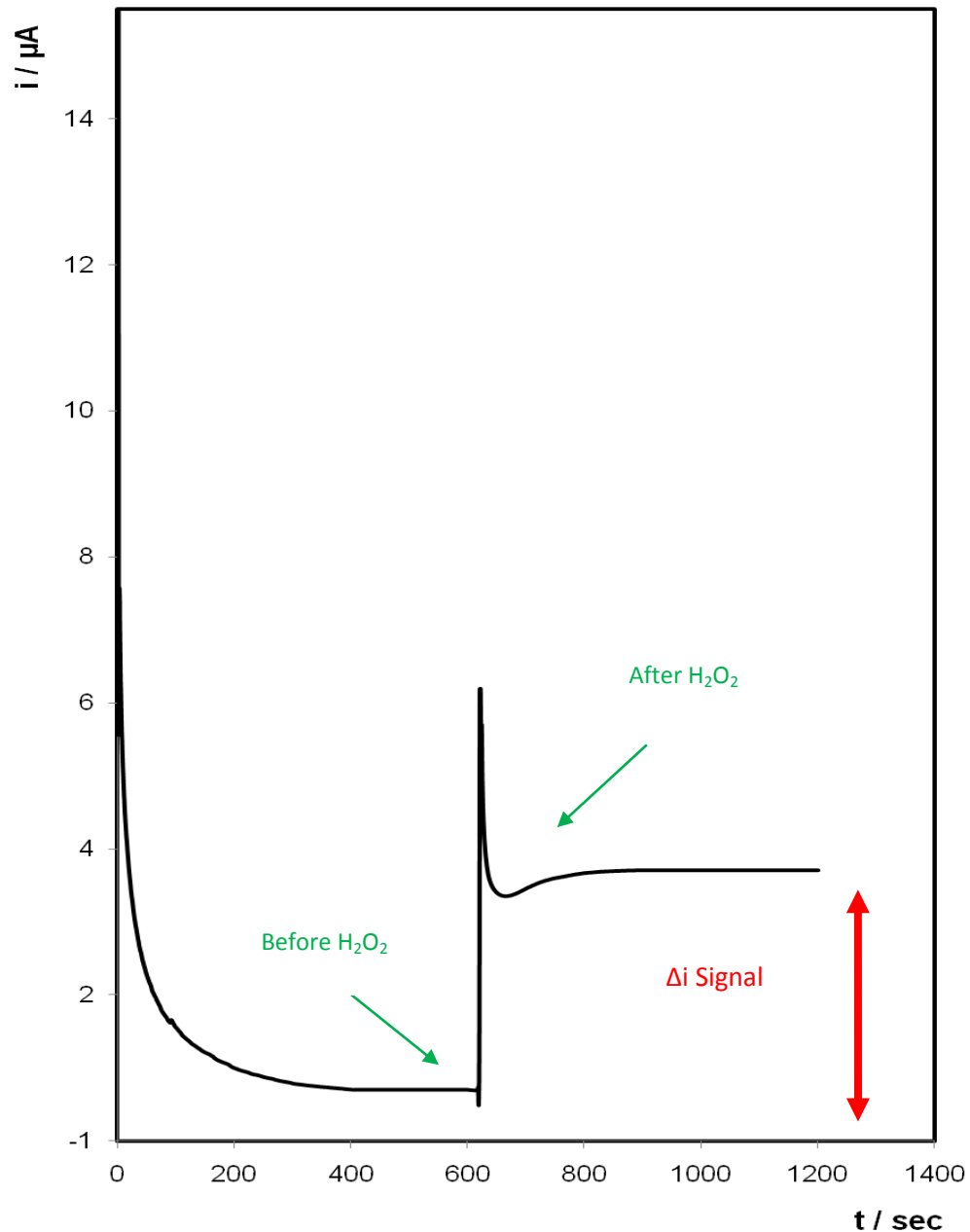


Figure 3.6 Amperometric i - t Curve for AuNP-electrode functionalised with ss-DNA (1 μ M capture strand, 150 pM target strand and 1 μ M probe HRP labelled DNA) cycled in phosphate buffer saline and 0.1 M KCl and a concentration of 1.8 mM hydroquinone. Difference in current response before and after addition of H_2O_2 is highlighted in red (Δi). Potential applied -0.40 V.

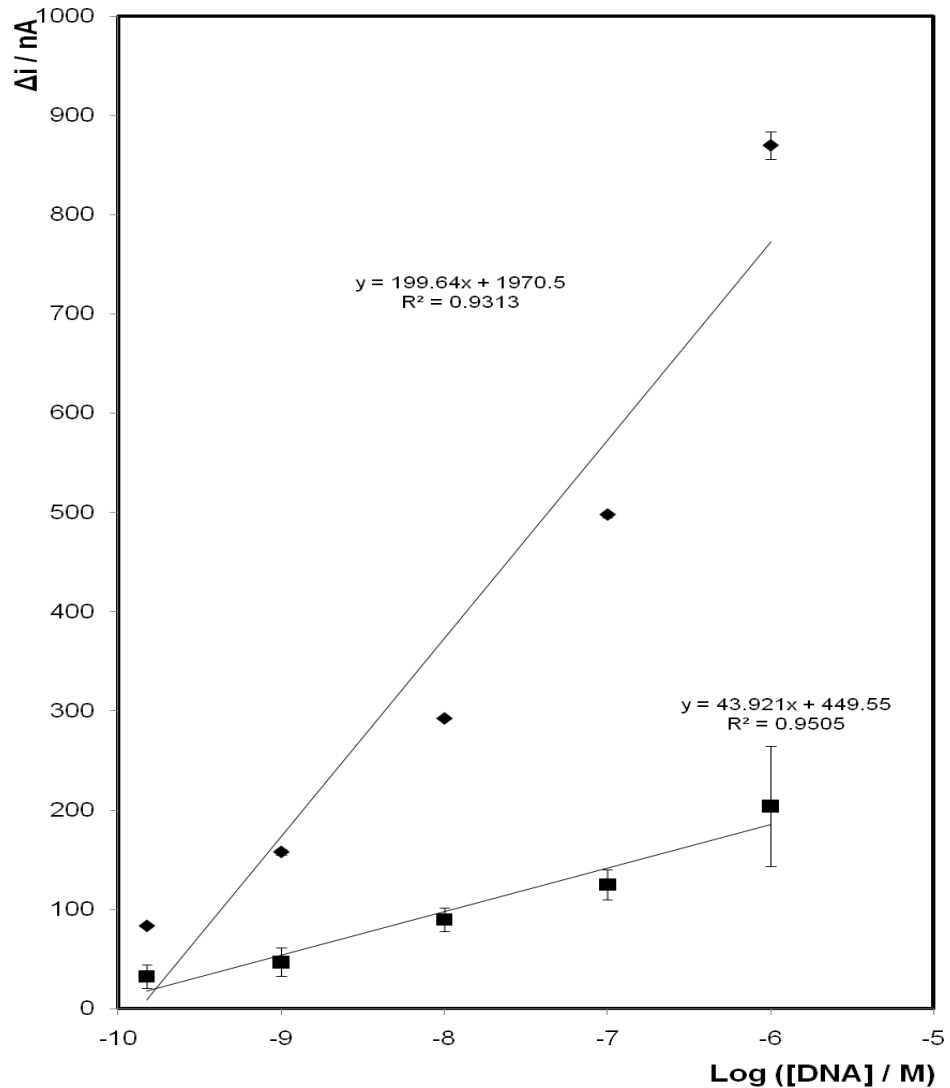


Figure 3.7 Electrochemical detection of sequence-specific *S. aureus* pathogen DNA concentration on a bare (■) and functionalised AuNP-electrode (◆). Capture strand, target strand and probe HRP strand were cycled in phosphate buffer saline and 0.1 M KCl and a concentration of 1.8 mM hydroquinone. Y axis is the difference in signal before and after addition of H_2O_2 (Δi). Potential applied -0.40 V. Where error bars are not visible, they are smaller than or comparable to, the size of the symbols and range from 0.6 % to 8.2 %.

3.3.5 The influence of HRP labelled DNA hybridisation time on an enzyme amplified DNA sensor

When the HRP labelled DNA in the hybridization buffer solution reaches the target DNA at the surface of the DNA sensor, it takes time for the contacting species to form a double strand DNA duplex. The effect of hybridization time of the HRP labelled DNA on amperometric signals has been investigated. The objective was to minimise the hybridisation time of the HRP while maintaining a sensor with high sensitivity and reproducibility. Assay preparation up until this point was carried out as described in Section 2.4.3. Figure 3.8 to 3.12 demonstrates that with increasing hybridisation time from 10 to 180 min, the amperometric current increases dramatically for each concentration of target oligo hybridised (150 pM to 1 μ M) and then tends to change only slightly for longer HRP hybridisation times. Each levelling of current is observed at different times at altering concentrations of pathogen DNA where the maximum binding of to HRP labelled DNA has taken place.

Figure 3.8 presents the differential current response (Δi) of 1 μ M target DNA at varying HRP hybridisation times using two independent electrodes. The current signal was monitored as a function of hybridisation time, and it is shown that the signal increases with time up to 60 min. However, as time increased past 60 min, a levelling of the current is observed with a maximum current of 872 nA being obtained at 60 min. This current levelling suggests that all available target DNA sites have been bound with HRP probe strands at times longer than 60 min. Comparing this result to Section 3.3.4, when the recommended HRP time of 90 min was carried out, minimal difference in absolute current is observed. For the 90 minute HRP hybridisation, a reading of 870 ± 14.14 nA was obtained. A comparison of maximum detection responses between altering HRP hybridising time and 90 minute hybridisation time is outlined in Table 3.4. This data suggests that 30 min could have been saved in hybridisation time for the [DNA] of 1 μ M.

Figure 3.9, show the differential current response for the 100 nM target oligos at varying HRP hybridisation time. There is a similar increase in current with

time, as observed previously in Figure 3.8. The signal increased with time up to 90 min after which the current intensity remains virtually unchanged. The maximum current of 498 nA is reported for the 100 nM target DNA concentration at 90 minute HRP hybridisation.

Figures 3.10 and 3.11, show the differential current responses obtained for the 10 nM and 1 nM target oligo's concentration vs. HRP hybridisation time. Similarly, for these concentrations of target DNA, a plateau was observed at times longer than 90 min, suggesting that for these individual experiments the optimum time required for HRP hybridisation had been reached. The maximum average absolute current response for the 10 nM and 1 nM solutions was found to be 292 and 158 nA, respectively. Table 3.1 compares the results of the 100 nM, 10 nM and 1 nM target oligo concentrations to the results found in Section 3.3.5. The recommended time of 90 min did prove to be the optimum time and no benefit was achieved by the allowing the hybridisation time of the HRP to be increased up to 3 h. Therefore, 90 min was selected throughout the experiments for nM concentrations of target pathogen DNA.

Figure 3.12 displays the effect of increasing the HRP hybridisation time on the lower concentration of target oligo (150 pM). The differential current increased rapidly with HRP hybridisation time at first (up to 2 h) and then started to level off after 2 h. A maximum current of 93 ± 2.3 nA was reached, which is a 10 % increase of absolute current detection when compared to the absolute current value of 83 ± 1.2 nA found at the recommended 90 minute HRP hybridisation time for the same target DNA concentration in Section 3.3.4.

A calibration experiment was plotted to elucidate the analytical performance of the electrochemical biosensor. Figure 3.13 shows the semi-log concentration vs. maximum electrode responses (Δi_{\max}) for the pathogen DNA detection using a Au modified gold electrode where the concentration of sequence-specific DNA of *S. aureus* is systematically varied from 150 pM to 1 μ M. The Δi_{\max} value is the average maximum electrode response ($n=2$) obtained in each experiment illustrated in Figure 3.8 to 3.12 and Table 3.1. A measurable response even for pathogen DNA concentrations as low as 150 pM was

observed. The observation that Δi_{\max} increases ($R^2 = 0.9522$) with $\log [\text{DNA}]$ rather than $[\text{DNA}]$ suggests that the current response is influenced by the concentration of the HRP co-reactant, H_2O_2 , as well as the DNA concentration. The sensitivity of the biosensor (slope of 200.3 nA^{-1}) has significantly increased when compared to the un-optimised sensor (slope of 199.6 nA^{-1}).

Assay shortening has been achieved for the higher concentration of target oligo. For the concentrations of target DNA in the μM range, a 60 minute HRP hybridisation time was required to reach the Δi_{\max} . All nanomolar concentrations of the target DNA, required a longer HRP hybridisation time of 90 min to achieve the maximum electrode response. Picomolar concentrations of the target DNA required a longer time of 120 min to achieve maximum attachment of the HRP labelled DNA to the complementary target oligos. Once the hybridisation time has been optimised for each [target], one would expect that most of the target DNA is binding with the HRP labelled DNA in the hybridization solution, forming compact complexes on the surface of the DNA sensor.²⁵ Also of note, the sensitivity of the HRP labelled DNA based assay was further improved by using longer hybridisation times for the picomolar target concentration. In our preliminary experiments employing a time of 90 min hybridisation time for HRP, we obtained a calculated detection limit of around 0.158 pM . This assay exhibits an improvement of the LOD (0.110 pM) to the corresponding assay.

Table 3.1 Comparison of the differential current response of target DNA at [Target Oligo Hybridised] at the recommended and optimised HRP probe strand hybridisation time.

Electrode Modification	Concentration of S. aureus (M)	Average current response ($\Delta i / nA$)	Standard deviation (n = 2)	Standard error
90 minute HRP hybridisation time	1.50E-10	83	1.23	1.47
	1.00E-09	158	2.83	1.79
	1.00E-08	293	0.71	0.24
	1.00E-07	498	2.83	0.57
	1.00E-06	870	14.14	1.63
Optimised HRP Hybridisation time				
120 min	1.50E-10	93	2.31	1.63
90 min	1.00E-09	158	2.83	2.00
90 min	1.00E-08	293	0.71	0.50
90 min	1.00E-07	498	2.56	1.81
60 min	1.00E-06	872	2.86	2.02

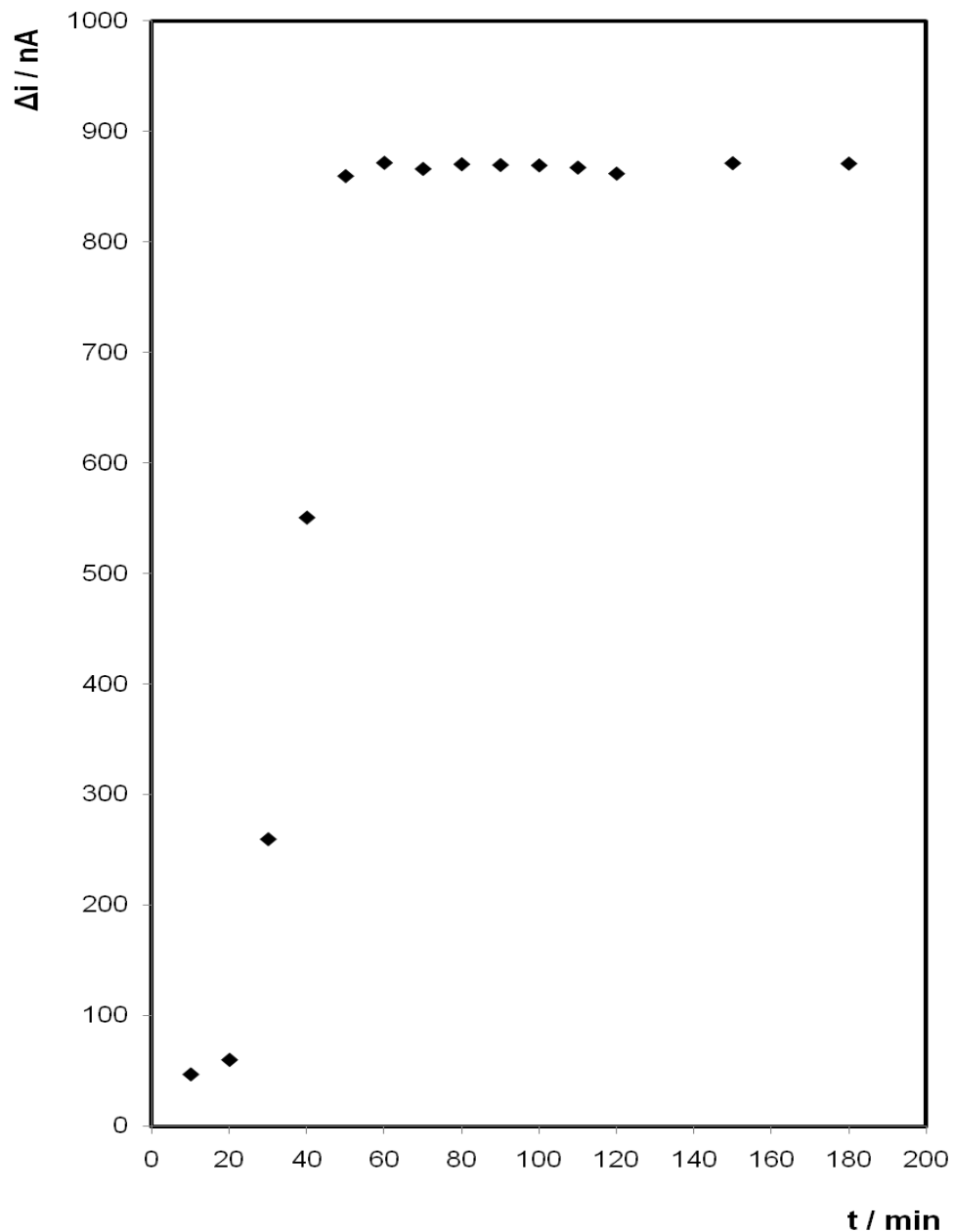


Figure 3.8 Dependence of the average ($n = 2$) electrode current response (Δi) on the $1 \mu\text{M}$ HRP labelled DNA hybridisation time, on an AuNP-modified electrode ($1 \mu\text{M}$ capture DNA and $1 \mu\text{M}$ target DNA). All experiments were carried out at a constant potential of -0.4 V in 1.8 mM hydroquinone containing an aqueous 0.1 M phosphate buffer ($\text{pH } 7.4$) with 0.1 M KCl supporting electrolyte.

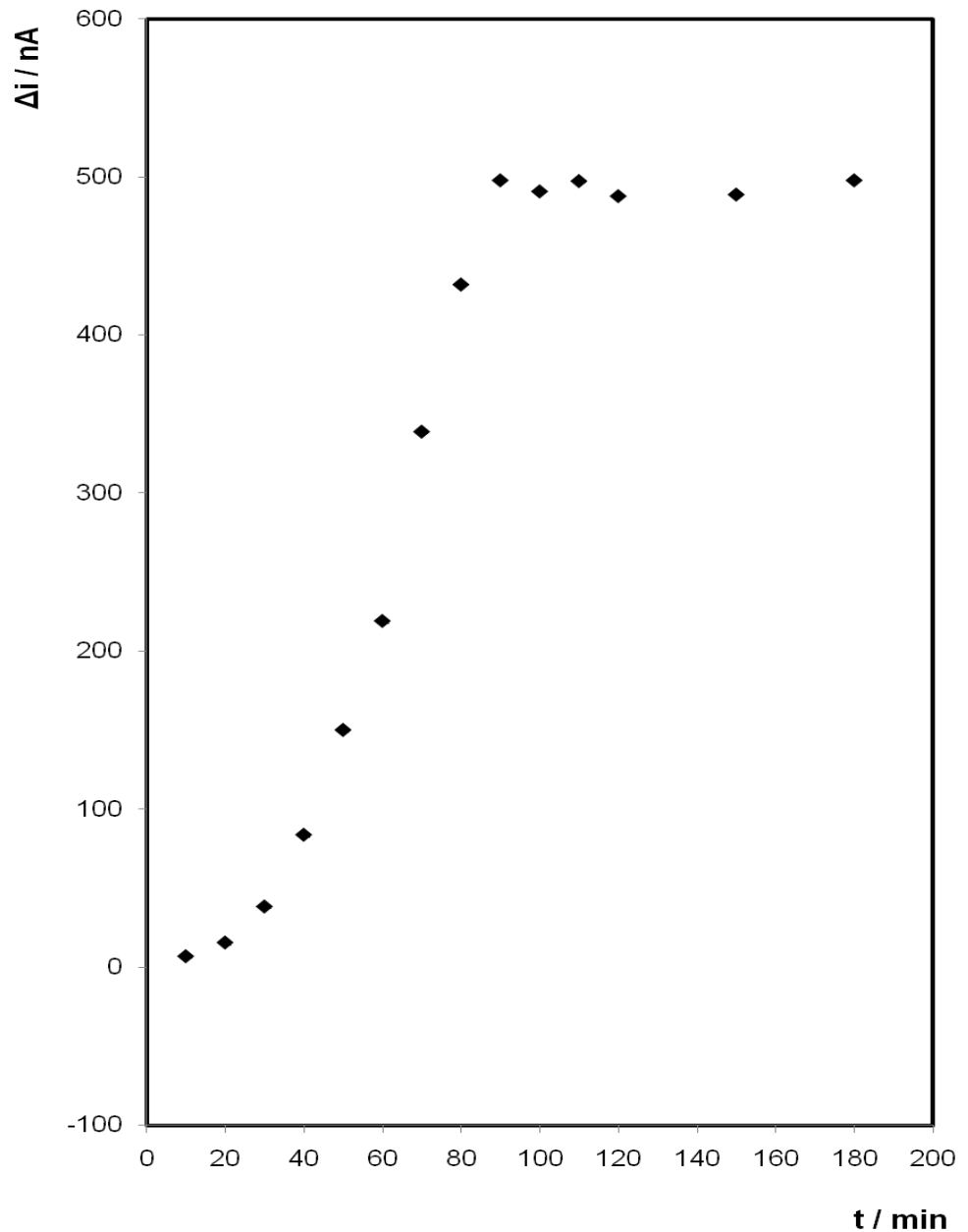


Figure 3.9 Dependence of the average ($n = 2$) electrode current response (Δi) on the $1 \mu\text{M}$ HRP labelled DNA hybridisation time, on an AuNP-modified electrode ($1 \mu\text{M}$ capture DNA and 100 nM target DNA). All experiments were carried out at a constant potential of -0.4 V in 1.8 mM hydroquinone containing an aqueous 0.1 M phosphate buffer ($\text{pH } 7.4$) with 0.1 M KCl supporting electrolyte.

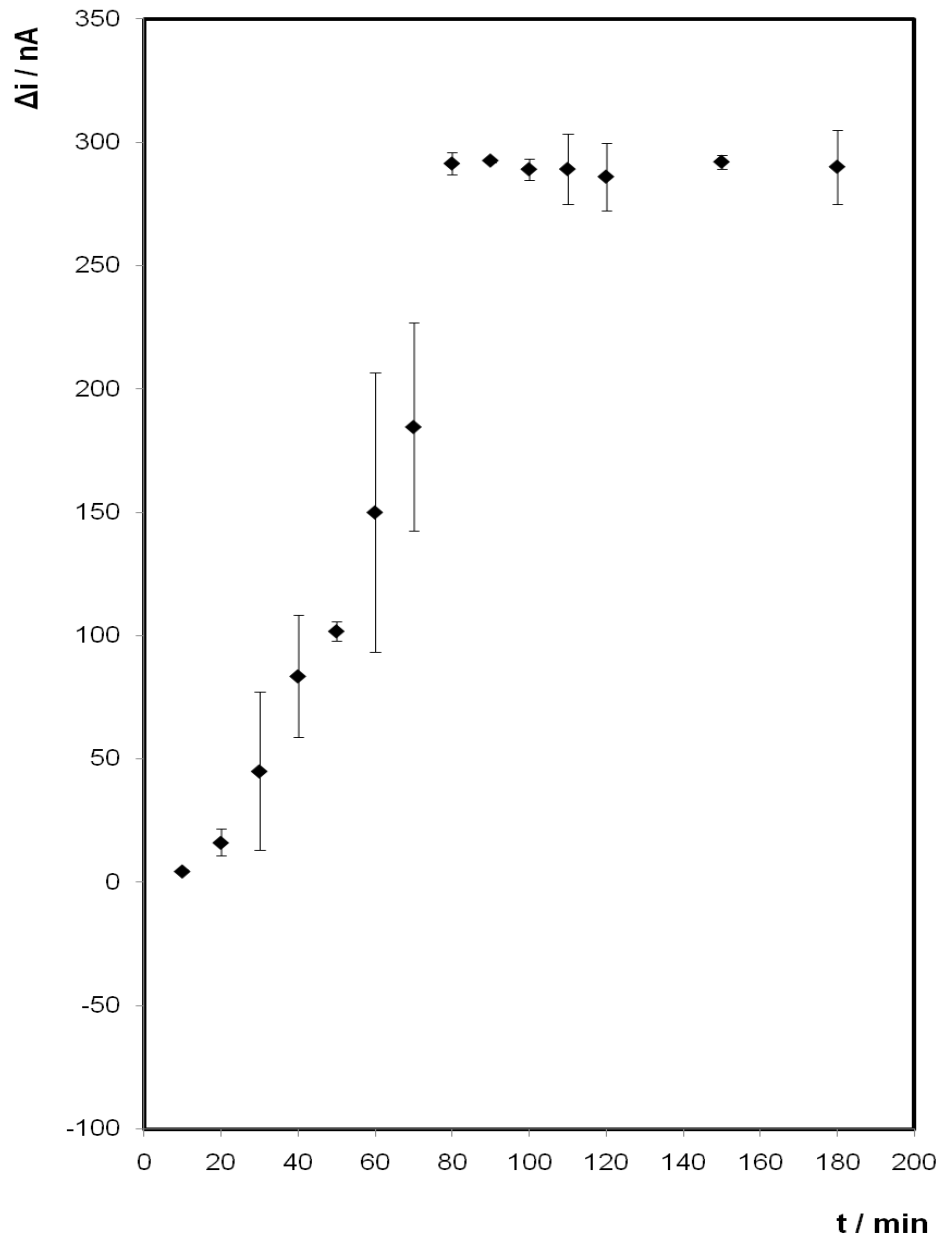


Figure 3.10 Dependence of the average ($n = 2$) electrode current response (Δi) on the $1 \mu\text{M}$ HRP labelled DNA hybridisation time, on an AuNP-modified electrode ($1 \mu\text{M}$ capture DNA and 10 nM target DNA). All experiments were carried out at a constant potential of -0.4 V in 1.8 mM hydroquinone containing an aqueous 0.1 M phosphate buffer ($\text{pH } 7.4$) with 0.1 M KCl supporting electrolyte.

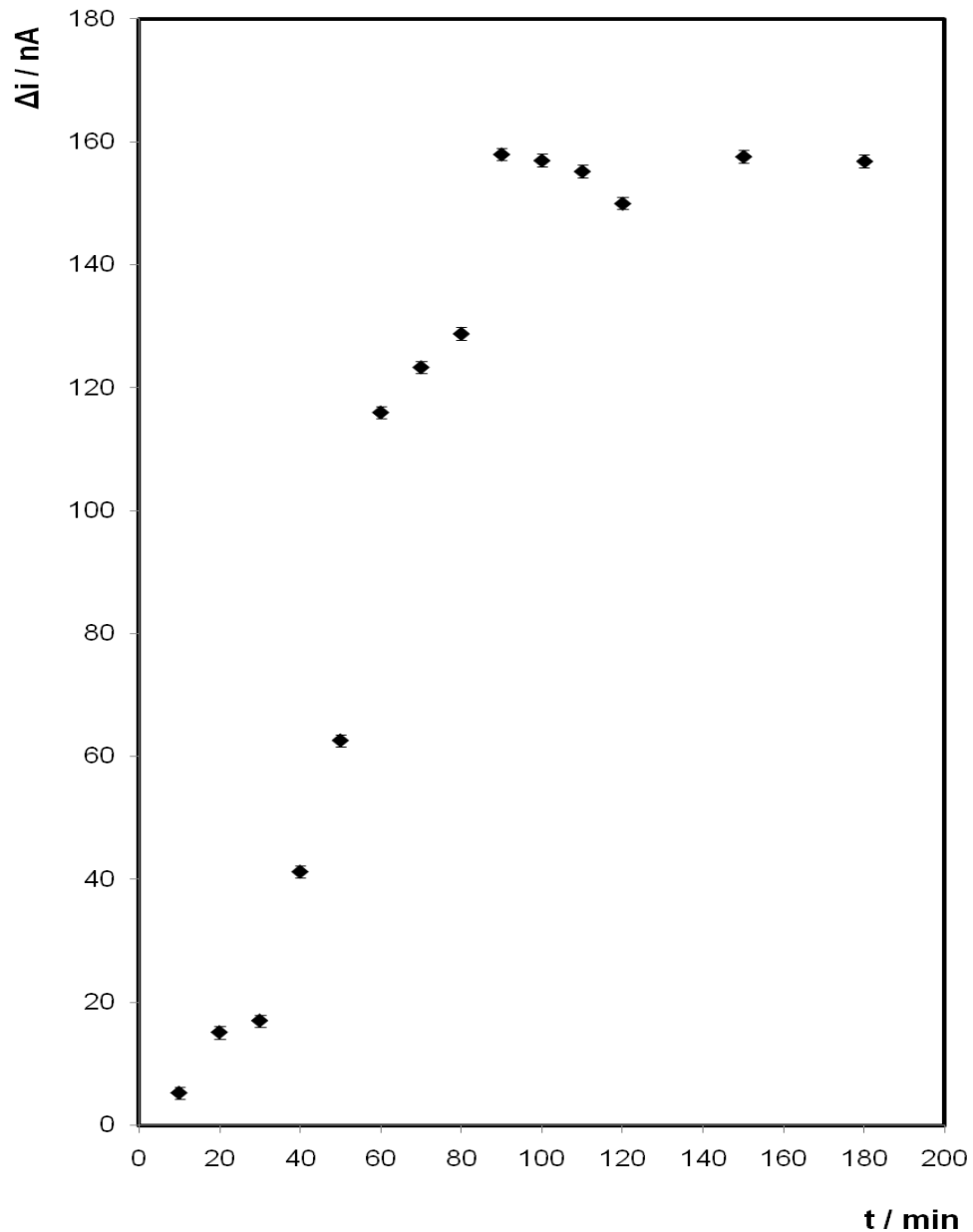


Figure 3.11 Dependence of the average ($n = 2$) electrode current response (Δi) on the $1 \mu\text{M}$ HRP labelled DNA hybridisation time, on an AuNP-modified electrode ($1 \mu\text{M}$ capture DNA and 1 nM target DNA). All experiments were carried out at a constant potential of -0.4 V in 1.8 mM hydroquinone containing an aqueous 0.1 M phosphate buffer ($\text{pH } 7.4$) with 0.1 M KCl supporting electrolyte.

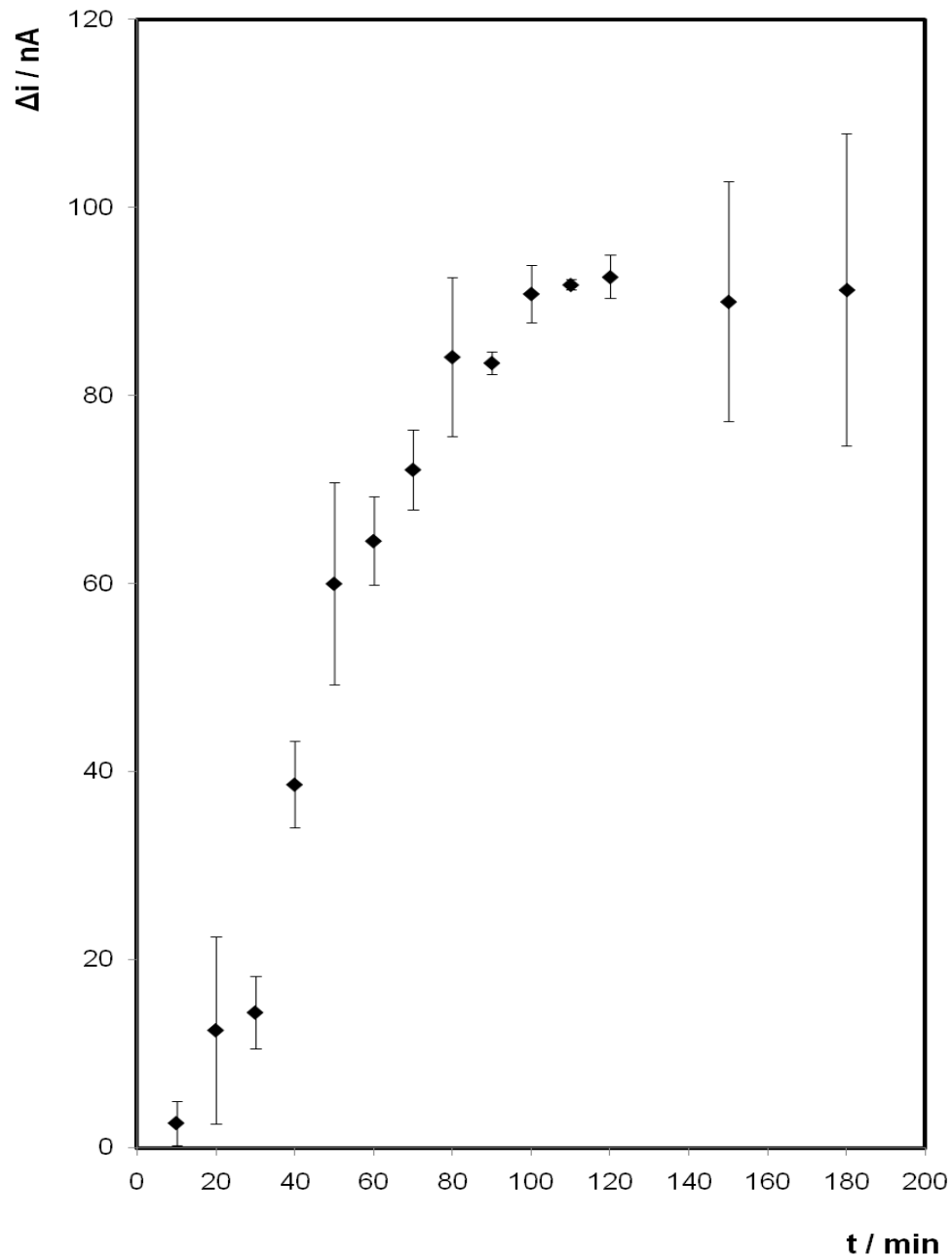


Figure 3.12 Dependence of the average ($n = 2$) electrode current response (Δi) on the $1 \mu\text{M}$ HRP labelled DNA hybridisation time, on an AuNP-modified electrode ($1 \mu\text{M}$ capture DNA and 150 pM target DNA). All experiments were carried out at a constant potential of -0.4 V in 1.8 mM hydroquinone containing an aqueous 0.1 M phosphate buffer ($\text{pH } 7.4$) with 0.1 M KCl supporting electrolyte.

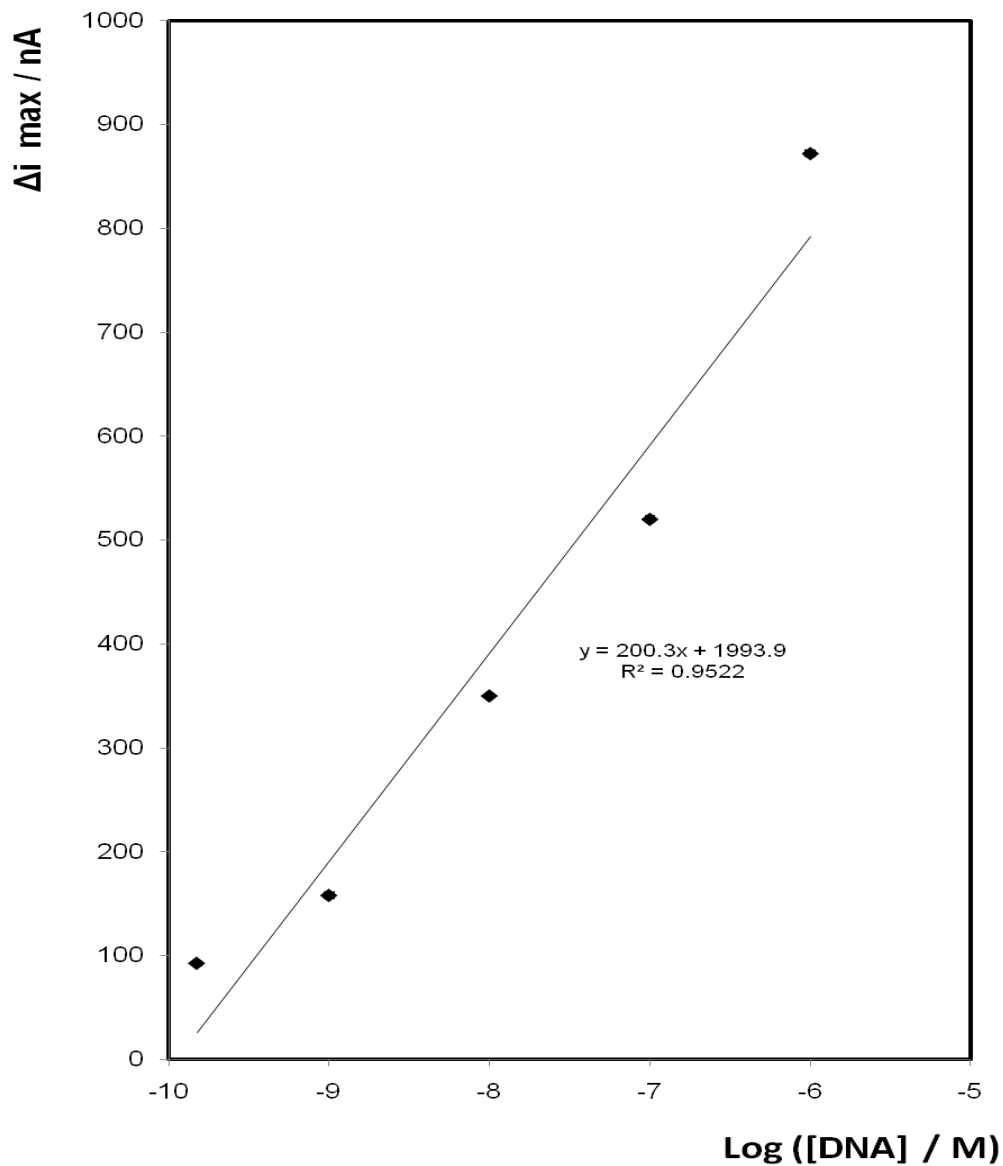


Figure 3.13 Semi-log concentration (150 pM to 1 μM) of sequence-specific DNA of *S. aureus* vs. maximum average ($n = 2$) electrode current response (Δi_{\max}) on an AuNP-modified electrode. All experiments were carried out at a constant potential of -0.4 V in 1.8 mM hydroquinone containing an aqueous 0.1 M phosphate buffer (pH 7.4) with 0.1 M KCl supporting electrolyte.

3.3.6 Species recognition ability (mismatch and non-pathogenic species)

3.3.6.1 1 Base mismatch

An assay was carried out to establish the selectivity of the biosensor to a specific DNA sequence in the presence of a mismatch DNA sequence. The DNA sequence differed by 1 mismatch base pairs i.e., oligomer G was changed to A. As seen in Figure 3.14 the electrochemical values of the hybridisation with mismatched oligonucleotide produced a lower analytical signal in comparison with the full matching oligonucleotide (-37 % decrease in signal). Therefore, the label-free DNA biosensor described here has shown to be able to detect specific sequences of oligonucleotides with high selectivity.

3.3.6.2 3 Base mismatch (*S. epidermidis* discrimination)

Taking into account the significant difference observed between the voltammetric signals obtained before and after hybridisation with the 1 base mismatch target oligonucleotide, the target probe was investigated for the response of noncomplementary 3 base mismatch oligonucleotides, named *Staphylococcus epidermidis* (*S. epidermidis*). In Figure 3.14, the electrochemical values of the hybridisation with mismatched oligonucleotide produced a lower analytical signal in comparison with the full matching oligonucleotide (-94 % decrease in signal). The results show that a three base mismatch showed excellent discrimination between the nucleic acid sequences. This is significant as *S. epidermidis* is really important as it can often be mistaken for *Staphylococcus aureus* (*S.aureus*) and its presence is sometimes incorrectly associated with mastitis.

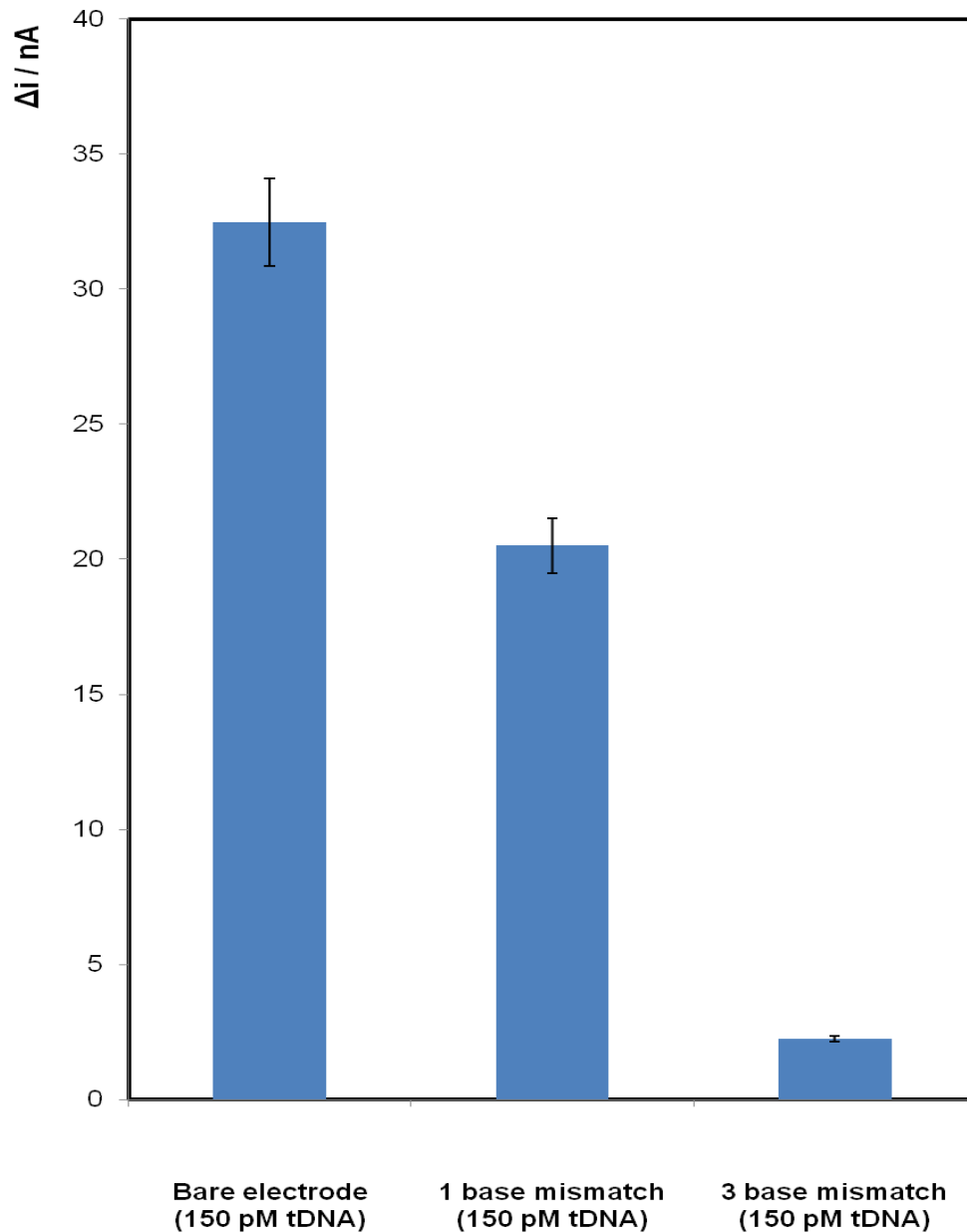


Figure 3.14 Average ($n = 2$) electrode current response (Δi) on the 150 pM target DNA (tDNA) modified bare electrode ($1 \mu\text{M}$ capture DNA and $1 \mu\text{M}$ HRP labelled DNA). All experiments were carried out at a constant potential of -0.4 V in a 1.8 mM hydroquinone containing an aqueous 0.1 M phosphate buffer ($\text{pH } 7.4$) with 0.1 M KCl supporting electrolyte.

3.3.7 Immobilisation buffer identity

Denhardt's

The most common technique to immobilise DNA capture probes onto the transducer surface is via the use of thiol link modified probe DNA molecules. The choice of the immobilisation buffer could influence the orientation and packing density of the capture strand DNA. The tendency of adsorption of thiolated probe onto the gold surface is found in higher buffer concentration such as 1 M NaCl-TE. This buffer is reported³² to give better coverage of the probes on the gold surface as the high ionic strength is believed to suppress the intermolecular electrostatic repulsion between neighbouring strands of DNA molecules. To verify the effect of the immobilisation buffer for capture DNA attachment, Denhardt's buffer was used instead of the 1 M NaCl-TE buffer. This buffer is widely renowned for its ease to use properties and can be used as received. It prevents non-specific hybridisation and is much preferred for long tailed probes as it contains a blocking agent.³³

The experimental conditions remained the same as those outlined in Section 2.4.3. The capture DNA was kept at a constant concentration of 1 μM , the target DNA concentration ranged from 150 pM to 1 μM and 1 μM HRP labelled DNA was allowed to hybridise for 90 min. The DNA modified electrodes in the absence of AuNPs were examined first. In agreement with results already present in Section 3.3.4, Figure 3.15 displays the effect of increasing the target concentration on the difference in current signal. The current response increased rapidly with increasing target concentration with a correlation coefficient of 0.9025. The dynamic linear range was from 1 nM and 100 nM with a calculated limit of detection of 0.61 pM. The detection limit of the assay is considered as the lowest analysed concentration which produces a signal distinguishable from blank and negative controls. The signal to noise ratio is defined as the power between a signal and background noise (unwanted signal). For the 150 pM DNA concentration the signal to noise (S/N) is at least 3 with a standard deviation of 5.85

Figure 3.15 (♦) shows a 2.7 fold enhancement of the analytical performance for the AuNP/ DNA modified electrode using Denhardt's immobilisation buffer even for low target DNA concentrations of 150 pM. The use of gold nanoparticles has greatly improved the hybridisation performances of the thiolated capture DNA with regards to its loading density.³⁴ When the concentration of the target DNA is high for example, 1 μM, the HRP modified on AuNP / electrode showed faster and more sensitive current response to the addition of hydrogen peroxide when compared with the enzyme electrode not containing gold nanoparticles. In the presence of AuNPs, calibration plots of the electrode current response Δi depends on the increasing concentration of target DNA with a dynamic range of 150 pM and 10 nM, with a correlation coefficient of 0.9215 and a signal to noise ratio of 7.6 as shown in Figure 3.15. The overall limit of detection has improved from 0.61 pM to 0.13 pM.

For the purpose of comparison, the average electrode current response for concentrations of 150 pM to 1 μM target DNA, for both the unmodified and Au modified electrode as well as the NaCl-TE and Denhardt's immobilisation buffers were compared in Table 3.2. For the unamplified DNA modified sensors, a 1.4 fold increase was seen in sensitivity when using the 1 M NaCl-TE (43.9 nA⁻¹) immobilisation buffer compared to the Denhardt's buffer (30 nA⁻¹). After the incorporation of AuNPs, a 2.4 fold increase was observed in the sensitivity by simply altering the immobilisation buffer for the capture DNA to 1 M NaCl-TE buffer (199.6 nA⁻¹) when compared to Denhardt's buffer (81.8 nA⁻¹).

While the current data does not allow us to discriminate between surface coverage and orientation events which could be addressed for example using fluorescently labelled DNA, it appears likely that the Denhardt's buffer does not provide ideal parameters for this biosensor. Comparing Denhardt's to the NaCl-TE buffer, Denhardt's buffer is usually preferred as the hybridisation buffer when using 3' tailed oligonucleotides. This buffer can be used as received and requires no additions. It prevents non-specific hybridisation of the tail to complementary sequences in target DNA hybridisation buffer. When the target sequence is DNA, Denhardt's also contains saline sodium citrate (SSC) which as mentioned above is used as a blocking agent and is much

preferred for long tailed probes.³³ SCC ensures that the capture DNA strongly attaches itself to the surface of the electrode. In this DNA biosensor, the signal for the determination of our target sequence is mainly affected by the efficiency of the hybridisation event (base pairing of the immobilised probe to the target). The hybridisation process is affected by the electrostatic repulsion between the hybridising strands of the DNA and the density of the probes on the transducer surface. This tendency of the capture DNA in Denhardt's buffer to adsorb onto the surface blocks the attachment of target DNA due to its high packing density.

Table 3.2 Average current response of an unmodified electrode and AuNP modified electrode at different concentrations of target DNA. The effects of 2 different immobilisation buffers were compared for the detection of the hybridisation event.

Immobilisation buffer	Concentration of S.aureus (M)	Average current response ($\Delta i / nA$)	Standard deviation (n = 2)	Standard error
Unmodified Electrode				
1 M NaCl-TE buffer	1.50E-10	32.49	12.03	8.51
	1.00E-09	47.07	14.40	10.18
	1.00E-08	89.86	11.96	8.46
	1.00E-07	125.25	15.06	10.65
	1.00E-06	204.00	60.81	43.00
Denhardt's buffer	1.50E-10	27.95	8.27	5.85
	1.00E-09	39.56	0.71	0.50
	1.00E-08	60.92	10.01	7.08
	1.00E-07	83.00	24.04	17.00
	1.00E-06	150.00	25.46	18.00
AuNP Modified Electrode				
1 M NaCl-TE buffer	1.50E-10	83.49	1.23	1.47
	1.00E-09	158.00	2.83	1.79
	1.00E-08	292.50	0.71	0.24
	1.00E-07	498.00	2.83	0.57
	1.00E-06	870.00	14.14	1.63
Denhardt's buffer	1.50E-10	40.77	3.00	2.12
	1.00E-09	66.95	3.07	2.17
	1.00E-08	140.02	0.64	0.46
	1.00E-07	308.00	33.94	24.00
	1.00E-06	313.25	34.29	24.25

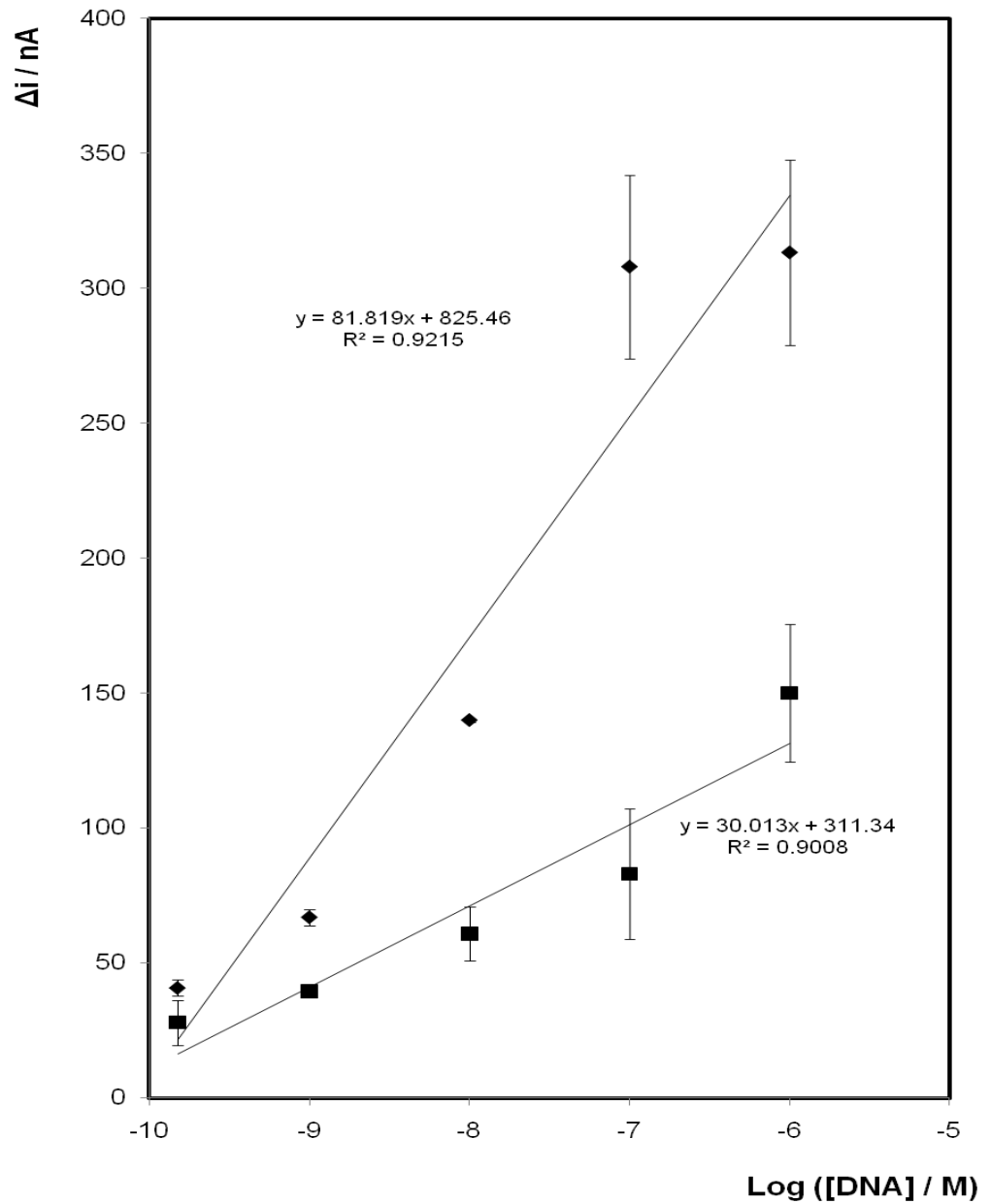


Figure 3.15 Electrochemical detection of sequence-specific *S. aureus* pathogen DNA concentration on a bare (■) and functionalised AuNP-electrode (◆). Capture strand, target strand and probe HRP strand (Denhardt's buffer) were cycled in phosphate buffer saline and 0.1 M KCl and a concentration of 1.81 mM hydroquinone. Y axis is the difference in signal before and after addition of H_2O_2 (Δi). Potential applied -0.40 V.

3.3.8 1 step hybridisation of enzyme amplified DNA

The analytical performance of the DNA biosensor using HRP was explored by using the immobilised probe to hybridize with the different concentrations of the complementary sequence. The sensitivity of the proposed biosensor was investigated by varying the target oligonucleotides concentration over the range of 150 pM to 1 μ M. The three oligonucleotides (capture, target and probe) were mixed to a final concentration of 1 μ M - 150 pM in 120 μ L Denhardt's buffer. After one hour of hybridisation at 37° C, the AuNP-electrode was immersed in the hybridised oligonucleotide mixture for five h to attach them to the electrode via the 3' thiolate group of the capture oligo. Experiments (Figure 3.16) showed that the reduction electrode current response ($n=2$) increased with the logarithmic value of the complementary target DNA sequence concentration ranging from 150 pM to 1 μ M. The differential current increased with increasing target concentrations up to 100 nM, until a ~6 fold increase in electrode response was observed for the higher concentration of 1 μ M DNA.

Comparing these results to the 3 step hybridisation DNA sensor (Table 3.5), the 1 step bulk immobilisation did not improve the absolute current response. The Williams¹² method gives a significant result for the 1 μ M target DNA; however the differential current response has decreased by 18 % when compared to our sensor. For the rest of the target oligonucleotides, a loss by a factor of 4 is observed for each of the differential current responses when compared to the 3 step hybridisation DNA sensor. For the lower target DNA concentrations, the sensor experiences either a loss of target DNA or a loss of HRP probe strand. In conclusion, it has been proven that the 3 step hybridisation sensor with altering buffers at optimum HRP hybridisation times can produce a biosensor that can give a reproducible current response from 25 % to 300 % greater than that already reported.

Table 3.5 Comparison of the average absolute current response at different concentrations of target DNA for the 3 step hybridisation sensor and bulk immobilisation assay.

[Target]	<u>3 step hybridisation</u> Average detection (nA)	<u>Bulk immobilisation</u> Average detection (nA)
1 μM	872 \pm 2.83	710 \pm 7.9
100 nM	498 \pm 2.83	124 \pm 12.3
10 nM	293 \pm 0.71	99 \pm 3.11
1 nM	158 \pm 2.82	83 \pm 1.36
150 pM	93 \pm 2.31	75 \pm 0.37

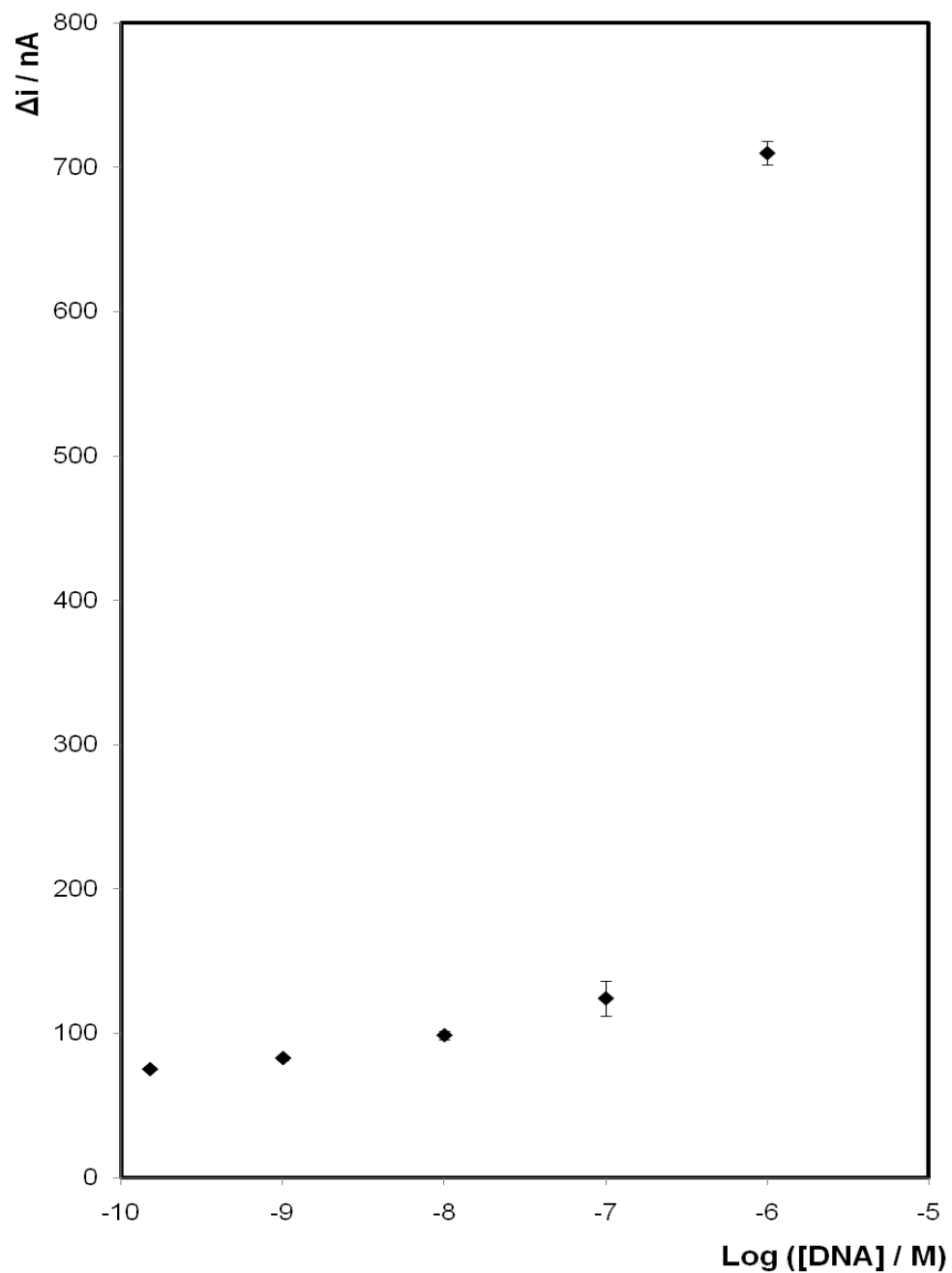


Figure 3.16 Average (n=2) electrochemical electrode response (Δi) for various concentrations of pathogen ss-DNA using a 1 step bulk immobilisation procedure within an AuNP-electrode, using constant potential chronoamperometry at approximately -0.4 V. A 1.8 mM hydroquinone in an aqueous 0.1 M phosphate buffer with 0.1 M KCl supporting electrolyte was used.

3.4 CONCLUSION

Nanotechnology is going to play an enormous role in the development of disposable DNA analytical chips, especially in electrochemical detection. These sensors will be fast, simple, specific and sensitive. Robust, low cost detection of low concentrations of NAs demands the development of novel highly sensitive detection strategies. The overall conclusion that can be drawn from the above experimental results is that it is possible to develop a reproducible, quantitative sequence specific biosensor. In this work, the electrochemical deposition of gold over the surface of a gold disc electrode has been investigated. Utilising a variety of characterization methods, namely cyclic voltammetry and scanning electron microscope (SEM), insights have been obtained into the surface profile of the electrode after the deposition of gold. Voltammetry in acidic electrolyte clearly demonstrates that the area available for immobilising DNA capture strands is significantly higher for the AuNP modified nanocomposite. This electrode showed a 2 fold increase in surface area after the fractional gold nanostructured deposition and thereby increased the additional area available for DNA binding and the sensitivity of DNA detection. These nanoparticles on the electrode allows for the amount of single strand DNA (ss-DNA) immobilised to be increased and therefore an enhancement in the hybridisation efficiency compared to a conventional DNA immobilisation system on a planar gold surface

A high-sensitive DNA sensor is reported based on HRP labelled probe to detect specific sequence of S.aureus which is associated with mastitis. A capture DNA modified with -SH was firstly chemically adsorbed on the gold electrode through self-assembly. The target DNA which contains the complementary sequence to the probe DNA is then captured through hybridisation. The HRP labelled oligonucleotide (detection DNA) which is complementary with a protruding section of target DNA was then hybridised in a sandwich way. Finally, H₂O₂ electro reduction current catalysed by HRP was measured amperometrically in the presence of hydroquinone as the mediator. The reduction current from the enzyme-generated product was related to the

number of target ssDNA molecules in the sample. The electrochemical signal of a DNA biosensor depends on both the DNA probe and the interaction of immobilised DNA with its complementary sequences. The fabrication procedure of the H₂O₂ sensor and the experimental parameters affecting the electrochemical response of the biosensor, such as mediator concentration, buffer identity, HRP hybridisation time and immobilization procedures have been systematically optimised.

The surface-immobilisation of single-stranded (ssDNA) capture DNA on electrodes is a key step for the development of electrochemical DNA biosensors. Immobilisation buffers are often used, however very little research into the effects of the buffer choice on the electrochemical response has been reported. Interestingly, while both the NaCl-TE and Denhardt's buffers have been reported³³ to have a strong tendency to absorb onto the surface, the analytical performance of the biosensor using 1 M NaCl-TE buffer was greater. The exact reason for this could not be clarified but it is possibly associated with the immobilisation of capture DNA in Denhardt's buffer having a stronger tendency to attach to the electrode surface and therefore blocks the attachment of the target DNA.

The influence of HRP labelled DNA hybridisation time on biosensor response was tested by increasing the time from 10 to 180 min and is demonstrated in Figure 3.8 to 3.12. Comparing the micro molar concentrations of target DNA hybridised to lower concentration (nM and pM), shorter HRP hybridisation times are required to obtain the maximum current response. A detection of pico molar target ssDNA was obtained with a longer HRP hybridisation time of 120 min. Allowing the system to run for a longer hybridisation time, an increase of 10 % was observed in the electrode current response when compared to the result obtained at the reported 90 min.¹² In conclusion, the time for assay completion has been reduced by a third for the higher concentrations of target DNA, while the sensitivity of the analytical performance for lower concentrations of target DNA has been improved greatly by using a longer HRP hybridisation time.

Having optimized the procedure for immobilising and hybridising the DNA to the electrode surface, the real test was to see if it could effectively discriminate complementary from non-complementary DNA sequence. Results in Figure 3.14 show that without the exact target strand, the electrode response is barely detectable suggesting that non-specific adsorption of the capture or probe strand is negligible. The selectivity of the sensor was also investigated by using the target DNA sequence that contained a single mismatch. Significantly the Δi value decreased by 37 % compared to the complementary DNA sequence, suggesting that a single base mismatch can be easily discriminated. Moreover, *Staphylococcus epidermidis* (*S. epidermidis*), which has 3 base mismatches gives no measureable differential current response demonstrating the system is robust with respect to false positives. This suggests that the enzyme-labelled DNA assay method holds great promises for sensitive electrochemical biosensor applications.

As a result from these competitive experiments, it has been concluded that a strategy of combining gold nanostructured electrodes and enzymatic amplification of electrochemical signal, to yield a highly sensitive detection of ss-DNA is useful. It was demonstrated that by carefully selecting the immobilisation buffers as well as optimising of the hybridisation times of HRP labelling, a significantly improved response is obtained. The developed protocol can be taken as a general method of DNA detection and is expected to be applicable to other types of DNA analysis. The optimised sensor was prepared by assembling AuNPs with DNA detection probe and HRP, where the DNA detection probe was used to construct the sandwich complex. HRP was for enzymatic catalysis and by using this novel method, one could conveniently detect as few as 0.65 pM target DNA and this sensitivity could be significantly improved after AuNP deposition followed by longer HRP hybridisation time (0.16 pM and 0.11 pM, respectively). It is hoped that the sensor in the future can be applied to analysis of real samples such as blood, urine or milk, where the capture strand is already immobilised onto the chip. Future development could involve moving the system to a flow cell and eventually convert to a miniaturized device.

3.5 REFERENCES

1. Polsky, R.; Gill, R.; Kaganovsky, L.; Willner, I. *Analytical Chemistry*. **2006**, *78*, 2268-2271.
2. Liu, T.; Tang, J.; Jiang, L. *Biochemical and Biophysical Research Communications*. **2002**, *295*, 14-16.
3. Liu, T.; Tang, J.; Zhao, H. Q.; Deng, Y. P.; Jiang, L. *Langmuir* **2002**, *18*, 5624-5626.
4. Cai, H.; Xu, C.; He, P.; Fang, Y. *Journal of Electroanalytical Chemistry* **2001**, *510*, 78-85.
5. Kissinger, P. T.; Heineman, W. R. *Journal of Chemical Education*. **1983**, *60*, 702-706.
6. Wang, J.; Xu, D.; Erdem, A.; Polsky, R.; Salazar, M. A. *Talanta*, **2002**, *56*, 931-938.
7. Wang, J.; Kawde, A. *Analyst (Cambridge, U.K.)* **2002**, *127*, 383-386.
8. Kim, J.; Chang, S.; Lee, H.; Kwon, Y.; Oh, Y. *Synthetic Metals* **1997**, *85*, 1371-1372.
9. Sánchez-Pomales, G.; Santiago-Rodríguez, L.; Rivera-Vélez, N. E.; Cabrera, C. R. *Journal of Electroanalytical Chemistry* **2007**, *611*, 80-86.
10. Tokuhisa, H.; Liu, J.; Omori, K.; Kanosato, M.; Hiratani, K.; Baker, L. A. *Langmuir* **2009**, *25*, 1633-1637.
11. Liu, S.; Li, Y.; Li, J.; Jiang, L. *Biosensors and Bioelectronics* **2005**, *21*, 789-795.
12. Williams, E.; Pividori, M. I.; Merkoçi, A.; Forster, R. J.; Alegret, S. *Biosensors and Bioelectronics*, **2003**, *19*, 165-175.
13. Levicky, R.; Herne, T. M.; Tarlov, M. J.; Satija, S. K. *Journal of the American Chemical Society*. **1998**, *120*, 9787-9792.
14. Taton, T. A.; Mirkin, C. A.; Letsinger, R. L. *Science* **2000**, *289*, 1757-1760.
15. Cai, H.; Cao, X.; Jiang, Y.; He, P.; Fang, Y. *Analytical and Bioanalytical Chemistry*. **2003**, *375*, 287-293.

16. Trasatti, S.; Petrii, O. A. *Pure and Applied Chemistry* **1991**, *63*, 711-734.
17. Hoogvliet, J. C.; Dijkstra, M.; Kamp, B.; van Bennekom, W. P. *Analytical Chemistry*. **2000**, *72*, 2016-2021.
18. Zhang, J.; Liu, P.; Ma, H.; Ding, Y. *Journal of Physical Chemistry C* **2007**, *111*, 10382-10388.
19. Zhang, X.; Shi, F.; Yu, X.; Liu, H.; Fu, Y.; Wang, Z. Q.; Jiang, L.; Li, X. Y. *Journal of the American Chemical Society*. **2004**, *126*, 3064-3065.
20. Zari, N.; Amine, A.; Ennaji, M. M. *Analytical Letters* . **2009**, *42*, 519-535.
21. Yang, Z. S.; Wu, W. L.; Chen, X.; Liu, Y. C. *Analytical Sciences* **2008**, *24*, 895-899.
22. Chetcuti, A. F.; Wong, D. K. Y.; Stuart, M. C. *Analytical Chemistry*. **1999**, *71*, 4088-4094.
23. Lei, C. X.; Long, L. P.; Can, Z. L. *Analytical Letters*. **2005**, *38*, 1721-1734.
24. Yang, S. M.; Chen, Z. H.; Li, Y. M.; Jiang, X. M.; Lin, X. F. *Canadian Journal of Analytical Sciences and Spectroscopy* **2006**, *51*, 174-179.
25. Wang, Z.; Yang, Y.; Leng, K.; Li, J.; Zheng, F.; Shen, G.; Yu, R. *Analytical Letters* . **2008**, *41*, 24-35.
26. Ryoo, H.; Kim, Y.; Lee, J.; Shin, W.; Myung, N.; Hong, H. G. *Bulletin of the Korean Chemical Society* **2006**, *27*, 672-678.
27. Liu, Z. M.; Yang, Y.; Wang, H.; Liu, Y. L.; Shen, G. L.; Yu, R. Q. *Sensors and Actuators B-Chemical* **2005**, *106*, 394-400.
28. Park, B. W.; Kim, D. S.; Yoon, D. Y. *Korean Journal of Chemical Engineering* **2011**, *28*, 64-70.
29. Laczka, O.; Maesa, J.; Godino, N.; del Campo, J.; Fougat-Hansen, M.; Kutter, J. P.; Snakenborg, D.; Muñoz-Pascual, F.; Baldrich, E. *Biosensors and Bioelectronics* **2011**, *26*, 3633-3640.
30. Zhang, H.; Lai, G.; Han, D.; Yu, A. *Analytical and Bioanalytical Chemistry* **2008**, *390*, 971-977.
31. Roth, K. M.; Peyvan, K.; Schwarzkopf, K. R.; Ghindilis, A. *Electroanalysis* **2006**, *18*, 1982-1988.

32. Herne, T. M.; Tarlov, M. J. *Journal of the American Chemical Society*. **1997**, *119*, 8916-8920.
33. Drew, A. F.; Editor **2001**, *Atherosclerosis: Experimental Methods and Protocols*, 247.
34. Dong, X.; Shi, Y.; Huang, W.; Chen, P.; Li, L. *Advanced Materials* **2010**, *22*, 1649-+.



CHAPTER 4

NANOPARTICLE FUNCTIONALISED POLYANILINE NANOFIBRES FOR DNA SENSOR DEVELOPMENT

4.1 INTRODUCTION

Polyaniline (PANI) is one of the most studied polymers of all the conducting polymers,¹ due to its straightforward preparation from common chemicals, high electronic conductivity, chemical stability, redox and ion-exchange properties and environmental stability.²⁻⁶ Professor A.G. MacDiarmid once quoted “*there are as many different types of PANI as there are people who synthesise it*”.⁷ This statement could not be more correct. However, it must be noted that, well defined and reproducible oxidation processes can be obtained in repeated synthesis following the same procedure.

The use of nanostructured materials electrochemical DNA sensing is relatively new and offers significant advantages. In this chapter, the use of a three-step electrochemical deposition procedure, to fabricate a polyaniline-AuNP electrode using the gold disc electrode, as the working electrode is described. This chapter focuses on a comparative study, where polyaniline with a similar composition was polymerised onto the electrode surface using three different approaches. Special attention was paid to the effect of each polymerisation technique on the electrode surface, along with different AuNP deposition and detection methodologies. The conducting polymer was synthesised in the presence of different inorganic and organic acids of different concentration, using chemical and vapour oxidative polymerisation and electrochemical methods. In this present work, polyaniline synthesised by each of these methods was characterised using cyclic voltammetry (CV), electron paramagnetic resonance (EPR), Raman spectroscopy and ultraviolet visible near infrared spectroscopy (UV - vis).

4.2 RESULTS AND DISCUSSION

4.2.1 Potentiodynamic polymerisation of PANI.

The electro oxidation of aniline follows a two-electron transfer process leading to polymerisation.⁸ Although there are many electrochemical techniques suitable for nucleation and growth of PANI, in the present work, potentiodynamic and potentiostatic procedures are used. PANI films which were electrochemically deposited via potentiodynamic polymerisation onto gold disc electrodes, as outlined in the experimental chapter in Section 2.5.1, was characterised using cyclic voltammetry (C.V.). The “dopant” in conducting polymers is the agent that adds or removes electron density to the polymer chain, depending on the conducting polymer. A counter-ion stabilises the charge on the backbone and can be confused with the dopant. In the case of polyaniline a proton is the dopant, while the counter ion stabilises the charge.⁹ The 0.1 M HCl added during polymerisation, acted as a dopant for the polymer while introducing a counter ion (Cl⁻). The overall polymerisation reaction of PANI¹⁰ can be simply shown in Figure 4.1.

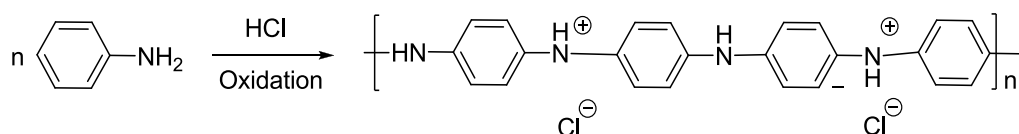


Figure 4.1 Polymerisation reaction of polyaniline Reproduced from Ref [10] Sarac, A. S.; Ates, M.; Kilic, B. *International Journal of Electrochemical Science* **2008**, 3, 777-786.

For electrochemical deposition of PANI, the growth potential of polyaniline was first determined using CV method as shown in Figure 4.2. Figure 4.2 illustrates the cyclic voltammogram recorded of the PANI deposition from 0.04 M aniline in 0.1 M HCl solution in the potential range between -0.5 and 1.0 V at a scan rate of 100 mV s⁻¹ on a gold disc electrode. On the first potential sweep, the oxidation of aniline occurs at approximately +0.9 V as a distinct irreversible

broad anodic peak.⁸ This is consistent with oxidation of the aniline monomer to a radical cation.⁹ In the first reverse cycle, cathodic peaks appear, which are almost reversible, confirming the initial deposition of an electro-oxidized polymer film.¹⁰ The two reversible redox couples observed are attributed to the leucoemeraldine ↔ emeraldine and the emeraldine ↔ pernigraniline couples.¹¹

An oxidation peak is observed at approximately +0.19 V which corresponds to the transformation of PANI from the reduced leucoemeraldine state (amine units) to the partly oxidized emeraldine salt state (semiquinone radical cations).^{8,9} A second oxidation peak at approximately +0.85 V is associated with the transition of the leucoemeraldine state to the pernigraniline state.⁹ During the succeeding scans, the oxidation of aniline which favors the adsorption of aniline and deposition of PANI, occurs at about 0.5 V due to the catalytic effect of PANI, which results in a growth of the emeraldine salt deposit.⁸

At +0.6 V, a reduction peak can be seen which corresponds to the reduction of pernigraniline to emeraldine salt and a second reduction peak at approximately +0.526 V which corresponds to the reduction of emeraldine salt to leucoemeraldine.⁹ In electropolymerisation processes the increase of the voltammetric peak current or charge in cyclic voltammograms with increasing sweep number is an indication for polymer growth.⁸ The conductive nature of these films was confirmed by a large increase in observed current for both the oxidation and reduction for each successive potential cycle as the polymer accumulates on the electrode.^{12,13}

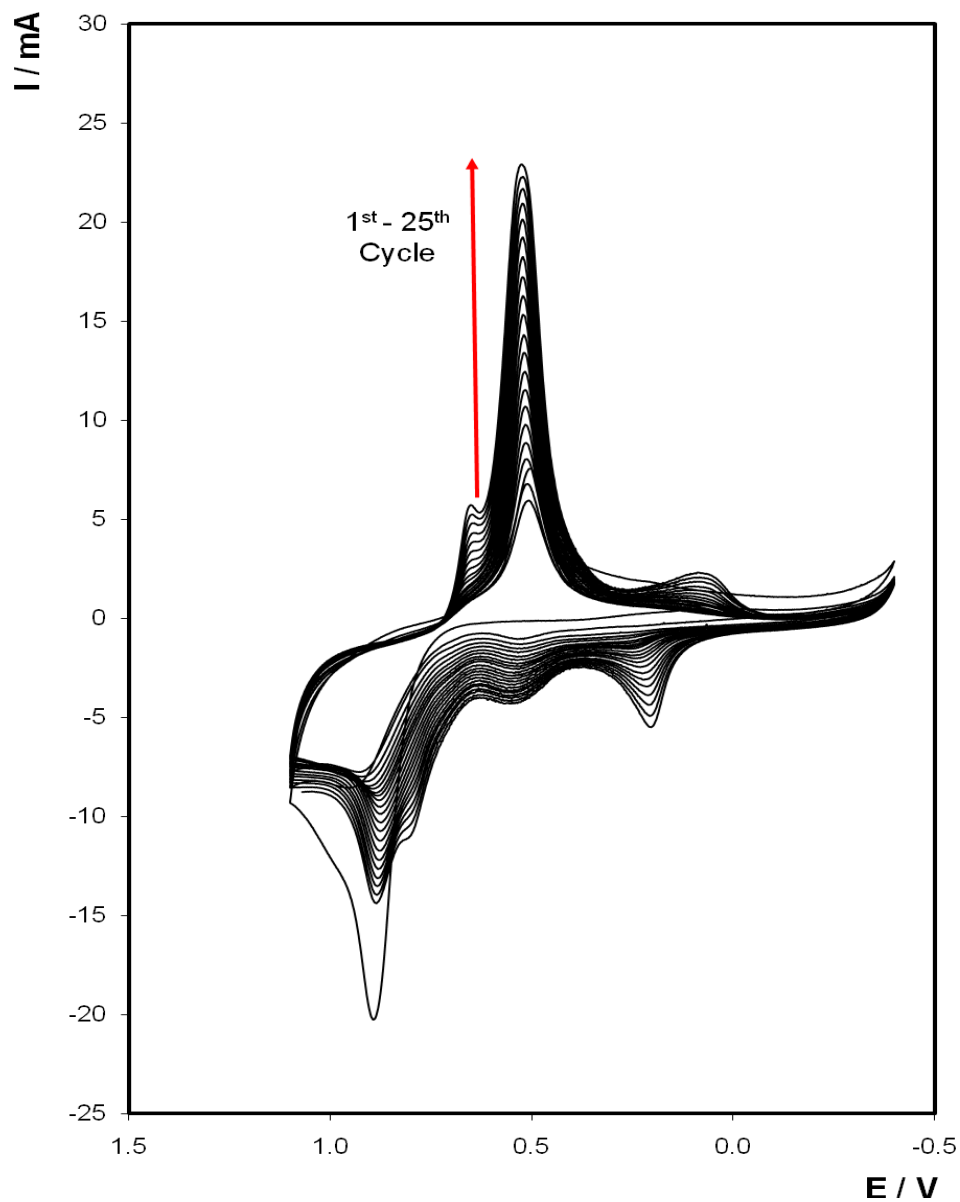


Figure 4.2 Cyclic voltammogram recorded during the potentiodynamic growth of PANI / HCl on a 2 mm diameter Au disc electrode. Electropolymerisation was carried out using a solution of 0.04 M aniline in 0.1 M HCl as supporting electrolyte. The potential was swept from -0.5 V to 1.0 V vs. Ag / AgCl, 25 cycles at 100 mVs⁻¹.

4.2.2 *Potentiostatic polymerisation of PANI.*

Preliminary experiments showed that PANI films could be grown on Au disc electrodes potentiodynamically by sweeping the potential from -0.5 V to 1 V at a scan rate of 100 mVs⁻¹. From the CV recorded during electrodeposition, it was found that a suitable potential for potentiostatic growth of polymer was found at approximately 0.55 V. Below this potential, the rate of oxidation was too low. Anodic polarisation at potentials more than 0.55 V causes oxidation leading to gradual degradation of polymer film. This potential was applied to the working electrode and the electric charge passing through this electrode was measured as a function of time, which is demonstrated in Figure 4.3.

Potentiostatic synthesis of PANI on the gold disc electrode was performed in the same medium employed in the potentiodynamic synthesis. The electrode was introduced at open circuit potential and then the potential was raised to the synthesis potential of +0.55 V. The electro synthesis elapsed for 90 s to achieve the desired current density growth of 0.8 mA/cm². Figure 4.3 illustrates the current density transient curve for the potentiostatic synthesis of PANI. As soon as the electrode potential had risen from the open circuit potential to 0.5 V, an increase of current density was observed. In the first part of the synthesis the current density decreased, which is characteristic of nucleation and growth kinetics and it is related to the double layer charging.¹⁴ After this initial decrease in current, the current then began to increase constantly, a sign that the electropolymerisation of aniline took place and the electroactive area of the electrode increased with the synthesis time.¹⁴ The maximum current density value achieved in the polymerisation before it was stopped was 0.826 mA/cm². After 90 s of this synthesis, a charge of 2 C cm⁻² was passed.

PANI modified gold disc electrodes were used for subsequent studies for the hybridisation of DNA. The films of PANI emeraldine salt was also formed on ITO-glass electrode (1 cm x 1 cm) from a solution containing 40 mM aniline and 0.1 M HCl at an applied potential of +0.55 V for 90 s. The transparency of ITO-glass made it a logical choice as an electrode material for spectral studies

even though Au was the electrode material for polymer growth and DNA hybridisation. Using the potentiostatic method, it was possible to control film thickness within the μm range and produce films suitable for UV - vis and Raman studies. A green polyaniline film was observed on the electrode surface.

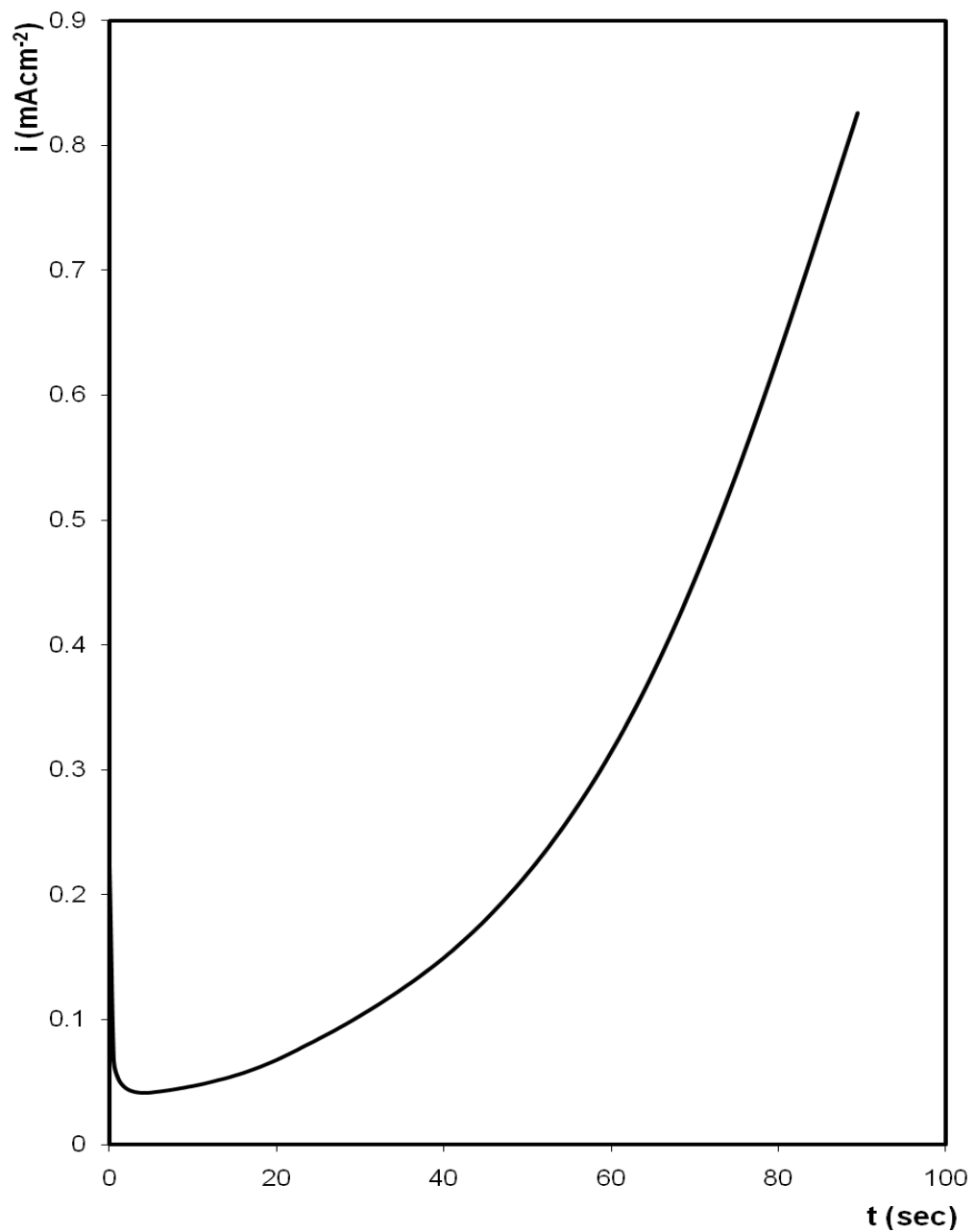


Figure 4.3 Potentiostatic electrodeposition of polyaniline onto a 2 mm diameter Au disc electrode from a solution containing 40 mM aniline and 0.1 M HCl at an applied potential of +0.55 V for 90 s.

4.2.3 Voltammetric characterisation of PANI and PANI-AuNP.

Gold nanoparticles (AuNPs) were deposited on the surface of the PANI to increase the surface area available for binding thiol terminated capture DNA and to modulate the conductivity of PANI. Figure 4.4 illustrates cyclic voltammograms for the chemically prepared PANI nanofibres (PANI-NF) and PANI-NF-AuNP modified electrodes when cycled in 0.1 M H₂SO₄ at 100 mVs⁻¹.

The polyaniline nanofibres exhibit two redox processes,¹⁵⁻¹⁷ one at +0.29 V and the other at +0.40 V. These correspond to the conversion from the leucoemeraldine to polaronic emeraldine form and conversion from the emeraldine to pernigraniline forms, respectively. The dominant features observed in Figure 4.4 are the oxidation and reduction processes centred at +1.230 and +0.880 V, respectively. These peaks are associated with the formation and subsequent re-reduction of a gold oxide monolayer on the underlying gold electrode and, in the case of the PANI-NF-AuNP films, the electrode and the immobilised gold nanoparticles.

Exposure of the PANI-NF film to 3 mM AuCl₄⁻ gold plating solution oxidises the reduced polymer and metallic gold nanoparticles are formed spontaneously on the surface of the nanofibres.¹⁸ The charge passed during the reduction of a monolayer of gold oxide is 390 μC cm⁻².¹⁹ The increased anodic peak corresponds to an increase in the gold surface area by a factor of 4. This implies that a greater area is available for binding DNA.

An example of the effect of the surface area on the electrode is given for the deposition of the chemically prepared PANI nanofibres in Figure 4.4. A decrease of the active gold area from 0.044 cm² for unmodified electrode (roughness factor of 1.4) to 0.031 cm² is seen. The characteristic features of the gold oxide are inhibited, which appear to result from the coverage of the gold disc electrode by the formed polyaniline. This suggests that the growth of polyaniline does occur and form coverage on the gold electrode surface.

The cooperation of the PANI-NF and the AuNP in the modified film amplified the peak current greatly. Compared with the bare electrode and PANI modified electrode alone, the CV at the PANI-NF-Au electrode exhibits a couple of well-defined redox peaks with further enhanced peak currents. Significantly, deposition of the gold nanoparticles increases the available gold surface area by a factor of approximately 3.6.

Throughout the chapter, electrochemical chemical and vapour polymerisation synthesis is carried out, as described in full in Section 2.5. Table 4.1 summaries the real surface area determined by cyclic voltammetry after each oxidative polymerisations were carried out. The overall calculated charge under the cathodic peak varies between $14 \mu\text{C cm}^{-2}$ for the unmodified electrode and up to $47 \mu\text{C cm}^{-2}$ for the nanocomposite, obtained after polymer oxidation and gold deposition. Potentially, one could create a biosensor either by electrochemical, chemical or vapour polymerisation methods, whose area can be further enhanced by nanogold deposition to increase the quantity of DNA on the electrode surface.

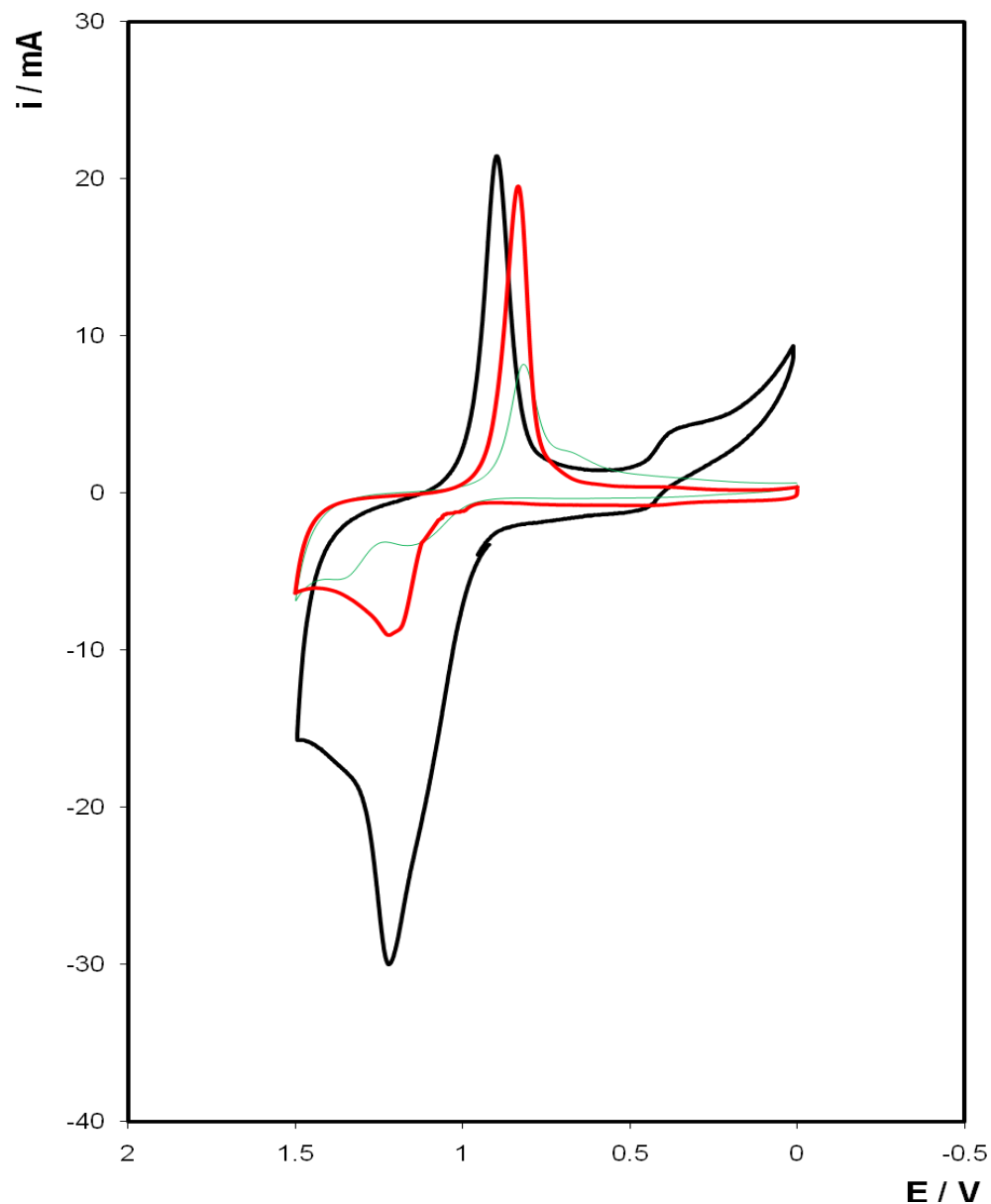


Figure 4.4 Cyclic voltammograms of 2 mm unmodified gold electrodes (green line), and electrodes modified with PANI-NF (red line) and PANI-NF-AuNP (bold line) in 0.1 M H_2SO_4 . The counter electrode was a platinum wire and the reference electrode was Ag/AgCl saturated in KCl. The scan rate is 100 mVs^{-1} . The voltammograms have been displaced vertically for clarity of presentation.

Table 4.1 Summary of real surface areas and surface roughness factor after polymer and gold nanoparticles deposition, determined by cyclic voltammetry on a 2 mm gold disc electrode. The potential was swept from -0.5 V to 1.0 V vs. Ag / AgCl, 25 cycles at 100 mVs⁻¹.

Electrode Surface	AuNP Deposition Time (Secs)	Charge Q (C cm ⁻²)	Real Surface Area (cm ²) ⁱ	Surface Roughness Factor ⁱⁱ
Bare	-	1.46 x 10 ⁻⁵	0.0374	1.2
AuNP only	20	1.65 x 10 ⁻⁵	0.0423	1.3
	30	1.84 x 10 ⁻⁵	0.0471	1.5
	40	2.55 x 10 ⁻⁵	0.0654	2.1
	50	2.45 x 10 ⁻⁵	0.0628	2.0
Echem PANI	-	1.17 x 10 ⁻⁵	0.0300	1.0
	20	1.96 x 10 ⁻⁵	0.0502	1.6
	30	3.06 x 10 ⁻⁵	0.0785	2.5
	40	3.54 x 10 ⁻⁵	0.0907	2.9
	50	3.97 x 10 ⁻⁵	0.1017	3.2
Vapour PANI	-	1.37 x 10 ⁻⁵	0.0351	1.1
	20	1.53 x 10 ⁻⁵	0.0393	1.3
	30	2.28 x 10 ⁻⁵	0.0584	1.9
	40	2.44 x 10 ⁻⁵	0.0626	2.0
	50	2.73 x 10 ⁻⁵	0.0700	2.2
Chemical PANI	-	1.24 x 10 ⁻⁵	0.0318	1.0
	20	2.33 x 10 ⁻⁵	0.0596	1.9
	30	3.23 x 10 ⁻⁵	0.0828	2.6
	40	3.93 x 10 ⁻⁵	0.1008	3.2
	50	4.78 x 10 ⁻⁵	0.1225	3.9
Chemical PANI	-	1.21 x 10 ⁻⁵	0.0310	1.0
PANI: Au (4:1)	-	4.40 x 10 ⁻⁵	0.1128	3.6

- i. Calculated as the charge passed during the reduction of the gold oxide monolayer divided by 390 x 10⁻⁶ C cm⁻².
- ii. Calculated as the real surface area divided by the geometrical area (πr^2 , 0.0314 cm²)

.4.2.4 Microscopic characterisation of PANI-NF and PANI-NF-AuNP

The synthesis of polyaniline was based on the well known chemical oxidative polymerisation of aniline.¹³ The synthesis was carried out in a strongly acidic environment, with ammonium peroxydisulfate as the oxidant as described in Section 2.5.3.2. Imaging and analytical characterisation of the polyaniline by transmission electron microscopy (TEM) was performed to determine the size and shape and morphology of the polyaniline. Figure 4.5 (A) shows TEM of generated HCl doped polyaniline, which are similar to the TEM images of chemically prepared PANI reported by Zhang *et al.*²⁰ The polyaniline displayed a fibrillar morphology for HCl doped PANI. The nanofibers were readily formed and the diameters of polyaniline nanofibers polymerised ranged from 35 to 70 nm, as shown in Figure 4.5 (A).

TEM was used to observe how AuNPs strongly affects the morphology of the polyaniline nanofibres. The chemical synthesis of doped emeraldine base polyaniline and the reduction of AuCl₄ exhibit fibrillar morphology. The nanofibres have a uniform diameter around 35 nm, with lengths varying from 500 nm to several micrometers as shown in Figure 4.5 A. Some of the nanofibres formed branched structures or interconnected networks. The darker shades seen in the TEM image is where the nanofibres have overlapped onto each other.

The images in Figure 4.5 B, show that the polymer exists as nanofibres with widths of 35 ± 20 nm. A closer look at the nanofibres reveals that many of them are overlapped. TEM studies indicate that >95% (volume fraction) of the sample are nanofibres with diameters of 30-50 nm. The nanofibres tend to form into interconnected nanofibre networks, rather than bundles.²¹

Figure 4.5 C, illustrates an expanded section of the image after the formation of PANI nanofibres and the reduction of HAuCl₄ to produce metallic gold nanoparticles.²² The TEM shows that after the gold reduction step, the surface of the PANI-NF fibres appears to be coated with nanoparticles clusters with

radii between approximately 2 and 5 nm, which seem to be spread over the whole length of the nanofibres. It can be seen that NPs is present only on the surface of fibres suggesting that gold reduction occurs preferentially on the surface of the PANI-NF fibres. Aggregates are well spread and do not concentrate in one region.

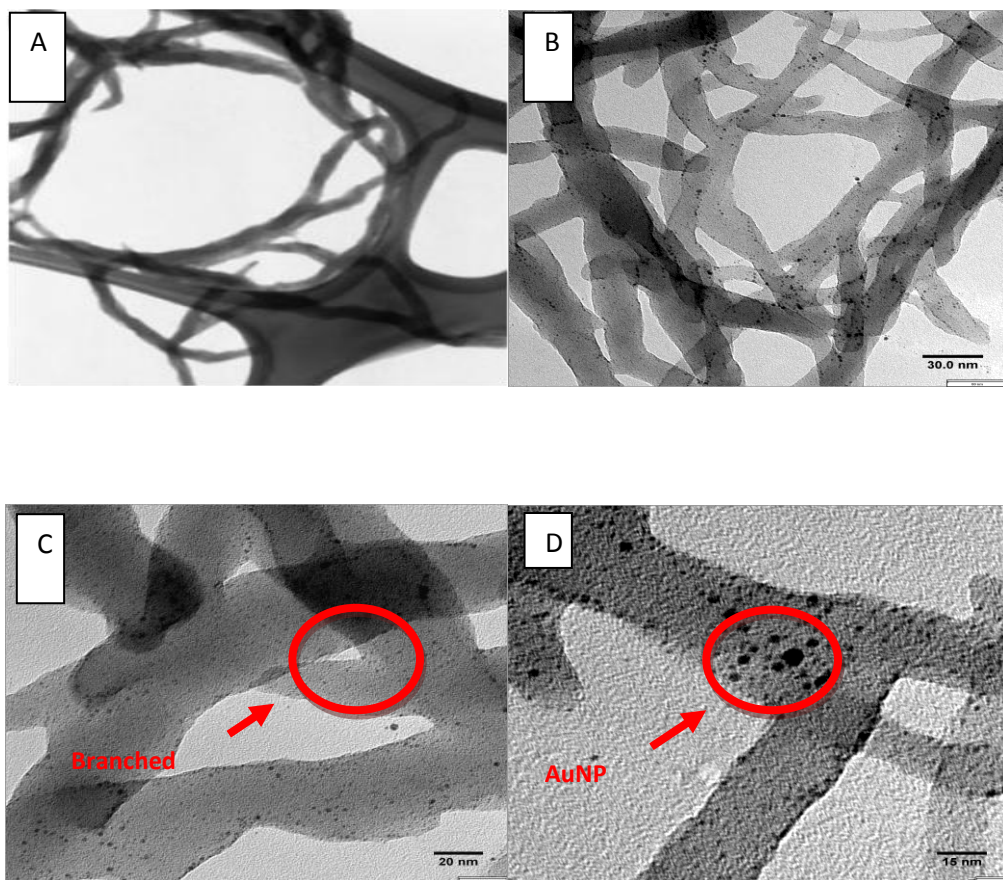


Figure 4.5 **A.** TEM image of purified polyaniline nanofibres grown in 0.55 mM ammonium peroxydisulfate in 1 M HCl in the absence of AuNPs.

B. TEM image of purified polyaniline nanofibres cast from a suspension after incorporation of 10 mM HAuCl_4 , at a low magnification (scale bar = 30 nm).

C. Enlarged TEM image of a branched network of polyaniline nanofibres. (Scale bar = 20 nm)

D. Magnified TEM image of the clusters of AuNP on the nanofibre surface, showing their size distribution. (Scale bar = 15 nm)

4.2.5 UV - visible spectra of polyaniline.

The transparency of the ITO glass working electrode allowed the colour changes in each stage of the polyaniline polymerisation to be observed. Green emeraldine salts, usually exhibit three absorption bands at ca. 350, 430 and 810 nm, assigned to a π - π^* band, a π -polaron and a polaron- π^* band transition respectively.²³ Green emeraldine salt is converted to a blue emeraldine base when in a basic medium.²⁴ The emeraldine base shows two strong bands in the region of 340 nm and 620 nm,²⁵ which correspond to the π - π^* band (benzoid rings) and an exciton band transition (quinoid rings), respectively.²⁶⁻²⁸

Colourless leucoemeraldine base which can be generated by an electrochemical or chemical reduction of emeraldine salt or base, shows an absorption band at ca. 320 nm which is associated with the π - π^* transition. Leucoemeraldine salts exhibit a π - π^* band, at a lower wavelength than leucoemeraldine base.²⁶ Violet pernigraniline base exhibits two strong bands at 340 and 540 nm assigned to the π - π^* band and a Peierls gap transition respectively.²⁹ Blue protonated pernigraniline salt shows two strong absorption bands at ca. 350 and 690 nm.²⁵ This is seen as a different shade of blue to emeraldine base. The colours, UV - visible absorption peaks and corresponding electronic transitions of the various polyaniline forms²⁶ are summarised in Table 4.2.

Another aspect to note is that polyaniline absorbance spectrum also depends on the conformation adopted by the polymer chains and on the conjugation length. An example of this is seen when the λ_{max} of the emeraldine salt is red shifted for polymers with a longer conjugation length and/or replaced by a broad, strong free-carrier tail in the near-infrared region. The λ_{max} is red shifted to 1500-2500 nm when the polyaniline chain changes conformation from a "compacted coil" to an "extended coil" conformation.^{27,30}

Table 4.2 Colours, UV - visible absorption peaks and corresponding electronic transitions of polyaniline forms.²⁶

Polyaniline Conductivity form	Colouration	λ (nm)	Electronic transition
Emeraldine salt	Green	350,430,810	π - π^* , π -polaron, polaron - π^*
Emeraldine base	Blue	340,620	π - π^* and exciton
Leucoemeraldine salt	Colourless	298	π - π^*
Leucoemeraldine base	Pale yellow green	320	π - π^*
Pernigraniline salt	Blue	350, 690	π - π^* and Peierls gap transition
Pernigraniline base	Violet	340, 540	π - π^* and Peierls gap transition

4.2.5.1 UV - vis of electropolymerised PANI film.

The gold-polyaniline nanocomposite was synthesised by an electrochemical route in two steps. In the first step, polyaniline films were deposited potentiostatically (0.55 V) onto the ITO coated glass substrate, and then gold nanoparticles were electrodeposited via current-time transients. The synthesized PANI with/without AuNPs films were confirmed by Ultra-violet spectroscopy (UV-vis).

Figure 4.6 (thin line) shows the UV - vis spectrum of the potentiostatically grown films of PANI as described in Section 2.3.1. The absorption peak at 357 nm is due to the π - π^* transition of the benzenoid rings. It has been reported²⁶ that when the polyaniline concentration is high, the benzenoid to quinoid excitonic transition can cover the whole range from 500 to 900 nm with an absorption peak at ~900 nm. This observation is seen in Figure 4.6, where the broad transition is centred at 593 nm and a peak is found at 959 nm. The broad nature of the band may also arise from the dispersed conjugation length of doped PANI. The absorption centred at ~959 nm could also suggest that the polyaniline chains have adopted a mixture of “compact coil” and “extended coil” conformations.²⁶

The UV-vis of the polyaniline after Au deposition was then compared to the UV-vis of the PANI in the absence of AuNPs. Typically, 3 bands are observed for the doped state of polyaniline at the regions 325–360, 400–430, and 780–825 nm.³¹ The peak at approximately 357 nm, as illustrated in Figure 4.6 (thick line), and the shoulder at 426 nm are both assigned to π - π^* transition. The absorption peak at 357 nm is due to the π - π^* transition of the benzenoid rings, whereas the peak at 426 nm is due to polaron/bipolaron transition. These are consistent with the expected spectra for emeraldine salt.²⁶ The presence of a shoulder at 833 nm and a second absorption centred at approximately 953 nm, suggests that the polyaniline chains have adopted a mixture of “compact coil” and “extended coil” conformations. These features are based on previous studies by MacDiarmid *et al*,²⁶ and can be attributed to the transition from the π band to the polaron band of PANI. Also the spectrum exhibits a broad

absorption peak at 600– 900 nm, which results from the combined effect of the gold surface plasmon and the p band to a localized polaron band transition of the doped PANI.³¹

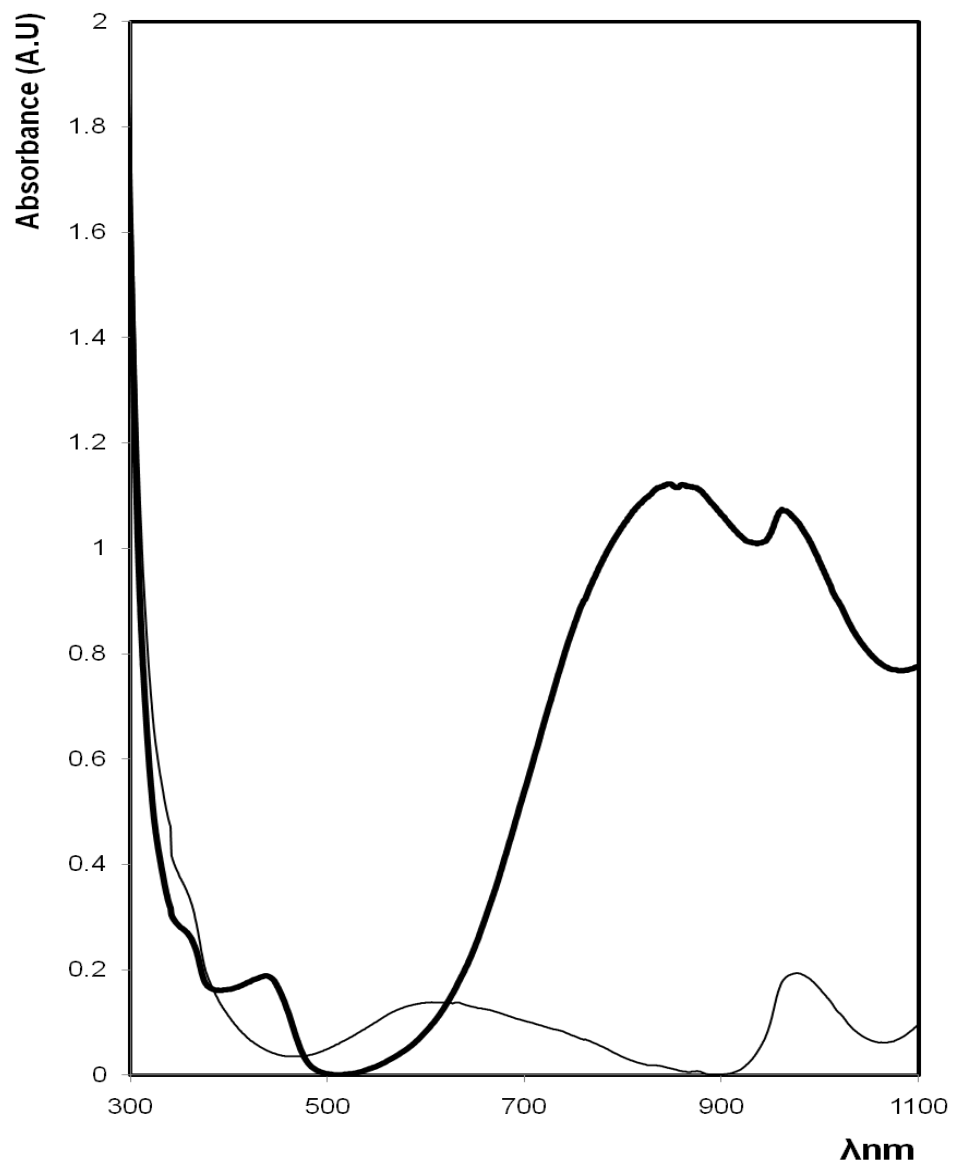


Figure 4.6 UV-vis spectra of polyaniline films grown potentiostatically (thin line) and after AuNP deposition (thick line) onto ITO glass electrode (+0.5 V for 90 s at 100 mVs^{-1}) from aqueous 40 mM aniline in 0.1 M HCl. Electrochemical deposition of AuNPs (3 mM cyan free gold plating solution) onto the polyaniline (thick line) was applied at a fixed potential of -1.5 V for 50 s.

4.2.5.2 UV - vis of vapour polymerised PANI film.

Figure 4.7 presents the UV-vis spectrum of a PANI film after vapour phase polymerisation. The vapour oxidised PANI that is illustrated in Figure 4.7, is similar to that previously reported by Kim *et al*³² where the π - π^* transitions and a polaron band obtained at 392 and 767 nm, are observed, respectively. It has been reported,³³ that the band at 392 nm is due to the π - π^* benzoid transition between quinoid and benzenoid in the PANI structure. A slight shoulder at 435 nm and 767 nm could be due to either the polaron lattice or the electron transfer between quinoid and benzenoid.³³ Other forms of polyaniline such as leuco-emeraldine or pernigraniline structure does not show a peak at 800 nm,³² therefore indicating that emeraldine salt is present. Comparing the vapour phase polymerisation to electrochemical polymerisation of PANI, a few similarities can be observed. The absorption centred at ~1000 nm in Figure 4.7 (thin line) suggests that the polyaniline chains have adopted a mixture of “compact coil” and “extended coil” conformations. This feature can be attributed to the transition from the π band to the polaron band. This as well as the peaks found at approximately 392 nm and 435 nm concludes that the PANI is in a compact-extended coil conformation. The noise that we are seeing could be due to a low concentration of Fe (III) still present on the ITO glass, the slit width is too small or a small reflection from the ITO.

The adsorption of the PANI films after AuNP incorporation is shown in Figure 4.7 which shows a significant increase in the absorbance when compared to PANI alone. A strong red shift was observed in the absorbance and broadening of the polyaniline polymerised with fractional gold deposits spectrum and this leads to the conclusion that functionalisation of the gold nanoparticles by the polyaniline has taken place.³⁴ The spectrum of the PANI-AuNP (Figure 4.7, thick line) exhibits a broad peak at 330 – 441 nm and a broad polaron peak centred at ~826 nm, which is consistent with compact coil – like conformation for polyaniline. The peaks found at 330 and 441 nm are due to the excitation of benzene and quinoid segments in the PANI chain.³²

As already discussed for the earlier UV - vis spectra, a band in the region of 500 – 700 nm is seen due to the collective oscillation of conduction electrons in

response to optical excitation.²⁶ The absorption spectra are composed of at least two absorbance bands, the first one being the gold plasmonic band with absorption maximum at about 720 nm which overlaps the second absorbance band with a maximum at about 825 nm.³⁵ The oxidized form of polyaniline, emeraldine salt, exhibits a strong peak at 800 nm³² which is shown in this spectrum of PANI-AuNP.

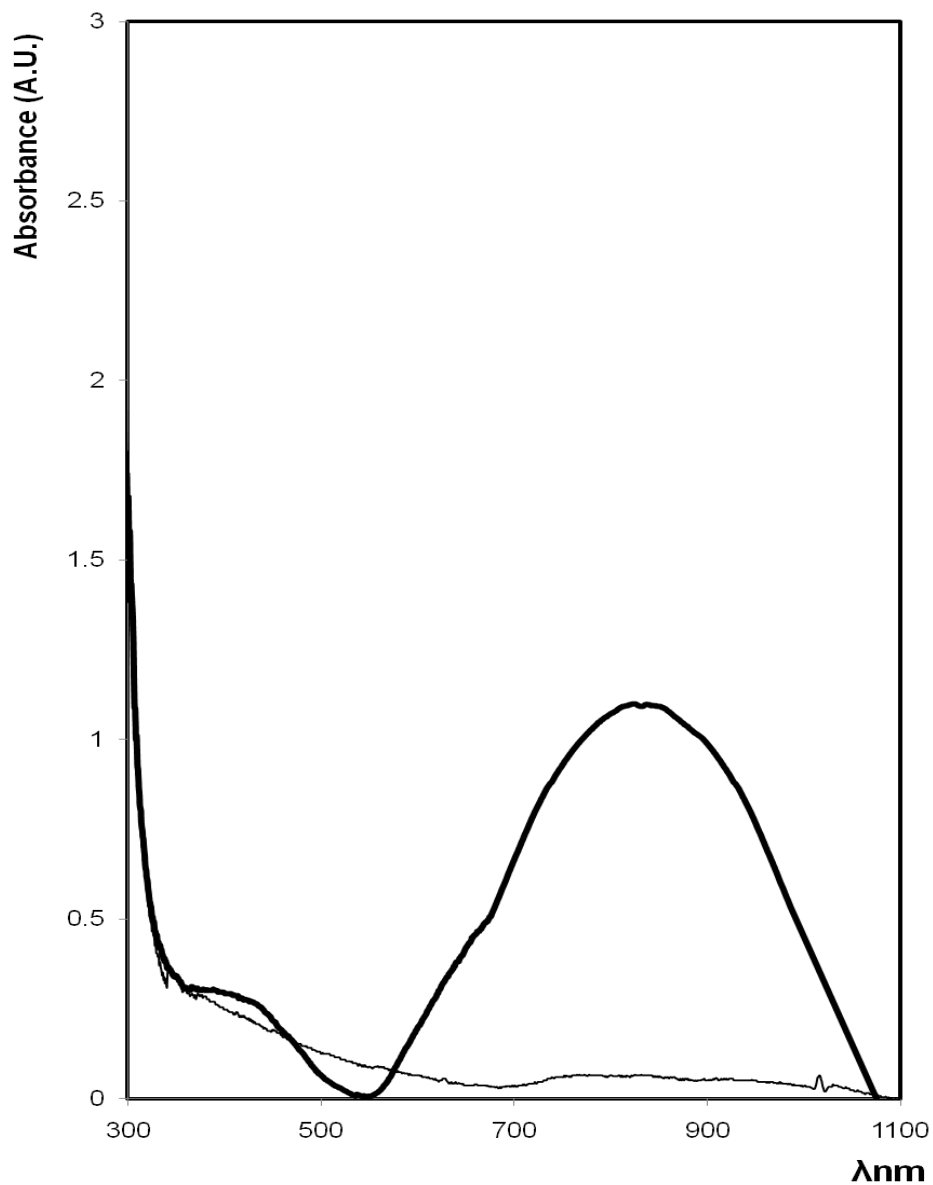


Figure 4.7 UV - vis spectra of PANI films (thin line) and PANI with AuNP (thick line). The films were grown by vapour oxidation by coating ITO glass electrode with 0.85 M aqueous Fe (III) tosylate (40 % ethanol) and exposing surface to 1 M aniline monomer vapour. Electrochemical deposition of AuNPs (3 mM cyan free gold plating solution) onto the polyaniline (thick line) was applied at a fixed potential of -1.5 V for 50 s.

4.2.5.3 UV - vis of chemically polymerised PANI film.

The leuco-emeraldine salt of PANI nanofibres was prepared using the synthetic procedure described in Section 2.5.3.1 involving PANI and APS. The precipitate was dark green in colour before purification and the filtrate became colourless after the addition of $\text{NH}_3\text{H}_2\text{O}$. This characteristic is also indicative of leucoemeraldine salt.³⁶ The likely chemical structure of emeraldine base nanofibres is highlighted in red below in Figure 4.8.

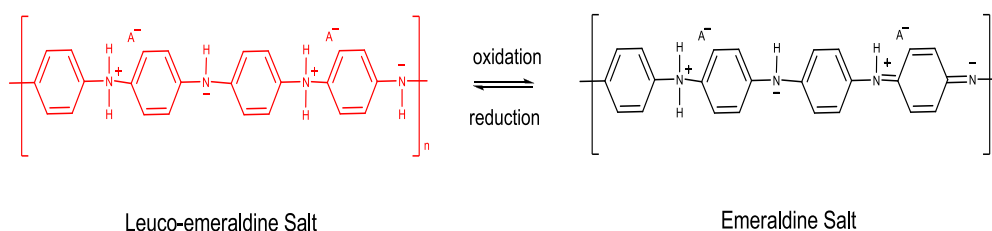


Figure 4.8 Chemical structure of leucoemeraldine salt. Reproduced from Ref [37] Ahn, S.; Hupp, J. T. *Bulletin of the Korean Chemical Society* **2006**, *27*, 1497-1499.

Figure 4.9 (thin line) shows the UV - vis spectrum of PANI nanofibres. These nanofibres prepared by chemical oxidation exhibit a similar spectrum to that observed in Figure 4.7 for the electrochemical oxidation (e.chem) of PANI. The absorption peak at 354 nm (357 nm for e.chem PANI) is due to the π - π^* transition of the benzenoid rings. For leucoemeraldine,³⁶ a single peak is typically observed at approximately 350 nm. A slight shoulder found at approximately 272 - 380 nm could also indicate a mixture of leucoemeraldine salt and emeraldine salt.³⁶ A broad benzenoid to quinoid excitonic transition covering the whole range from 500 to 1000 nm with an absorption peak at \sim 962 nm is also in agreement to that reported for the e.chem PANI (Figure 4.9). The broad nature of the band most likely arises from a dispersed conjugation length of doped PANI. The absorption centred at \sim 962 nm could also suggest that the polyaniline chains have adopted a mixture of “compact coil” and “extended coil” conformations.²⁶

The spectrum shown in Figure 4.9 (thick line) is consistent with that expected for emeraldine salt.²³ As already mentioned, 3 bands are observed for the doped state of polyaniline at the regions 325–360, 400–430, and 780–825 nm.³¹ The absorption peak at 319 nm is due to the π - π^* transition of the benzenoid rings. This spectrum has a strong π - π^* transition centred at 475 nm and a shoulder at approximately 808 nm which is assigned to the lower wavelength polaron band, typically observed in emeraldine salt.²³ The broad absorptions at wavelengths longer than 700 nm have been assigned to a delocalised polaron transition,²³ with the presence of the latter peak at ~1030 nm suggesting a coil like conformation. The broad absorbance is characteristic of emeraldine form i.e., the partially oxidized form. The intensity of this broad band is weaker than that of the band at ca. 319 nm, indicating that oxidation from the leucoemeraldine to the emeraldine form has occurred.³⁷

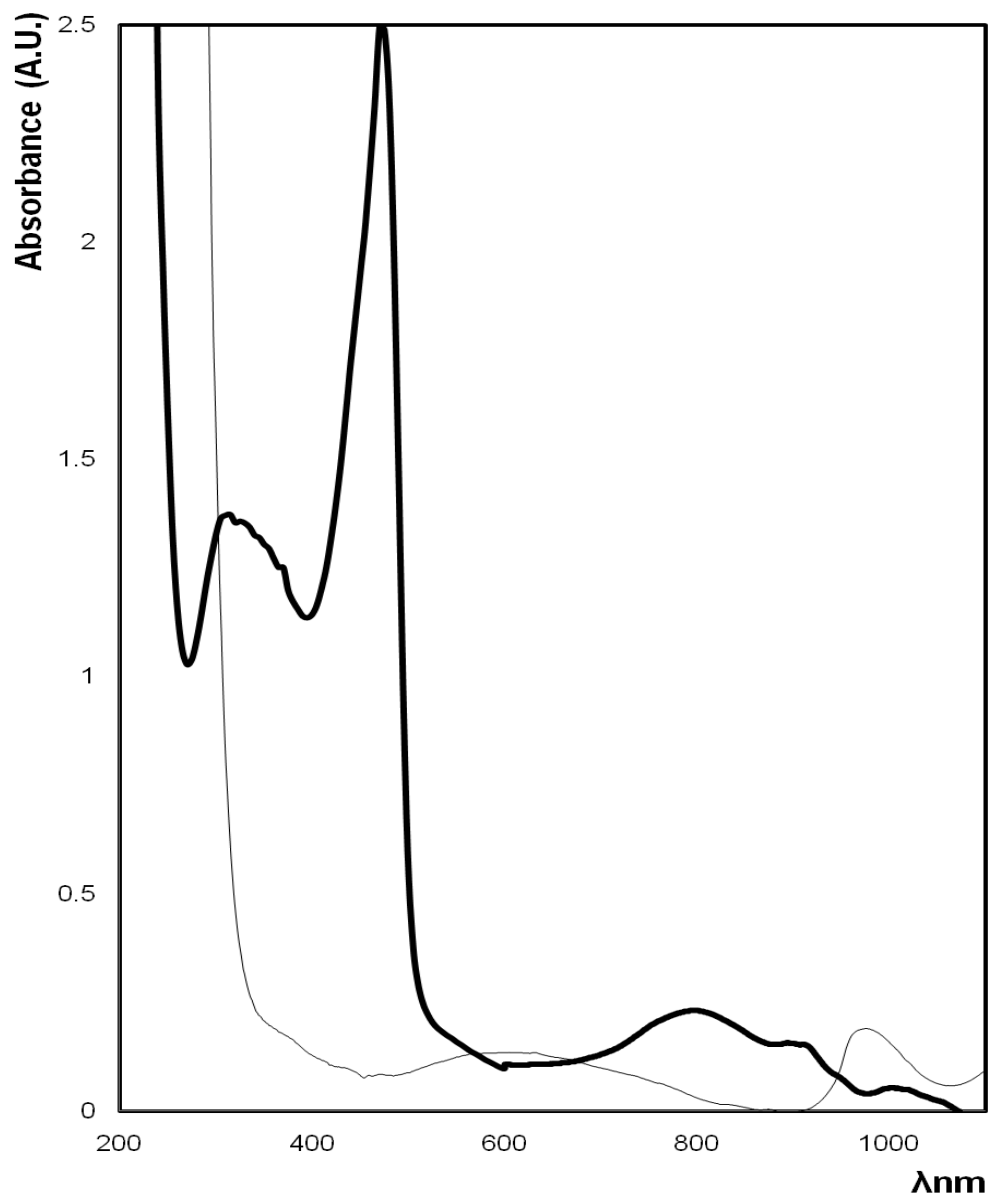


Figure 4.9 UV - vis spectra of chemically prepared polyaniline (thin line) drop cast onto ITO glass electrode. The polymer was prepared using 3.2 mM polyaniline in 0.8 mM APS in HCl film. Thick line shows the spectrum after AuNPs were electrochemically deposited onto the chemically prepared polyaniline at an applied potential of -1.5 V for 50 s.

4.2.5.4 UV-vis of chemically polymerised emeraldine base nanofibres.

The emeraldine salt form of polyaniline is generally readily converted to emeraldine base via alkaline doping.⁹ PANI-NF films were converted from their emeraldine salt form to the corresponding emeraldine base form via treatment with aqueous 1.0 M NH_4OH as described in Section 2.5.3.2. Within seconds, the films changed from green to blue colour indicating the formation of emeraldine base. The likely chemical structure of the emeraldine base nanofibres is highlighted in red below in Figure 4.10. The difference between these chemically prepared nanofibres and those previously discussed in Section 4.2.5.3, is the dopant (APS vs. NH_4OH) used and the deposition of AuNPs

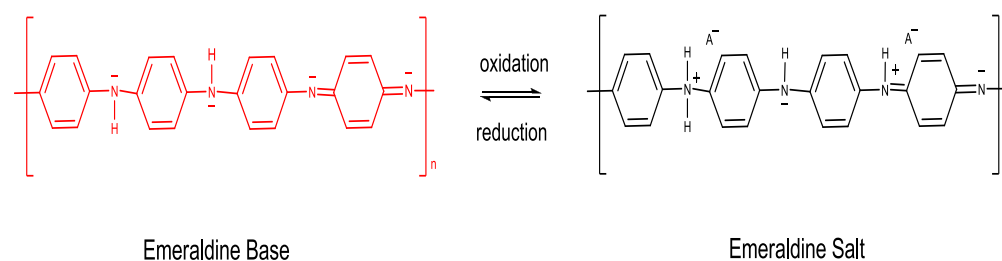


Figure 4.10 Chemical structures of emeraldine salt and base. Reproduced from Ref [37] Ahn, S.; Hupp, J. T. *Bulletin of the Korean Chemical Society* **2006**, 27, 1497-1499.

Figure 4.11 shows the UV-vis spectra of emeraldine base PANI nanofibres composite with and without AuNPs. The emeraldine base (Figure 4.11, thin line) exhibits a benzenoid to quinoid excitonic transition between 500 to 900 nm with an absorption maximum at ~ 713 nm. The conversion to emeraldine base with characteristic absorption bands at approximately 320 nm is seen in PANI-NF spectrum. This is one confirmation that the PANI-NFs are present in the emeraldine base form.³⁸ A shoulder at 713 nm is the benzenoid to quinoid excitonic transition.³⁸

A suspension of emeraldine base was diluted to a 0.2 % w/v and combined in a 4:1 ratio with a 10 mM H₂AuCl₄ solution at 4 °C. The solution was left to react for 24 hours at 4 °C, to yield the nanocomposite material, PANI-NF-AuNP. The PANI-NF-AuNP nanocomposite spectrum displays a characteristic UV - vis²³ in Figure 4.11 (thick line), with the dominant feature in the spectrum being a broad band centred around 801 nm which is most likely associated with the plasmon absorbance of gold particle aggregates.³⁸ The spectrum displays one optical absorption peak at 394 nm, which is assigned to the π - π^* transition band of the benzenoid rings of PANI. This band overlaps with the broad 420 nm polaron band suggesting a high level of doping. The broad peak at 801 nm (Figure 4.11, thick line), has been previously interpreted as excitations of valence electrons to the polaron band formed when emeraldine base is doped to the conducting emeraldine salt form.³⁹ The dominance of this band is consistent with the relatively high surface coverage of nanoparticles revealed by the TEM and voltammetry in acidic electrolyte as well as the large extinction coefficient of gold nanoparticles.⁴⁰

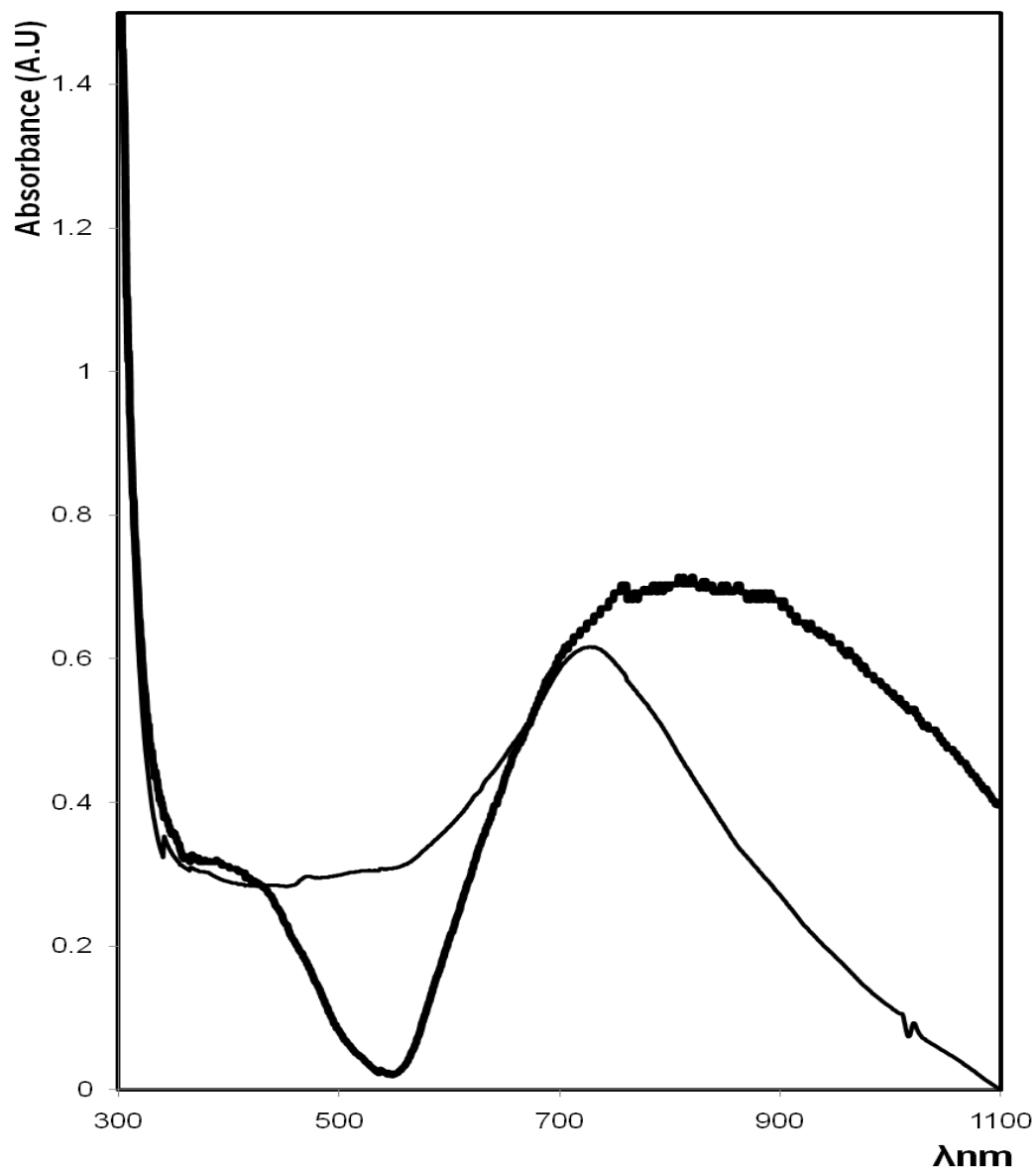
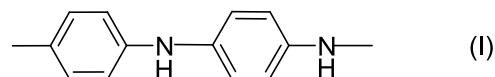


Figure 4.11 UV-vis spectra of blue chemically prepared emeraldine base (thin line) drop cast onto ITO glass electrode. The polymer was prepared using 2.2 mM emeraldine base in 1 M NH₄OH. Thick line shows the spectrum after a suspension of 2.2 mM emeraldine base was combined in a 4:1 ratio with a 10 mM HAuCl₄ solution at 4 °C. and the film drop cast onto an ITO glass

4.2.6 RAMAN spectroscopy of polyaniline

PANI has been extensively studied by Raman spectroscopy for several years. Due to the complexity of the PANI structure, Raman studies were essentially limited to the qualitative discrimination between the different forms of PANI. Numerous work has been carried out to identify the different vibrations typical of the different oxidation states of PANI.⁴¹ Most of them dealt with the study of the PANI insulating forms: leucoemeraldine, emeraldine and pernigraniline bases.⁴¹ The electronic structures illustrated below are found in polyaniline chains depending on the oxidation and protonation state which can be confirmed by Raman.

Unprotonated reduced segment of para – substituted benzenoid rings joined together by amine nitrogens



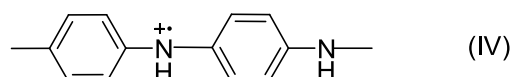
Unprotonated oxidised segment consisting of benzenoid and quinoid rings joined together by imine nitrogen



Protonated oxidised segment (bipolaron form)



Protonated oxidised segment (polaron form / semiquinone radical cation)



Number (I) is found in leucoemeraldine base (fully reduced) and part of emeraldine base (half oxidised). Number (II) occurs in emeraldine base (half

oxidised) and pernigraniline base (fully oxidised). Number (III) and (IV) appear only in the emeraldine salt form.

Typically, Raman bands of polyaniline are found in the 1000 – 1700 cm^{-1} range.⁴² Number (I) shows three major raman bands which are associated with C-C stretching (ca. 1600-1620 cm^{-1}), C-H bending (ca. 1160-1180 cm^{-1}) and C-N stretching (ca. 1230-1255 cm^{-1}) the bipolaron and semiquinone radical segments seen in number (III) and (IV) appear in 1300 – 1350 cm^{-1} region at ca. 1317 and 1338 cm^{-1} .⁴²⁻⁴⁵

The oxidised, quinoid ring of Number (II) is seen in the Raman bands in the 1450 – 1580 cm^{-1} region. A band is seen at ca. 1580 cm^{-1} which is associated with the C=C stretching while a band at ca. 1470-1490 cm^{-1} originates from C=N stretching. A band at ca. 1515-1520 cm^{-1} is associated with N-H bending deformations of polyaniline. An unusual bond C–N•+ stretch, which arises from head to head coupling, can be observed at ca. 1317 cm^{-1} .^{46,47} Table 4.3 summarises the Raman assignments.

Table 4.3 Frequencies (cm^{-1}) of Raman modes observed for PANI and their assignments (B = benzenoid ring and Q = quinoid ring.) according to references.⁴²⁻⁴⁵

Frequencies (cm^{-1})	Assignments
1160-1180	C-H bending
1220-1225	C-N stretching
1317-1338	C-N ⁺ Stretching
1470-1490	C=N stretching (Q)
1515-1520	N-H bending
1580-1590	C=C stretching (B)
1600-1620	C-C stretching (B)

4.2.6.1 Raman of electropolymerised PANI film.

Raman spectroscopy was employed to observe bond stretching differences on both the amine and imine nitrogens of the bare PANI with no nanoparticles (Figure 4.12, thin line) and the PANI-Au nanocomposites (Figure 4.12, thick line). Using an excitation line of 632.8 nm strongly enhances the spectral features associated with the presence of oxidized (quinoid) units. The range between 1100 and 1650 cm^{-1} corresponds to different stretching modes of different bonds (C-C, C-N) as well as C-H bending modes. Different modes of vibration are observed, the rings C-H bending modes between 1100 and 1210 cm^{-1} , the rings C-C stretching modes between 1520 and 1650 cm^{-1} and C-N stretching modes between 1210 and 1520 cm^{-1} . The chemical bonds of C-N, protonated C-N+, C=N, and protonated C=N+ are assigned at 1320, 1340, 1478, and 1495 cm^{-1} according to literature reports.⁴⁸

Figure 4.12 (thin line) shows the Raman spectra of doped emeraldine PANI. PANI exhibits a peak at 1334.2 cm^{-1} corresponding to the C-N•+ stretching mode of the delocalized polaronic charge carrier. The absorption peak at 1525 cm^{-1} corresponds to the N-H bending deformation band of protonated amine. The C-C deformation band of the benzenoid ring positioned at 1580 cm^{-1} is characteristic of the semiquinone rings. The vibration modes illustrated in Figure 4.12 at 1580 cm^{-1} (C=C quinoid stretching), 1208 cm^{-1} (benzenoid, C-N) and 1470 – 1490 cm^{-1} (quinoid C=N) are typically observed for PANI.⁴⁸

Figure 4.12 (thick line) shows that both the amine and imine stretches are affected by metal nanoparticle deposition. A shift to higher wave numbers is observed in the PANI-Au compared to doped emeraldine PANI, indicating that the gold nanoparticles bonded to the PANI.⁴⁸ A shift in intensity by approximately 2.5 fold is observed in the PANI-Au compared to doped emeraldine PANI, also indicating that the gold nanoparticles bonded to the PANI giving a SERS enhancement. A shift in wavenumber and relative peak intensity (RI) is observed for PANI (1580 cm^{-1} , RI = 474) after Au nanoparticle deposition (1583.8 cm^{-1} , RI = 843) where C=C quinoid stretching typically occurs. There is also an increase in peak intensity and frequency for the

modes at 1208 cm^{-1} (RI = 408) to 1210 cm^{-1} (RI = 903) for the benzenoid C-N stretching and a shift at 1470 cm^{-1} (RI = 991) to 1472 cm^{-1} (RI = 2394) for the quinoid C=N stretching after Au deposition. The electron clouds at the conjugate C=N bond can partially transfer to the gold nanoparticles because in this case the PANI is partially positively charged and the gold nanoparticles are partially negatively charged.⁴⁸ This charge transfer effect indicates that the PANI and gold nanoparticles act as donor and acceptor, respectively.⁴⁸

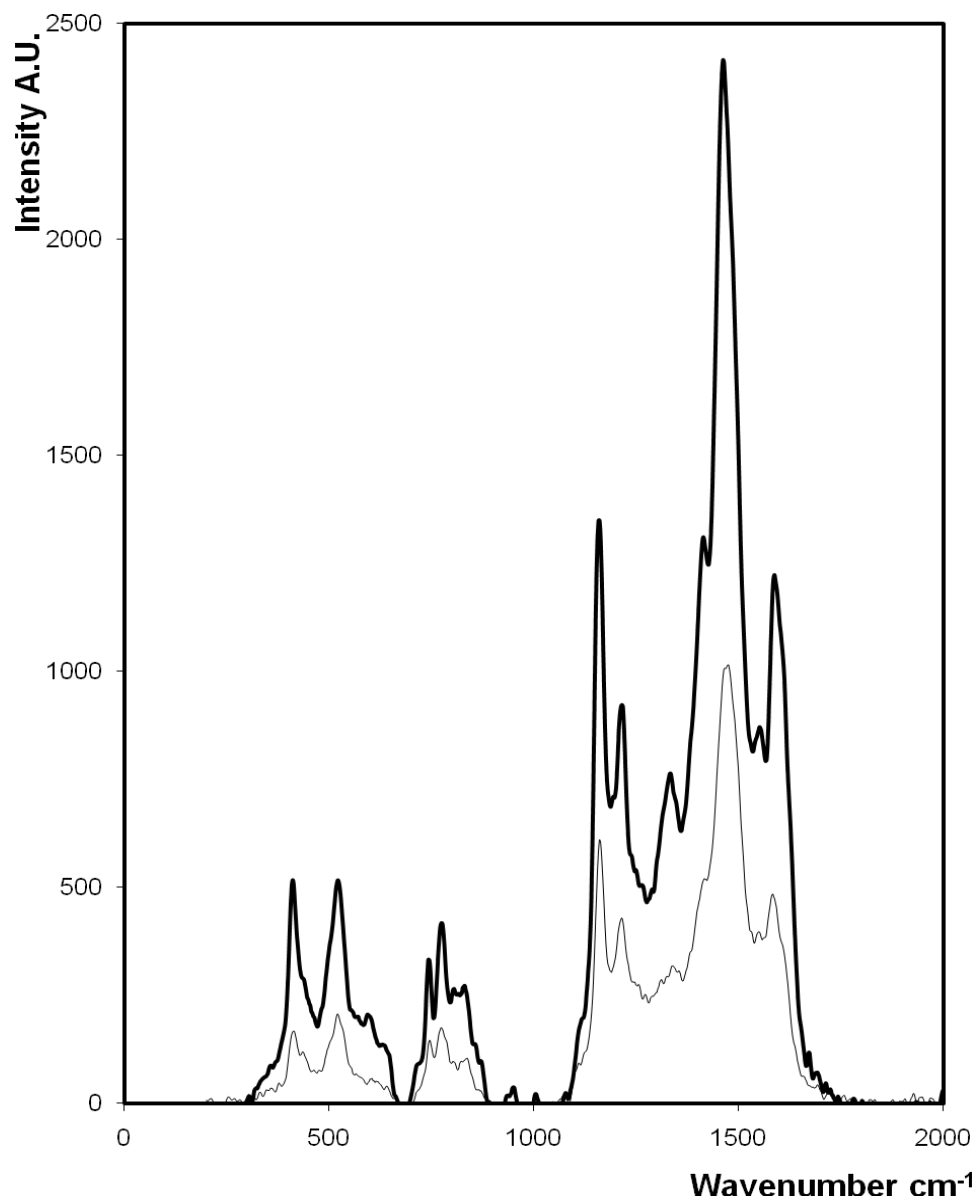


Figure 4.12 Resonance Raman spectra of PANI films grown potentiostatically (thin line) and after AuNP deposition (bold line) onto ITO glass electrode (+0.55 V for 90 s at 100 mVs⁻¹) from aqueous 40 mM aniline in 0.1 M HCl. Electrochemical deposition of AuNPs (3 mM cyan free gold plating solution) onto the polyaniline was applied at a fixed potential of -1.5 V for 50 s. Samples were irradiated using He-Ne laser excitation at 632.8 nm.

4.2.6.2 Raman of vapour polymerised PANI film.

In the typical Raman spectrum of vapour polymerised PANI,⁴⁹ specific bands are observed at 1592, 1488, 1438, 1351, 1230, and 1172 cm^{-1} , respectively. According to a previous paper,⁴⁹ the band at approximately 1590 cm^{-1} may be assigned to a C-C stretching vibration of the quinoid ring and the 1488 cm^{-1} band to the C-C stretching vibration of the benzenoid ring.

Raman spectroscopy was employed to characterise the chemical bonds in the PANI before and after Au deposition as shown in Figure 4.13. The PANI before Au modification is discussed first (Figure 4.13, thin line). The bands observed at approximately 1158, 1248 and 1329 cm^{-1} are assigned to C-H in-plane bending of quinoid ring, the antisymmetrical C-N stretching of the benzene diamine, and the C-N⁺ radical cation stretching, respectively. The quinoid rings are mostly coupled at C and N position (head-to-tail coupling) because the C-N⁺ stretching raman band (1329 cm^{-1} , RI = 190) is very strong and the corresponding C-N stretching of benzene is observed at 1248 cm^{-1} .⁵⁰

The vapour polymerised material shows an increase in intensity and frequency after gold nanoparticle deposition (Figure 4.13, thick line), indicating that the gold nanoparticles have attached to the PANI film. A 4.8 fold increase in peak intensity is observed at 1248 cm^{-1} (RI = 120) for the PANI benzenoid, C-N stretching to 1259 cm^{-1} (RI = 586) after nanoparticle deposition. The relative peak intensity found at 1329 cm^{-1} for the PANI quinoid C=N stretching increased significantly from 190 to 878 after Au deposition. The relative intensity (RI) of the double band around 1335 cm^{-1} (RI = 176), assigned to C-NS⁺ vibration, is lower for PANI compared to PANI-AuNP (1406 cm^{-1} , RI = 695). An increase of a relative intensity of the band at 1585 cm^{-1} (RI = 307) as compared to that at 1611 cm^{-1} with a RI value of 787 (PANI with Au) indicates an increase in the number of quinone type rings relative to the benzene type ones.⁵¹ Also for the PANI-AuNP sample, the bands around 898 - 1268 cm^{-1} are better defined and more intense than in the absence of the AuNPs. Based on these observations, we can conclude that PANI has a lower doping level in the absence of gold.⁵² Overall there is a positive shift to higher wave numbers

when PANI-Au is compared to PANI, indicating that the gold nanoparticles have bonded to the PANI giving a charge transfer.⁴⁸

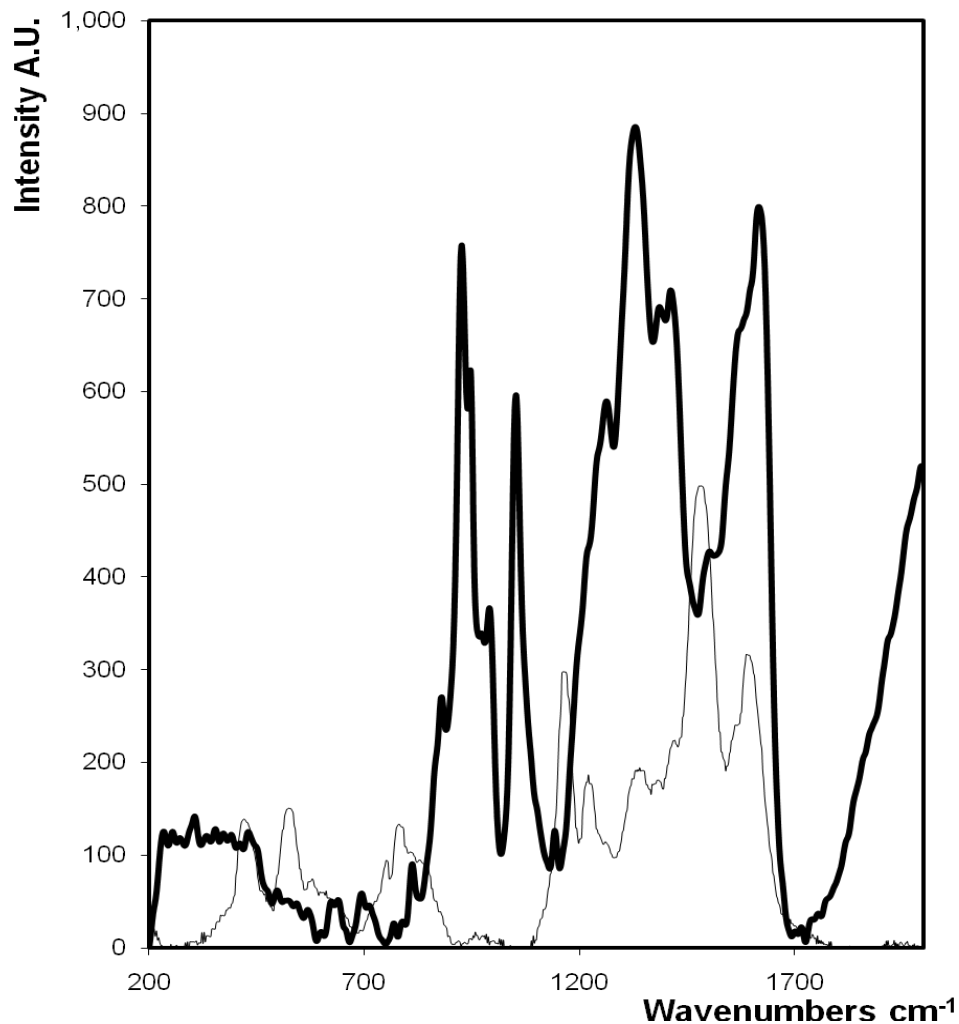


Figure 4.13 Resonance Raman spectra of the vapour polymerised PANI before (thin line) and after AuNP deposition (bold line) onto ITO glass electrode. The films were grown by vapour oxidation by coating ITO glass electrode with 0.85 M aqueous Fe (III) tosylate (40 % EtOH) and exposing surface to 1 M aniline monomer vapour. Electrochemical deposition of AuNPs (3 mM cyan free gold plating solution) onto the polyaniline was applied at a fixed potential of -1.5 V for 50 s. Samples were irradiated using He-Ne laser excitation at 632.8 nm.

4.2.6.3 Raman of chemically polymerised PANI film.

Raman spectroscopy was carried out for the chemically prepared emeraldine base PANI nanofibres composite with and without the AuNPs present. Figure 4.16 (thin line) illustrates the Raman bands for chemically polymerised PANI film in the absence of AuNPs. The C=C stretches are observed at 1585 cm^{-1} with a strong band at 1162 cm^{-1} attributed to bending C–H vibration mode of quinoid-like rings. The bands observed at approximately 1162, 1251 and 1336 cm^{-1} may also be assigned to C–H in-plane bending of quinoid ring, anti-symmetrical C–N stretching of benzene diamine, and C–N⁺ radical cation stretching vibration, respectively. The quinoid rings are mostly coupled at the C and N position (head-to-tail coupling) because the C–N stretching Raman band is intense and the corresponding C–N stretching of benzene is observed at 1251 cm^{-1} (RI = 390).⁵³

For the chemically prepared PANI containing gold (Figure 4.14, thick line), C–N stretches corresponding to imine sites in emeraldine form of PANI appear dominating at 1468 cm^{-1} (RI increased from 662 to 1341). Also, C–N⁺ stretches corresponding to amine sites are well developed at 1327 cm^{-1} (RI = 742). Within the spectral region below 1210 cm^{-1} , C–H bending vibrations of aromatic rings appear most prominent⁵⁴ at 1158 cm^{-1} , (RI increased from 846 to 1350).

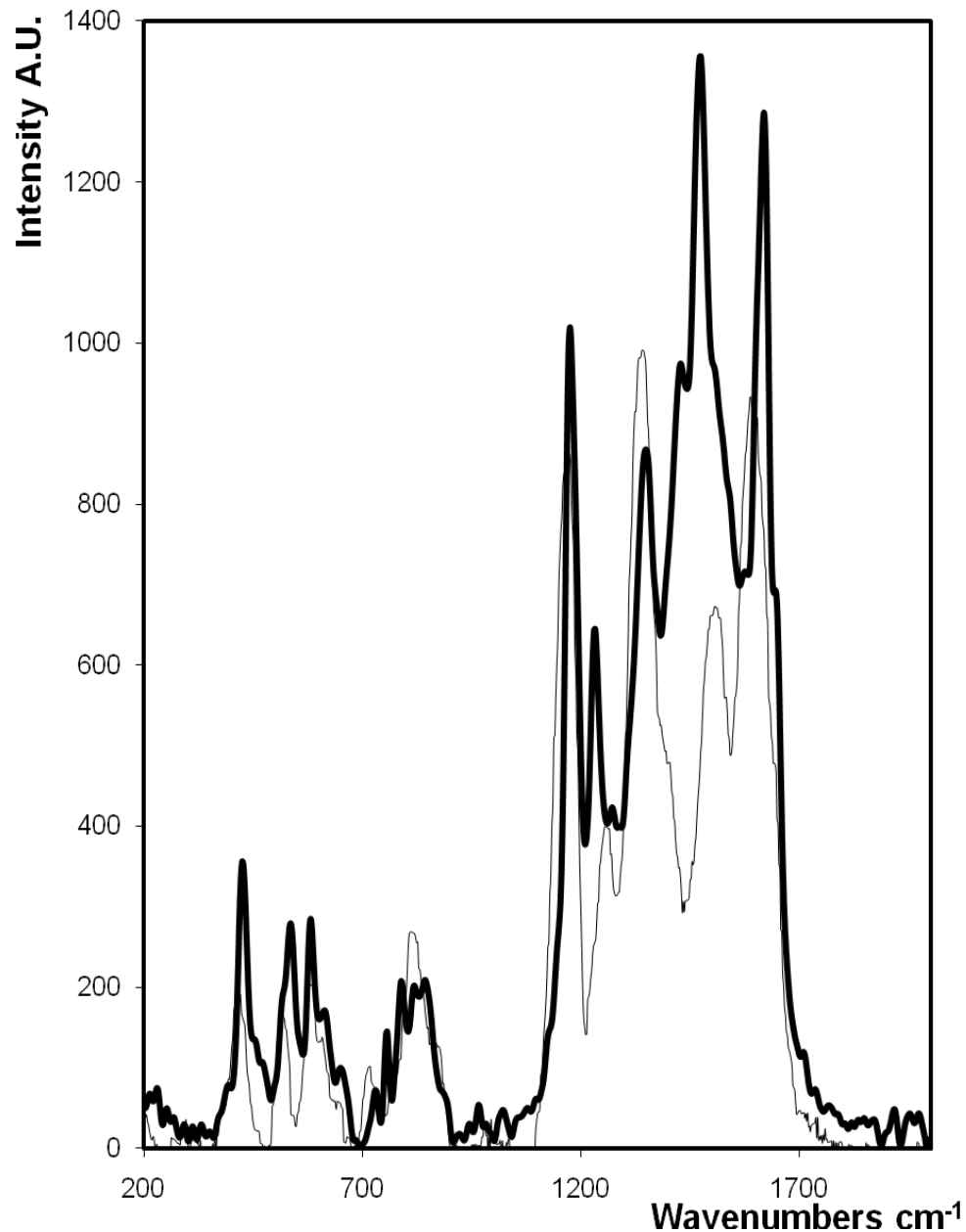


Figure 4.14 Resonance Raman spectra of chemically synthesized PANI films (thin line) and after AuNP deposition (bold line) drop cast onto ITO glass electrode from aqueous 3.2 mM aniline in 0.8 mM APS in HCl. Electrochemical deposition of AuNPs from a 3 mM cyan free gold plating solution onto the PANI was applied at a fixed potential of -1.5 V for 50 s. Spectra were collected using He-Ne laser excitation at 632.8 nm.

In the present work, Raman spectroscopy was used to identify the PANI form and the differences between the structures of the 3 techniques of PANI synthesis. The Raman spectra obtained for the electrochemical, chemical and vapour polymerised PANI films are shown in Figure 4.15 A.

The positions of the main vibrations have been compared to the typical vibrations of leucoemeraldine, pernigraniline, emeraldine base and salt reported in the literature (Table 4.3). For each of the PANI films produced the emeraldine salt has been undoubtedly identified in all cases, where a band around 1334 cm^{-1} , assigned to the protonated nitrogen, is found in the spectra. Though PANI films were produced in each case, and the Raman spectra are rather similar, one can notice some differences in each method of polymerisation. Essentially, there are three spectral ranges sensitive to the redox state of PANI:⁵⁵

1. $1650\text{--}1520\text{cm}^{-1}$ range. Here, C–C and C C stretching vibrations of benzene and quinone type rings appear mostly prominent.
2. $1520\text{--}1210\text{cm}^{-1}$ range with dominating C–N, C N, and C-N+ (i.e., an intermediate bond between a single and a double) bond stretching vibrations of a polymer chain.
3. $1210\text{--}1100\text{cm}^{-1}$ range, where C–H bending vibrations of benzene and quinone rings are mostly characteristic.⁵⁵

Within the first range, C-C stretching vibrations of quinoid rings of PANI at $\sim 1585\text{cm}^{-1}$ where PANI is presumably in its oxidised form, appears the most dominant for the chemically polymerised PANI (1585.85 cm^{-1} , RI= 932), followed by the electrochemically prepared PANI (1579.5 cm^{-1} , RI = 474) and then the vapour polymerised PANI (1585.9 cm^{-1} , RI =307).

Within the spectral range of $1520\text{--}1210\text{cm}^{-1}$, C-N stretching vibrations appear most prominent for the oxidised forms of polymers. The frequencies for C-N stretches range from 1462.3 cm^{-1} (RI=991) for electrochemically prepared

PANI, 1499.31 cm^{-1} (RI = 662) for chemically prepared PANI and 1475.2 cm^{-1} (RI = 489) for vapour polymerised PANI. This dominating Raman band drastically decreases in intensity by changing the method in which the PANI is synthesized, thus indicating that the polymer synthesized from vapour polymerisation is in a more reduced form.⁵⁵

Within the range of $1210\text{--}1100\text{cm}^{-1}$, C–H bending vibrations are most characteristic. From these, C–H bending in emeraldine (half-oxidized) form is observed for each PANI film. The chemical PANI is located at 1162.7 cm^{-1} (RI = 846) and the electrochemical and vapour PANI are both found at 1158.1 cm^{-1} (RI = 586.7 and 261, respectively). A decrease in the band intensity indicates that the polymer is in a more reduced form, which means it could be turning into leucoemeraldine.⁵⁵

A serious attempt has also been made provide surface enhanced Raman spectroscopy (SERS) to each of our synthesized PANI films, making use of the electrochemical deposition of metal nanoparticles. SERS is a spectroscopic method where the Raman scattering signal, which is sensitive to the molecular structure, is enhanced in the presence of gold nanoparticles and has emerged as a powerful tool for the detection of specific molecules.⁵⁶ This technique has improved the Raman lines intensities for each of our PANI films.

Figure 4.15 B shows the SERS spectra on the various syntheses (electrochemical, chemical and vapour) of PANI films after the electrochemical deposition of gold. Comparing the Raman peaks of the C–H bending in the range of $1160\text{--}1180\text{ cm}^{-1}$, it can be seen that the relative intensity of the peak at high frequency is higher for the PANI polymerised electrochemically (1327) than for PANI polymerised by chemical (1018) or vapour (121) methods. On the other hand, the relative intensity of the band around $1317\text{--}1338\text{ cm}^{-1}$, assigned to C–N⁺ vibration, is lower for electrochemically prepared PANI (RI=742) than for the chemically prepared PANI (RI=853) and vapour polymerized film (RI=878). The bands around 1220 cm^{-1} , corresponding to C–N stretching, and around 1470 cm^{-1} , corresponding to C=N stretching, are better defined and more intense in the electrochemically prepared PANI (RI= 903 and 2394) spectra than the chemically (RI = 642 and 1341) and vapour

polymerised PANI (RI= 586 and 421) film spectrum. The change of optical properties of gold nanoparticles upon slight modification of the surrounding environment is the basis for the development of biosensors.⁵⁶ Therefore, there is need for nanostructures that give maximum SERS signal. In the present work, gold nanoparticles electrochemically deposited on a electrochemically modified PANI electrode has demonstrated to be an excellent SERS substrate compared to SERS effect of the gold nanoparticles deposited onto the chemically and vapour polymerized PANI modified electrode.

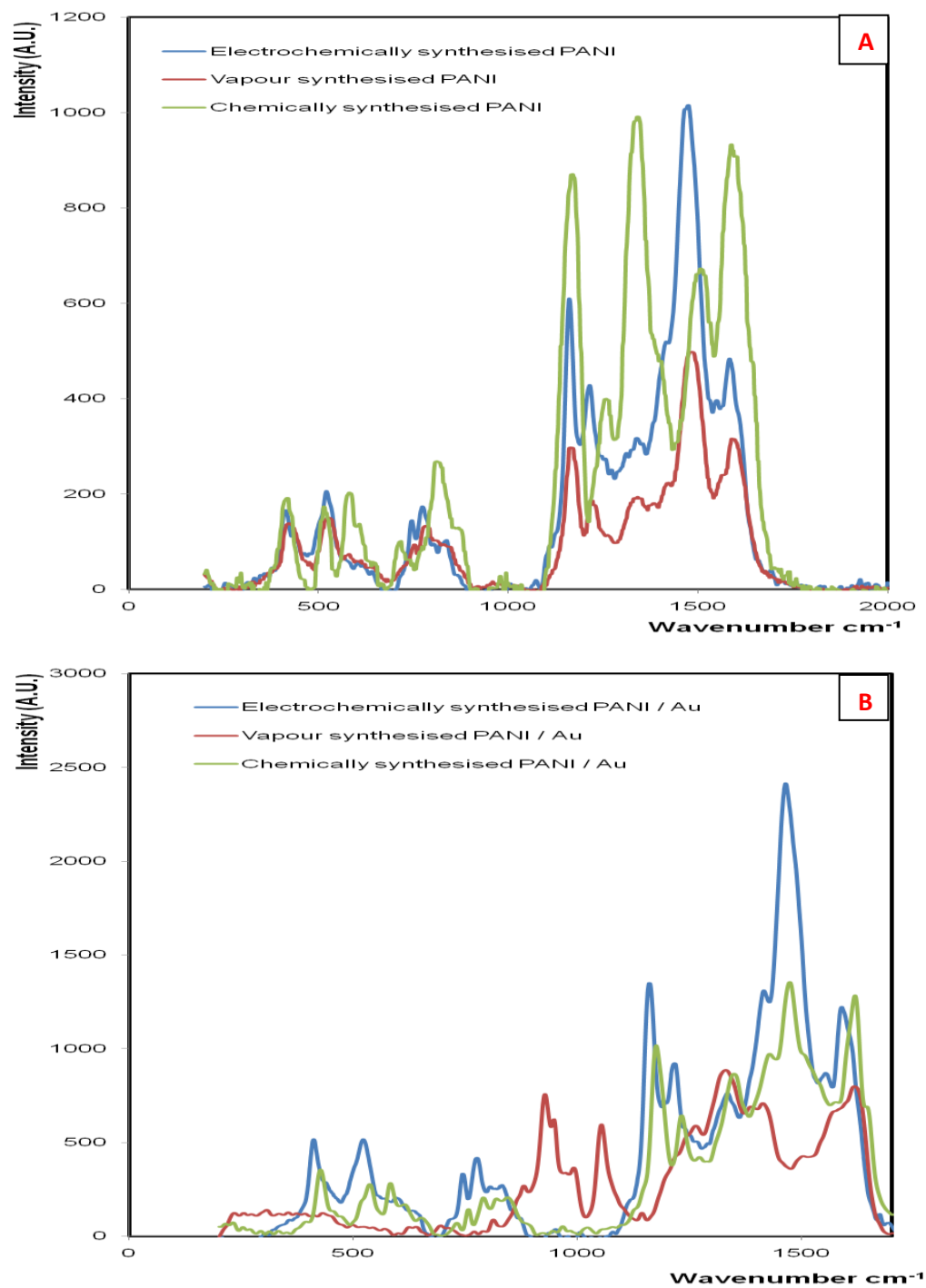


Figure 4.15 Comparative resonance Raman spectra of the electrochemically, chemically and the vapour polymerised PANI before (A) and after AuNP deposition (B) on ITO glass respectively. Spectra were collected using He-Ne laser excitation at 632.8 nm.

4.2.7 Electron paramagnetic resonance of polyaniline

Electron Paramagnetic Resonance, EPR, can provide powerful insights into the structure and properties of conducting polymers and has frequently been used to investigate the nature of various quasi-particles⁵⁷⁻⁶¹ (such as excitons,⁵⁸ solitons, polarons,⁵⁷ and bipolarons⁵⁹) which are thought to play a central role in charge transport. For example, a single resonance line located close to the g value of 2.003, is assigned to polaronic quasi-particles,^{60,62} while the zero spin bipolaron has $s = 0$ and hence presents no EPR spectrum.^{63,64} Hence, it is useful for relating PANI and PANI/AuNP samples to their g factor, which can verify if the radical is different for each sample and can be related to other properties such as electrical conductivity.

EPR acts as a very straight forward tool in recovering information on electron spins. The interaction of the external magnetic field with electron spin of materials depends on the magnetic moment of that spin. The nature of the isolated electron spin has only two possible orientations. The application of the magnetic fields which present a magnetic potential energy splits the spin state by an amount which is proportional to the magnetic field, commonly known as the “Zeeman Effect”. Radio frequency radiation can cause a transition from one state to another. The energy associated with the transition described is expressed as applied magnetic field B , the electron spin g – factor g and Bohr magneton (constant m_p).⁶⁵

4.2.7.1 EPR studies of electropolymerised PANI film.

Typical EPR spectra of the solid-state electrochemically grown PANI films are shown in Figure 4.16 before and after the electrochemical deposition of Au. The EPR technique verifies the existence of unpaired electrons in the samples. Figure 4.16 (thin line, y axis) shows a free radical peak indicating the presence of polarons for the electrochemically prepared PANI. In the PANI, the g factor of ca. ~ 2.002 and a gauss of 3526 G was observed and the peak-to-peak line width (ΔH) was 3 G. This g factor is consistent with previously obtained values⁶⁶ and the symmetrical singlet can be attributed to the presence of electrons that are unpaired and delocalized over the entire backbone in the π – system of the carbon atoms. This is not to suggest that the electron may be delocalized over single phenyl; the polarons have a significant spatial distribution in conjugated polymers.⁶⁷⁻⁶⁹

The PANI incorporated with AuNPs show an EPR signal that has a peak area five orders of magnitude smaller than the parent PANI. However the chains of the polymer after gold deposition are more expanded and the interactions with the polymer with the gold are increased, resulting in the broad line width observed in the EPR spectrum. The change in g factor from low to high field accompanied with a line broadening effect has been reported previously⁷⁰ and has been ascribed to a spin-orbital coupling phenomenon induced by the presence of the coordinating metal centre.⁷¹ In the PANI-Au EPR, the g factor of 2.006 (3510 G) and the line width value of $\Delta H = 9$ G was recorded. The large peak-to-peak line widths ($\Delta H = 9$ G) indicates a high electronic delocalisation which is consistent with an extended conformation of the polymeric chain.^{72,73} An additional broad spectral line is observed at $g = 2.009$, which possibly arises from free radical species in the polymer chain interacting with paramagnetic metal centers.⁷⁴

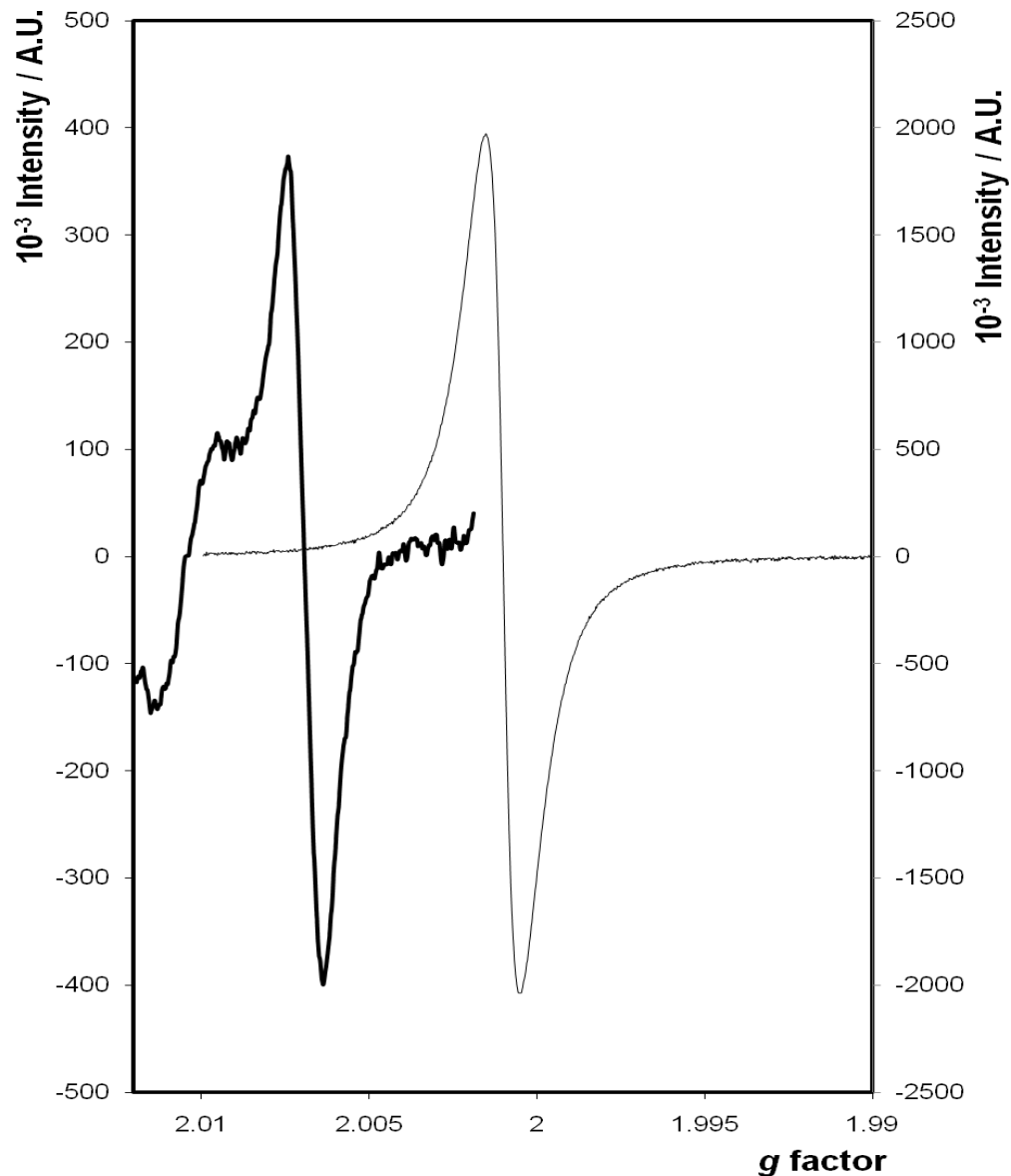


Figure 4.16 EPR response of a solid state sample of electrochemically prepared PANI (thin line, y-axis on right) and PANI-AuNP (thick line, y-axis on left). The microwave frequency of 9.763 GHz, attenuator of 10.0 dB, sweep width of 50 G, modulation frequency of 100 kHz, modulation amplitude of 1 G, time constant of 327.7 ms, conversion time of 1310.7 ms, and sweep time of 1342.2 s were employed.

4.2.7.2 EPR studies of chemically polymerised PANI film.

The magnetic properties of the chemically synthesised PANI (Figure 4.17) are in agreement to the EPR structure illustrated in Figure 4.16 for the electrochemically synthesised PANI. The EPR spectrum of the chemically polymerised conducting polymer represents a singlet with a g value of 2.002 (gauss of 3508 G), which is typical for PANI (2.003), indicating the spins are apparently more localised on the nitrogen sites.^{66,75} This finding confirms the existence of cation radicals in the PANI chains, characteristic for the polaron lattice of the conducting PANI emeraldine salt.⁷⁰

Figure 4.17 shows the EPR spectra of both the chemically prepared PANI (thin line) and PANI after electrochemical deposition of Au (thick line). A free radical peak appeared in the EPR spectra of both samples, indicating the presence of polarons. In the PANI sample, the g value observed was 2.002 and the peak-to-peak line width (ΔH) was 16 G. In the PANI sample after Au deposition, the values were g was 2.0001 (gauss of 3507 G) and the ΔH was 9.6 G. A shift from high field to low field is typically observed when polymers interact with gold nanostructures, indicating that an increase in the degree of localisation of electron resonance over the entire length of the polymer has occurred.

The PANI incorporated with AuNPs show the EPR signal with three orders of magnitude smaller peak area compared with the signal of the PANI. However, the chains of the polymer after gold deposition are more expanded and the interactions with the polymer with the gold are increased, resulting in the broad line width observed in the EPR spectrum. The AuNP decreases the interactions between adjacent chains and/or motional broadening occurs.⁷⁶ The fact that this graph does not show a hyperfine structure indicates that the electrons are distributed more evenly over the polymer chains.⁷⁶ In conclusion, this means that the chemically prepared PANI-AuNP has facilitated electron transfer throughout the polymer film, which ought to improve the performance of electrochemical biosensors.

By observing the values of the line width (ΔH) it was possible to get an idea of the degree of delocalization of the cation radical.⁷⁶ The ΔH of PANI decreased from 16 G to 9.6 G for PANI after Au deposition, indicating more radical formation throughout the polymer chain. With the decrease in the ΔH there will be an increase in the polaron mobility because of more free radical generation and delocalization of electrons.⁷⁶

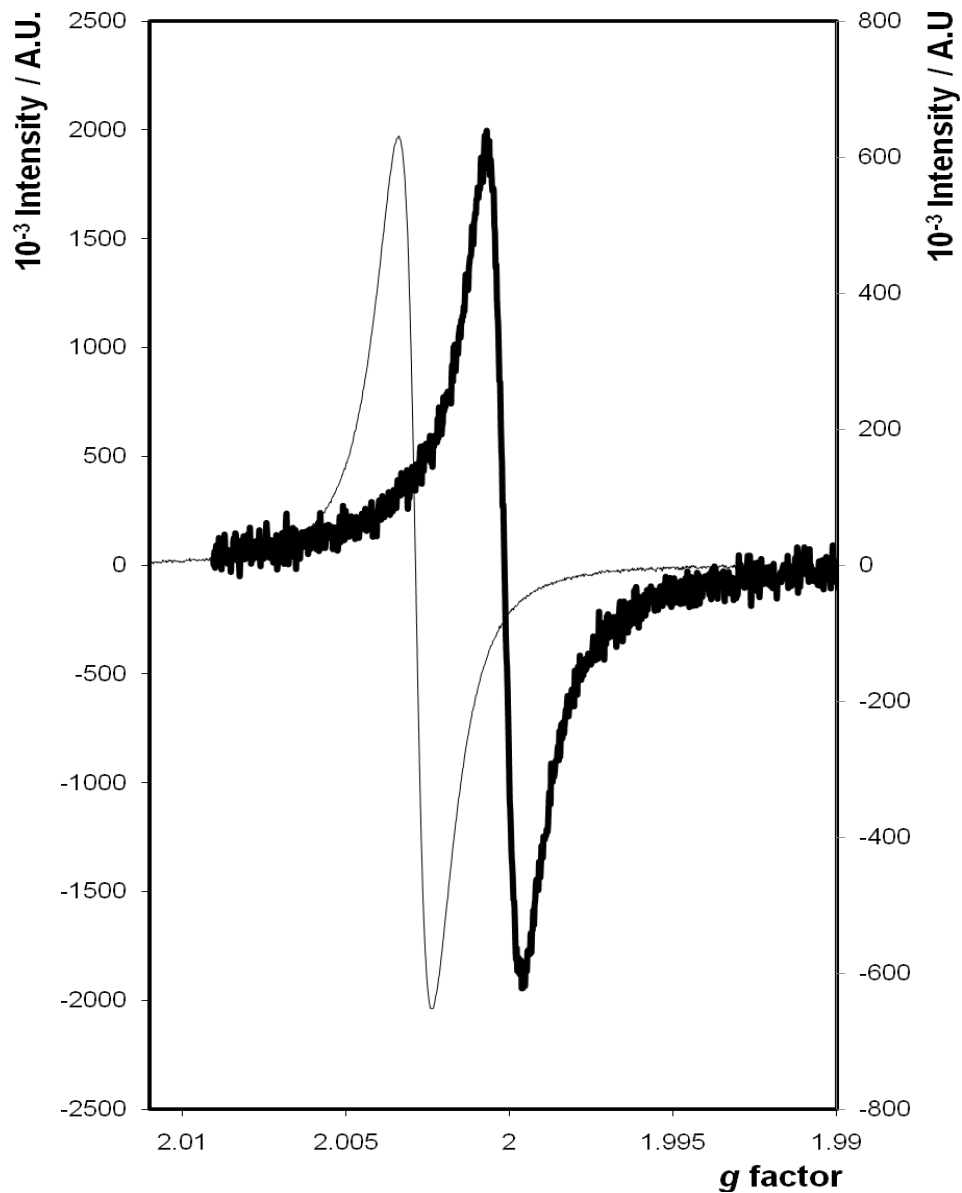


Figure 4.17 EPR response of a solid state sample of chemically prepared PANI (thin line, y-axis on left) and PANI-AuNP (thick line, y-axis on right). The microwave frequency of 9.763 GHz, attenuator of 10.0 dB, sweep width of 50 G, modulation frequency of 100 kHz, modulation amplitude of 1 G, time constant of 327.7 ms, conversion time of 1310.7 ms, and sweep time of 1342.2 s were employed.

4.2.7.3 EPR studies of chemically polymerised emeraldine base nanofibres.

Figure 4.18 illustrates the EPR responses of the emeraldine base of PANI-NF. It exhibits a symmetrical singlet that can be attributed to electron resonance that is delocalised in the π -system of the carbon atoms forming the polymer backbone in the main chain.^{61,66,77-79} The spectra have been fitted to Lorentzian lines and a g-factor of 2.0028 was obtained for the PANI-NF, which is close to the free electron g value ($g_0 = 2.0023$). The EPR spectra showed no significant hyperfine structure, which is characteristic of delocalised free radicals that exist along the polymer backbone.^{5,61} The peak-to-peak line widths ($\Delta H = 8$ G) also indicate a high electronic delocalisation which is consistent with an extended conformation of the polymeric chain.^{72,73}

Incorporation of Au nanoparticles (Figure 4.19) causes the g-factor to shift from 2.0028 to 1.9986 (high to low field). This shift can be interpreted as an increase in the degree of localisation of electron resonance. The spin intensity also increases significantly, being approximately 2.5 times greater than the PANI-NF without Au. There is also a notable change in the line width (ΔH) of PANI, which decreased from 8 G to 1.5 G for PANI after Au deposition, indicating more radical formation throughout the polymer chain. This implies that the addition of the Au nanoparticles decreases the interactions between adjacent chains and/or motional broadening.⁷⁶ With the decrease in the ΔH there will be increase in polaron mobility because of more free radical generation and delocalization of electrons.⁷⁶

Typically, a decrease in ΔH is accompanied by a sharp decrease in spin intensity and thereby a decrease in conductivity. However, the opposite is true of this system. This suggests that the Au nanoparticles effectively increase the spin intensity by allowing electron movement between adjacent chains without any “spin trapping” being evident, producing a higher number of spin states without increasing the doping or bipolaron levels. In addition to these exchange interactions, the Au present within the PANI-NF may also allow for more facile electron transfer throughout the nanofibre network which would in

turn improve the redox switching for electrochemical sensors in comparison to the PANI nanofibre without any Au present.

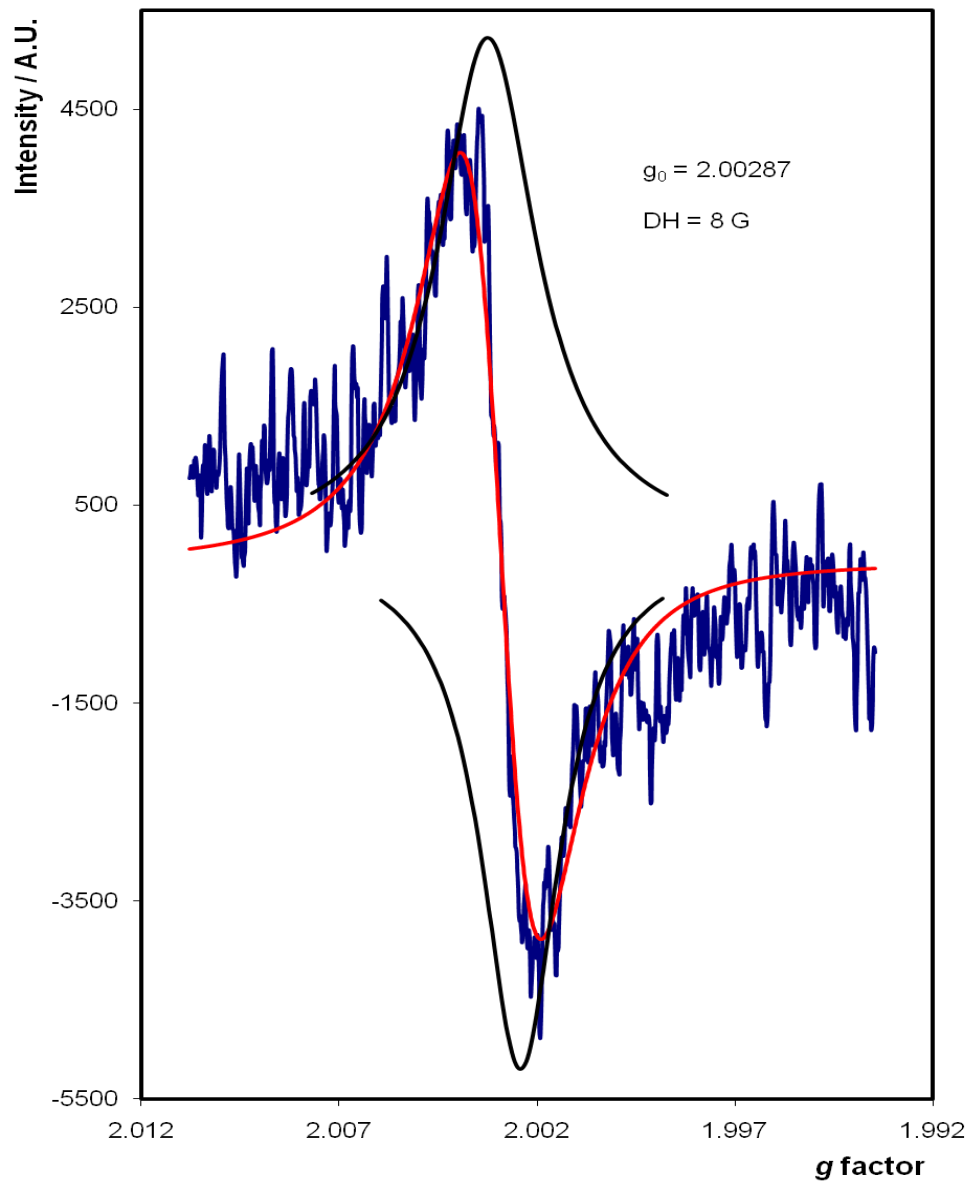


Figure 4.18 EPR response of a solid state sample PANI-NF emeraldine base. The microwave frequency of 9.763 GHz, attenuator of 10.0 dB, sweep width of 50 G, modulation frequency of 100 kHz, modulation amplitude of 1 G, time constant of 327.7 ms, conversion time of 1310.7 ms, and sweep time of 1342.2 s were employed. (Blue = experimental data, Red = fitted data and Black = Lorentzian profile.)

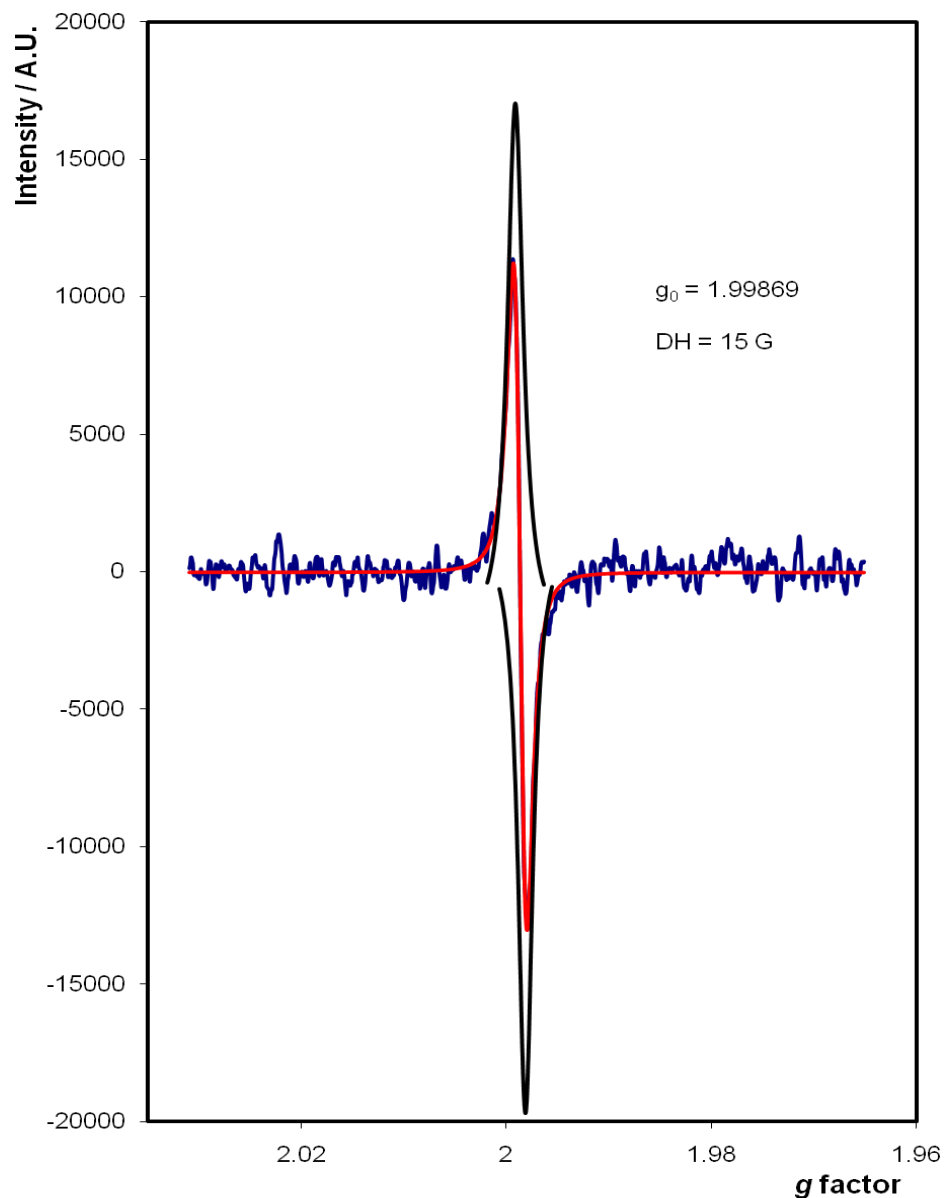


Figure 4.19 EPR response of a solid state sample PANI-NF-AuNP. The microwave frequency of 9.763 GHz, attenuator of 10.0 dB, sweep width of 50 G, modulation frequency of 100 kHz, modulation amplitude of 1 G, time constant of 327.7 ms, conversion time of 1310.7 ms, and sweep time of 1342.2 s were employed. (Blue = experimental data, Red = fitted data and Black = Lorentzian profile.)

4.2.8 Detection of the hybridisation reaction

Different physical, chemical and electrochemical methods of synthesizing the conducting polymer PANI, together with the advantages and disadvantages associated therein are discussed in detail in Section 4.2.8.1 – 4.2.8.4. Advances in the fabrication of conducting polymers, the effect on DNA hybridisation, sensing techniques and related disciplines constantly lead to new principles and enable improvements to be made in the methods and devices previously developed.

4.2.8.1 Electropolymerisation of aniline.

Here the use of gold nanoparticles (AuNP) and polyaniline to create a high sensitivity DNA hybridization assay is reported. Polyaniline (PANI) has been electrochemically deposited on gold electrodes and modified with electrochemically deposited gold nanoparticles to give a nanocomposite material (PANI - AuNP). As described in the previous chapter (Figure 3.1), single stranded capture DNA was bound to the gold nanoparticles and the underlying electrode and allowed to hybridise with a complementary target strand that is uniquely associated with the pathogen, *Staphylococcus aureus* (*S.aureus*) that causes mastitis. Finally, a second horse radish peroxidases (HRP) labelled strand hybridises with the target allowing the concentration of the target DNA to be detected by monitoring the reduction of a hydroquinone mediator in solution.

Cyclic voltammetric responses for electrocatalytic reduction of H_2O_2 at the PANI/DNA and PANI/Au/DNA biosensor electrode were firstly observed. In the potential window studied, no reduction peak was observed for either electrode in the phosphate buffer (pH 7.4) solution without H_2O_2 . Upon addition of 3 mM H_2O_2 , an increase of reduction current was detected at -0.4 V, indicating an obvious electrocatalytic reduction of H_2O_2 by the hybridised HRP labeled DNA. Amperometric determination of H_2O_2 was conducted at an applied potential of -0.4 V. After the background current decayed to a constant value, hydrogen

peroxide solution was injected into the detection solution, and the resulting steady state currents were recorded.

For comparison purposes, the absolute current measured for 150 pM to 1 μ M target DNA, the slope of the calibration curve and the lower concentrations of the target that could be detected was considered. The effect of the surface modification on the electron transfer is also clearly shown in calibration results. Figure 4.20 compares the 3 cases of (a) HRP labelled DNA hybridised on a bare electrode (b) on an electrochemically prepared PANI electrode and (c) on the electrochemically prepared PANI after AuNP surface modification.

Figure 4.20 shows the semi-log concentration vs. Δi calibration curves for the pathogen DNA detection using a bare gold electrode (\blacktriangle) where the concentration of sequence-specific DNA of *S. aureus* is systematically varied from 150 pM to 1 μ M, with a correlation coefficient of 0.95. The observation that Δi increases linearly with $\log [DNA]$ rather than $[DNA]$ suggests that the current response is influenced by the concentration of the HRP co-reactant, H_2O_2 , as well as the DNA concentration and that the performance may be further enhanced by increasing the concentration of the co-reactant. Significantly, this approach generated a measurable response even for pathogen DNA concentrations as low as 150 pM. The calculated limit of detection was 0.34 pM with a signal to noise ratio at least ten. Determination of the signal-to-noise ratio is performed by comparing measured signals from samples with known low concentrations of analyte with those of the blank sample.

The PANI modified electrode (Figure 4.20, \blacklozenge) readily achieved a detection for the 150 pM target DNA. Furthermore, the change of amperometric current showed a linear relationship with the target DNA concentration in the range of 150 pM to 1 μ M with the correlation coefficient of 0.9895. The dynamic linear calibration range of the PANI-AuNP modified electrode is 150 pM -1 nM with a correlation coefficient of 0.9977. This system also provides highly reproducible detection even at low DNA concentrations, e.g., at 150 pM the signal-to-noise ratio is at least 7, with a standard error of 0.108. When comparing these

results, to the current response found on a bare electrode, a significant increase of the Faradaic current from nanoamps to micro amps is exhibited after the electrochemical oxidation of PANI onto the bare electrode. Significantly, the polymerisation approach shows a greater sensitivity (slope of $0.5 \mu\text{A}^{-1}$) compared to the unmodified bare electrode (slope of $0.05 \mu\text{A}^{-1}$). The method offers an impressive detection limit of 9.29 fM for DNA detection on a PANI modified electrode.

The third part of this study involved combining the electrochemically synthesised PANI with the AuNP amplification, so as to improve the sensitivity of the PANI systems. Figure 4.20 shows the semi log calibration curve of the maximum average current response of the PANI-Au nanocomposite (■) films versus the concentration of target DNA. The net signal gain produced by this approach is significantly enhanced. For example, a 36% increase in current response for target DNA at a concentration of $1 \mu\text{M}$ was observed after AuNP formation. The HRP modified on the PANI-AuNP electrode shows faster and more sensitive current response to the addition of hydrogen peroxide when compared with the enzyme electrode not containing gold nanoparticles. In the presence of AuNPs, the sensitivity of the current response of S.aureus was amplified by 6.2 fold with increasing concentrations of target DNA hybridised when compared to the PANI modified electrode. The dynamic linear calibration range of the PANI-AuNP modified electrode is $1 \text{ nM} - 1 \mu\text{M}$ with a correlation coefficient of 0.9961 (not shown). The standard error for the lowest DNA concentration (150 pM) was 0.001 with a S/N ratio above 15 compared to the standard error of 0.108 for the PANI electrode.

This PANI - AuNP nanostructured surfaces showed a greater analytical performance than the unmodified gold electrode. Significantly, the sensitivity of the DNA detection is approximately 62 fold greater for the PANI-AuNP (slope of $3.14 \mu\text{A}^{-1}$) modified electrodes compared to the DNA on the unmodified electrode surface (slope of $0.05 \mu\text{A}^{-1}$). The enhancement in signal was attributed to the improved condition for effective hybridisation between the capture DNA and the target as a result of the surface modification. Also the increase in signal can be due to the enhanced reactivity of the NPs allowing for

a higher level of capture DNA immobilisation. It demonstrates superior sensitivity with a detection limit of target of 1.12 fM, which is one of the most sensitive methods for detection and analysis of DNA. The fabrication repeatability of four HRP electrodes, prepared independently, shows an acceptable reproducibility, with a RSD of 4.8% for the response to the same concentration of 200 μM H_2O_2 . Table 4.4 lists the average current response for the electrochemical synthesis of PANI before and after AuNP electrodeposition on a gold disc electrode at various concentrations of S.aureus.

Table 4.4 Average current response of electrochemically deposited PANI with and without AuNPs at different concentrations of target DNA.

Electrode Modification	Concentration of <i>S. aureus</i> (M)	Average current response ($\Delta i / \mu A$)	Standard deviation (n = 2)	Standard error
Bare Electrode	1.50E-10	0.03	0.06	0.04
	1.00E-09	0.05	0.02	0.01
	1.00E-08	0.09	0.01	0.01
	1.00E-07	0.13	0.01	0.01
	1.00E-06	0.20	0.01	0.01
Electrochemically synthesised PANI	1.50E-10	1.09	0.15	0.108
	1.00E-09	1.53	0.01	0.005
	1.00E-08	1.97	0.07	0.047
	1.00E-07	2.40	0.12	0.088
	1.00E-06	3.13	0.04	0.025
Electrochemically synthesised PANI with AuNPs	1.50E-10	6.182	0.01	0.01
	1.00E-09	10.065	0.05	0.04
	1.00E-08	12.477	0.05	0.03
	1.00E-07	15.218	0.09	0.07
	1.00E-06	18.822	0.72	0.51

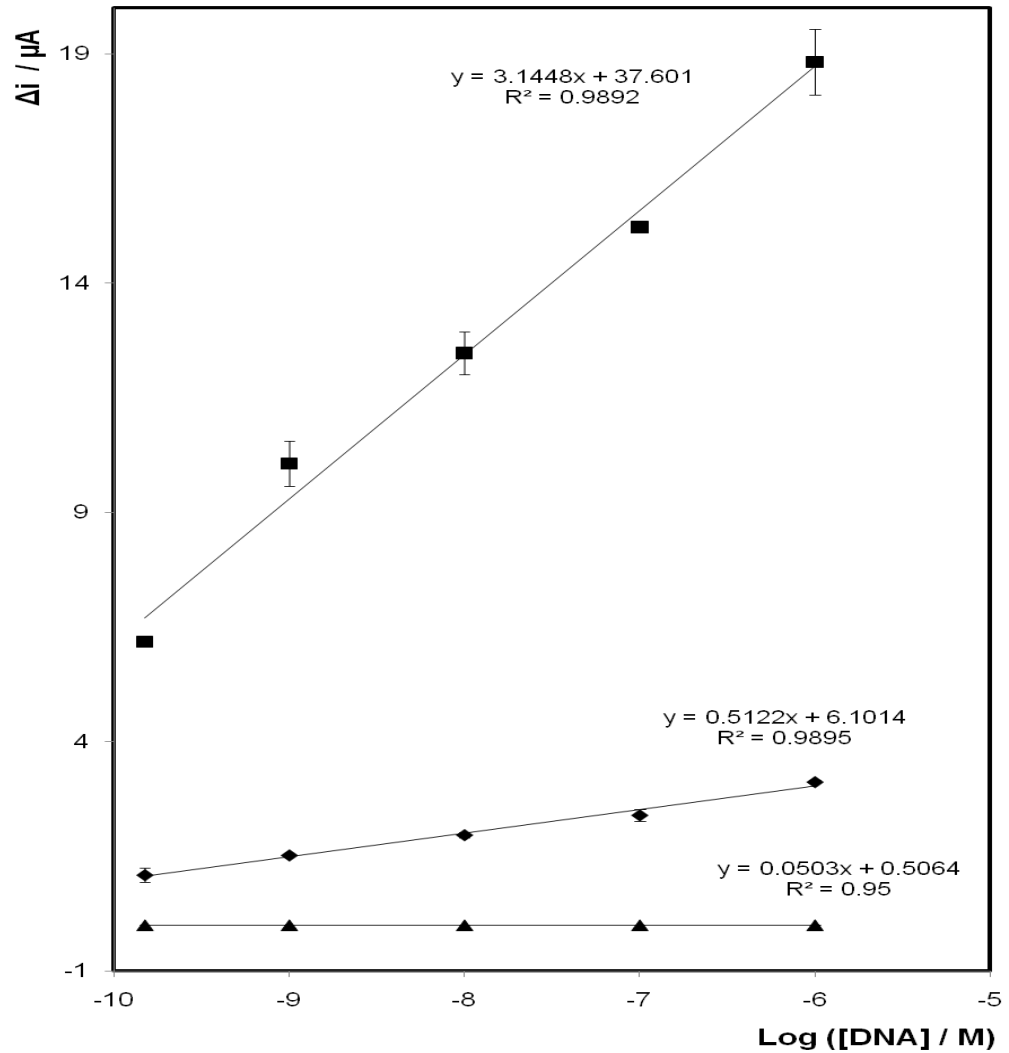


Figure 4.20 Electrochemical detection of sequence-specific *S. aureus* pathogen DNA concentration on a bare electrode (▲), electrochemically synthesised PANI (◆) and electrochemically synthesised PANI after AuNP deposition (■). Capture strand, target strand and probe HRP strand (Denhardt's buffer) were cycled in phosphate buffer saline and 0.1 M KCl and a concentration of 1.81 mM hydroquinone. Y axis is the difference in signal before and after addition of H₂O₂ (Δi). Potential applied -0.40 V. Where error bars are not visible, they are smaller than or comparable to, the size of the symbols and range from 0.6 % to 8.2 %.

4.2.8.2 Vapour polymerisation of aniline.

Polyaniline films were deposited under the conditions described in Section 2.5.2.1. The hybridisation was then carried out as described in Section 4.2.8.1. For the purpose of comparison, the detection of DNA was carried out on bare electrodes as well as the modified electrodes with the vapour polymerised PANI before and after Au modification.

Figure 4.21 shows the calibration curves for the detection of HRP for a bare, PANI and PANI-AuNP modified electrode. Firstly, a significant increase (approximately 24 fold) of the current response is observed when comparing the sensitivity of the vapour prepared PANI (slope of $1.2 \mu\text{A}^{-1}$) to the unmodified electrode (slope of $0.05 \mu\text{A}^{-1}$). The PANI-DNA biosensor showed that the reproducibility is excellent even at low DNA concentrations, e.g., at 150 pM the signal-to-noise ratio is at least nine. The calibration curve for the detection of DNA from 150 pM to 1 μM gives a correlation coefficient of 0.9578, however, the dynamic linear range between 1 nM – 1 μM gives a correlation coefficient of 0.9912. The calculated limit of detection was found to be 12 pM.

The sensitivity of the PANI-NF-AuNP film is significantly greater than that found in the absence of gold nanoparticles. When the assay is conducted in the presence of AuNP, the correlation coefficient is 0.9895 for the increasing DNA concentrations. The dynamic linear calibration range is 150 pM – 100 nM for the maximum average current response of the PANI-Au nanocomposite (■) films versus the concentration of target DNA with a correlation coefficient of 0.9986. The current response of the PANI-AuNP modified electrode (slope of $2.1 \mu\text{A}\text{M}^{-1}$) is universally 2 times more sensitive than the PANI modified electrode ($1.2 \mu\text{A}\text{M}^{-1}$). The enhancement of response for hydrogen peroxide detection was likely due to the structure of the gold–polyaniline nanocomposites.

Compared with electrochemically synthesized PANI-AuNP sensor (slope of $3.1 \mu\text{A}\text{M}^{-1}$), the vapour polymerised PANI after Au deposition sensor showed less sensitivity in electrode response (slope of $2.1 \mu\text{A}^{-1}$). The electrochemical

depositions of the AuNPs were carried out identically for both materials. The significant difference in the average maximum current response was due to the method in which the polyaniline was synthesized. The PANI-amplified assay can detect target DNA at concentrations as low as 41 fM, which represents a significant improvement over the PANI modified DNA assay alone (LOD = 12 pM). A threefold increase was also observed for the signal to noise ratio for the lower concentrations of DNA e.g. 150 pM the signal to noise ratio for the electrochemical PANI-AuNP is at least 15 (standard error = 0.07) and the vapour prepared PANI-AuNP is at least 5 (standard error = 0.48).

The polyaniline obtained by the vapor-phase polymerization shows lower sensitivity, at room temperature compared with that of conventionally electrochemically synthesized polyaniline. The higher electrode response of PANI electrochemically deposited may be due to its higher crystallinity, higher degree of doping, and lower interchain separation compared with the electrode vapour polymerised with PANI. In correlation with the EPR and Raman indicates, as gold was deposited to the vapour polymerised PANI, the sensor was perhaps in a slightly reductive state and therefore the system became slightly insulating instead of conducting. This property of the vapourised PANI with AuNP film, would therefore explain the electrode response differences between the two polyaniline sensors. Table 4.5 lists the average current response for the vapour phase synthesis of PANI before and after AuNP electrodeposition on a gold disc electrode at various concentrations of *S. aureus* DNA.

Table 4.5 Average current response of vapour oxidised PANI with and without AuNPs at different concentrations of target DNA.

Electrode Modification	Concentration of S. aureus (M)	Average current response ($\Delta i / \mu A$)	Standard deviation (n = 2)	Standard error
Bare Electrode	1.50E-10	0.03	0.06	0.04
	1.00E-09	0.05	0.02	0.01
	1.00E-08	0.09	0.01	0.01
	1.00E-07	0.13	0.01	0.01
	1.00E-06	0.20	0.01	0.01
Vapour oxidation of PANI	1.50E-10	1.10	0.10	0.07
	1.00E-09	1.50	0.54	0.38
	1.00E-08	3.41	0.07	0.05
	1.00E-07	3.94	0.09	0.06
	1.00E-06	6.13	0.95	0.67
Vapour oxidation of PANI with AuNPs	1.50E-10	3.63	0.68	0.48
	1.00E-09	5.00	0.23	0.16
	1.00E-08	6.83	0.87	0.62
	1.00E-07	8.34	0.19	0.14
	1.00E-06	12.19	0.02	0.01

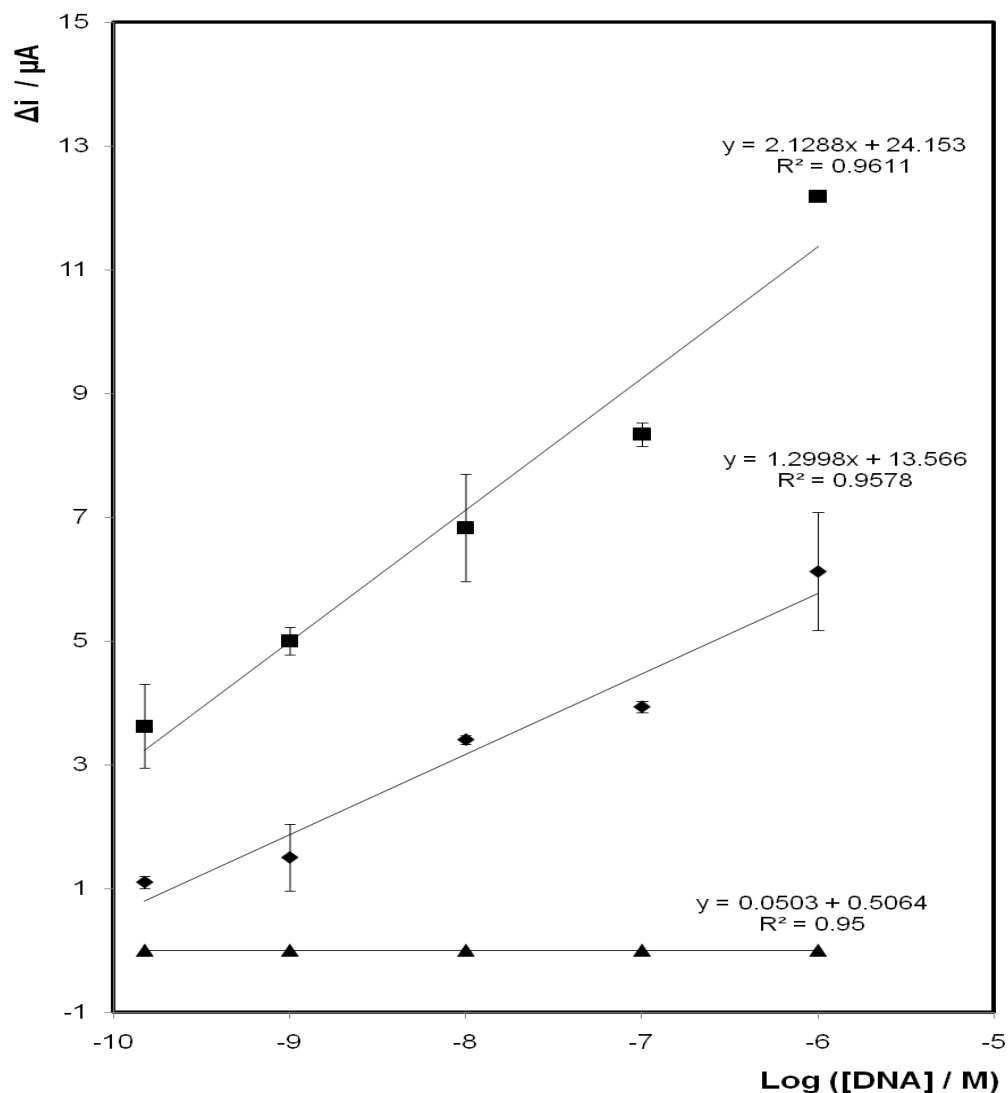


Figure 4.21 Electrochemical detection of sequence-specific *S. aureus* pathogen DNA concentration on a bare electrode (▲), vapour polymerised PANI (◆) and vapour polymerised PANI after AuNP deposition (■). Capture strand, target strand and probe HRP strand (Denhardt's buffer) were cycled in phosphate buffer saline and 0.1 M KCl and a concentration of 1.81 mM hydroquinone. Y axis is the difference in signal before and after addition of H₂O₂ (Δi). Potential applied - 0.40 V. Where error bars are not visible, they are smaller than or comparable to, the size of the symbols and range from 2 % to 15 %.

4.2.8.3 Chemical polymerisation of aniline

For this experiment chemical polymerisation of PANI was carried out as described in Chapter 2.3.3.1 and the calibration plots are shown in Figure 4.22. This graph highlights the results of the hybridisation of the specific sequence target DNA in a linear concentration of 150 pM to 1 μ M for 3 comparative studies. These three studies involved the detection of pathogen DNA after the hybridisation of complementary DNA strands onto a bare electrode (\blacktriangle) and an electrode modified with chemically synthesised PANI (\blacklozenge) and PANI – AuNP (\blacksquare).

The PANI modified electrode (Figure 4.22, \blacklozenge) achieved a current response for the 150 pM concentration of target DNA. The calibration curve for the detection of DNA from 150 pM to 1 μ M gives a correlation coefficient of 0.9438. Overall, it is clear from the calibration curve that the current response using a PANI modified electrode is linear over a dynamic range of 1 nM and 100 nM with detection limit of 32 pM and a correlation coefficient of 0.9907. This system also provides highly reproducible detection with a standard error of 0.005 nA for the 150 pM target DNA concentration and a signal to noise ratio of 4. When comparing these results, to the sensor detection of mastitis on a bare electrode, a significant increase of the Faradaic current from nanoamps to micro amps is exhibited.

The chemically synthesised PANI after AuNP amplification was investigated to report the enhancement of the analytical performance and sensitivity of the sensor. The sensitivity was evaluated in Figure 4.22 as the slope from the linear portion (150 pM to 1 μ M) of the semi-logarithmic concentration versus the maximum average current response of the PANI-Au nanocomposite (\blacksquare). Significantly, after AuNP modification, a greater sensitivity in current response (slope of $6.8 \mu\text{A}^{-1}$) was observed when compared to the current response in the absence of AuNP (slope of $0.67 \mu\text{A}^{-1}$). The dynamic linear calibration range for the PANI-AuNP is 1 nM and 100 nM with a LOD of 0.17 pM and a correlation coefficient of 0.9986.

The net signal gain produced by this approach is significantly enhanced. For example, a 7.2 fold increase in current for target DNA at a concentration of 1 μM was observed after AuNP formation. In the presence of AuNPs, the overall sensitivity of the electrode response of *S. aureus* was amplified by 10 fold with increasing concentrations of target DNA hybridised when compared to the PANI modified electrode. The standard error for the 150 pM concentration of target DNA was 0.01 with a S/N ratio of 11.

This PANI - AuNP nanostructured surfaces showed a greater analytical performance than the unmodified gold electrode. Significantly, the sensitivity of the DNA detection is approximately 136 fold greater for the PANI-AuNP (slope of $6.8 \mu\text{A}^{-1}$) modified electrodes compared to the bare electrode surface (slope of $0.05 \mu\text{A}^{-1}$). The enhancement in signal was attributed to the improved condition for effective hybridisation between the capture DNA and the target as a result of the surface modification. Overall, for each polymerisation process of PANI (electrochemical, vapour or chemical oxidation), the detection of target DNA is analogous for all 3 processes, resulting in a respectable differential current without the presence of any nanoparticle enhancement. When having the option of incorporating a polymer and AuNP into your biosensor, a larger surface area is formed with a conductive polymer. Both of these materials allow for more hybridisation of DNA strands, demonstrating a simple rapid and extremely sensitive method for the detection of DNA molecules. The result also illustrated that the electrochemical synthesis of PANI method has a wide range detection of DNA from 1.12 fM to 1 μM . However, comparing the current responses reported from the chemical synthesis to the other calibration plots, a 53 % and 68 % decrease is reported in the sensitivity (slope of $6.81 \mu\text{A}^{-1}$) of the electrochemical and vapour phase PANI electrode response, respectively. The other advantage of these synthesized materials was that the aniline could be distilled in bulk and could be stored for months in the freezer. This PANI was deposited in thin films and analysis of such films demonstrated that materials based on this method are best suited for biosensor applications as the results clearly revealed that the PANI-AuNPs platform was sensitive to target DNA concentration and increased with the increase of target DNA concentration. Table 4.6 lists the average differential current response for the

chemically synthesized PANI before and after AuNP electrodeposition on a gold disc electrode at various concentrations of *S. aureus* DNA.

Table 4.6 Average current response of chemically synthesized PANI with and without AuNPs at different concentrations of target DNA.

Electrode Modification	Concentration of <i>S. aureus</i> (M)	Average current response ($\Delta i / \mu\text{A}$)	Standard deviation (n = 2)	Standard error
Bare Electrode	1.50E-10	0.03	0.06	0.04
	1.00E-09	0.05	0.02	0.01
	1.00E-08	0.09	0.01	0.01
	1.00E-07	0.13	0.01	0.01
	1.00E-06	0.20	0.01	0.01
Chemically synthesized PANI	1.50E-10	1.03	0.01	0.01
	1.00E-09	1.42	0.04	0.03
	1.00E-08	1.79	0.01	0.01
	1.00E-07	2.53	0.21	0.14
	1.00E-06	3.72	0.05	0.03
Chemically synthesized PANI with AuNPs	1.50E-10	3.39	0.01	0.01
	1.00E-09	5.49	0.02	0.01
	1.00E-08	12.38	0.06	0.04
	1.00E-07	23.23	2.11	1.49
	1.00E-06	27.26	0.20	0.14

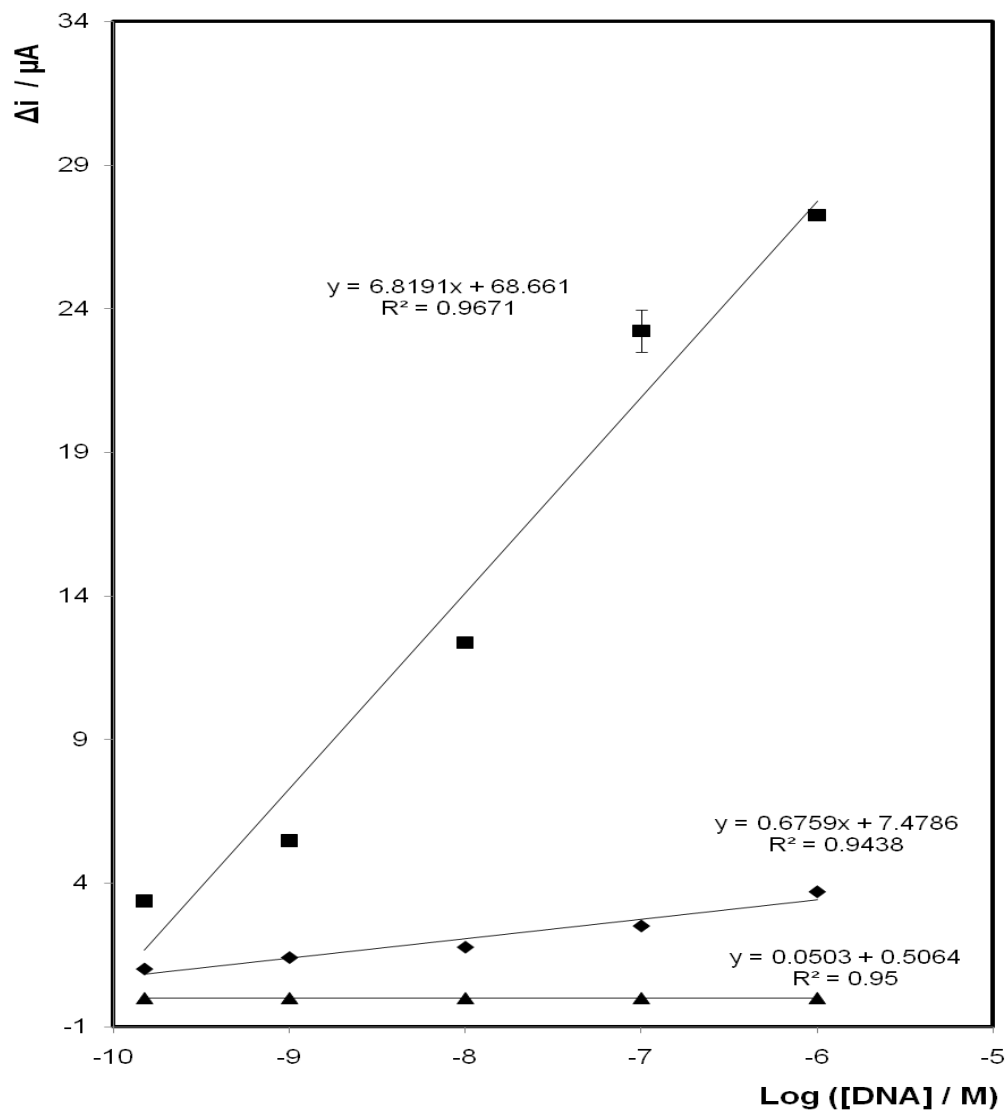


Figure 4.22 Electrochemical detection of sequence-specific *S. aureus* pathogen DNA concentration on a bare electrode (▲), chemically synthesised PANI (◆) and chemically synthesised PANI after AuNP deposition (■). Capture strand, target strand and probe HRP strand (Denhardt's buffer) were cycled in phosphate buffer saline and 0.1 M KCl and a concentration of 1.81 mM hydroquinone. Y axis is the difference in signal before and after addition of H₂O₂ (Δi). Potential applied -0.40 V. Where error bars are not visible, they are smaller than or comparable to, the size of the symbols and range from 0.5% to 5.8 %.

4.2.8.3.1 *Chemically polymerised emeraldine base nanofibres.*

Polyaniline (PANI) nanofibres have been chemically synthesised again and have been deposited on gold electrodes. However, the PANI-NFs have been modified with chemically grown gold nanoparticles instead of electrodeposited gold nanoparticles to give an alternative nanocomposite material (PANI-NF-AuNP).

Figure 4.23 (♦) shows the semi-log concentration vs. Δi calibration curves for the pathogen DNA detection using a bare gold electrode as well as films of both PANI-NF and PANI-NF-AuNP where the concentration of sequence-specific DNA of *S. aureus* is systematically varied from 150 pM to 1 μ M. Significantly, all three approaches generate a measurable response even for pathogen DNA concentrations as low as 150 pM without the need for molecular amplification like PCR or NASBA. The observation that Δi increases linearly with $\log [\text{DNA}]$ rather than $[\text{DNA}]$ suggests that the current response is influenced by the concentration of the HRP co-reactant, H_2O_2 , as well as the DNA concentration and that the performance may be further enhanced by increasing the concentration of the co-reactant. Significantly, the sensitivity of the DNA detection is approximately 40 fold greater for the PANI-NF (slope of $1.84 \mu\text{A}^{-1}$) modified electrodes compared to the bare electrode surface (slope of $0.05 \mu\text{A}^{-1}$) with an improved LOD of 8.51 pM.

The sensitivity of the PANI-NF-AuNP (Figure 4.23, ■) film is approximately twice that observed in the absence of gold nanoparticles and the absolute currents measured at each DNA concentration are significantly higher due to the increased concentration of DNA capture strands due to the presence of the gold nanoparticles. The limit of detection had improved to 2 pM with a increased sensitivity (slope of $3.72 \mu\text{A}^{-1}$) compared to the PANI-NF alone. However, the key issue is the signal-to-noise ratio (S/N). In all cases the reproducibility is excellent even at low DNA concentrations, e.g., at 150 pM the signal-to-noise ratio is at least ten.

The chemically grown nanoparticles did not increase the electrochemical activity of the chemically modified PANI sensor. A 52 % decrease in analytical performance is observed for the electrode response of this PANI-NF-AuNP when compared to the response found for the chemically grown PANI-AuNPs in Section 4.2.3.1. Hence, it is confirmed that for the oxidation of PANI at electrode, the method of synthesis and nanoparticle deposition may alter the electrochemical signal. Table 4.7 lists the average current response for the chemically synthesized PANI before and after the chemical synthesis of AuNP on a gold disc electrode at various concentrations of S.aureus DNA.

Table 4.7 Average current response of chemically synthesized PANI with and without AuNPs at different concentrations of target DNA.

Electrode Modification	Concentration of S. aureus (M)	Average current response ($\Delta i / \mu\text{A}$)	Standard deviation (n = 2)	Standard error
Bare Electrode	1.50E-10	0.03	0.06	0.04
	1.00E-09	0.05	0.02	0.01
	1.00E-08	0.09	0.01	0.01
	1.00E-07	0.13	0.01	0.01
	1.00E-06	0.20	0.01	0.01
Chemically synthesized PANI	1.50E-10	0.66	0.09	0.07
	1.00E-09	2.66	0.05	0.03
	1.00E-08	3.63	0.08	0.06
	1.00E-07	4.81	0.12	0.09
	1.00E-06	8.44	0.04	0.03
Chemically synthesized PANI with AuNPs	1.50E-10	1.84	0.02	0.02
	1.00E-09	4.25	0.07	0.05
	1.00E-08	7.85	0.07	0.05
	1.00E-07	9.25	0.16	0.11
	1.00E-06	17.23	0.88	0.62

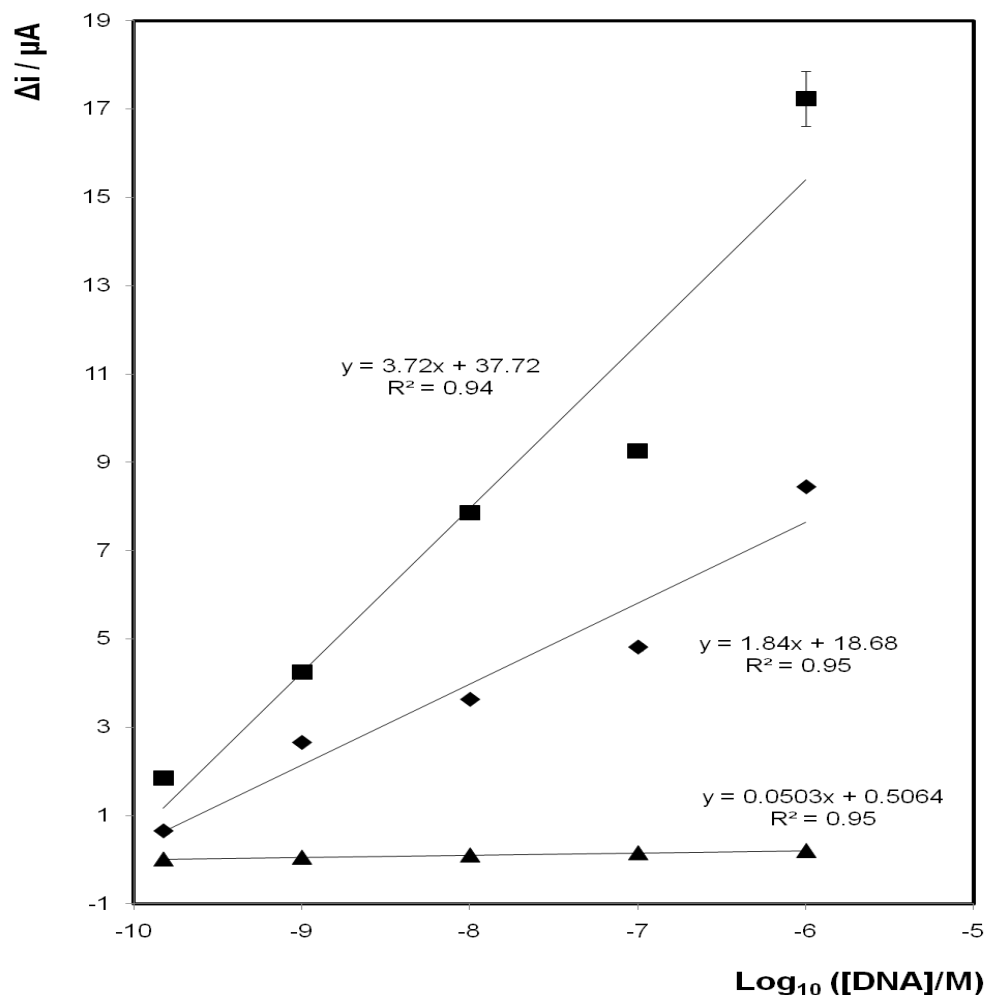


Figure 4.23 Electrochemical detection of sequence-specific *S. aureus* pathogen DNA concentration on a bare electrode (\blacktriangle), chemically synthesised PANI (\blacklozenge) and chemically synthesised PANI-NF AuNP nanocomposite (\blacksquare). Capture strand, target strand and probe HRP strand (Denhardt's buffer) were cycled in phosphate buffer saline and 0.1 M KCl and a concentration of 1.81 mM hydroquinone. Y axis is the difference in signal before and after addition of H_2O_2 (Δi). Potential applied -0.40 V. Where error bars are not visible, they are smaller than or comparable to, the size of the symbols and range from 1.6 % to 9.5 %.

4.3 CONCLUSION

More and more researchers are working in pursuit of bringing nano scale technology into mainstream. The research carried out here is a small step towards a similar goal. Two kinds of nanostructures are developed and their optical properties investigated. One of these is nanofibers processed from a polymer known as polyaniline (PANI). The second type of nano-structure developed and investigated, is gold nanoparticles. The focus of this study is to investigate the different PANI-AuNP optical and conductive properties under different conditions of doping environments, polymerisation conditions and gold nanoparticles modification. Characterisation included electrochemically and spectroscopic characterisation (CV, Raman and UV - vis) as well as EPR before and after addition of the AuNP.

The voltammetry in acidic electrolyte clearly demonstrates that the area available for immobilising DNA capture strands is significantly higher for the PANI-AuNP nanocomposite. However, given the focus on enzyme based electrocatalysis so as to amplify the response obtained for the capture of a small number of DNA copies, the conductivity of the composite is as important as the available gold area. The addition of the AuNP showed by adhering itself to the surface the DNA sulphur groups had a better chance of hybridising itself to the functionalised surface of the electrode. Quite simply, the best detection was achieved by the electrochemical and chemical polymerisation of PANI. The vapour polymerisation gave lesser detection results and this can be due to the fact that perhaps it has lost some of its conductivity in the presence of gold. Another reason for this is the fact that vapour polymerisation is not stable enough to stay onto the electrode after the gold deposition takes place and perhaps some of the polymer desorbed. This can lead to loss in surface area and therefore loss in capture DNA hybridisation.

Overall, by using electrochemical and chemical polymerisation of the polymer PANI, the sensitivity has been increased for an already well established Elisa assay. Vapour polymerisation which is not typically used in research, showed a somewhat great selectivity towards the mastitis sensor. PANI films prepared

by vapour phase polymerisation showed somewhat good biosensing properties with nanoscale thickness films of PANI.

Raman spectroscopic was utilised, to examine how the DNA and capture molecules are aligned on the PANI. The Raman data clearly presented the transition between the conducting states to a reduced state when in the presence of gold chloride. Electron paramagnetic resonance, EPR, is a very powerful method in the investigation of the fundamental conduction mechanisms of conducting polymers and can quickly provide information regarding the nature of the radical and their relative concentration. EPR was used to investigate PANI in its conductive state. By looking at the movement of electrons and the interpretation of the peaks after the deposition of gold, it can be concluded that, even though some conductivity is lost, the gold is dispersed over the whole polymer and has interacted fully with the PANI. This correlates with our detection readouts that the increase in Δi is due to the presence of AuNP incorporated within the PANI film.

Rapid, specific detection of nucleic acid sequences has been applied in both clinical and research diagnostic applications for a number of years.⁸⁰⁻⁸² A wide range of electronic DNA detection schemes have been described to date,^{83,84} the best of which can achieve limits of detection ranging from picomolar to femtomolar. Although these detection limits of the above-described sensor technologies are impressive, achieving them requires the addition of label-containing secondary probes and, typically, complicated, multicomponent deposition/amplification steps. Here, in contrast, we report a platform that couples the femtomolar detection limits of sequence specific DNA with the single-step polymerisation of the PANI sensing platform. This work demonstrates the use of a conducting polymer PANI for DNA sequence detection using conventional electrochemical instrumentation. The combination of PANI and AuNPs provides a powerful yet relatively simple method of detecting specific DNA sequences. Within this research, a full electrochemical investigation was performed for the polymerised PANI, LODs, S/N and examination of all possible interferences. Stability of the PANI nanofibres at the potentials where the majority of samples are detected was

also assessed, along with its reproducibility. These sensors were shown to have a wide dynamic range, excellent ability to discriminate DNA mismatches and a significantly lower limit of detection compared to that achieved using either material alone. From these results it has been proven it is possible to design a more sensitive sensor, which will have numerous properties allowing for its miniaturisation.

4.4 REFERENCES

1. Niaura, G.; Mazeikiene, R.; Malinauskas, A. *Synthetic Metals*, **2004**, *145*, 105-112.
2. Li, N. B.; Zhang, S. T.; Ding, P. D. *Chinese Chemical Letters*. **2000**, *11*, 681-684.
3. Mohilner, D. M.; Adams, R. N.; Argersinger, W. J., Jr *Journal of the American Chemical Society*. **1962**, *84*, 3618-3622.
4. Stilwell, D. E.; Park, S. M. *Journal of the Electrochemical Society* . **1988**, *135*, 2491-2496.
5. Takahashi, K.; Nakamura, K.; Yamaguchi, T.; Komura, T.; Ito, S.; Aizawa, R.; Murata, K. *Synthetic Metals*, **2002**, *128*, 27-33.
6. Chen, S. A.; Fang, W. G. *Macromolecules* **1991**, *24*, 1242-1248.
7. Sapurina, I.; Stejskal, J. *Polymer International* . **2008**, *57*, 1295-1325.
8. Pournaghi-Azar, M. H.; Habibi, B. A. *Journal of Solid State Electrochemistry* **2007**, *11*, 505-513.
9. Wallace, G. G.; Spinks, G. M.; Kane-Maguire, L. A. P. **2002**, , 224.
10. Sarac, A. S.; Ates, M.; Kilic, B. *International Journal of Electrochemical Science* **2008**, *3*, 777-786.
11. Innis, P. C.; Mazurkiewicz, J.; Nguyen, T.; Wallace, G. G.; MacFarlane, D. *Current Applied Physics* **2004**, *4*, 389-393.
12. Macdiarmid, A. G.; Chiang, J. C.; Huang, W. S.; Humphrey, B. D.; Somasiri, N. L. D. *Molecular Crystals and Liquid Crystals* **1985**, *125*, 309-318.
13. Huang, W. S.; Humphrey, B. D.; Macdiarmid, A. G. *Journal of the Chemical Society-Faraday Transactions i* **1986**, *82*, 2385-&.

14. Molina, J.; del Río, A. I.; Bonastre, J.; Cases, F. *European Polymer Journal* **2009**, *45*, 1302-1315.
15. Huang, H.; Feng, X.; Zhu, J. *Nanotechnology* **2008**, *19*, 145607.
16. Turyan, I.; Mandler, D. *Journal of the American Chemical Society*. **1998**, *120*, 10733-10742.
17. Sharma, M.; Kaushik, D.; Singh, R. R.; Pandey, R. K. *Journal of Materials Science-Materials in Electronics* **2006**, *17*, 537-541.
18. Sheridan, E.; Hjelm, J.; Forster, R. J. *Journal of Electroanalytical Chemistry* **2007**, *608*, 1-7.
19. Trasatti, S.; Petrii, O. A. *Pure and Applied Chemistry* **1991**, *63*, 711-734.
20. Zhang, H.; Wang, X.; Li, J.; Wang, F. *Synthetic Metals*. **2009**, *159*, 1508-1511.
21. Huang, J.; Kaner, R. B. *Journal of the American Chemical Society*. **2004**, *126*, 851-855.
22. Wang, Y.; Liu, Z. M.; Han, B. X.; Sun, Z. Y.; Huang, Y.; Yang, G. Y. *Langmuir* **2005**, *21*, 833-836.
23. Xia, Y. N.; Wiesinger, J. M.; Macdiarmid, A. G.; Epstein, A. J. *Chemistry of Materials* **1995**, *7*, 443-445.
24. Wei, Y.; Focke, W. W.; Wnek, G. E.; Ray, A.; Macdiarmid, A. G. *Journal of physical chemistry*. **1989**, *93*, 495-499.
25. Klavetter, F. L.; Cao, Y. *Synthetic Metals* **1993**, *55*, 989-994.
26. Huang, W. S.; Macdiarmid, A. G. *Polymer* **1993**, *34*, 1833-1845.
27. Egan, V.; Bernstein, R.; Hohmann, L.; Tran, T.; Kaner, R. B. *Chemical Communications* **2001**, , 801-802.
28. Mccall, R. P.; Ginder, J. M.; Leng, J. M.; Ye, H. J.; Manohar, S. K.; Masters, J. G.; Asturias, G. E.; Macdiarmid, A. G.; Epstein, A. J. *Physical Review B* **1990**, *41*, 5202-5213.

29. Albuquerque, J. E.; Mattoso, L. H. C.; Balogh, D. T.; Faria, R. M.; Masters, J. G.; MacDiarmid, A. G. *Synthetic Metals*. **2000**, *113*, 19-22.
30. Macdiarmid, A. G.; Epstein, A. J. *Synthetic Metals* **1995**, *69*, 85-92.
31. Mukherjee, P.; Nandi, A. K. *Journal of Colloid and Interface Science* . **2011**, *356*, 145-150.
32. Kim, J.; Lee, J.; Kwon, S. *Synthetic Metals*. **2007**, *157*, 336-342.
33. Yin, W.; Ruckenstein, E. *Synthetic Metals*. **2000**, *108*, 39-46.
34. Kumar, S.; Aaron, J.; Sokolov, K. *Nature Protocols* **2008**, *3*, 314-320.
35. Lange, U.; Ivanov, S.; Lyutov, V.; Tsakova, V.; Mirsky, V. M. *Journal of Solid State Electrochemistry* **2010**, *14*, 1261-1268.
36. Wei, Y.; Hsueh, K. F.; Jang, G. W. *Macromolecules* **1994**, *27*, 518-525.
37. Ahn, S.; Hupp, J. T. *Bulletin of the Korean Chemical Society* **2006**, *27*, 1497-1499.
38. Zhang, K.; Jing, X. *Polymers for Advanced Technologies*. **2009**, *20*, 689-695.
39. Chen, J.; Winther-Jensen, B.; Pornputtkul, Y.; West, K.; Kane-Maquire, L.; Wallace, G. G. *Electrochemical and Solid State Letters* **2006**, *9*, C9-C11.
40. Tseng, R. J.; Huang, J.; Ouyang, J.; Kaner, R. B.; Yang, Y. *Nano Letters* **2005**, *5*, 1077-1080.
41. Dauginet-De Pra, L.; Demoustier-Champagne, S. *Thin Solid Films* **2005**, *479*, 321-328.
42. Lapkowski, M.; Berrada, K.; Quillard, S.; Louarn, G.; Lefrant, S.; Pron, A. *Macromolecules* **1995**, *28*, 1233-1238.
43. Boyer, M.; Quillard, S.; Louarn, G.; Lefrant, S.; Rebourt, E.; Monkman, A. P. *Synthetic Metals* **1997**, *84*, 787-788.

44. Quillard, S.; Louarn, G.; Buisson, J. P.; Boyer, M.; Lapkowski, M.; Pron, A.; Lefrant, S. *Synthetic Metals*, **1997**, *84*, 805-806.
45. de Torresi, S. I. C.; Maranhao, S. L. D.; Torresi, R. M. *Synthetic Metals*, **1999**, *101*, 797-797.
46. Louarn, G.; Lapkowski, M.; Quillard, S.; Pron, A.; Buisson, J. P.; Lefrant, S. *Journal of physical chemistry*. **1996**, *100*, 6998-7006.
47. Cintra, E. P.; de Torresi, S. I. C. *Journal of Electroanalytical Chemistry***2002**, *518*, 33-40.
48. Tseng, R. J.; Baker, C. O.; Shedd, B.; Huang, J.; Kaner, R. B.; Ouyang, J.; Yang, Y. *Applied Physics Letters*. **2007**, *90*, 053101.
49. Furukawa, Y. *Journal of physical chemistry*. **1996**, *100*, 15644-15653.
50. Kim, J.; Lee, J.; Kwon, S. *Synthetic Metals* **2007**, *157*, 336-342.
51. Mažeikienė, R.; Niaura, G.; Malinauskas, A. *Polymer Degradation and Stability* **2008**, *93*, 1742-1746.
52. Dauginet-De Pra, L.; Demoustier-Champagne, S. *Thin Solid Films* **2005**, *479*, 321-328.
53. Mažeikienė, R.; Niaura, G.; Malinauskas, A. *Electrochemistry Communications* **2005**, *7*, 1021-1026.
54. Saheb, A.; Smith, J. A.; Josowicz, M.; Janata, J.; Baer, D. R.; Engelhard, M. H. *Journal of Electroanalytical Chemistry* **2008**, *621*, 238-244.
55. Mažeikienė, R.; Niaura, G.; Malinauskas, A. *Synthetic Metals*. **2010**, *160*, 1060-1064.
56. Liu, Y. *Journal of Electroanalytical Chemistry***2004**, *571*, 255-264.
57. Pratt, F. L.; Blundell, S. J.; Hayes, W.; Nagamine, K.; Ishida, K.; Monkman, A. P. *Physical Review Letters*. **1997**, *79*, 2855-2858.
58. Salafsky, J. S. *Physical Review B* **1999**, *59*, 10885-10894.

59. Chakrabarti, S.; Das, B.; Banerji, P.; Banerjee, D.; Bhattacharya, R. *Physical Review B* **1999**, *60*, 7691-7694.
60. Chipara, M.; Hui, D.; Notingher, P. V.; Chipara, M. D.; Lau, K. T.; Sankar, J.; Panaitescu, D. *Composites Part B: Engineering* **2003**, *34*, 637-645.
61. Dennany, L.; Innis, P. C.; Wallace, G. G.; Forster, R. J. *Journal of Physical Chemistry B* **2008**, *112*, 12907-12912.
62. Kahol, P. K. *Solid State Communications*. **2000**, *117*, 37-39.
63. Yang, S. M.; Li, C. P. *Synthetic Metals*. **1993**, *55*, 636-641.
64. Lippe, J.; Holze, R. *Synthetic Metals*. **1991**, *43*, 2927-2930.
65. van Hal, P. A.; Christiaans, M. P. T.; Wienk, M. M.; Kroon, J. M.; Janssen, R. A. J. *Journal of Physical Chemistry B* **1999**, *103*, 4352-4359.
66. Sakharov, I. Y.; Ouporov, I. V.; Vorobiev, A. K.; Roig, M. G.; Pletjushkina, O. Y. *Synthetic Metals*. **2004**, *142*, 127-135.
67. Kuroda, S.; Marumoto, K.; Sakanaka, T.; Takeuchi, N.; Shimoi, Y.; Abe, S.; Kokubo, H.; Yamamoto, T. *Chemical Physics Letters* **2007**, *435*, 273-277.
68. Kuroda, S.; Marumoto, K.; Shimoi, Y.; Abe, S. *Thin Solid Films* **2001**, *393*, 304-309.
69. Kuroda, S.; Marumoto, K.; Ito, H.; Greenham, N. C.; Friend, R. H.; Shimoi, Y.; Abe, S. *Chemical Physics Letters* **2000**, *325*, 183-188.
70. McCormac, T.; Cassidy, J. F.; Crowley, K.; Trouillet, L.; Lafolet, F.; Guillerez, S. *Electrochimica Acta* **2006**, *51*, 3484-3488.
71. Mentus, S.; Ciric-Marjanovic, G.; Trchova, M.; Stejskal, J. *Nanotechnology* **2009**, *20*, 245601.
72. Pereira da Silva, J. E.; De Faria, D. L. A.; Cordoba de Torresi, S. I.; Temperini, M. L. A. *Macromolecules* **2000**, *33*, 3077-3083.

73. Pereira da Silva, J. E.; Temperini, M. L. A.; Córdoba de Torresi, S. I. *Electrochimica Acta* **1999**, *44*, 1887-1891.
74. Izumi, C. M. S.; Constantino, V. R. L.; Ferreira, A. M. C.; Temperini, M. L. A. *Synthetic Metals*. **2006**, *156*, 654-663.
75. Zhuang, L.; Zhou, Q.; Lu, J. *Journal of Electroanalytical Chemistry*. **2000**, *493*, 135-140.
76. Golczak, S.; Kanciurzevska, A.; Langer, J. J.; Fahlman, M. *Polymer Degradation and Stability*. **2009**, *94*, 350-354.
77. Chen, S. A.; Hwang, G. W. *Macromolecules* **1996**, *29*, 3950-3955.
78. Lafolet, F.; Genoud, F.; Divisia-Blohorn, B.; Aronica, C.; Guillerez, S. *Journal of Physical Chemistry B* **2005**, *109*, 12755-12761.
79. Zotti, G.; Schiavon, G.; Zecchin, S.; Berlin, A.; Pagani, G.; Canavesi, A. *Synthetic Metals*. **1996**, *76*, 255-258.
80. He, P.; Xu, Y.; Fang, Y. *Analytical Letters*. **2005**, *38*, 2597-2623.
81. Xu, K.; Huang, J.; Ye, Z.; Ying, Y.; Li, Y. *Sensors* **2009**, *9*, 5534-5557.
82. Chen, X.; Su, B.; Song, X.; Chen, Q.; Chen, X.; Wang, X. *Trac-Trends in Analytical Chemistry* **2011**, *30*, 665-676.
83. Xia, L.; Wei, Z.; Wan, M. *Journal of Colloid and Interface Science*. **2010**, *341*, 1-11.
84. Fernando Sérgio Rodrigues Ribeiro, T. *Analytica Chimica Acta* **2011**, *687*, 28-42.



CHAPTER 5

NANOPARTICLE FUNCTIONALISED PEDOT NANOFIBRES FOR DNA SENSOR DEVELOPMENT

5.1 INTRODUCTION

Chemical methods have been explored to modify the thiophene monomer by substitution of functional groups at the C₃ or β position.¹ Poly (3, 4-ethylenedioxythiophene), which is often abbreviated as PEDT or PEDOT, is one of the best studied p-conjugated polymers. It was first discovered in **1991** after being initially chemically prepared as a thin film coating for antistatic plastics.² The additions of functional groups have improved the processibility somewhat by lowering the oxidation potential and making a more soluble material. PEDOT was found to be almost transparent in thin, oxidized films shows very high stability in the oxidized state.³⁻⁷

Conducting polymer and metal nanoparticle composites (nanocomposites) have received much attention recently due to their potential applications in electrochemical sensors.⁸ A variety of methods for the preparation of these composites have been described, including electrochemical deposition of nanoparticles onto electrodes previously coated with a conducting polymer.⁸ Researchers⁹ have successfully incorporated gold nanoparticles (AuNP) within the PEDOT polymer for a variety of biosensors. PEDOT can be synthesised in a number of ways such as direct chemical oxidation, electrochemical oxidation and vapour oxidation. The monomer 3,4 ethylenedioxythiophene (EDOT) has made this polymer very desirable as the C₃ and C₄ positions are blocked and therefore avoid structural and electronic defects which is a regular hindrance found in PTh and PPY.⁹

The use of PEDOT functionalised with gold nanoparticles (AuNPs) for the highly sensitive detection of DNA hybridization is reported in this chapter. The performance as well as the characterisation of this conducting polymer and the enhancement of AuNP will be discussed for three types of PEDOT syntheses carried out. The conducting polymer was synthesised in the presence of different inorganic and organic acids of different concentration, using chemical and vapour oxidative polymerisation and electrochemical techniques. Scanning electron microscope studies are used to show the formation of

polymer clusters of 30-40 nm diameters on the electrode surface. The chapter will highlight a system of high stability, as well as, proof of the enhancement of the optical and electrical properties of the polymer.¹⁰

5.2 RESULTS AND DISCUSSION

5.2.1 *Potentiodynamic polymerisation of PEDOT*

Electrochemical polymerisation of the electron rich EDOT monomer was used. A sky blue doped PEDOT film at the anode was the result of the electrochemical polymerisation. The main features of the voltammogram illustrated in Figure 5.2, show the anodic and cathodic scan of the polymers prepared potentiostatically at 1.1 V vs. Ag/AgCl. For the anodic scan a small peak at -0.55 V is observed. After this two oxidation peaks are resolved, the principal peak is found at 0.5 V and a lower intensity peak at 0.9 V. A plateau is then established which extends to a potential of 1.3 V which confirms polymerisation of the monomer.

In agreement with literature¹¹ values, the voltammogram also illustrates a broad reduction peak at -0.1 V and another peak found at -0.6 V. During the polymerisation process, the polymer accumulates on the electrode and the current increases for both the oxidation and reduction. An increase in the current magnitude with each and every cycle is a clear indication of the polymerisation of PEDOT at the electrode. A decrease in conductivity of a system is often indicated by a decrease in the magnitude of the current between successive scans, which is not observed in this system. This however can be avoided by simply expanding the potential window during each cycle to allow for a greater oxidation potential. The oxidative doping which increases the electronic conductivity can be confirmed in spectroelectrochemical experiments discussed later in this chapter.

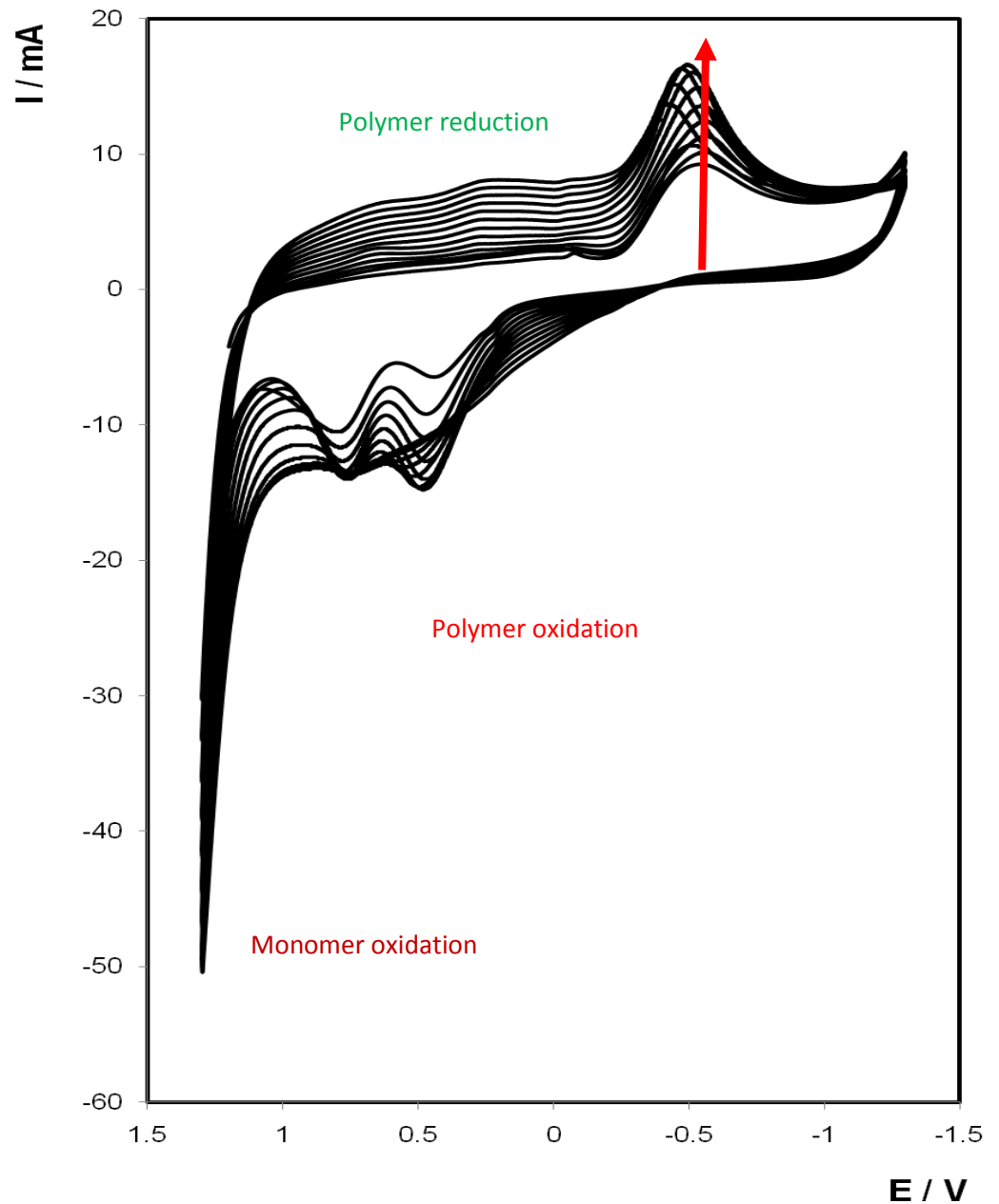


Figure 5.2 Cyclic voltammogram recorded during the potentiodynamic growth of PEDOT / LiClO_4 on a 2 mm diameter Au disc electrode. Electropolymerisation was carried out using a solution of 50 mM EDOT in 0.1 M LiClO_4 as supporting electrolyte. The potential was swept from -1.5 V to 1.5 V vs. Ag / AgCl, 25 cycles at 100 mVs^{-1} .

5.2.2 Potentiostatic polymerisation of PEDOT

Preliminary experiments showed that PEDOT films could be grown on Au disc electrodes potentiodynamically by sweeping the potential from -0.5 V to 1 V at a scan rate of 100 mVs^{-1} . The oxidation potential of the monomer was found from the sweeping potential of the CV and it was found that a suitable potential for potentiostatic growth of polymer was found at approximately 0.5 V. This potential is sufficient for the monomer oxidation and should not lead to over oxidation of the polymer.

The initial stage of polymerization of PEDOT can be readily studied using current–time transients. The polymerization was carried out under potentiostatic conditions at room temperature using a fixed potential of 0.5 V. The constant potential was applied on the working electrode, and the charge passed was measured as a function of time, as shown in Figure 5.3. The initial spike of current corresponds to double layer charging, a transient diffusion process prior to a steady-state on a gold disc electrode and rapid nucleation of the polymer.¹² Thereafter, the current slowly increases corresponding to the formation of PEDOT nuclei followed by the growth of the polymer where current did not vary with time. At this applied potential of the monomer generates an oxidised monomer species which is available for coupling on the electrode surface. The monomer species oxidises and reacts while more monomer diffuses toward the electrode from the bulk solution of the electrolyte.¹³

For spectroscopic studies, the current increases over 120 s on the ITO glass until it reaches a quasi-plateau and a blue polymer film could be easily seen. Such behaviour may result from a three-dimensional nucleation.¹⁴ For all PEDOT studies with DNA hybridisation, electrochemical polymerisation was carried out by using a constant potential at 60 s when using gold disc electrodes. The maximum current density value achieved in the polymerisation before it was stopped was 0.5 mA/cm^{-2} . The growth of PEDOT films was allowed to continue for 60 s until a total charge of 1.4 Ccm^{-2} was reached. The amount of polymer coated on the electrode site was controlled by the total

charge passed during polymerization. Electrochemical polymerisation creates positive charges along the backbone of the PEDOT and causes interactions with the counter ions with the working electrode. This incorporation of charge is equivalent to electrochemical doping and therefore allows the PEDOT to be deposited in a conducting manner. This method has the advantages of its simplicity and the absence of over oxidation of the polymer.

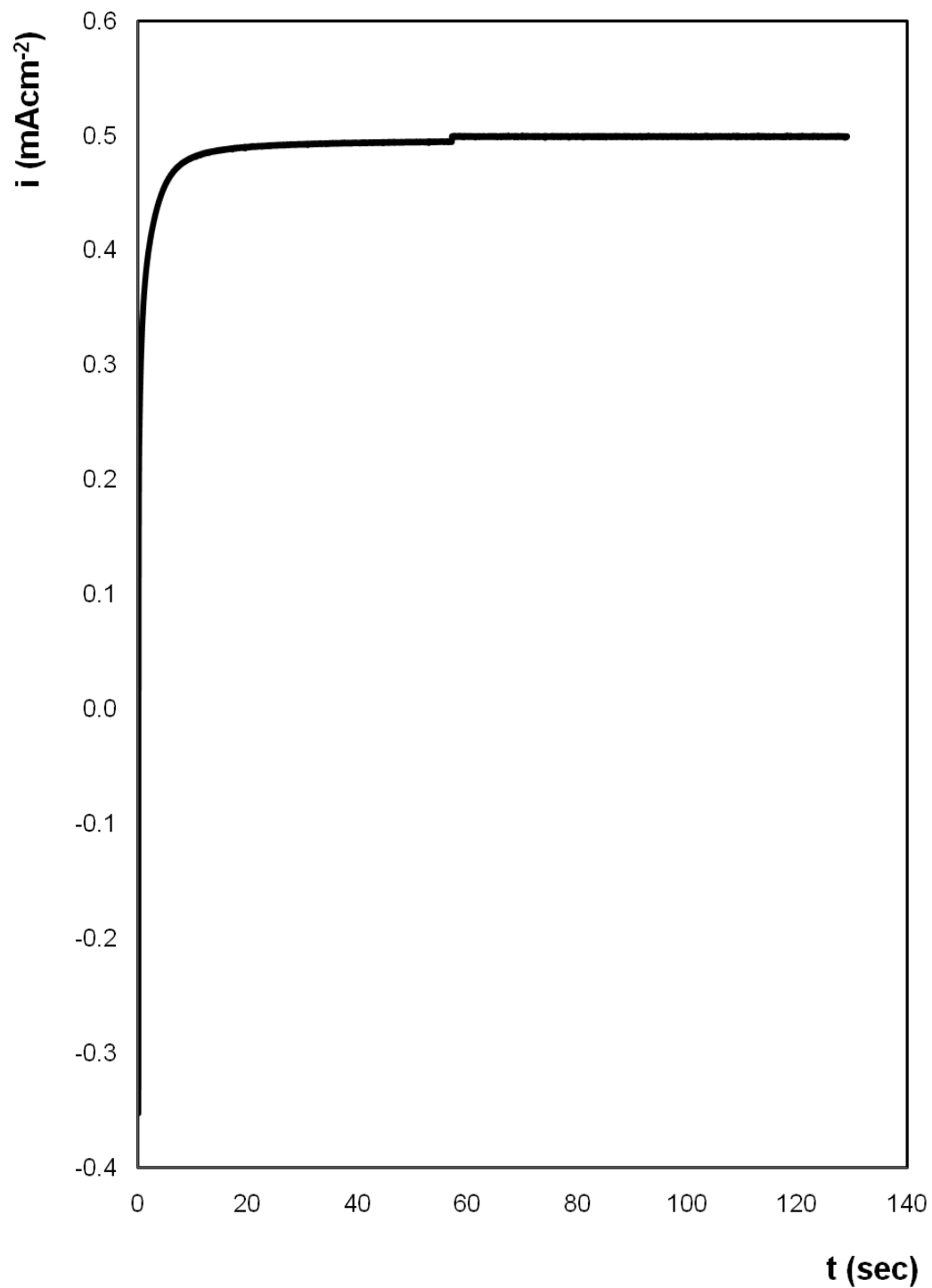


Figure 5.3 Potentiostatic electrodeposition of PEDOT onto a 2 mm diameter Au disc electrode from a solution containing 50 mM EDOT and 0.1 M LiClO₄ at an applied potential of +0.5 V for 120 s.

5.2.3 Voltammetric characterisation of PEDOT and PEDOT-AuNP

The electrochemical reduction of gold chloride acid (HAuCl_4) in the presence of electropolymerised PEDOT was performed to improve the conductivity of the polymer film and to increase the surface area available for thiolated capture DNA. This is similar to methods previously carried out when carbon black was added to chemically polymerized films to improve their conductivity.¹⁵ In the first stage poly(3,4-ethylenedioxythiophene) (PEDOT) clusters are introduced onto the working electrode surface by in situ oxidative polymerisation. In the second stage, hydrogen tetrachloroaurate is used to transform PEDOT chains to an oxidized state when a negative voltage bias was applied on the working electrode. The reduction of chloroaurate ions induces the formation of gold nanoparticles (AuNPs) predominantly located on the PEDOT surface.

Cyclic voltammetry is used to demonstrate the changes on the electrode surface after the simple and direct synthesis of PEDOT-AuNPs.¹⁵ Cyclic voltammograms of a gold disc electrode modified with gold nanoparticles and self assembled monolayers were recorded in sulphuric acid medium. Figure 5.4 displays cyclic voltammograms for the bare gold disc electrode and the electrochemically prepared PEDOT (bold line) and PEDOT-AuNP (dashed line) modified electrodes when cycled in a 0.1 M H_2SO_4 solution at a scan rate of 100 mVs^{-1}

The response for the bare gold in Figure 5.4 (green line) was a typical diffusion-limited process.¹⁶ The electrodes modified with gold nanoparticles (not shown) exhibited the characteristic gold anodic and cathodic peaks thus confirming the successful modification process.

A voltammogram was recorded after the electropolymerisation of 0.05 M EDOT (black line) solution in LiClO_4 for 2 min on the gold disc electrodes. The presence of the polymer film produced slight shifts of cathodic and anodic peak potentials to less and more positive values, respectively, giving rise to a smaller peak-to-peak separation. Moreover, the peak current increased

notably with respect to that of the bare electrode.¹⁷ An increase of the active gold area from 0.037 cm² for unmodified electrode (roughness factor of 1.2) to 0.067 cm² is seen.

The SEM images discussed later in Section 5.2.4, showed gold nanoparticles that were electrodeposited on the electrode. They were distributed throughout the polymer forming a continuous array of gold nanoparticles on the electrode. Figure 5.4 highlights the voltammetric behaviour of these AuNPs on the PEDOT modified gold electrode surface. The response shows redox peaks were obtained with an increased cathodic and anodic current response compared to the unmodified electrode. This response upon repeated cycles remained unchanged and in that sense they are reversible. Higher peak currents and a smaller peak-to-peak potential separation were observed at the PEDOT-AuNP electrode when compared with the unmodified electrode, which can be attributed to the increased roughness of the gold nanoparticle-modified electrode surface.¹⁷ The use of the electrode modified with gold nanoparticles and PEDOT gave rise to voltammograms with a remarkable further increase in the peak current when compared to the PEDOT sample. The available gold surface area increased by a factor of approximately 4. The increase in surface roughness is thus expected to increase the number of DNA binding sites on the electrode surface thus contributing towards an increase in signal intensity.

Table 5.1 summaries the real surface areas (calculation in Section 2.4.1) determined by cyclic voltammetry for each of the PEDOT synthesis carried out in this chapter. The overall calculated charge under the cathodic peak varies between 14 μCcm^{-2} for the unmodified electrode and up to 50 μCcm^{-2} for the most porous sample obtained after vapour phase polymerisation and gold electrodeposition. These results were obtained after polymer oxidation and gold deposition. Enhancement of the surface area has been provided after the electrochemical, chemical or vapour oxidation of PEDOT. This polymer platform was further enhanced by nanogold to ultimately increase the hybridisation amount of DNA molecules on the electrode surface.

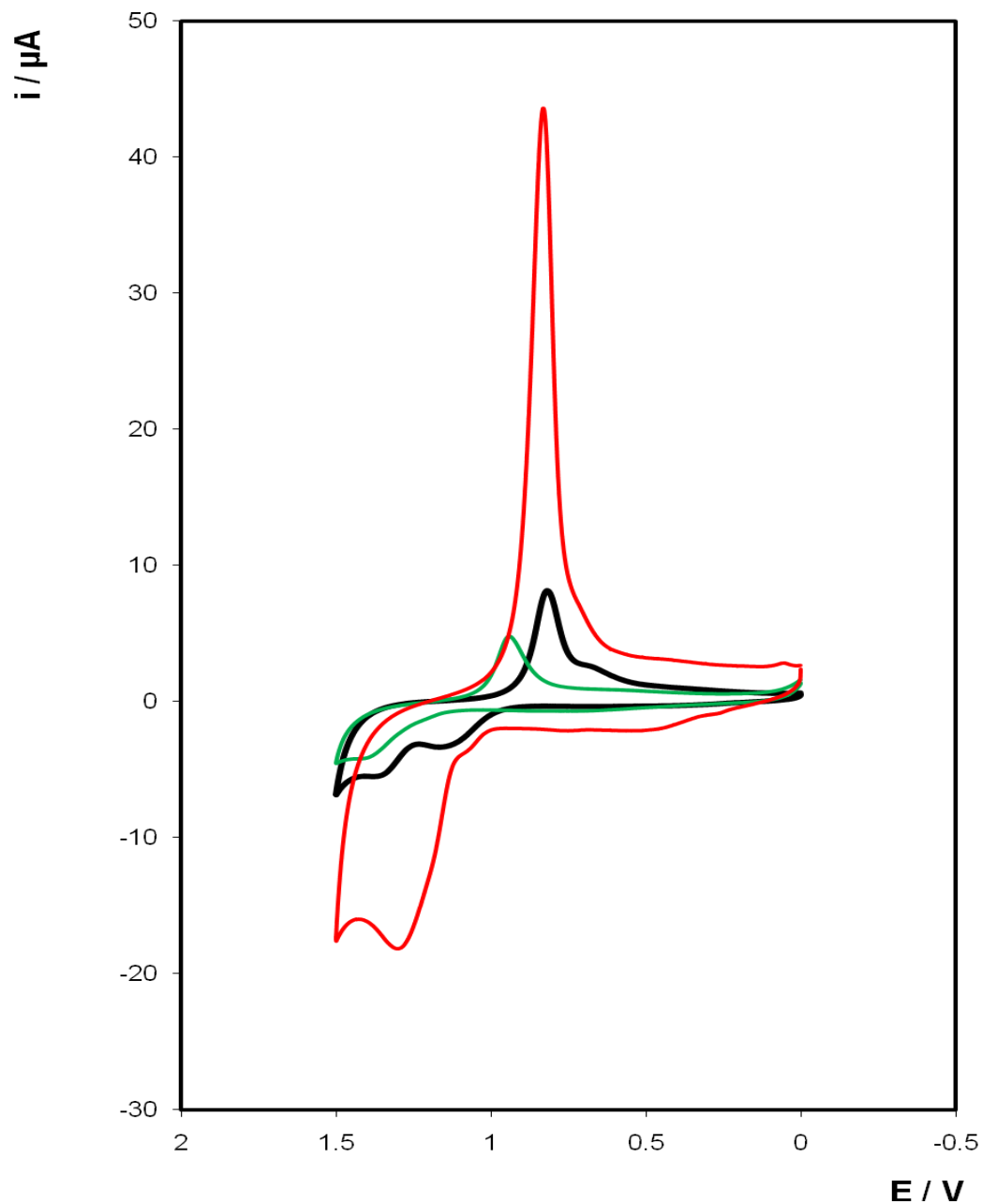


Figure 5.4 Cyclic voltammograms of 2 mm unmodified gold electrodes (Green line), and electrodes modified with PEDOT (Black line) and PEDOT - AuNP (Red line) in 0.1 M H_2SO_4 . The counter electrode was a platinum wire and the reference electrode was Ag/AgCl saturated in KCl. The scan rate is 100 mVs^{-1} .

Table 5.1 Real surface areas and surface roughness factors after polymer and gold nanoparticle deposition, determined by cyclic voltammetry on a 2 mm gold disc electrode. The potential was swept from -1.5 V to 1.0 V vs. Ag / AgCl, 25 cycles at 100 mVs⁻¹.

Electrode Surface	AuNP Deposition Time (Secs)	Charge Q (C cm ⁻²)	Real Surface Area (cm ²) ⁱ	Surface Roughness Factor ⁱⁱ
Bare	-	1.46 x 10 ⁻⁵	0.0374	1.2
AuNP only	20	1.65 x 10 ⁻⁵	0.0423	1.3
	30	1.84 x 10 ⁻⁵	0.0471	1.5
	40	2.55 x 10 ⁻⁵	0.0654	2.1
	50	2.45 x 10 ⁻⁵	0.0628	2.0
Echem PPy	-	2.61 x 10 ⁻⁵	0.0669	2.1
	20	2.71 x 10 ⁻⁵	0.0695	2.2
	30	3.11 x 10 ⁻⁵	0.0798	2.5
	40	3.51 x 10 ⁻⁵	0.0899	2.9
	50	4.04 x 10 ⁻⁵	0.1036	3.3
Vapour PPy	-	1.91 x 10 ⁻⁵	0.0490	1.6
	20	2.58 x 10 ⁻⁵	0.0660	2.1
	30	3.55 x 10 ⁻⁵	0.0911	2.9
	40	4.06 x 10 ⁻⁵	0.1041	3.3
	50	5.02 x 10 ⁻⁵	0.1287	4.1
Chemical PPy	-	1.62 x 10 ⁻⁵	0.0414	1.3
	20	2.03 x 10 ⁻⁵	0.0521	1.7
	30	2.63 x 10 ⁻⁵	0.0674	2.1
	40	3.52 x 10 ⁻⁵	0.0903	2.9
	50	3.83 x 10 ⁻⁵	0.0981	3.1

- i. Calculated as the charge passed during the reduction of the gold oxide monolayer divided by 390 x 10⁻⁶ C cm⁻².
- ii. Calculated as the real surface area divided by the geometrical area (πr^2 , 0.0314 cm²)

5.2.4 Microscopic characterisation of PEDOT and PEDOT-AuNP

The SEM surface morphologies of the electrodeposited PEDOT films are shown in Figure 5.5, where ITO is the electrode material used. In Figure 5.5 (A, scale bar = 50 μM) shows that the film consists of a globular morphology about 1 μm size in diameter without any AuNP modification. As the oxidation is applied over the 2 min; smaller globules of PEDOT about 100 nm have grown on bigger globules due to three-dimensional growth. The conductivity of LiClO_4 films depends on the incorporation of counter-ions into the growing polymer during deposition. PEDOT incorporates anions present in the LiClO_4 medium.¹⁸ The surface morphology of the PEDOT films prepared by a potentiostatic growth showed a porous polymer film as shown in Fig. 5.5. Such a porous structure may be favourable for the high surface area porous counter electrode as the polymer can easily entrap nanoparticles yielding a composite.¹⁹

The image in Figure 5.5 B and C show smaller clusters within the polymer film after the electrochemical deposition of gold nanoparticles (AuNPs). The polymer surface still possesses a globular morphology and it appears that AuNPs have grown on the bigger globules, due to three-dimensional growth. The images show a difference of higher contrast after AuNP deposition and a less clustered alignment. The shapes of the AuNPs are more grain like than globular. Figure 5.5 C, illustrates an expanded section of the image after the formation of PEDOT and the reduction of HAuCl_4 to produce metallic gold nanoparticles.²⁰ The SEM shows that after the gold reduction step, the surface of the PEDOT appears to be coated with nanoparticles clusters with radii between approximately 50 and 120 nm, which seem to be spread over the whole length of the PEDOT. It can be seen that NPs show a broader distribution of grain sizes on the surface of polymer suggesting that gold reduction occurs preferentially on the surface of the PEDOT. Aggregates are well spread and do not concentrate in one region.

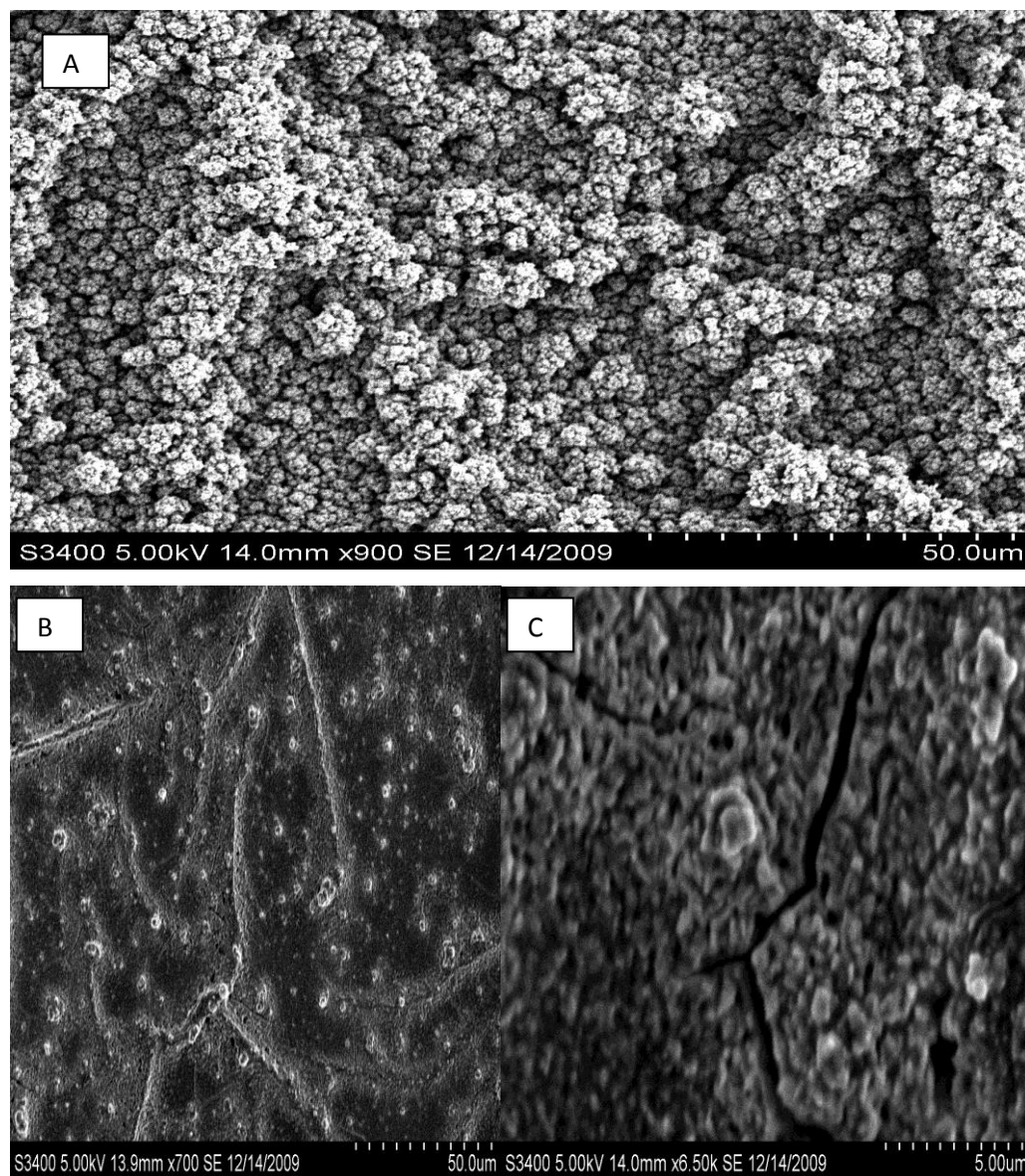


Figure 5.5 **A.** SEM image of PEDOT nanoclusters grown potentiostatically (0.5 V vs. Ag/AgCl) in 50 mM EDOT in 0.1 M LiClO₄ in ACN in the absence of AuNPs on ITO glass (scale bar = 50.0 μm). **B.** SEM image of PEDOT after the electrochemical deposition of AuNPs from a 3 mM HAuCl₄ solution, at a low magnification (scale bar = 50.0 μm). **C.** Enlarged TEM image of a globular network of AuNP on the PEDOT surface. (Scale bar = 5.0 μm).

The SEM images of the PEDOT and PEDOT-AuNP electrochemically deposited onto the gold disc electrode, showing their structural morphologies are illustrated in Figure 5.6. SEM micrographs of PEDOT/LiClO₄ electrodes in the absence of AuNPs prepared potentiostatically at a sweep rate of 10mVs⁻¹ are presented in Figure 5.6 A and B. The PEDOT has taken on a fibrillar network structure with fibre dimensions of ~30um in length. This is attributed to the growth of PEDOT between each potential cycle as the formation of PEDOT has taken place layer by layer. As can be seen from Figure 5.6 B, the fibrils retain a high porosity fibrillar network structure.²¹ The average diameter of the fibers is less than 100 nm and some of the nanofibres have formed branched structures. There are noticeable porous clusters of PEDOT, which may serve to ease the charge transportation through the polymer film.²²

The image in Figure 5.6 C and D, show the effect on the polymer surface after the electrodeposition of AuNPs. The polymer layer has changed significantly as the images illustrate a polymer surface that has become porous and a spongy-like morphology is observed. The regions where AuNPs are deposited clearly showed discrete areas of high contrast, suggesting the presence of AuNPs. The morphology of the resulting nanocomposites is 50– 100 nm in size with incorporated Au nano-clusters. A closer view of the nano-clusters (Figure 5.6 D) shows that it comprises numerous nanoparticles, thus joined to form an aggregate.

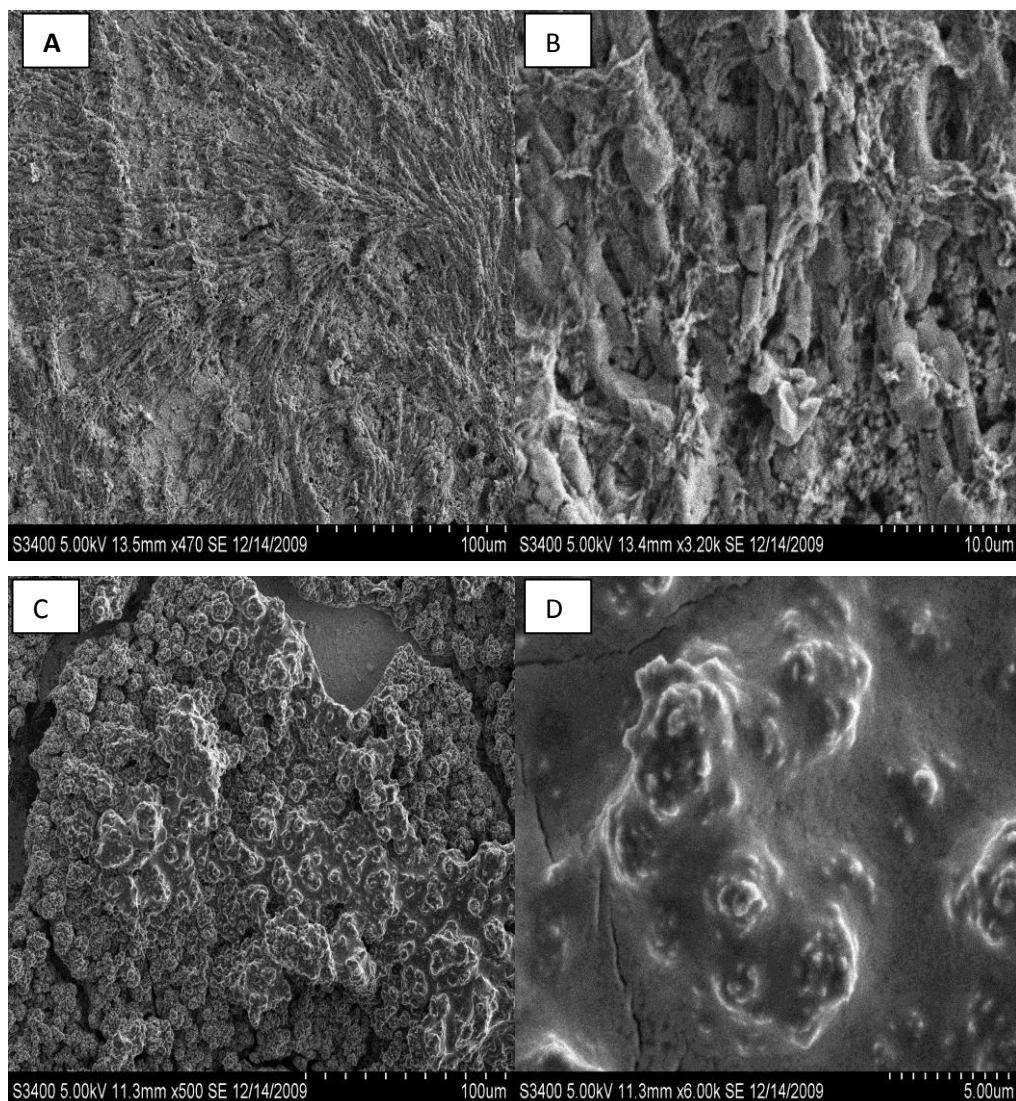


Figure 5.6 **A.** SEM of 50 mM PEDOT/LiClO₄ in ACN films on 2 mm gold disc electrodes deposited potentiostatically at 0.5 V vs. Ag/AgCl in the absence of AuNPs (Scale bar = 100 μm). **B.** Enlarged SEM image of a branched network of PEDOT nanofibres. (Scale bar = 10 μm). **C.** SEM image of electrochemically deposited PEDOT nanoclusters after the electro synthesis of AuNPs, at a low magnification (scale bar = 100 μm). **D.** Magnified SEM image of the clusters of AuNP on the nanocluster surface, showing their size distribution. (Scale bar = 5 μm).

5.2.5 UV - visible spectra of PEDOT

The combination of an especially low oxidation potential as well as a relatively low band gap, gives PEDOT unique electrochemical and spectroscopic properties which are not found in other conducting polymers.²³ When PEDOT is in the oxidized state, it receives an electron and a bipolaron changes into a polaron to have the radical cation structure. The free radical is highly reactive and capable of generating a new covalent bond which may couple with another free radical to form a bipolaron to give two cations.²⁴

PEDOT exhibits a strong sky blue colour when in the conducting state. Changes in redox state leads to changes in the electronic structure,²³ which fortunately can be analysed as an optical colour evolution from clear transparent polymer to dark blue. It is because of this that PEDOT is labelled as an electro chromic polymer.¹¹

5.2.5.1 UV - vis of electropolymerised PEDOT film

The gold-PEDOT nanocomposite was synthesised by an electrochemical route in two steps. Ultra-violet spectroscopy (UV-vis) of the potentiostatically grown films of PEDOT in acetonitrile using 0.1 M LiClO₄ as supporting electrolyte, as described in Section 2.3.1 were carried out. The ITO glass exhibited a colour change from pale blue to a deep blue film as the PEDOT film was deposited potentiostatically (0.5 V) onto the surface. After the electrochemical synthesis of PEDOT-AuNP nanocomposite via current-time transients, the colour then changed to a violet colour.

Figure 5.7 (thin line) shows the UV-vis spectrum of potentiostatically grown films of aqueous PEDOT, with a strong absorption band centered at 612 nm.²⁵ suggesting that most of the polymer is in a polaronic state.²⁶ The broad nature of the band may also arise from a dispersed conjugation length of doped PEDOT. The PEDOT film is also characterized by broad bipolaron absorption between 800 and 1100 nm which is often referred to as a “free carrier tail”.^{25,27} Broad absorption bands in the 800 nm region are attributed to polarons and/or bipolarons. The appearance of this free carrier tail has been previously reported²⁸ as electrons that are delocalized on the PEDOT chains and that the charge hopping motion in the PEDOT/LiClO₄ film is facilitated. The absorption bands in the 300 - 400-nm range are assigned to transitions from the valence band to the uppermost bipolaron band.²⁹

The UV-vis absorption spectrum of the generated nanoparticles on the PEDOT surface (Figure 5.7, thick line) show the absorption resonance peak associated with gold nanoparticles and the band associated with PEDOT polymer. The PEDOT film after the incorporation of AuNPs shows a shoulder at 433.5 nm, which has been assigned to the π - π^* transition of the main chain of PEDOT²⁷ and the surface plasmon resonance of the gold nanoparticles. The surface plasmon band with a maximum centered at 605 nm is significantly broader when compared to the PEDOT film (612 nm), which is indicative of the close proximity of the AuNP to the PEDOT absorption.²⁷ A broad absorption band, attributable to bipolaron formation,³⁰ in the doping process during the

electrochemical polymerisation, extends from approximately 904 nm. This results from the combined effect of the gold surface plasmon and the p band to a localized polaron band transition of the doped PEDOT.³¹

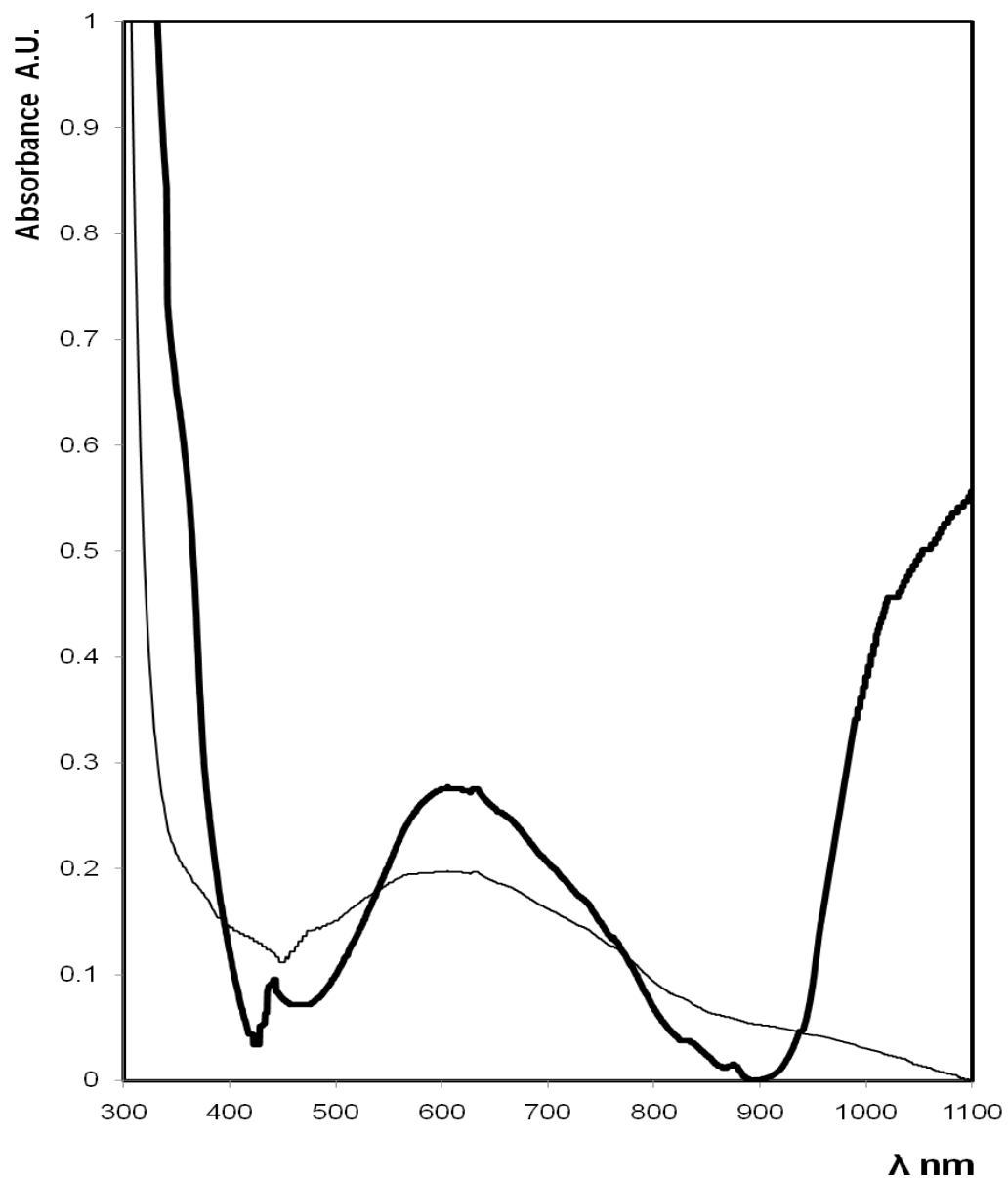


Figure 5.7 UV-vis spectra of PEDOT films grown potentiostatically (thin line) and after AuNP deposition (bold line) onto ITO glass electrode (+0.5 V for 120 s at 100 mVs^{-1}) from aqueous 50 mM EDOT in 0.1 M LiClO_4 . Electrochemical deposition of AuNPs (3 mM cyan free gold plating solution) onto the PEDOT was applied at a fixed potential of -1.5 V for 50 s. Samples were irradiated using He-Ne laser excitation at 632.8 nm.

5.2.5.2 UV - vis of vapour polymerised PEDOT film

An oxidant layer (0.85 M Fe (III) tosylate in 40 % solution of ethanol) was deposited onto the ITO glass substrate by spin coating. A typical vapour polymerisation³²⁻³⁶ involved a glass reaction vessel containing approximately 5 mL of the monomer EDOT and the electrode. The electrode was exposed to the EDOT monomer vapour for approximately 1 hour at room temperature. As the EDOT monomer vapour comes into contact with the oxidant layer on the ITO, a PEDOT film was formed. A UV-vis spectrum was recorded, after the modified electrode was removed, washed in ethanol and allowed to dry quickly under a hot air blower. PEDOT films can be made up in a neutral state and could be subsequently oxidized by the reaction with AuCl₃. AuCl₃ has sufficient power to oxidize PEDOT film in neutral state while it is reduced to form Au particles.

The redox behaviour of the PEDOT film after vapour phase polymerisation was studied *in situ* by UV-vis spectroscopy as shown in Figure 5.8. For PEDOT, the absorption peak centered at 650 nm is characteristic of π - π^* transition. This behaviour has been reported for previous oxidized PEDOT films with a sky blue colour.³⁷ The band near 883 nm is related to the bipolaron sub-gap transition in the polymer.³⁷

The electrochemical reduction process of AuCl₃ onto the PEDOT films was monitored by UV-vis spectroscopy. It is clearly seen that the oxidation of PEDOT film by AuCl₃ causes a decrease in the absorption band at 650 nm as well as an increase in the broad absorption band at 700 nm. The broad absorption above 700 nm, suggests that the polymer structure is in a bipolaron state, which indicates the formation of a sufficient number of charge carriers.²⁶ In addition, a characteristic absorption band due to atomic gold formation was observed at ~440 nm. This band has been previously assigned to the π - π^* transition of the main chain of PEDOT²⁷ as well as the surface plasmon resonance of the gold nanoparticles. This peak has shifted from 447 nm when compared to the PEDOT UV-vis. The reason for this could be due to a decrease of the conjugation length when the electronic delocalization

decreases. The noise that we are seeing could be due to a low concentration of Fe (III) still present on the ITO glass, the slit width is too small or a small reflection from the ITO.

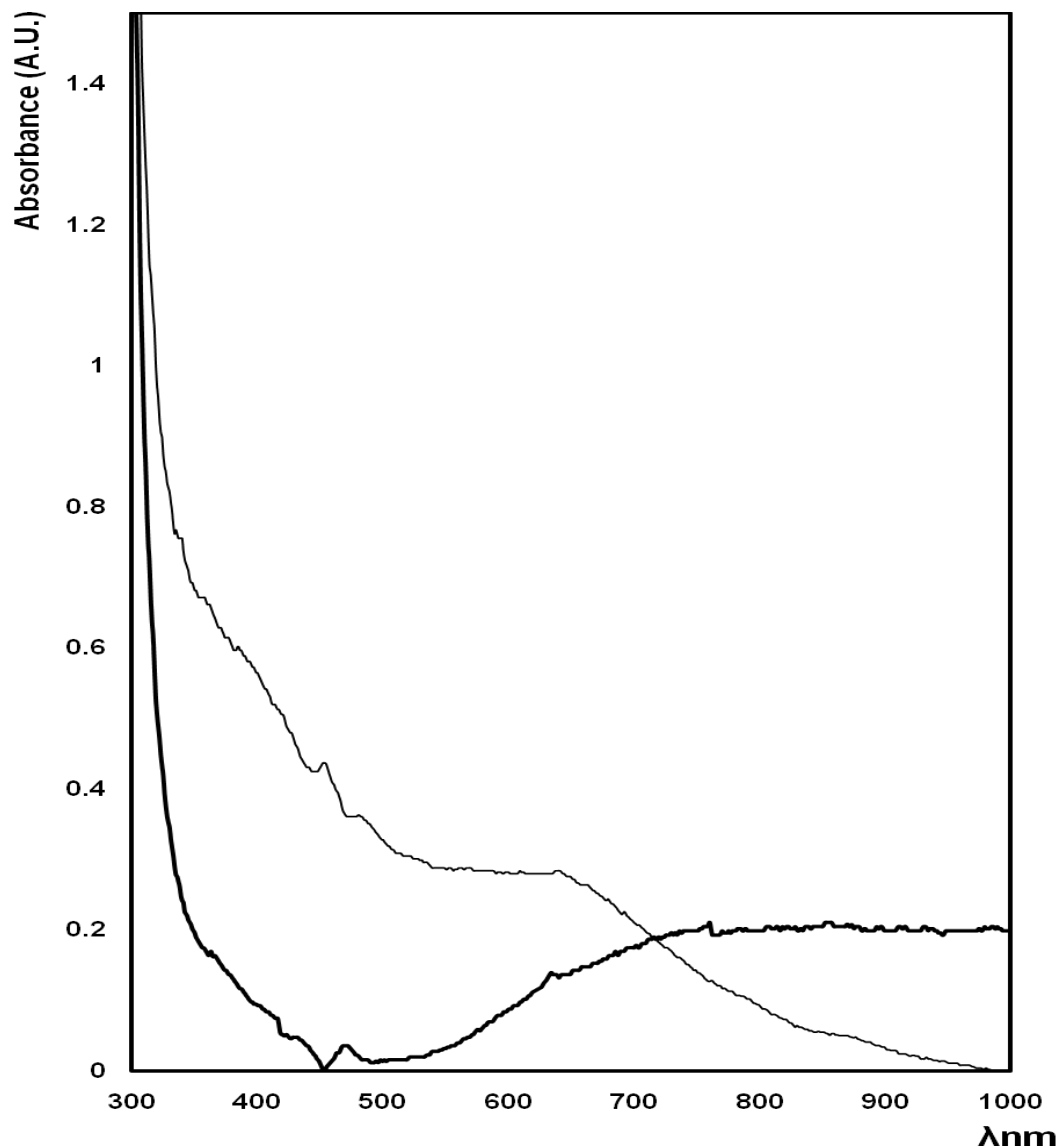


Figure 5.8 UV-vis spectra of PEDOT films grown by vapour oxidation (thin line) and after AuNP deposition (bold line) onto ITO glass electrode. The films were grown by vapour oxidation by coating ITO glass electrode with 0.85 M aqueous Fe (III) tosylate (40 % EtOH) and exposing surface to 1 M EDOT monomer vapour. Electrochemical deposition of AuNPs (3 mM cyan free gold plating solution) onto the PEDOT was applied at a fixed potential of -1.5 V for 50 s. Samples were irradiated using He-Ne laser excitation at 632.8 nm.

5.2.5.3 UV - vis of chemically polymerised PEDOT film

The PEDOT nanofibres were prepared using the synthetic procedure described in Section 2.5.3.3 involving PEDOT and APS. Optical absorption was also studied for the chemically oxidised PEDOT on ITO glass and is shown in Figure 5.9. The PEDOT (thin line) exhibits a broad band around 400 nm, which is associated with the transition of π - π^* . This is associated with the conjugated chain length of the polymer. An additional band is seen at 800 nm, which is typical of the doping process of conjugated polymers and is attributed to bipolaron sub-gap states.³⁸

A UV-visible spectrum of the PEDOT after the electrodeposition of AuNPs (thick line) is also shown in Figure 5.9. A major broad band is situated at the central point of the absorbance around 500 nm, which continues to grow until it reaches 800 nm where a tail like band is then observed onwards till 983 nm. The broad absorption band is due to π - π^* transition of PEDOT.³⁹ This behaviour has been reported for previous oxidized PEDOT films with a sky blue colour.⁴⁰ The other broad absorption feature in the 700 to 900 nm range is related to the charge-carrier band of PEDOT, further indicating that the PEDOT-AuNPs are a form of PEDOT present in the doped state.³⁷ Further, the spectrum of PEDOT-AuNP displays a high absorption at short wavelength and a shoulder band around 420 nm. The absorption around 420 nm was attributed to the valence-conduction band transition of the Au nanoparticles.⁴¹ The result confirmed the formation of the Au nanoparticles simultaneously with polymerization of EDOT during the reaction.

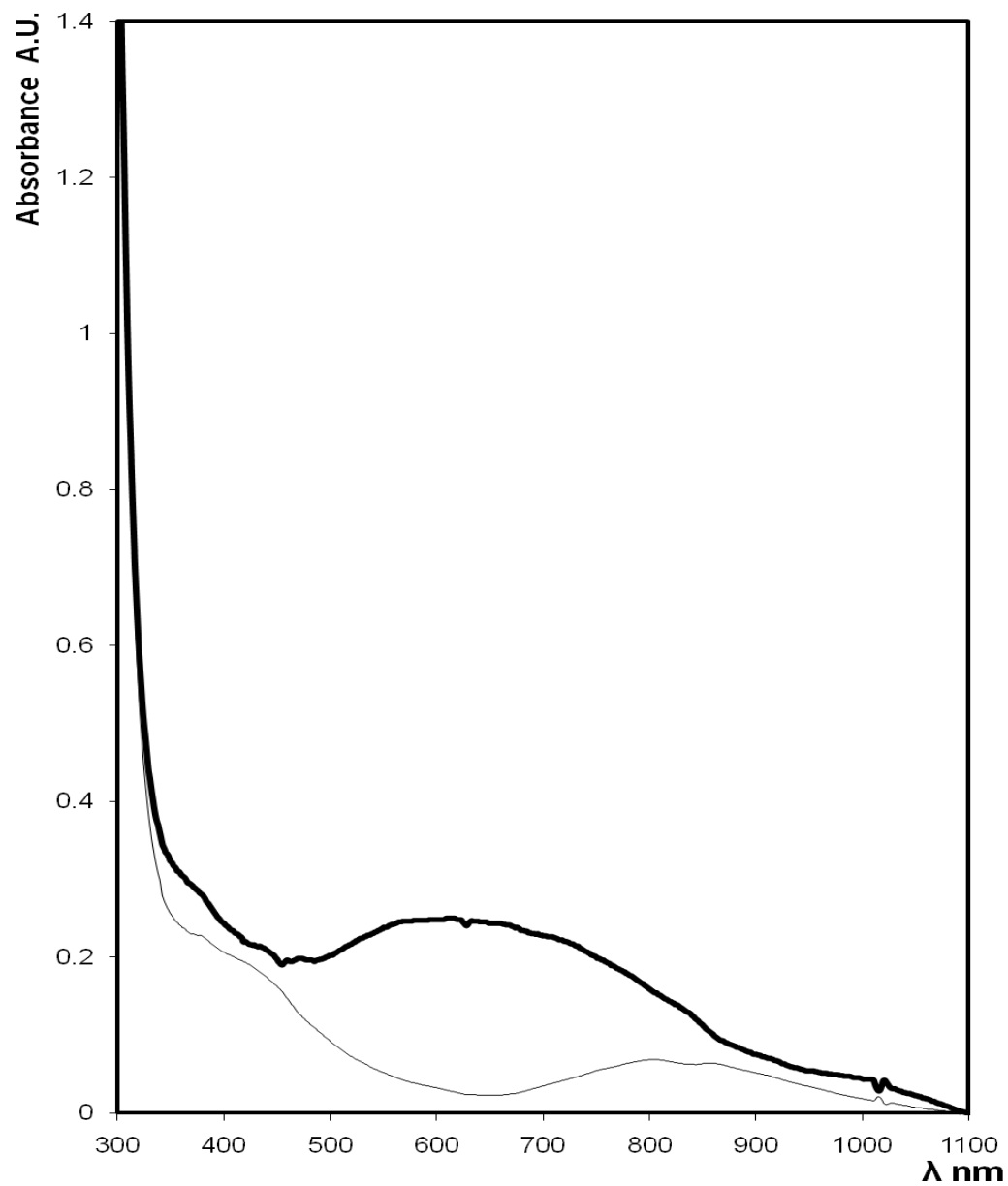


Figure 5.9 UV - vis spectra of chemically prepared PEDOT (thin line) drop cast onto ITO glass electrode. The polymer was prepared using 37 mM EDOT in 22.6 mM APS in PSS (1:0.61 ratio). Thick line shows the spectrum after AuNPs were electrochemically deposited onto the chemically prepared PEDOT at an applied potential of -1.5 V for 50 s.

5.2.6 Raman spectroscopy of PEDOT

In this work, gold-incorporated polyethylenedioxythiophene nanocomposite materials have been synthesised chemically, electrochemically and by vapour oxidation. Different Raman excitation lines can be used to study PEDOT. A 514 nm line or the green line in the middle of the visible range is used for analysing neutral segments and assign experimental bands to vibrational modes. The infrared line (1064 nm) is used for doped segments. In all experiments carried out, the 676 nm or red line is used for ambiguous spectra. Of all three lines, the red line provides superior information on the oxidised state.³⁸ The electronic structures found in PEDOT chains depending on the oxidation and protonation state are illustrated in Figure 5.10, which can be confirmed by Raman.

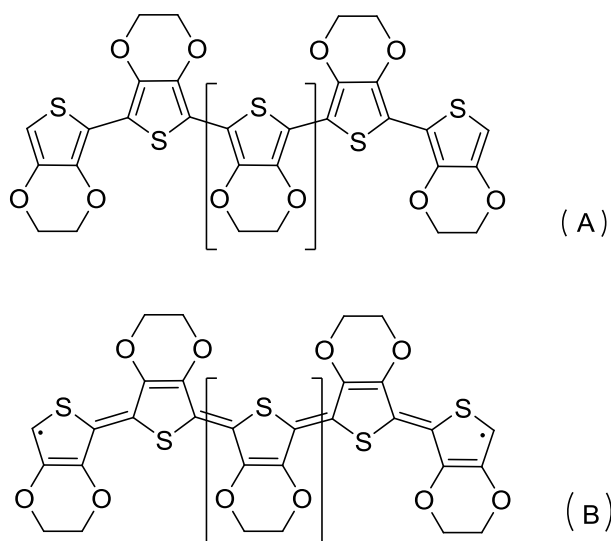


Figure 5.10 General structures of PEDOT in the (A) benzoid form representing the ground state HOMO orbital and (B) quinoid form being the ground state LUMO orbital of the polymer. Reproduced from [42] Zykwinska, A.; Domagala, W.; Czardybon, A.; Pilawa, B.; Lapkowski, M. *Chemical Physics*. **2003**, 292, 31-45.

The linear conformation orients the neighbouring thiophene rings of the PEDOT chain into almost in the same plane.⁴² This causes the conjugated π -

electrons to be delocalised over the whole chain and the quinoid structure becomes favoured. Chains of linear conformation have high charge-carrier mobility and inter-chain interactions increase after conformational change. This can also be determined by EPR.³⁷

PEDOT with its alkylendioxy substituents in the 3 and 4 position prevents α,β coupling and ensures linear chain formation. The electron donating oxygen atoms lower the oxidation potential compared to thiophene and this stabilizes the oxidized polymer.⁴⁰ This information is extremely important in Raman spectra due to

- A. Raman spectra give a clearer indication of the highly regioregular chain in a regiospecific poly(3-alkylthiophenes) because of the longer conjugation length and narrower conjugation lengths distribution.
- B. Raman spectroscopy combined with electrochemical doping studies, allows for doping induced structural changes in conjugated polymer chains to be analysed.⁴²

The typical frequencies (cm^{-1}) and assignments of Raman bands of PEDOT are shown in Table 5.2. The effect of the AuNPs electrochemically deposited onto the PEDOT films, was also investigated. It is thought that the nanoparticles are integrated within the polymer backbone through the interactions of the Au and sulphur thiophene as illustrated in Figure 5.11.⁸

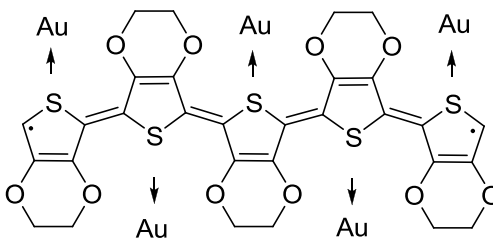


Figure 5.11 Au nanoparticles incorporated within the polymer backbone. Reproduced from Ref [8] Selvaganesh, S. V.; Mathiyarasu, J.; Phani, K. L. N.; YegnaRaman, V. *Nanoscale Research Letters* **2007**, 2, 546-549.

Table 5.2 Frequencies (cm^{-1}) and assignments of Raman bands of PEDOT.⁴⁰

Frequencies (cm^{-1})	Assignments
691	C-S-C deformation
1228	C_α - C_α inter ring stretching (very weak)
1267	C_α - C_α inter ring stretching (weak)
1366	C_β - C_β stretching (strong)
1444	$\text{C}_\alpha = \text{C}_\beta$ stretching (sym)
1517	C=C stretching (antisym)
1620	C-C stretching

5.2.6.1 Raman of electropolymerised PEDOT film

The structure identity of the polymer chain can be conserved after oxidative doping. However, the vibrational properties show significant changes after the transformation of the insulating phase into a conductive form. In Figure 5.12 the Raman spectra of PEDOT is illustrated, where the peaks are attributed as follows: 1513 cm^{-1} $C_{\alpha} - C_{\beta}$ anti symmetric vibrations; 1453 cm^{-1} $C_{\alpha} - C_{\beta}$ symmetric vibrations; 1395 cm^{-1} C_{β} - C_{β} stretching deformations; 1275 cm^{-1} $C_{\alpha} - C_{\alpha}$ symmetric stretching and 1126 cm^{-1} $C_{\beta} - H$ bending. For the peak at 1453 cm^{-1} , studies have shown that during the electropolymerisation of EDOT in $\text{LiClO}_4/\text{ACN}$, the ClO_4 anions are degraded releasing Cl which then becomes linked to the polymer which can attributed to two peaks - ClO_4 and $-\text{Cl}$.⁴³

The Raman spectra of the PEDOT incorporated with Au illustrated in Figure 5.12 (thick line), show similar peak patterns compared to the PEDOT in the absence of AuNPs. This observation indicates that the polymer structure has not changed. However, it should be noted that there is a great enhancement in the intensity which relates to **surface enhanced Raman spectroscopy** (SERS). The most obvious difference was observed for the strongest band between 1455 and 1541 cm^{-1} . The PEDOT - AuNP exhibited a narrower peak at a higher intensity than the PEDOT which is identified as a broad shoulder. The disappearance of this broad shoulder at 1453 cm^{-1} indicates the effect of the Au incorporation on the chemical structure of the PEDOT chains. These vibrations are assigned to the $C_{\alpha}=C_{\beta}$ symmetric stretching of the five-member thiophene ring on the PEDOT chains.⁸

As already stated, two resonant structures have been proposed for PEDOT-benzoid and quinoid. In the case of the benzoid structure there are two conjugated π -electrons on the $C_{\alpha}=C_{\beta}$, whereas there is no conjugated π -electron on the C_{α} - C_{β} bond for the quinoid structure. Therefore, one will see a red shift of the symmetrical $C_{\alpha}=C_{\beta}$ stretching vibration as the structure goes from benzoid to the quinoid.³⁷ As seen in Figure 5.12 there is a slight red shift by 2 cm^{-1} after the incorporation of Au. Both benzoid and quinoid resonant structures may be present in the PEDOT. The benzoid structure may have

transformed into a quinoid structure after the Au salt deposition, which, causes the quinoid structure to become more dominant in the high-conductivity PEDOT - AuNP film. Such resonance structure transformations of the PEDOT chains were observed in the RAMAN spectrum at 1541 cm^{-1} which relates to the quinoid structure. This peak is much more prominent for the PEDOT - AuNP sample.³⁷

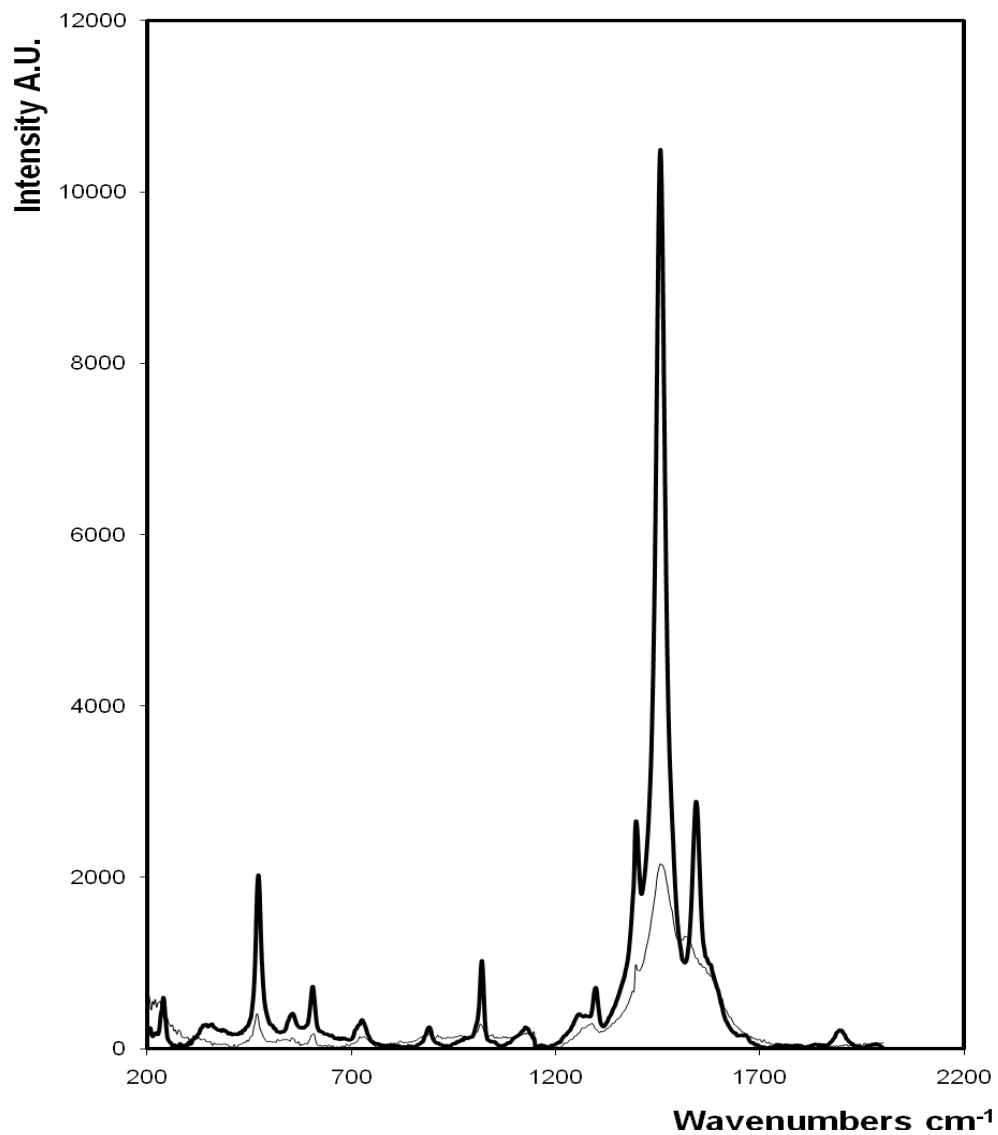


Figure 5.12 Resonance Raman spectra of PEDOT films grown potentiostatically (thin line) and after AuNP deposition (bold line) onto ITO glass electrode (+0.5 V for 120 s at 100 mVs⁻¹) from aqueous 50 mM EDOT in 0.1 M LiClO₄. Electrochemical deposition of AuNPs (3 mM cyan free gold plating solution) onto the PEDOT was applied at a fixed potential of -1.5 V for 50 s. Samples were irradiated using He-Ne laser excitation at 632.8 nm.

5.2.6.2 Raman of vapour polymerised PEDOT film

The Raman spectra of vapour polymerised PEDOT is illustrated in Figure 5.14. The most intense band at 1422 cm^{-1} is assigned to the symmetric stretching ($C_{\alpha} - C_{\beta}$) mode of the aromatic C=C band while a less intense band at $1526\text{--}1546\text{ cm}^{-1}$ is assigned to the C=C antisymmetric stretching ($C_{\alpha} - C_{\beta}$) vibration. Other weaker bands are assigned to the stretching mode of the single C-C bond ($C_{\beta}\text{-}C_{\beta}$) at 1363 cm^{-1} and to the stretching mode of the C-C inter-ring bond ($C_{\alpha} - C_{\alpha}$) at 1237 cm^{-1} .⁴³

The Raman spectrum of the vapour polymerisation after gold deposition shows an increase in intensity, indicating that the AuNPs have bonded to the PEDOT. A strong peak at 1449 cm^{-1} is attributed to the symmetric stretching vibration of $C_{\alpha}\text{=}C_{\beta}$ and a weak peak at 1473 cm^{-1} is assigned to the asymmetric stretching vibration of $C_{\alpha}\text{=}C_{\beta}$. Other peaks observed at 1321 , 1208 , 1058 , 958 , 675 cm^{-1} are due to $C_{\beta}\text{=}C_{\beta}$ stretching, C-C inner ring stretching, C-O-C deformation and symmetric C-S-C deformation, respectively. Examining this spectral information allows for the validation, that PEDOT in the PEDOT-AuNP film is in a highly doped state.⁴⁴

The PEDOT spectrum shows a band centered at $\sim 1422\text{ cm}^{-1}$ which is quite broad. This band is actually the combination of three peaks at 1422 , 1526 and 1546 cm^{-1} , and this can be compared to single peak found at 1473 cm^{-1} for the PEDOT - AuNP sample. This change in the Raman spectrum indicates a transformation of the resonant structure (Figure 5.13) of the polymer upon incorporation of the Au, from a mixture of benzoid and quinoid in the polymer, to a mostly quinoid structure for the Au nanostructure.⁴⁵

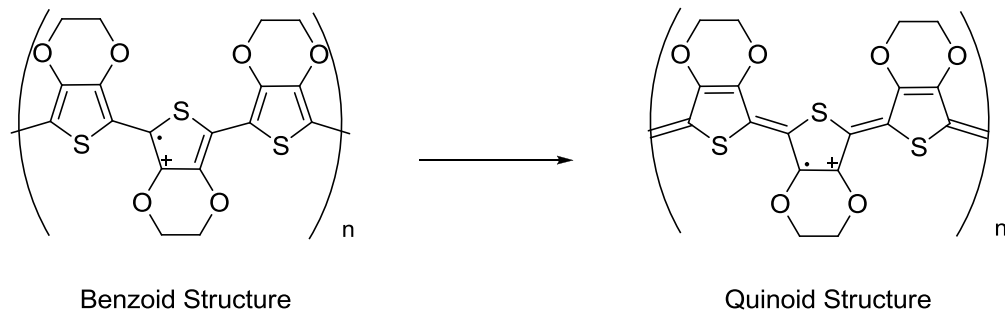


Figure 5.13 Transformation of the PEDOT chain from the benzoid to the quinoid structure. The 'dot' and 'plus' represents the unpaired electron and positive charge on the PEDOT chain, respectively. Reproduced from [42] Zykwincka, A.; Domagala, W.; Czardybon, A.; Pilawa, B.; Lapkowski, M. *Chemical Physics*. **2003**, *292*, 31-45.

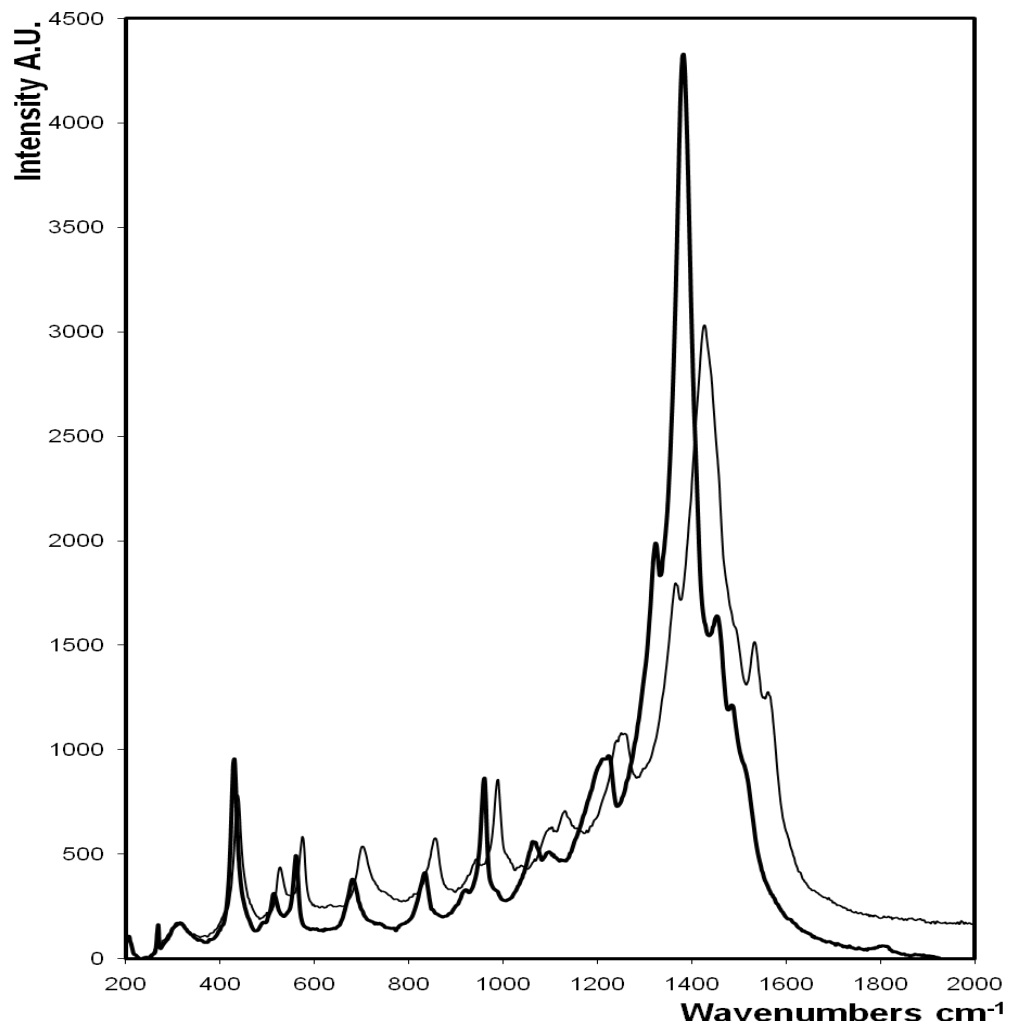


Figure 5.14 Resonance Raman spectra of the vapour polymerised PEDOT before (thin line) and after AuNP deposition (bold line) onto ITO glass electrode. The films were grown by vapour oxidation by coating ITO glass electrode with 0.85 M aqueous Fe (III) tosylate (40 % EtOH) and exposing surface to 1 M EDOT monomer vapour. Electrochemical deposition of AuNPs (3 mM cyan free gold plating solution) onto the PEDOT was applied at a fixed potential of -1.5 V for 50 s. Samples were irradiated using He-Ne laser excitation at 632.8 nm.

5.2.6.2 Raman of chemically polymerised PEDOT film

The effect of the conformation of the chemically prepared PEDOT chains before and after the AuNP treatment was studied by Raman spectroscopy as illustrated in Figure 5.15. For the PEDOT film without AuNP modification, an intense band at 1422 cm^{-1} is exhibited and assigned to the symmetric stretching ($C_{\alpha} - C_{\beta}$) mode of the aromatic C=C band. A less intense band at 1529 cm^{-1} is assigned to the C=C antisymmetric stretching ($C_{\alpha} - C_{\beta}$) vibration. Other weaker bands are assigned to the stretching mode of the single C-C bond ($C_{\beta}-C_{\beta}$) at 1365 cm^{-1} and to the stretching mode of the C-C inter-ring bond ($C_{\alpha} - C_{\alpha}$) at 1248 cm^{-1} .⁴³

After the modification with AuNPs, the Raman spectrum exhibits a SERS effect for the chemical polymerisation of PEDOT. It exhibits similar peaks as the PEDOT film, however by adding Au into the PEDOT backbone, the band between 1400 and 1500 cm^{-1} which corresponds to the stretching vibration of $C_{\alpha}=C_{\beta}$ on the five-member ring of PEDOT becomes narrower and is red shifted by 22 and 9 cm^{-1} , respectively. This indicates that the resonance structure of PEDOT chain has undergone structural changes from a benzoid to a quinoid form.³⁷ A strong peak at 1380 cm^{-1} is attributed to the symmetric stretching vibration of $C_{\alpha}=C_{\beta}$ and a weak peak at 1453 cm^{-1} is assigned to the asymmetric stretching vibration of $C_{\alpha}=C_{\beta}$. Other peaks observed at 1323 , 1197 , 1055 , 960 , 673 cm^{-1} are due to $C_{\beta}=C_{\beta}$ stretching, C-C inner ring stretching, C-O-C deformation and symmetric C-S-C deformation, respectively.

Examining this spectral information allows for the validation that PEDOT in the PEDOT - AuNP is in a highly doped state.⁴⁴ As already explained, the benzoid structure may be the preferred structure for a coil conformation, whereas the quinoid structure may be the favoured structure for a linear/ expanded-coil structure. Therefore, it is anticipated that both coil and linear conformations will be present in a PEDOT film and this turns into linear conformation after the conductivity enhancement. The interaction among the PEDOT - AuNP chains of linear conformation will be stronger than that among the PEDOT chains of coil conformation.³⁷

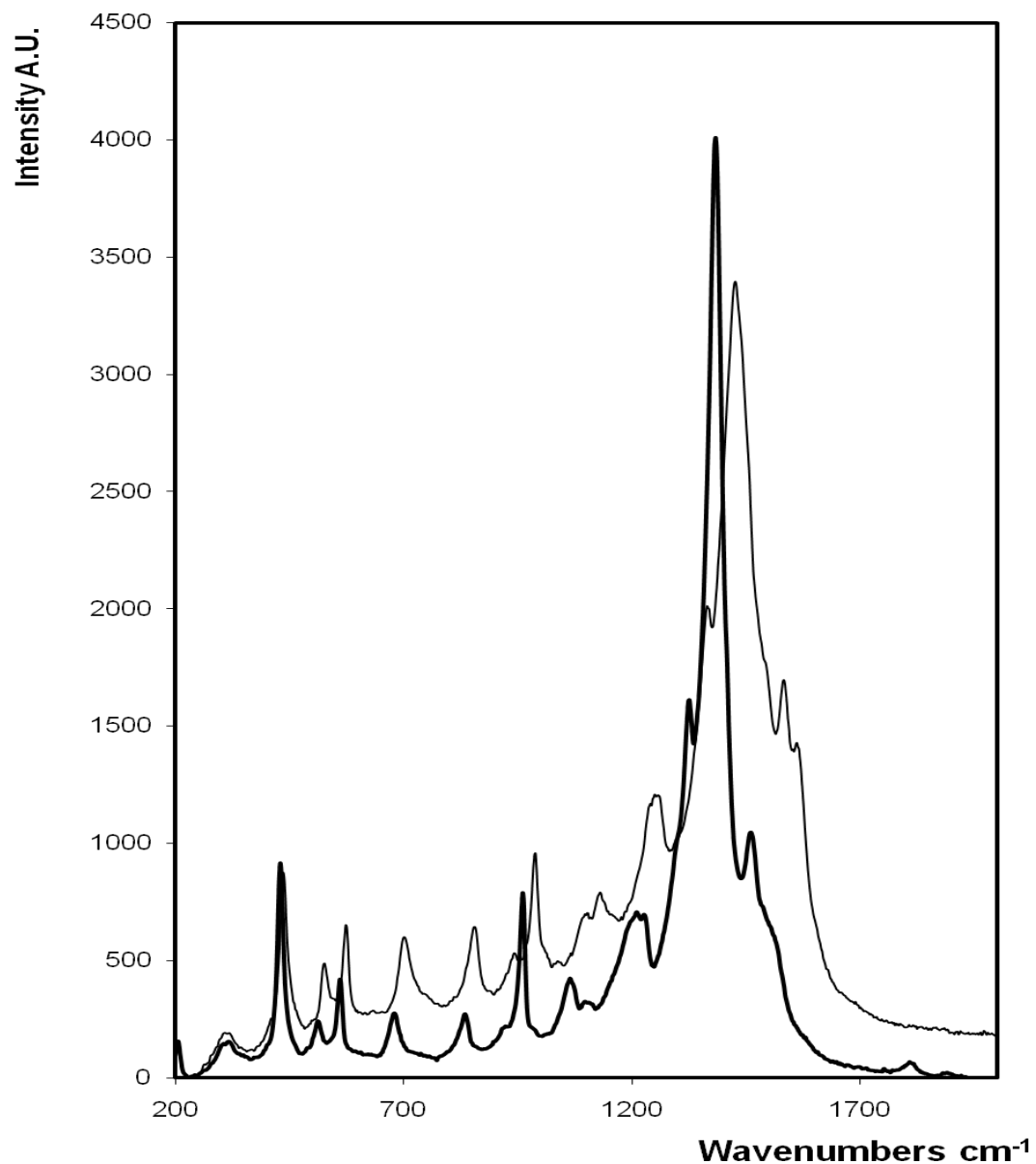


Figure 5.15 Resonance Raman spectra of chemically synthesized PEDOT films (thin line) and after AuNP deposition (bold line) drop cast onto ITO glass electrode from aqueous 37 mM EDOT in 22.6 mM APS in PSS (1:0.61 ratio). Electrochemical deposition of AuNPs (3 mM cyan free gold plating solution) onto the PEDOT was applied at a fixed potential of -1.5 V for 50 s. Samples were irradiated using He-Ne laser excitation at 632.8 nm.

5.2.7 *Electron paramagnetic resonance of PEDOT*

PEDOT with its conjugated π -bond systems has a promising feature with its electrical conductivity in its doped state. It is widely accepted that the charge carriers of conducting polymers are polarons and bipolarons, and both of them are responsible for electrical current propagation along the polymer chain.⁴⁶ Spinless bipolarons dominate and cannot be quantitatively evaluated by EPR. Polarons on the other hand are a paramagnetic species and EPR is perfect to identify and distinguish these species from diamagnetic bipolarons.^{47,48}

EPR line widths depend on the type of magnetic interactions between paramagnetic centers in the sample. Broadening of the EPR lines is due to the statistical distribution of the magnetic fields in the sample. Individual paramagnetic centers are located not only at the external magnetic field but also located at fields of the neighbouring magnetic dipoles. A di-polar interaction between unpaired magnetic moments of paramagnetic centers in the samples is what broadens the EPR lines. Paramagnetic centers in the polymer chains with averaged magnetic fields are responsible for the narrow lines. This group of paramagnetic centers may be formed by highly mobile spins.

5.2.7.1 EPR studies of electrochemically polymerised PEDOT film

The spin density is localized on particular sites, leading to changes in the g factor of different polymers. A typical EPR spectrum of the solid-state electrochemically grown film of PEDOT is shown in Figure 5.16, with a g -factor of the experimental line oscillating around the free electron's value of 2.0024 and a gauss of 3541 G.⁴⁹ This g factor is consistent with previously obtained values⁴⁹ due to the presence of electrons that are unpaired and delocalized over the overall backbone. For organic radicals, a g value above the g value of a free electron (2.0023) indicates spin-orbit coupling of spins with carbon or oxygen. A decrease in the g factor usually signifies some degree of localisation of spins.⁵⁰ The peak-to-peak line width (ΔH) was 3.3 G and the symmetrical singlet can be attributed to the presence of electrons that are unpaired and delocalized over the entire backbone in the π – system of the carbon atoms. This is not to suggest that the electron may be delocalized over a single thiophene ring; the polarons have a significant spatial distribution in conjugated polymers.

The PEDOT incorporated with AuNPs show the EPR signal (Figure 5.16, thin line) 1.8 fold smaller compared with the signal of the PEDOT/LiClO₄ films. However, the chains of the polymer after gold deposition are more expanded and the interactions with the polymer with the gold are increased, resulting in the broad line width observed in the EPR spectrum. Polarons have a spin of 1/2 while a bipolaron is spinless. Looking at the analysis, it suggests that roughly half of the polarons in the PEDOT/LiClO₄ film pair to bipolarons. A polaron corresponds to a positive charge on a unit while a bipolaron corresponds to two positive charges delocalized over several units. This explains the transition from polarons to bipolarons when there is a conformational change from a coil to linear structure, reflecting the delocalization of the π -electrons and thus to the conjugation length of the PEDOT chains.⁵¹ In the PEDOT-AuNP EPR, the g factor of 2.0022 (3520 G) and the line width value of $\Delta H = 12$ G was recorded. The large peak-to-peak line widths indicate a high electronic delocalisation which is consistent with an extended conformation of the polymeric chain.^{52,53} This change in g factor from

low to high field, accompanied with a line broadening effect has been reported previously⁵⁴ for polymers induced by the presence of a coordinating metal centre. This phenomenon has been ascribed to a spin-orbit coupling.⁵⁴

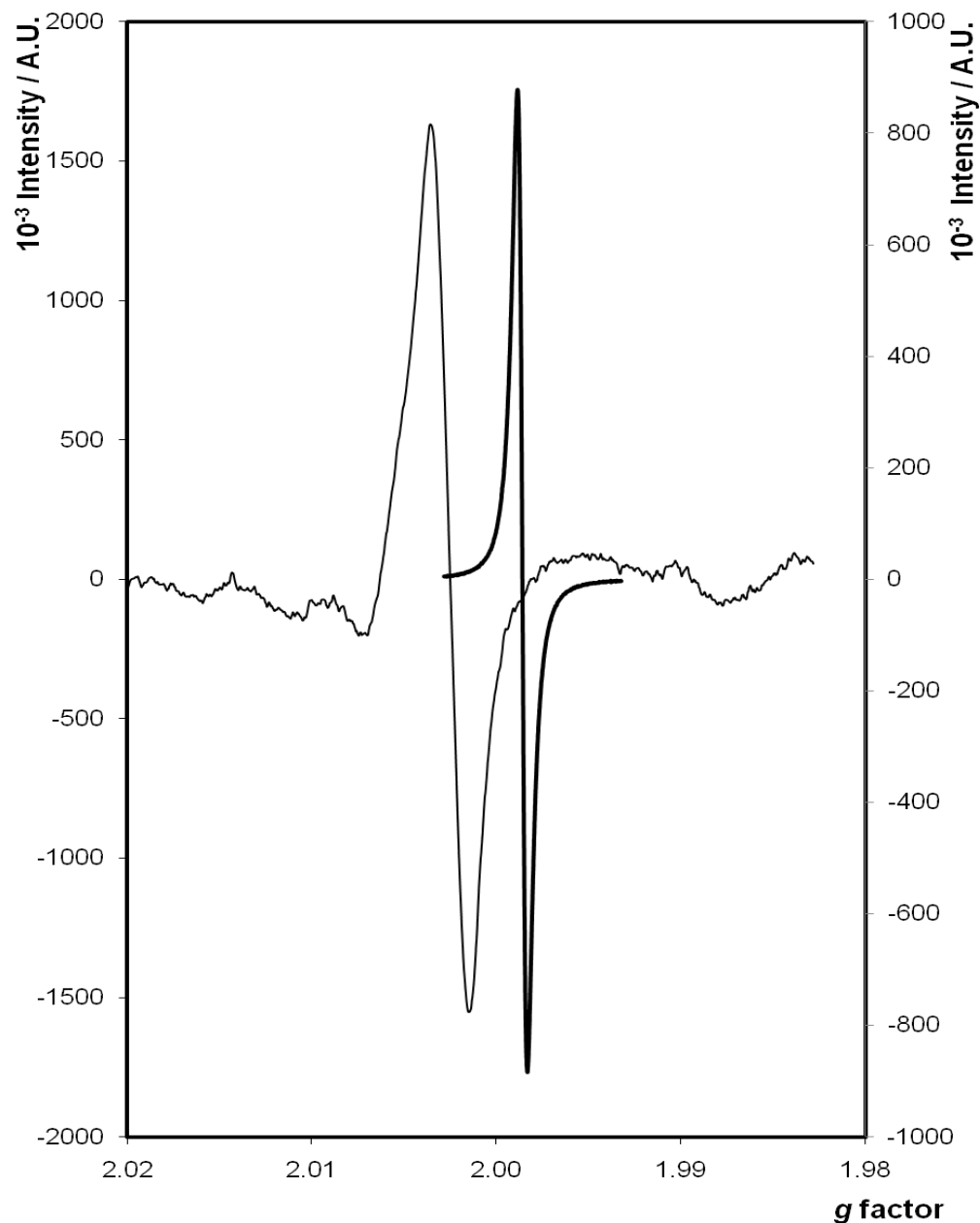


Figure 5.16 EPR response of a solid state sample of electrochemically prepared PEDOT (thick line, y-axis on right) and PEDOT-AuNP (thin line, y-axis on left). The microwave frequency of 9.763 GHz, attenuator of 10.0 dB, sweep width of 50 G, modulation frequency of 100 kHz, modulation amplitude of 1 G, time constant of 327.7 ms, conversion time of 1310.7 ms, and sweep time of 1342.2 s were employed.

5.2.7.2 EPR studies of chemically polymerised PEDOT film

A typical EPR spectrum of the solid-state chemically oxidised film of PEDOT is revealed in Figure 5.17. The graph presents the state of electrons that are unpaired and delocalized over the overall backbone. Again, this is not to suggest that the electron may be delocalized over a single thiophene ring; the polarons have a significant spatial distribution in conjugated polymers. Figure 5.17 shows the EPR spectra of both the chemically prepared PEDOT (thick line) and PEDOT after electrochemical deposition of Au (thin line). A free radical peak appeared in the EPR spectra of both samples, indicating the presence of polarons. In the PEDOT sample, the g value observed was 2.0005 (3505 G) and the peak-to-peak line width (ΔH) was 1.3 G. The spin density is shifted slightly downfield (0.0026 g) when compared to the electrochemical polymerisation of PEDOT. However, the observed g factor is close to the free electron value and in the range reported for various conducting polymers.⁴⁹

The PEDOT incorporated with AuNPs show the EPR signal with a 1.2 fold decrease found for the peak area when compared with the signal of the PEDOT alone. However, the chains of the polymer after gold deposition are more expanded and the interactions with the polymer with the gold are increased, resulting in the line broadening width observed in the EPR spectrum. The fact that this graph does not show a hyperfine structure indicates that the electrons are distributed more evenly over the polymer chains.⁵⁵ In the PEDOT sample after Au deposition, the g factor was 2.0024 (gauss of 3514 G) and the ΔH was 37 G. The ΔH of PEDOT increased from 1.3 G to 37 G for PEDOT after Au deposition, indicating more radical formation throughout the polymer chain. A shift from high field to low field is typically observed when polymers interact with gold nanostructures, indicating that the electrons are distributed more evenly over the films. In conclusion, this means that the chemically prepared PEDOT-AuNP has facilitated electron transfer throughout the polymer film, which ought to improve the performance of electrochemical biosensors.

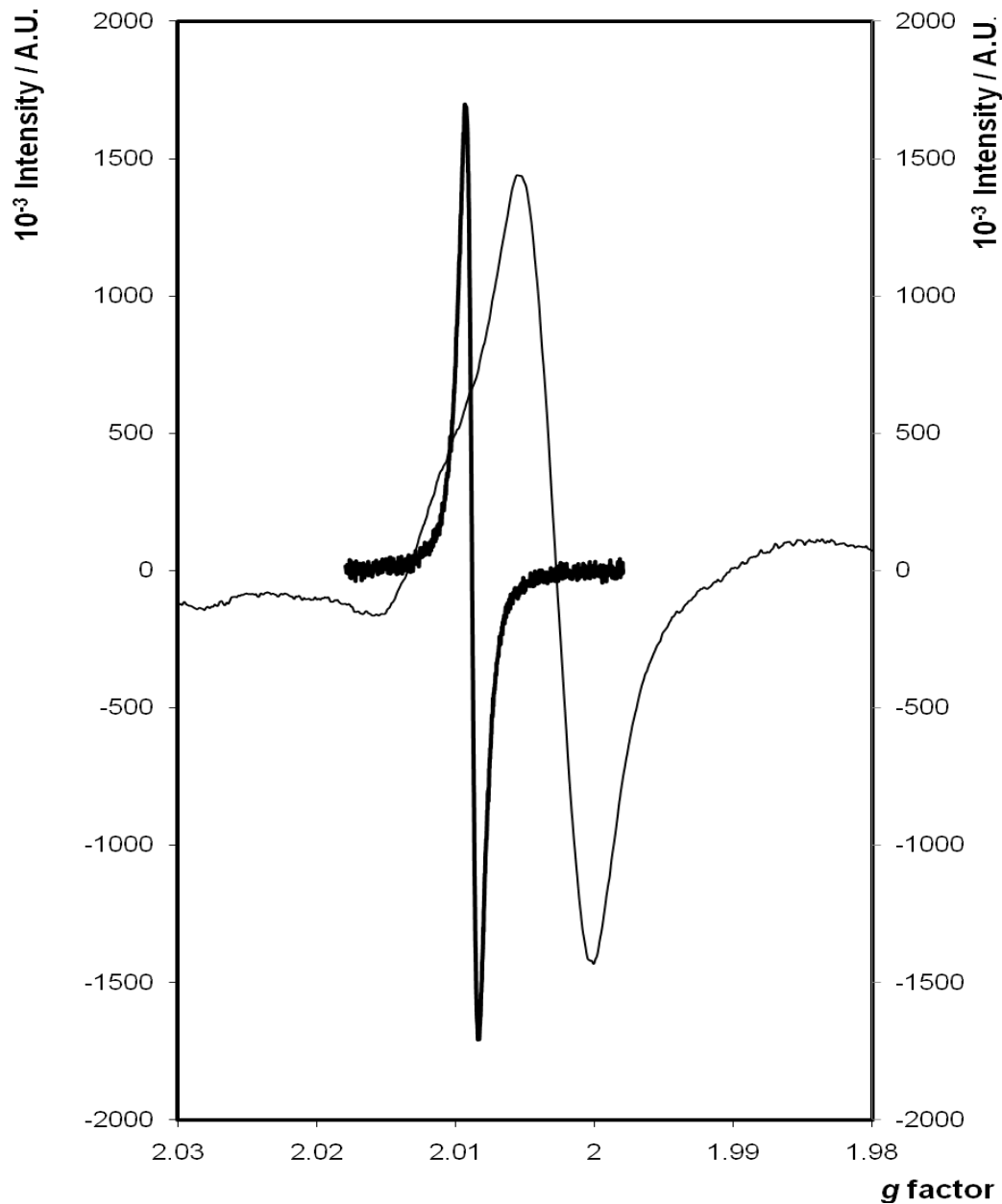


Figure 5.17 EPR response of a solid state sample of chemically prepared PEDOT (thick line, y-axis on left) and PEDOT-AuNP (thin line, y-axis on right). The microwave frequency of 9.763 GHz, attenuator of 10.0 dB, sweep width of 50 G, modulation frequency of 100 kHz, modulation amplitude of 1 G, time constant of 327.7 ms, conversion time of 1310.7 ms, and sweep time of 1342.2 s were employed.

5.2.8 Detection of the hybridisation reaction

The electrochemical DNA sensor is one of most widely investigated sensing applications of conducting polymers (CPs).⁵⁶ During the past twenty years, numerous CPs have been developed and used in the preparation of electrochemical DNA sensors with considerable sensitivity and selectivity. The unique electronic structure of CPs makes them highly suitable materials for electrochemical label-free DNA detection.⁵⁶ Single-stranded DNA capture probes are attached to the conducting polymer via covalent binding at a base site or via other types of interactions. The target DNA is captured by base-pairing to generate a recognition signal, which can be recorded through an electrode. In order to improve sensitivity, selectivity and stability of biosensors different synthesis of nanocomposite materials with enhanced performance have been developed and utilised for biosensor fabrication. Nanocomposites containing Au nanoparticles and the conducting polymer PEDOT have shown facile flow of charge transportation through the polymer film (ESR) and unique properties (SEM) that are obtained with these materials. Morphological characterization of PEDOT revealed a globular porous structure which also explains the ease of charge transportation through the polymer film. Different physical, chemical and electrochemical methods of synthesizing the conducting polymer PEDOT and the effect on DNA hybridisation are discussed in detail in Section 5.2.8.1 – 5.2.8.3.

5.2.8.1 Electropolymerisation of EDOT

In this work, we report on the use of gold nanoparticles (AuNP) and PEDOT to create a high sensitivity DNA hybridization assay is reported. PEDOT has been electrochemically deposited on gold electrodes and modified with electrochemically deposited gold nanoparticles to give a nanocomposite material (PEDOT - AuNP). DNA was then hybridised and detected as described in Section 2.4.3 and 2.4.4, respectively. For comparison purposes, the absolute current measured for 150 pM to 1 μ M target DNA, the slope of the calibration curve and the lower concentrations of the target that could be detected were measured. The effect of the surface modification on the DNA

detection is also clearly shown in calibration results. Figure 5.18 compares the 3 cases of HRP labelled DNA hybridised on a bare electrode (\blacktriangle), on an electrochemically prepared PEDOT electrode (\blacklozenge) and on the electrochemically prepared PEDOT after AuNP surface modification (\blacksquare).

Firstly, Figure 5.18 shows the semi-log concentration vs. Δi calibration curves for the pathogen DNA detection using a bare gold electrode (\blacktriangle) where the concentration of sequence-specific DNA of *S. aureus* is systematically varied from 150 pM to 1 μ M, with a correlation coefficient of 0.95. Significantly, this approach generated a measurable response even for pathogen DNA concentrations as low as 150 pM. The limit of detection was 4 pM with a signal to noise ratio less than ten.

Electrochemical polymerisation results in the formation of a sky-blue, doped PEDOT film at the anode. The electrochemical polymerisation of PEDOT shows a high reproducibility for the specific sequence target DNA, in the linear range of 150 pM to 1 μ M concentration (correlation coefficient of 0.9289), demonstrating a highly sensitive system. Figure 5.18 (\blacklozenge and \blacksquare) shows the differential amperometric response of HRP reduction in the presence of H₂O₂ after hybridization with various concentrations of *S. aureus* DNA targets. The differential current response increased with increasing concentration of target DNA for the PEDOT biosensor without and with the attachment of AuNPs.

In the absence of the AuNPs, the dynamic range was 10 nM to 1 μ M with a correlation coefficient of 0.9995 ($n = 2$). In the case where AuNPs were attached, however, the dynamic range was enlarged to concentrations from 1 nM to 1 μ M with a correlation coefficient of 0.9988 ($n = 2$). A larger sensitivity (slope of $3.81 \mu\text{A}^{-1}$) was obtained for the biosensor with attached AuNPs compared to sensitivity for the PEDOT sensor without AuNPs (slope of $1.24 \mu\text{A}^{-1}$). This system also provides highly reproducible detection even at low DNA concentrations. The standard error for the lowest DNA concentration (150 pM) for the PEDOT-AuNP electrode was 0.44 with a S/N ratio above 8 compared to the standard error of 0.67 (S/N = 3) for the PEDOT modified electrode. This improved signal gain of the PEDOT-AuNP leads in turn to

significantly improved sensitivity; the directly calculated detection limit of the sensor is 17 fM compared to LOD of 4 pM for the PEDOT material alone.

This PEDOT - AuNP nanostructured surface showed a greater analytical performance than the unmodified gold electrode. Significantly, the sensitivity of the DNA detection is approximately 76 fold greater for the PEDOT-AuNP (slope of $3.81 \mu\text{A}^{-1}$) modified electrodes compared to the bare electrode surface (slope of $0.05 \mu\text{A}^{-1}$). The enhancement in signal was attributed to the improved condition for effective hybridisation between the capture DNA and the target as a result of the surface modification. Table 5.3 lists the average current response for the electrochemical synthesis of PEDOT before and after AuNP electrodeposition on a gold disc electrode at various concentrations of *S.aureus* DNA.

Table 5.3 Average current response of electrochemically deposited PEDOT with and without AuNPs at different concentrations of target DNA.

Electrode Modification	Concentration of <i>S. aureus</i> (M)	Average current response ($\Delta i / \mu\text{M}$)	Standard deviation (n = 2)	Standard error
Bare Electrode	1.50E-10	0.03	0.06	0.04
	1.00E-09	0.05	0.02	0.01
	1.00E-08	0.09	0.01	0.01
	1.00E-07	0.13	0.01	0.01
	1.00E-06	0.20	0.01	0.01
Electrochemically synthesised PEDOT	1.50E-10	1.29	0.95	0.67
	1.00E-09	2.29	0.78	0.55
	1.00E-08	2.55	0.21	0.15
	1.00E-07	4.19	0.55	0.39
	1.00E-06	6.34	1.24	0.88
Electrochemically synthesised PEDOT with AuNPs	1.50E-10	5.22	0.62	0.44
	1.00E-09	8.25	1.13	0.80
	1.00E-08	12.71	0.18	0.13
	1.00E-07	17.51	0.07	0.05
	1.00E-06	19.03	0.69	0.49

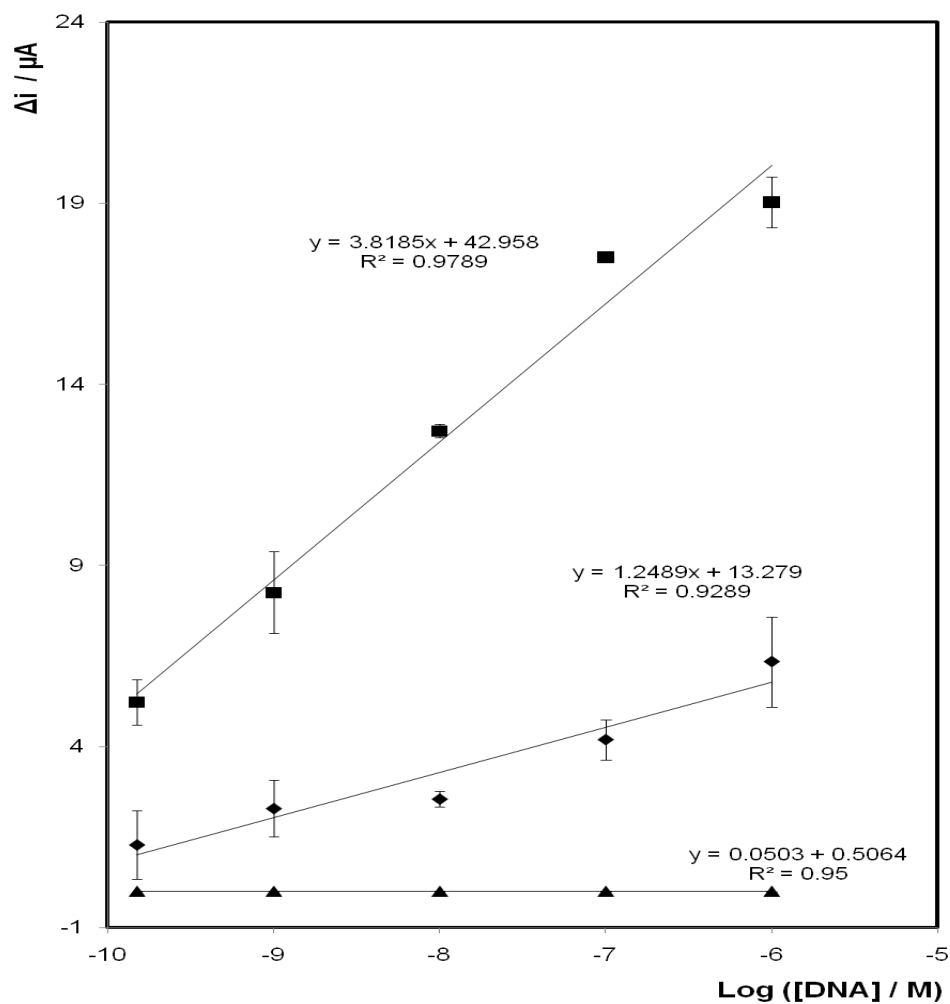


Figure 5.18 Electrochemical detection of sequence-specific *S. aureus* pathogen DNA concentration on a bare electrode (▲), electrochemically synthesised PEDOT (◆) and electrochemically synthesised PEDOT after AuNP deposition (■). Capture strand, target strand and probe HRP strand (Denhardt's buffer) were cycled in phosphate buffer saline and 0.1 M KCl and a concentration of 1.81 mM hydroquinone. Y axis is the difference in signal before and after addition of H₂O₂ (Δi). Potential applied -0.40 V. Where error bars are not visible, they are smaller than or comparable to, the size of the symbols and range from 1.4 % to 19 %.

5.2.8.2 Vapour Polymerisation of EDOT

EDOT monomer is known for its relatively high vapour pressure and the polymerisation of EDOT by vapour oxidation can be easily initiated by exposing an oxidant to EDOT vapour. EDOT has a higher oxidation potential than pyrrole, however it has the advantage of facile polymerisation in the presence of oxidants such as FeCl_3 , $\text{Fe}(\text{ClO}_4)$ and iron (III) salts of organic/inorganic acids containing organic radicals. PEDOT films were deposited under the conditions described in Section 2.5.2.2. The DNA hybridisation was then carried out as described in Section 2.4.3. For the purpose of comparison, the detection of DNA was carried out on bare electrodes as well as the modified electrodes with the vapour polymerised PEDOT before and after Au modification.

Figure 5.19 shows the calibration curves for the detection of HRP for a bare (\blacktriangle), PEDOT and PEDOT-AuNP (\blacksquare) modified electrode. Initially, a significant increase (approximately 23 fold) of the current response is observed when comparing the sensitivity of the vapour prepared PEDOT (slope of $1.18 \mu\text{A}^{-1}$) to the unmodified electrode (slope of $0.05 \mu\text{A}^{-1}$). The PEDOT-DNA biosensor showed that the reproducibility is excellent even at low DNA concentrations, e.g. at 150 pM the signal-to-noise ratio is at least ten with a correlation coefficient of 0.9664. The dynamic linear range between 150 pM – 10 nM achieved a correlation coefficient of 0.9992. We know that the PEDOT sensor is able to detect DNA concentrations down to 150 pM. It has also been estimated that we can detect as little as 34 fM on the PEDOT modified surface.

The sensitivity of the PEDOT-AuNP film is significantly greater than that found in the absence of gold nanoparticles. When the assay is conducted in the presence of AuNP, the correlation coefficient is 0.97 however the expanded dynamic linear calibration range is 1 nM – 1 μM for the maximum average current response of the PEDOT-Au nanocomposite (\blacksquare) films versus the concentration of target DNA has a correlation coefficient of 0.9957. The current response of the PEDOT-AuNP modified electrode (slope of $4.07 \mu\text{A}^{-1}$) is 3.4 times more sensitive than the PEDOT modified electrode ($1.19 \mu\text{A}^{-1}$),

hence the greater slope. The net signal gain produced by this approach is significantly enhanced. For example, a 3.2 fold increase in current for target DNA at a concentration of 1 μM was observed after AuNP formation. In the presence of AuNPs, the overall sensitivity of the electrode response of *S.aureus* was amplified 4 fold with increasing concentrations of target DNA hybridised when compared to the PEDOT modified electrode. The standard error for the 150 pM concentration of target DNA was 0.77 with a S/N ratio of 10. The analytical sensitivity (limit of Detection (LOD)) of the PEDOT-AuNP DNA assay for target DNA was 3.8 fM.

Compared with the electrochemically synthesized PEDOT-AuNP sensor (slope of $3.82 \mu\text{A M}^{-1}$), the vapour polymerised PEDOT after Au deposition sensor showed greater sensitivity in electrode response (slope of $4.07 \mu\text{A}^{-1}$). The electrochemical depositions of the AuNPs were identical for both experiments. The significant difference in the average maximum current response was due to the method in which the PEDOT was synthesised. The limit of detection for both the electrochemical polymerised PEDOT (17 fM) and the PEDOT prepared by vapour polymerisation (3.8 fM) is significantly different. A 1.2 fold increase was also observed for the signal to noise ratio for the lower concentrations of DNA. For example at 150 pM the signal to noise ratio for the electrochemical PEDOT-AuNP is at least 8 (standard error = 0.44) and the vapour prepared PEDOT-AuNP is at least 10 (standard error = 0.77).

While the current data does not allow us to discriminate between surface coverage and orientation events which could be addressed for example, using fluorescently labelled DNA, such significant differences suggest that the polymerisation by vapour oxidation technique has provided a polymer film which is highly efficient. The PEDOT obtained by the vapour-phase polymerization shows greater sensitivity, compared with that of conventionally electrochemically synthesized PEDOT. The higher electrode response of PEDOT deposited may be due to its higher crystallinity, higher degree of doping, and lower interchain separation compared with the electrode electrochemically polymerised with PEDOT. In correlation with Raman spectroscopy, the vapour oxidised PEDOT indicated a quinoid structure after

gold deposition. This illustrates a sensor in a highly oxidative state and therefore the system became highly conducting. This property of the vapourised PEDOT with AuNP, would therefore explain the electrode response differences between the two PEDOT sensors. Table 5.4 lists the average current response for the vapour phase synthesis of PEDOT before and after AuNP electrodeposition on a gold disc electrode at various concentrations of S.aureus

Table 5.4 Average current response of vapour oxidised PEDOT with and without AuNPs at different concentrations of target DNA.

Electrode Modification	Concentration of S. aureus (M)	Average current response ($\Delta i / \mu\text{A}$)	Standard deviation (n = 2)	Standard error
Bare Electrode	1.50E-10	0.03	0.06	0.04
	1.00E-09	0.05	0.02	0.01
	1.00E-08	0.09	0.01	0.01
	1.00E-07	0.13	0.01	0.01
	1.00E-06	0.20	0.01	0.01
Vapour oxidation of PEDOT	1.50E-10	3.22	0.14	0.10
	1.00E-09	4.65	0.51	0.36
	1.00E-08	6.23	0.92	0.65
	1.00E-07	6.71	0.28	0.20
	1.00E-06	7.94	0.56	0.39
Vapour oxidation of PEDOT with AuNPs	1.50E-10	11.219	1.09	0.77
	1.00E-09	11.75	0.56	0.39
	1.00E-08	16.78	0.11	0.08
	1.00E-07	21.04	1.51	1.07
	1.00E-06	26.094	1.27	0.90

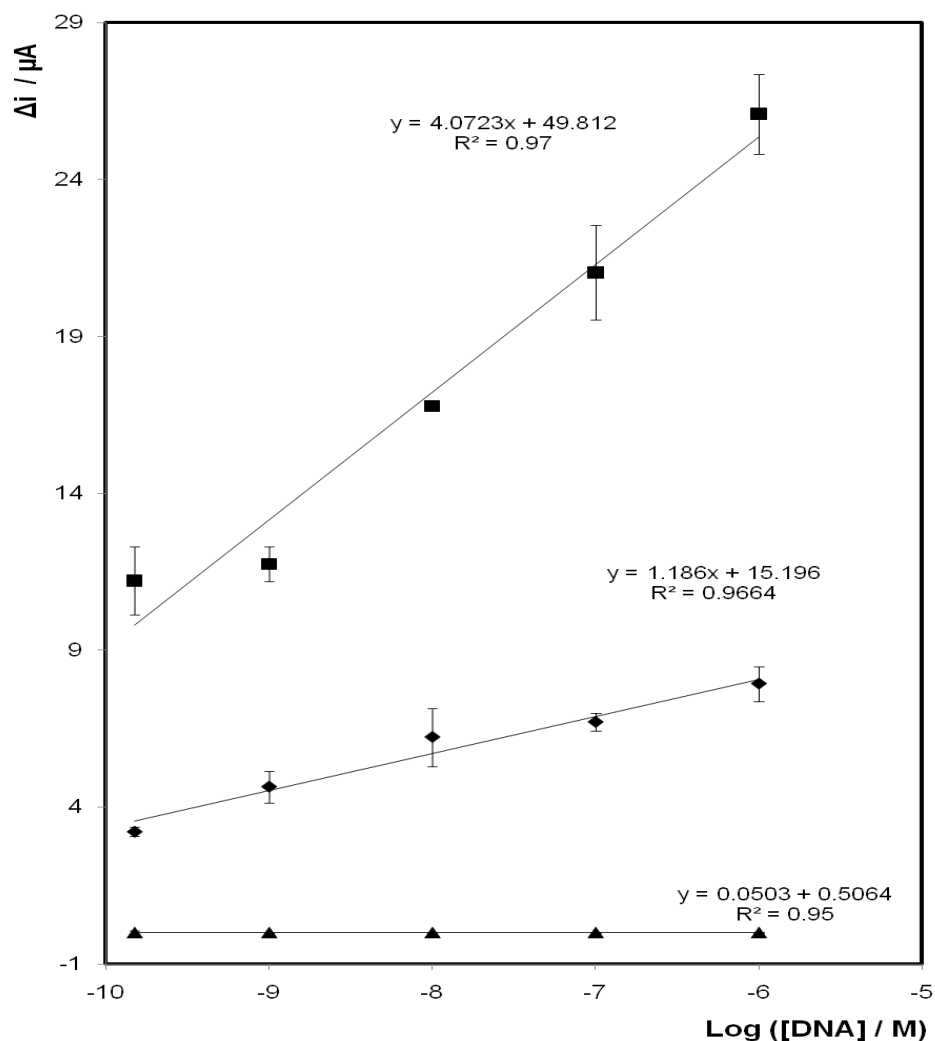


Figure 5.19 Electrochemical detection of sequence-specific *S. aureus* pathogen DNA concentration on a bare electrode (\blacktriangle), vapour polymerised PEDOT (\blacklozenge) and vapour polymerised PEDOT after AuNP deposition (\blacksquare). Capture strand, target strand and probe HRP strand (Denhardt's buffer) were cycled in phosphate buffer saline and 0.1 M KCl and a concentration of 1.81 mM hydroquinone. Y axis is the difference in signal before and after addition of H_2O_2 (Δi). Potential applied -0.40 V. Where error bars are not visible, they are smaller than or comparable to, the size of the symbols and range from 0.6 % to 14 %.

5.2.8.3 Chemical polymerisation of EDOT

Chemical oxidative polymerisation is the most useful method for preparing large amounts of conducting polymer powders and has been extensively used in industry. Chemical polymerisation of PEDOT was carried out as described in Section 2.5.3.3 before the hybridising with DNA. The calibration plots shown in Figure 5.20, highlights the results of the hybridisation of the specific sequence target DNA in a linear concentration of 150 pM to 1 μ M for 3 comparative studies. Polymer and AuNP electrodeposition surface modification of the gold disc electrode was carried out for the detection of the *S. aureus* DNA. Figure 5.20 compares the 3 cases of HRP labelled DNA hybridised on a bare electrode (\blacktriangle), on an chemically synthesized PEDOT electrode (\blacklozenge) and on the chemically synthesized PEDOT modified electrode after AuNP electrodeposition (\blacksquare).

The PEDOT modified electrode (Figure 5.20, \blacklozenge) readily achieved a amperometric current response for the 150 pM concentration of target DNA. In this study, the lower limit of detection (LOD) was defined as the lowest amount of target DNA that could be detected above background noise with a signal-to-background ratio of two or greater. The LOD was calculated to be 91.2 fM and this system has also provided highly reproducible detection with a standard error of 0.048 for the 150 pM target DNA concentration and a signal to noise ratio of at least 15 and a correlation coefficient of 0.9345. Overall, it is clear from the calibration curve that the current response increased with increasing concentration of *S.aureus* DNA with a dynamic range of 1 nM and 1 μ M and a correlation coefficient of 0.9863. When comparing these results, to the sensor detection of mastitis on a bare electrode, a significant increase of the Faradaic current from nanoamps to micro amps is exhibited.

The chemically synthesised PEDOT after AuNP amplification was investigated to report the enhancement of the analytical performance and sensitivity of the sensor. The sensitivity was evaluated in Figure 5.20 as the slope from the linear portion (150 pM to 1 μ M) of the semi-logarithmic concentration versus the maximum average current response of the PEDOT-Au nanocomposite (\blacksquare).

Significantly, after AuNP modification, a larger sensitivity in current response (slope of $1.38 \mu\text{A}^{-1}$) was observed when compared to the current response in the absence of AuNP (slope of $1.24 \mu\text{A}^{-1}$). The dynamic linear calibration range for the PEDOT-AuNP is 10 nM and 1 μM with a correlation coefficient of 0.9979 and an improved LOD of 6.9 fM.

Overall, for each polymerisation process of PEDOT irrespective of the oxidation process, the detection of target DNA is similar for all 3 processes, resulting in a respectable differential current response without the presence of any nanoparticle enhancement. Both PEDOT and AuNPs allow for more immobilisation of DNA strands, demonstrating a simple rapid and extremely sensitive method for the detection of DNA molecules. The vapour oxidation of PEDOT showed the best sensitivity and wider dynamic range. The analytical performance of the PEDOT biosensor increased after AUNP deposition. This vapour method has simplified the coating process and has been previously proven to be the most efficient method to achieve uniform coatings.⁵⁷ The process has several major advantages over the electrochemical and chemical routes for depositing conjugated polymers.⁵⁷

1. The conjugated polymer can be readily deposited on non-conductive substrates.
2. There is no requirement to immerse the target substrate into the conjugated monomer solution with dispersants or stabilizers.
3. This process results in conductive coatings with a smoother surface morphology.

Comparing the current responses found for the vapour oxidation of PEDOT-AuNP to the other calibration plots, a 6.1 % and 66 % decrease is reported in the sensitivity of the electrochemical and chemical synthesized PEDOT -AuNP electrode response, respectively. Table 5.5 lists the average current response for the chemically synthesized PEDOT before and after AuNP electrodeposition on a gold disc electrode at various concentrations of *S. aureus*.

Table 5.5 Average current response of chemically synthesized PEDOT with and without AuNPs at different concentrations of target DNA.

Electrode Modification	Concentration of <i>S. aureus</i> (M)	Average current response ($\Delta i / \mu\text{A}$)	Standard deviation (n = 2)	Standard error
Bare Electrode	1.50E-10	0.03	0.06	0.04
	1.00E-09	0.05	0.02	0.01
	1.00E-08	0.09	0.01	0.01
	1.00E-07	0.13	0.01	0.01
	1.00E-06	0.20	0.01	0.01
Chemically synthesized PEDOT	1.50E-10	1.06	0.07	0.05
	1.00E-09	1.13	0.58	0.41
	1.00E-08	2.09	0.20	0.14
	1.00E-07	4.22	0.42	0.30
	1.00E-06	5.44	0.48	0.34
Chemically synthesized PEDOT with AuNPs	1.50E-10	5.098	0.37	0.26
	1.00E-09	6.375	0.77	0.55
	1.00E-08	6.563	0.50	0.35
	1.00E-07	8.558	0.67	0.47
	1.00E-06	10.625	1.40	0.99

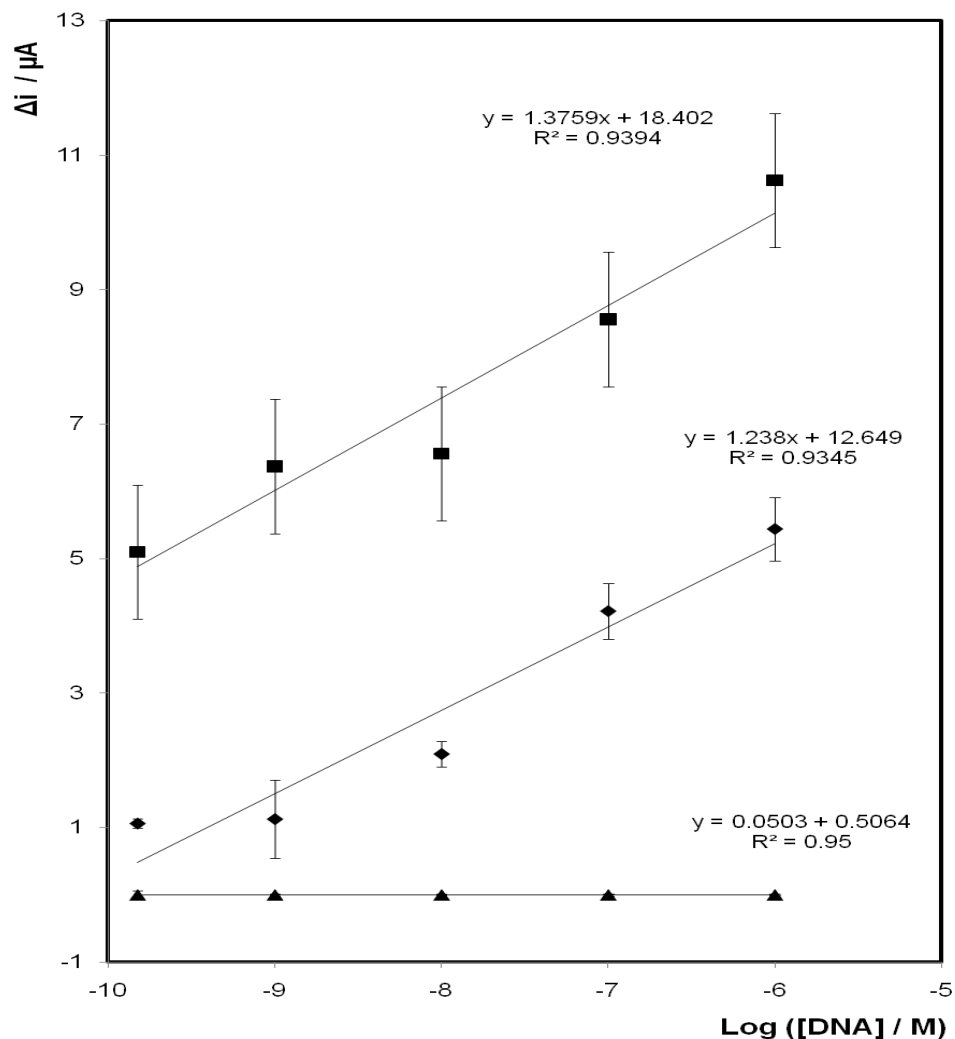


Figure 5.20 Electrochemical detection of sequence-specific *S. aureus* pathogen DNA concentration on a bare electrode (▲), chemically synthesised PEDOT (◆) and chemically synthesised PEDOT after AuNP deposition (■). Capture strand, target strand and probe HRP strand (Denhardt's buffer) were cycled in phosphate buffer saline and 0.1 M KCl and a concentration of 1.81 mM hydroquinone. Y axis is the difference in signal before and after addition of H₂O₂ (Δi). Potential applied -0.40 V. Where error bars are not visible, they are smaller than or comparable to, the size of the symbols and range from 6 % to 13 %.

5.3 CONCLUSION

Conducting polymers such as PANI and supporting metal nanoparticles (NPs) are nanocomposite materials that have attracted great interest in scientific research because of their application in electrocatalysis, as sensors or capacitors. Poly (3,4-ethylenedioxythiophene) (PEDOT) has proven to be a good candidate to support gold nanoparticles due to its high conductivity and good environmental stability. Many researchers have reported different synthetic pathways of making conducting polymers: chemical synthesis by reaction of the monomer with the metal salt, layer-by-layer deposition, electrochemical synthesis of the polymer in the presence of chemically synthesized metal nanoparticles, vapour phase polymerisation etc. Electrodeposition of metal nanoparticles on the pre-formed conducting polymer film has been reviewed as the favoured technique. However, poor classification of the best synthesis of conducting polymer deposition mechanisms has been reported in the literature. Here, the synthesis of PEDOT-AuNPs composites, occurring in two steps: polymerization of PEDOT followed by the electrochemical deposition of AuNPs on the PEDOT film was presented. The synthesis of the PEDOT film was performed electrochemically, chemically or by vapour oxidation processes. The enzyme electrode is based on the hybridisation of HRP labelled DNA with complementary DNA monolayer formed on AuNP which were electrochemically deposited onto the synthesised PEDOT on a gold disc electrode surface.

The composite materials demonstrated the effect of the presence of AuNPs inside the polymer film. In order to obtain an in-depth understanding of all phenomena associated with this synthetic strategy, electrochemical and spectroscopic characterisation (CV, Raman, UV-vis) was carried out before and after the electrochemical deposition of Au NPs onto PEDOT film. Raman spectroscopic studies revealed that the polymerization of ethylenedioxythiophene leads to the formation of polymer polyethylenedioxythiophene incorporating gold nanoparticles. Electron paramagnetic resonance, EPR, is already known as a very powerful method

for the investigation of the fundamental mechanisms relating to the electronic conduction of polymers. The results show PEDOT both before and after Au deposition and also show structural changes in the polymer backbone. The electrochemical properties of the polymer have been altered and this influences the behaviour and properties of the charge carriers which appear in PEDOT after doping. The movement of electrons and the interpretation of the peaks after the deposition of gold indicate radical formation throughout the polymer chain. A shift from high field to low field in EPR is observed when polymers interact with gold nanostructures, indicating that the electrons are distributed more evenly over the films. In conclusion, this means that the PEDOT-AuNP act as tiny conduction centers and have facilitated the electron transfer throughout the polymer film, which ought to improve the performance of electrochemical biosensors. Morphological characterisation (SEM) of PEDOT revealed a globular porous structure which explains the ease of charge transportation through the polymer film. This concludes that our nucleic acids which have been hybridised onto both the PEDOT and gold nanostructures have gained a high surface area and conductivity.

After all characterisation steps and detection of the hybridisation event, the HRP/ AuNPs/ vapour oxidised PEDOT /electrode show a more sensitive amperometric response for H_2O_2 reduction than the HRP/ AuNPs/ electrochemically or chemically synthesised PEDOT / electrode in the presence of hydroquinone as a mediator. The electrochemical polymerisation is generally preferred due to its advanced conductivity and mechanical properties, however in this work we reported a slightly lower sensitivity in DNA detection than the HRP / AuNPs / vapour oxidised PEDOT / electrode. Low detection of the hybridisation was found for the chemically prepared PEDOT and this could be due to a number of reasons. The drop cast polymer synthesised chemically may not have been stable post Au deposition and may have fallen off. This can lead to loss in surface area and therefore loss in capture DNA immobilisation. Another reason for the poor sensitivity could be that the polymer had no problem adhering to the surface, however the ability to transport enough charge through an insulating layer can be limiting especially if the thickness has increased. Perhaps if more AuNP were deposited, a

sensor conductive enough could be established to collect the same quantitative results as the other two methods. In conclusion, by using electrochemical and vapour oxidation of the polymer PEDOT, we are achieving one of the best ways to increase the sensitivity of the already well established ELISA assay.

Vapour polymerisation which is not typically used in research, showed the higher analytical performance and the best sensitivity towards the *S. aureus* biosensor. The increase in the sensitivity of the DNA detection is not attributed to the crystallization behaviour of PEDOT, but to the change of the resonant structure of PEDOT chain from a 'benzoid' to a 'quinoid' structure, as highlighted in the Raman section, which increased the rigidity of PEDOT chain. In addition, there is a conformational conversion of the PEDOT chains from the coil structure to expanded-coil or linear structure as observed from our Raman spectra. These chains changes are helpful to charge transport through the PEDOT chains and conductivity enhancement of composite films and should perhaps be used in more applications of biosensor research.

5.4 REFERENCES

1. Bjornholm, T.; Greve, D. R.; Reitzel, N.; Hassenkam, T.; Kjaer, K.; Howes, P. B.; Larsen, N. B.; Bogelund, J.; Jayaraman, M.; Ewbank, P. C.; McCullough, R. D. *Journal of the American Chemical Society* **1998**, *120*, 7643-7644.
2. Jonas, F.; Schrader, L. *Synthetic Metals* **1991**, *41*, 831-836.
3. Groenendaal, B. L.; Jonas, F.; Freitag, D.; Pielartzik, H.; Reynolds, J. R. *Advanced Materials* **2000**, *12*, 481-494.
4. Heywang, G.; Jonas, F. *Advanced Materials* **1992**, *4*, 116-118.
5. Dietrich, M.; Heinze, J.; Heywang, G.; Jonas, F. *Journal of Electroanalytical Chemistry* **1994**, *369*, 87-92.
6. Winter, I.; Reese, C.; Hormes, J.; Heywang, G.; Jonas, F. *Chemical Physics* **1995**, *194*, 207-213.
7. Pei, Q. B.; Zuccarello, G.; Ahlskog, M.; Inganas, O. *Polymer* **1994**, *35*, 1347-1351.
8. Selvaganesh, S. V.; Mathiyarasu, J.; Phani, K. L. N.; Yegnaraman, V. *Nanoscale Research Letters* **2007**, *2*, 546-549.
9. Chan, H. S. O.; Ng, S. C. *Progress in Polymer Science* **1998**, *23*, 1167-1231.
10. Pettersson, L. A. A.; Carlsson, F.; Inganas, O.; Arwin, H. *Thin Solid Films* **1998**, *313*, 356-361.
11. Łapkowski, M.; Pron, A. *Synthetic Metals* **2000**, *110*, 79-83.
12. Wallace, G. G.; Spinks, G. M.; Kane-Maguire, L. A. P. **2002**, *Conductive Electroactive Polymers: Intelligent Materials Systems, Second Edition*, 224.

13. Vos, J. G.; Forster, R. J.; Keyes, T. E. **2003**, *Interfacial Supramolecular Assemblies*, 408.
14. Li, Y. G.; Lasia, A. *Journal of Applied Electrochemistry*. **1997**, 27, 643-650.
15. Zhong, X.; Yuan, R.; Chai, Y. Q.; Dai, J. Y.; Liu, Y.; Tang, D. P. *Analytical Letters* **2005**, 38, 1085-1097.
16. Shen, Y.; Gong, S.; Zhou, W.; Li, J. *Colloids and Surfaces A: Physicochemical and Engineering Aspects* **2005**, 257-258, 149-154.
17. Serafín, V.; Agüí, L.; Yáñez-Sedeño, P.; Pingarrón, J. M. *Journal of Electroanalytical Chemistry, In Press, Corrected Proof*.
18. Martin, D. C.; Wu, J.; Shaw, C. M.; King, Z.; Spanninga, S. A.; Richardson-Burns, S.; Hendricks, J.; Yang, J. *Polymer Reviews* **2010**, 50, 340-384.
19. Xia, J.; Masaki, N.; Jiang, K.; Yanagida, S. *Journal of Materials Chemistry* **2007**, 17, 2845-2850.
20. Wang, Y.; Liu, Z. M.; Han, B. X.; Sun, Z. Y.; Huang, Y.; Yang, G. Y. *Langmuir* **2005**, 21, 833-836.
21. Harish, S.; Mathiyarasu, J.; Phani, K. L. N.; Yegnaraman, V. *Journal of Applied Electrochemistry*. **2008**, 38, 1583-1588.
22. Ner, Y.; Invernale, M. A.; Grote, J. G.; Stuart, J. A.; Sotzing, G. A. *Synthetic Metals*. **2010**, 160, 351-353.
23. Zotti, G.; Schiavon, G.; Zecchin, S.; Berlin, A.; Pagani, G.; Canavesi, A. *Synthetic Metals*. **1996**, 76, 255-258.
24. Kim, D. Y.; Choi, J. H.; Kim, S. H.; Cho, H. N.; Kim, C. Y. *Synthetic Metals*. **1997**, 84, 161-162.
25. Zheng HuaJing; Jiang YaDong; Xu JianHua; Yang YaJie *Science China-Technological Sciences* **2010**, 53, 2355-2362.
26. Cho, M.; Kim, S.; Kim, I.; Kim, B.; Lee, Y.; Nam, J. *Macromolecular Research* **2010**, 18, 1070-1075.

27. Pacios, R.; Marcilla, R.; Pozo-Gonzalo, C.; Pomposo, J. A.; Grande, H.; Aizpurua, J.; Mecerreyes, D. *Journal of Nanoscience and Nanotechnology* **2007**, *7*, 2938-2941.
28. Kim, T.; Kim, J.; Kim, Y.; Lee, T.; Kim, W.; Suh, K. S. *Current Applied Physics* **2009**, *9*, 120-125.
29. Saunders, B. R.; Murray, K. S.; Fleming, R. J.; McCulloch, D. G.; Brown, L. J.; Cashion, J. D. *Chemistry of Materials* **1994**, *6*, 697-706.
30. Goto, H.; Nomura, N.; Akagi, K. *Journal of Polymer Science Part A-Polymer Chemistry* **2005**, *43*, 4298-4302.
31. Mukherjee, P.; Nandi, A. K. *Journal of Colloid and Interface Science*. **2011**, *356*, 145-150.
32. Winther-Jensen, B.; Forsyth, M.; West, K.; Andreasen, J. W.; Bayley, P.; Pas, S.; MacFarlane, D. R. *Polymer* **2008**, *49*, 481-487.
33. Winther-Jensen, B.; Winther-Jensen, O.; Forsyth, M.; MacFarlane, D. R. *Science* **2008**, *321*, 671-674.
34. Winther-Jensen, B.; Forsyth, M.; West, K.; Andreasen, J. W.; Wallace, G.; MacFarlane, D. R. *Organic Electronics* **2007**, *8*, 796-800.
35. Winther-Jensen, B.; Chen, J.; West, K.; Wallace, G. *Macromolecules* **2004**, *37*, 5930-5935.
36. Winther-Jensen, B.; West, K. *Macromolecules* **2004**, *37*, 4538-4543.
37. Ouyang, J.; Chu, C. W.; Chen, F. C.; Xu, Q. F.; Yang, Y. *Journal of Macromolecular Science-Pure and Applied Chemistry* **2004**, *A41*, 1497-1511.
38. Garreau, S.; Duvail, J. L.; Louarn, G. *Synthetic Metals*. **2001**, *125*, 325-329.
39. Huh, P.; Kim, S.; Kim, Y.; Kumar, J.; Kim, B.; Jo, N.; Lee, J. *Polymer Engineering & Science*. **2007**, *47*, 71-75.

40. Tran-Van, F.; Garreau, S.; Louarn, G.; Froyer, G.; Chevrot, C. *Journal of Materials Chemistry* **2001**, *11*, 1378-1382.
41. Yin, K.; Zhu, Z. *Synthetic Metals*. **2010**, *160*, 1115-1118.
42. Zykwinska, A.; Domagala, W.; Czardybon, A.; Pilawa, B.; Lapkowski, M. *Chemical Physics*. **2003**, *292*, 31-45.
43. Sakmeche, N.; Aaron, J. J.; Fall, M.; Aeiyaeh, S.; Jouini, M.; Lacroix, J. C.; Lacaze, P. C. *Chemical Communications* **1996**, , 2723-2724.
44. Harish, S.; Mathiyarasu, J.; Phani, K. L. N. *Materials Research Bulletin*. **2009**, *44*, 1828-1833.
45. Semaltianos, N. G.; Logothetidis, S.; Hastas, N.; Perrie, W.; Romani, S.; Potter, R. J.; Dearden, G.; Watkins, K. G.; French, P.; Sharp, M. *Chemical Physics Letters* **2010**, *484*, 283-289.
46. Tong, L.; Li, C.; Chen, F.; Bai, H.; Zhao, L.; Shi, G. *The Journal of Physical Chemistry C*. **2009**, *113*, 7411-7415.
47. Yamato, H.; Ohwa, M.; Wernet, W. *Journal of Electroanalytical Chemistry* **1995**, *397*, 163-170.
48. Estrany, F.; Aradilla, D.; Oliver, R.; Aleman, C. *European Polymer Journal* **2007**, *43*, 1876-1882.
49. Zykwinska, A.; Domagala, W.; Pilawa, B.; Lapkowski, M. *Electrochimica Acta* **2005**, *50*, 1625-1633.
50. Moskwa, T.; Domagala, W.; Czardybon, A.; Pilawa, B.; Lapkowski, A. *Synthetic Metals*. **2005**, *152*, 189-192.
51. Kros, A.; Sommerdijk, N. A. J. M.; Nolte, R. J. M. *Sensors and Actuators B-Chemical* **2005**, *106*, 289-295.
52. Pereira da Silva, J. E.; De Faria, D. L. A.; Cordoba de Torresi, S. I.; Temperini, M. L. A. *Macromolecules* **2000**, *33*, 3077-3083.

53. Pereira da Silva, J. E.; Temperini, M. L. A.; Córdoba de Torresi, S. I. *Electrochimica Acta* **1999**, *44*, 1887-1891.
54. Mentus, S.; Ciric-Marjanovic, G.; Trchova, M.; Stejskal, J. *Nanotechnology* **2009**, *20*, 245601.
55. Golczak, S.; Kanciurzevska, A.; Langer, J. J.; Fahlman, M. *Polymer Degradation and Stability*. **2009**, *94*, 350-354.
56. Wallace, G. G.; Spinks, G. M.; Teasdale, P. R.; Editors **1996**, L.A.P., , 169.
57. Haller, P. D.; Flowers, C. A.; Gupta, M. *Soft Matter* **2011**, *7*, 2428-2432.



CHAPTER 6

CONCLUSIONS AND FUTURE WORK

6.1 Summary

Thanks to the deep research of genes, we are experiencing an innovative era of medicine design and disease diagnosis, namely personalised medicine and early-stage disease diagnostics. Personalized medicine designs a medicine according to the specific conditions occurring within a specific person, whereas current medicine design depends on statistical models. FDA-approved medicine has only 40% to 60% possibility of affecting a targeted disease and therefore, doctors are trained to prescribe 'average' types and dosage of drugs to patients and develop the "optimal" dosage regimen for a patient largely via a trial and error process. This approach often leads to adverse drug reactions (ADR) that can cause serious injuries and deaths.

When dealing with life-threatening illnesses, such a trial and error approach is unacceptable and therefore it is crucial to get the diagnosis right the first time as many drugs have potentially serious side effects. By taking advantage of personalised medicines, the right dose of the right drug to the right patient at the right time is achieved. Personalised medicine will enable doctors as well as patients to make informed decisions about treatments that will deliver maximum therapeutic benefit, with the minimum amount of toxicity.

Early-stage disease diagnosis also shows paramount importance. The discovery of a disease is often reported by observed illness in a patient (especially mastitis), caused by the long term effects of the disease. Numerous life-threatening illnesses, such as mastitis, do not manifest detectable symptoms till they are well established and incurable rates are high. Fortunately, mastitis as well as many of life-threatening diseases are curable in their early-stages. Therefore, to fully cure these diseases or even prevent them, diagnosing diseases in their earliest stage is the main aim of this research.

This thesis focuses on the development of a sensitive electrochemical sensor for single stranded DNA (ss-DNA) detection. As the concentrations of the analytes are extremely low at the early stage of any disease, an increased

sensitivity and lower limits of detection are essential for successful detection. Biosensors are promising devices which are convenient over traditional analytical techniques as they are highly specific, fast response, portable and simple to operate analytical tools. It is clear that they will have a major role in the field of self-care or point of care in the next decade. Thus, this work is focused on improving the detection sensitivity of DNA biosensors or genosensors.

Following chapters that review the current state-of-the-art and present the experimental strategies employed, Chapter 3 reported on the electrodeposition of gold nanoparticles on a gold disc electrode to provide a nanostructured surface for the formation of alkanethiol based DNA SAMs. The ss-DNA of interest is from the mastitis causing pathogen *Staphylococcus aureus* (target DNA). Biosensor signals can be enhanced by specifically designing transducer surfaces with the objective of providing the best environment to the target DNA. This is particularly evident in the case of biosensors, where spacing and orientation of immobilised DNA capture probes need to be carefully controlled to maximise subsequent surface hybridisation with the target sequence and achieve high binding responses. In order to optimise the immobilisation and hybridisation processes, parameters such as the immobilisation buffer used and the HRP labelled DNA hybridisation time were investigated. It is found that by selecting a 1 M NaCl-TE immobilisation buffers as well as optimising the hybridisation times of HRP labelled DNA to the concentration of the target analyte, a significantly improved response can be obtained. To further address the spacing and orientation requirements, electrode surface modification methods were exploited for the development of electrochemical biosensors to alleviate problems related to surface crowding of capture probes and the creation of a suitable environment for enhancement of the biorecognition events. Electrode surface modification using deposited gold nanoparticles for signal enhancement and improving sensitivity of the DNA biosensor was demonstrated. SAMs of 15 base thiolated DNA capture probe formed on the NP functionalised surface were employed for the detection of a 41 bases target oligonucleotides using horseradish peroxidase as enzymatic labelled DNA. The electrochemical signal recorded at the nanostructured interface was compared against a gold planar electrode. In this approach,

captured target DNA is detected by complementary strand binding to HRP labelled DNA and the nanostructured electrode resulted in a 4.5 fold signal enhancement compared to the signal recorded using a planar gold electrode. The AuNPs modified electrode using a 1 M NaCl-TE immobilisation buffer exhibited sensitivity of 200 (nA^{-1}) and a limit of detection around 160 fM, whereas for the unmodified gold electrodes the sensitivity was 44 nA^{-1} with a limit of detection of about 650 fM. In future work, further investigation on the control of surface density and orientation of probe molecules could be crucial for extracting the required signal as a result of the interaction with the target DNA/RNA sequence. The parameters developed in this study may find applications in other biosensor applications such as immunosensors and aptamer based sensors.

The extension of these findings for the successful development of low cost biosensors is crucial. Hence, electrodes modified with polyaniline-gold nanocomposites (PANI-AuNP) were used for the detection of HRP labelled DNA in Chapter 4. Here, a PANI-AuNP electrode is fabricated that couples the femtomolar detection limits of the optimised PANI film with the single-step convenience of AuNP electrodeposition for the DNA sensing platform. This work demonstrates the use of PANI for DNA sequence detection using conventional electrochemical instrumentation. The combination of the electropolymerisation of PANI and the electrodeposition of AuNPs provides a powerful yet relatively simple method of fabricating high sensitivity, highly specific genosensors. This PANI - AuNP nanostructured surfaces showed a greater analytical performance than the unmodified gold electrode. Significantly, the sensitivity of the DNA detection is approximately 62 fold greater for the PANI-AuNP (slope of $3.14 \mu\text{A}^{-1}$) modified electrodes compared to the DNA on the unmodified electrode surface (slope of $0.05 \mu\text{A}^{-1}$). It demonstrates superior sensitivity with a detection limit of target of 1.12 fM (LOD of planar gold = 0.645 pM), which is one of the most sensitive methods reported for the detection and analysis of DNA.

The formation mechanisms of PEDOT conducting polymer micro/nanostructures fabricated by different methods were investigated.

Chapter 5 highlights the effect and importance of the properties of the synthesized PEDOT films and a thorough understanding of the formation mechanisms of the various syntheses was also carried out. Very few papers are available on the vapour polymerisation of PEDOT, yet this method of oxidation of the conducting polymer has shown the highest analytical performance and the best sensitivity towards the *S. aureus* biosensor, when compared to conventional electrochemical and chemical synthesis. Characterisation of the vapour oxidised PEDOT shows that this material is distinctively different from the electrochemical and chemical polymerisation form. Different properties such as UV-Vis, EPR, Raman as well as the electrochemical detection are exhibited. The increase in the sensitivity of the DNA detection is not attributed to the crystallization behaviour of PEDOT, but to the change of the resonant structure of PEDOT chain from a 'benzoid' to a 'quinoid' structure, as highlighted in the Raman section, which increased the rigidity of PEDOT chain. The porous PEDOT-AuNPs modified electrode exhibited sensitivity of $4.07 \mu\text{A}^{-1}$ and a detection limit of 3.8 fM. The vapour synthesis of PEDOT in the absence of gold gave a substantial sensitivity of $1.18 \mu\text{A}^{-1}$ with a limit of detection of 34 fM. For future design, fabrication and characterisation of biosensors, the electronic, structural and electrochemical properties as well as the noticeable effects on the PEDOT surface after modification, must be fully explored.

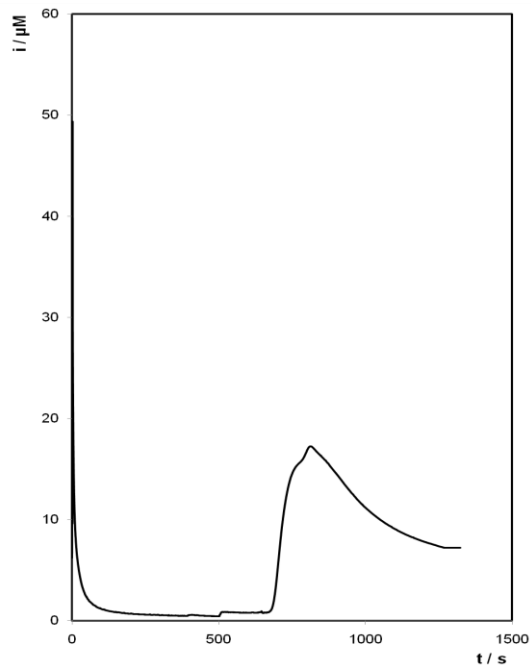
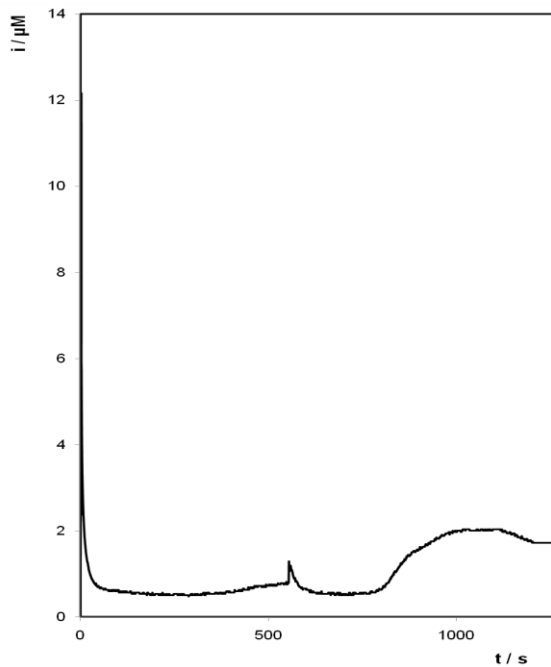
Based on the achievements discussed in previous chapters, it is concluded that AuNPs/conducting polymer sensors are capable of deploying fast and ultra-low-cost DNA detection, thus achieve widely accessible DNA analysis toolkits for early-stage disease diagnosis and personalised medicine. The power of our sensor system is made even apparent by comparing the protocols used herein with conventional protocols. Three critical steps exist in both protocols, namely immobilization, hybridization and signal readout. In conventional protocols, both immobilization and hybridization are time-consuming steps because they require multi-step complex chemical reactions. Meanwhile, using this new platform, the most time-consuming portion is the immobilisation step (5 hours).



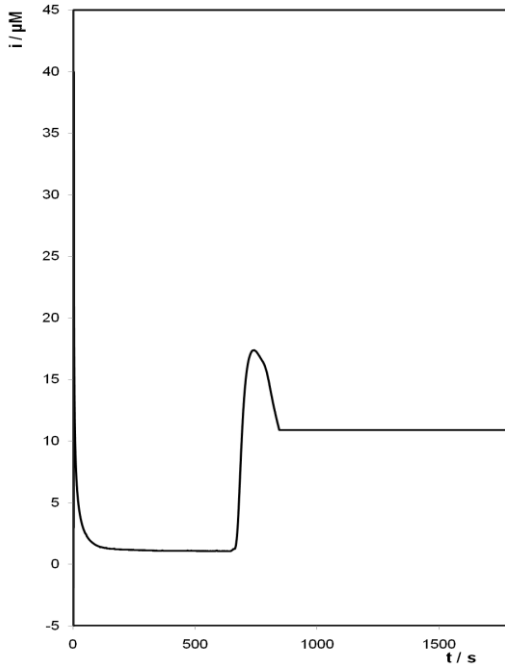
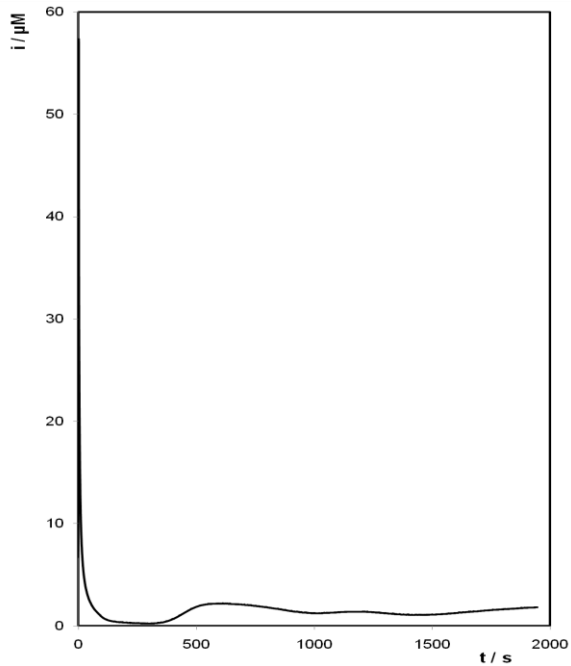
APPENDIX B

i-t curves for the detection of DNA from 150 pM to 1 μ M after the electrochemical polymerisation of PANI with (column 1) and without (column 2) AuNPs

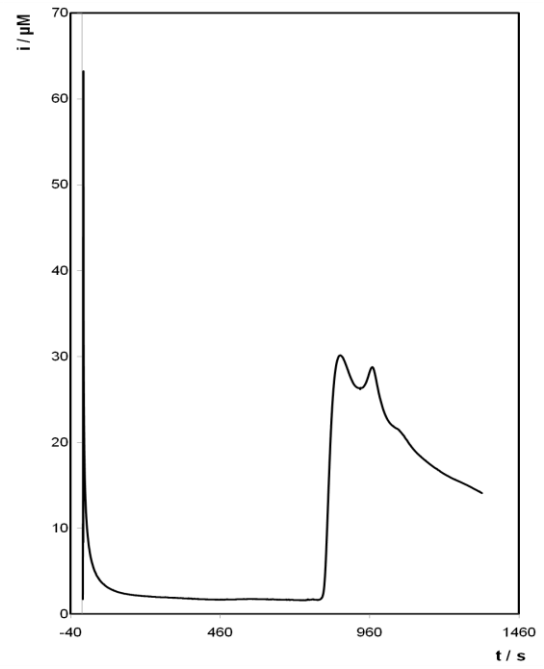
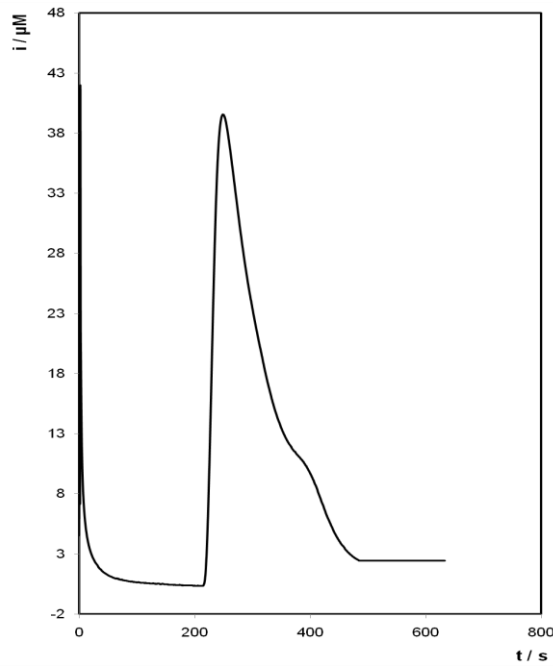
150 pM



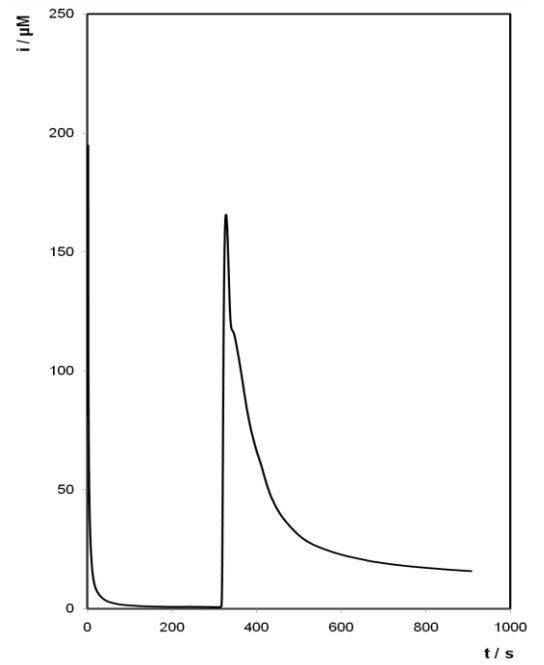
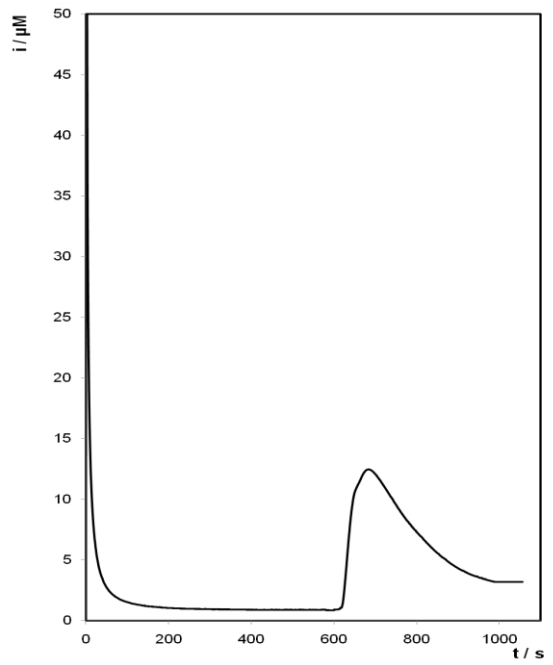
1nM



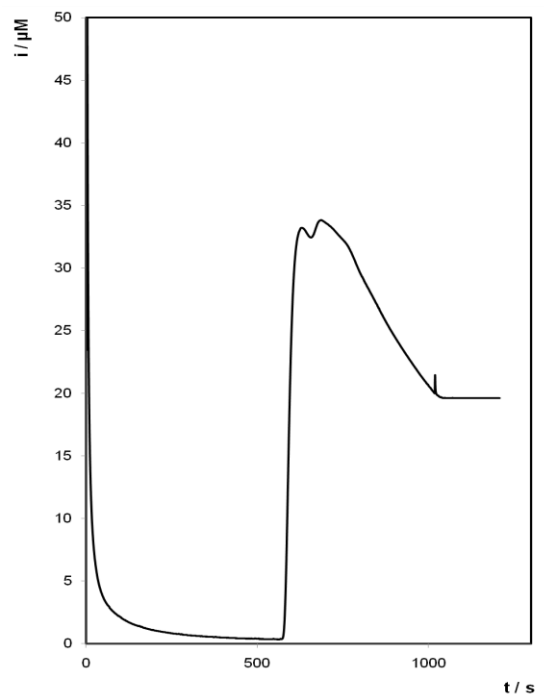
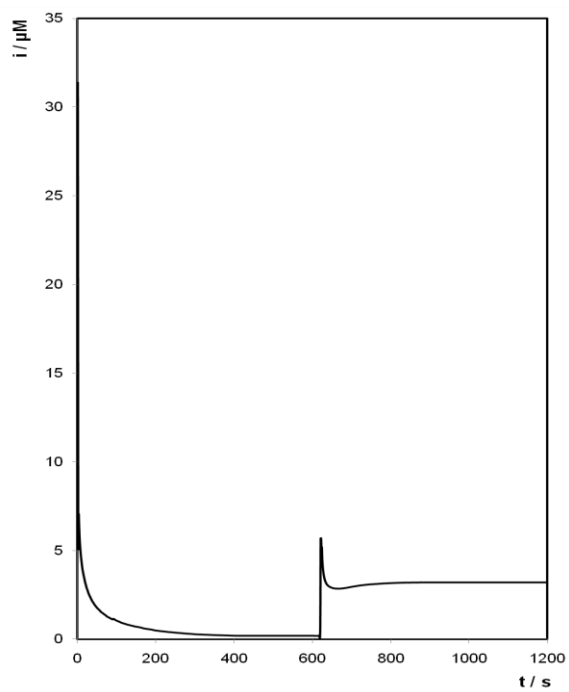
10 nM



100 nM

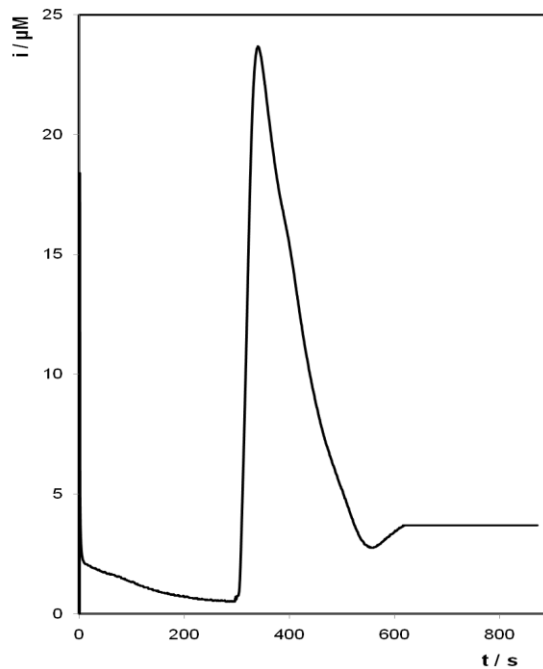
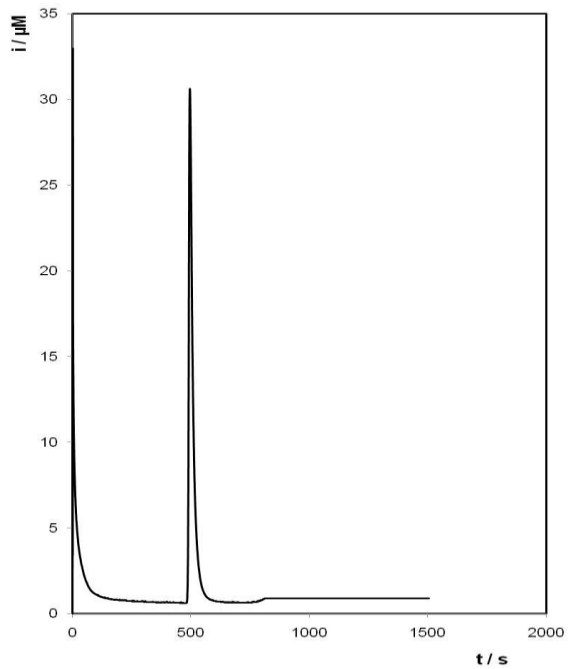


1 μM

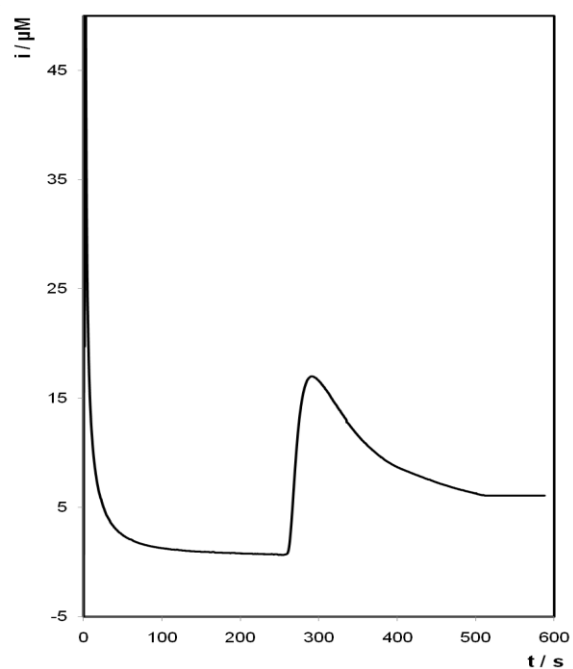
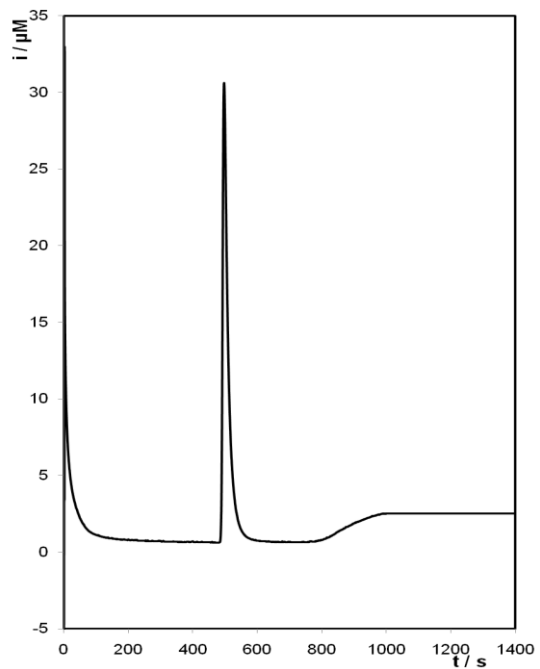


i-t curves for the detection of DNA from 150 pM to 1 μ M after vapour polymerisation of PANI with (column 1) and without (column 2) AuNPs.

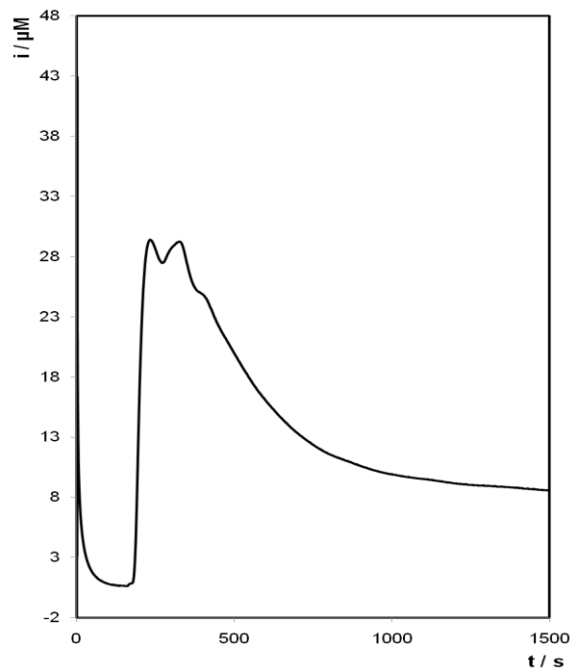
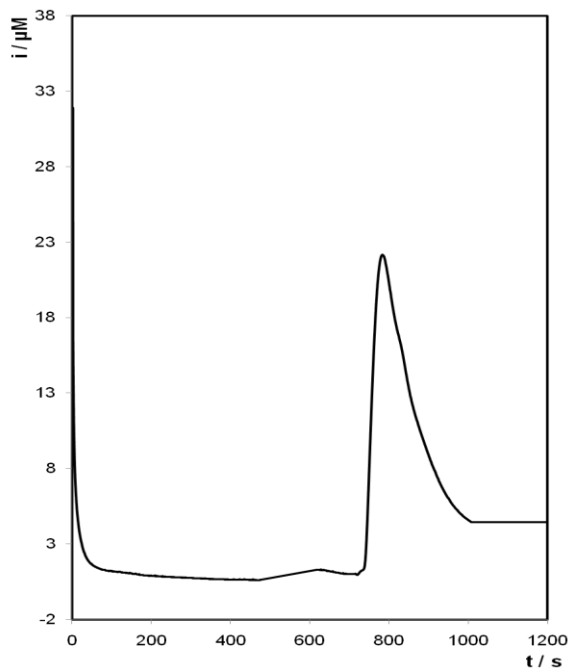
150 pM



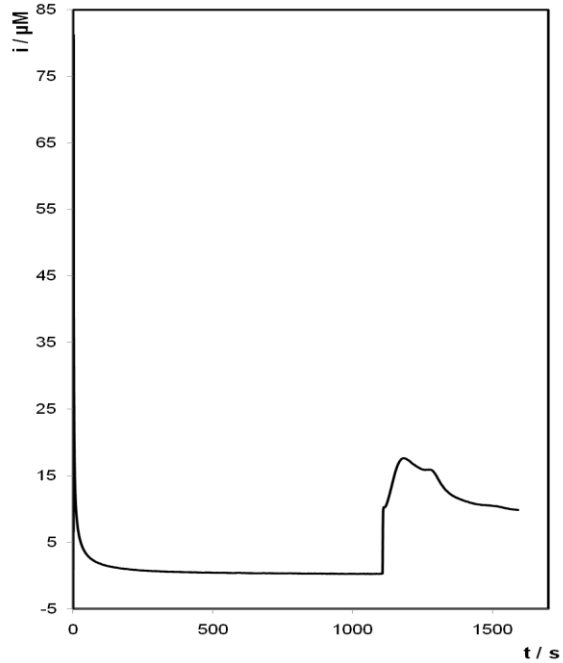
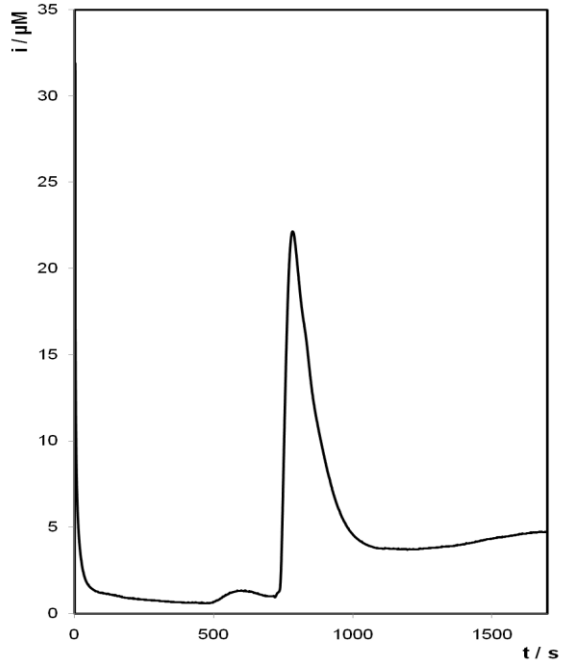
1 nM



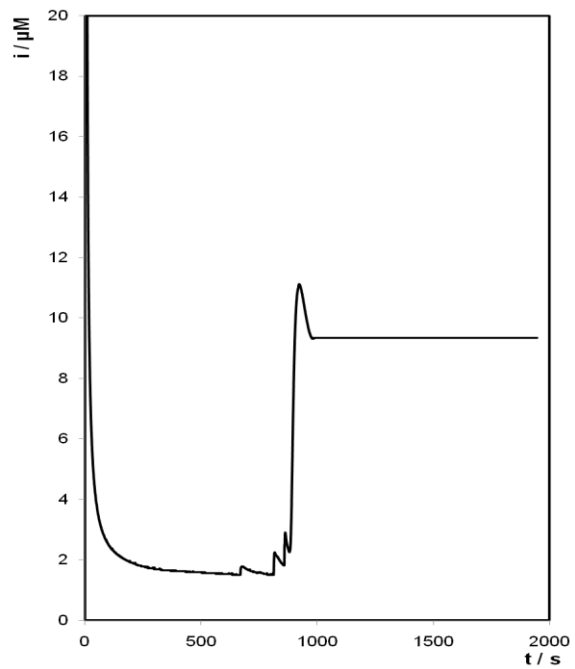
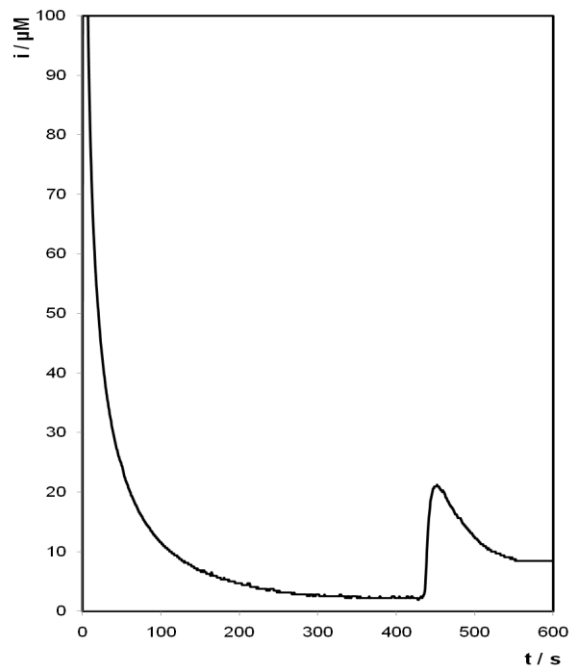
10 nM



100 nM

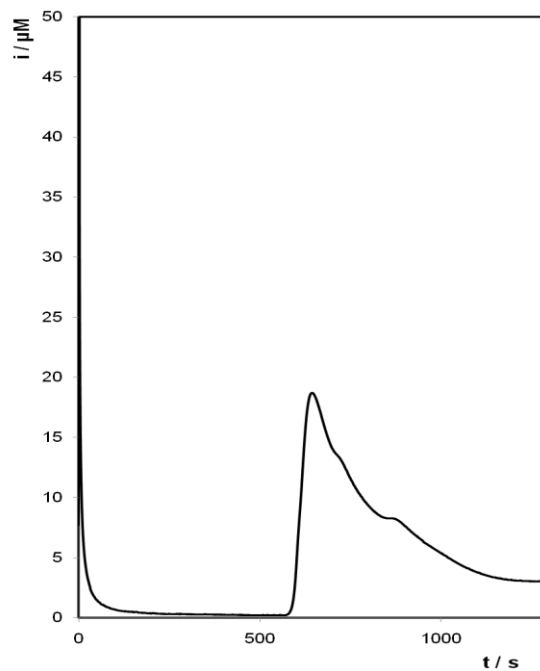
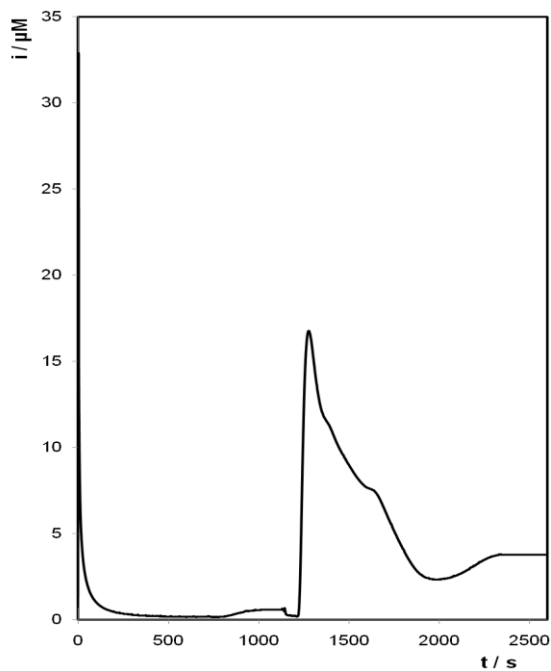


1 μM

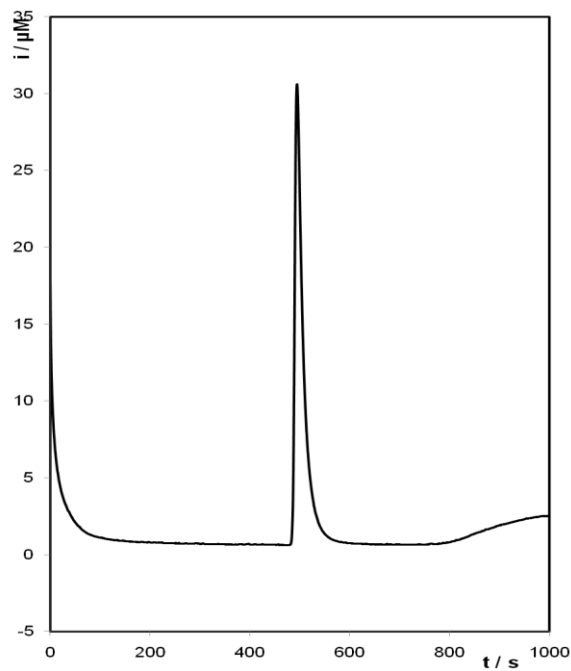
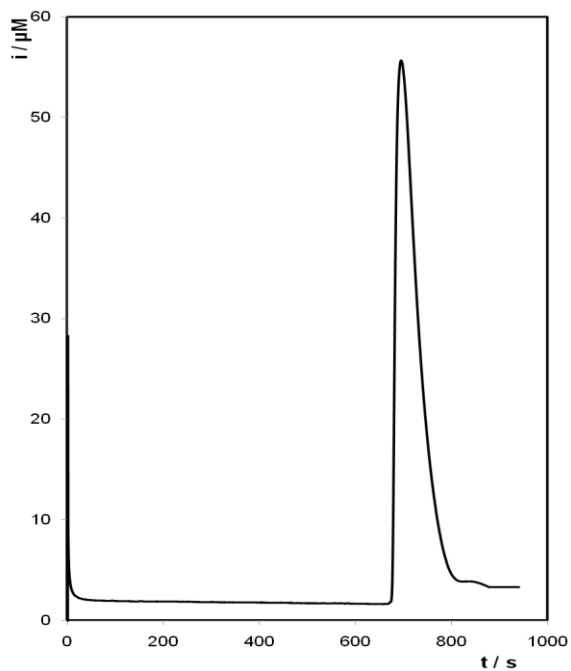


i-t curves for the detection of DNA from 150 pM to 1 μ M after the chemical polymerisation of PANI with (column 1) and without (column 2) AuNPs

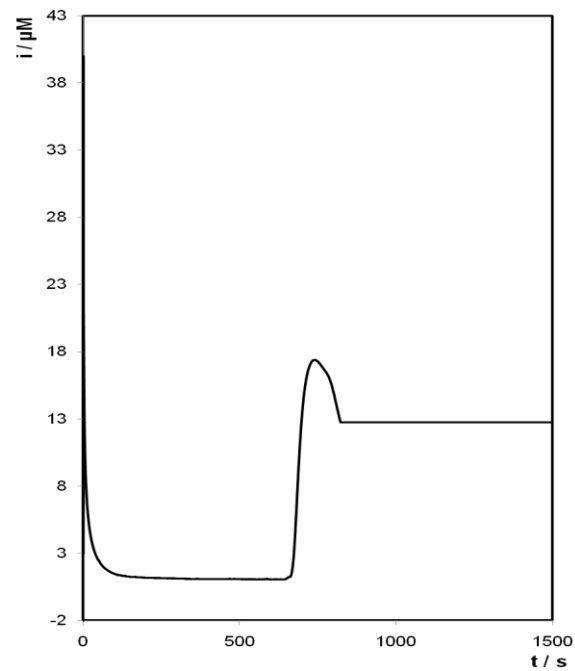
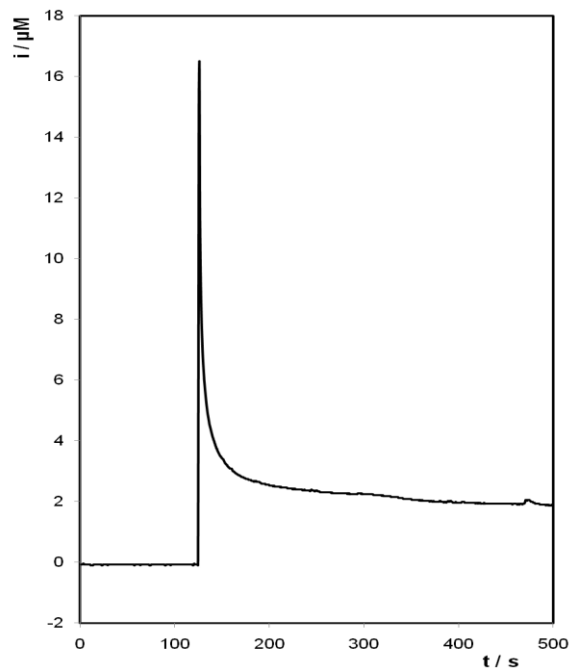
150 pM



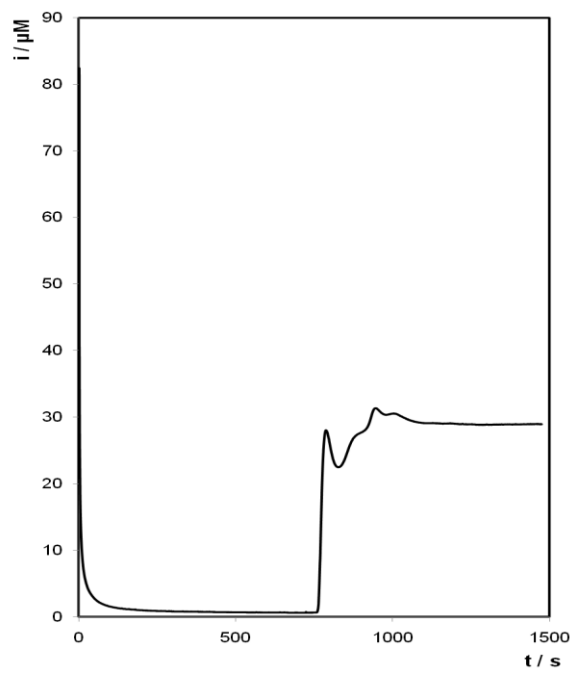
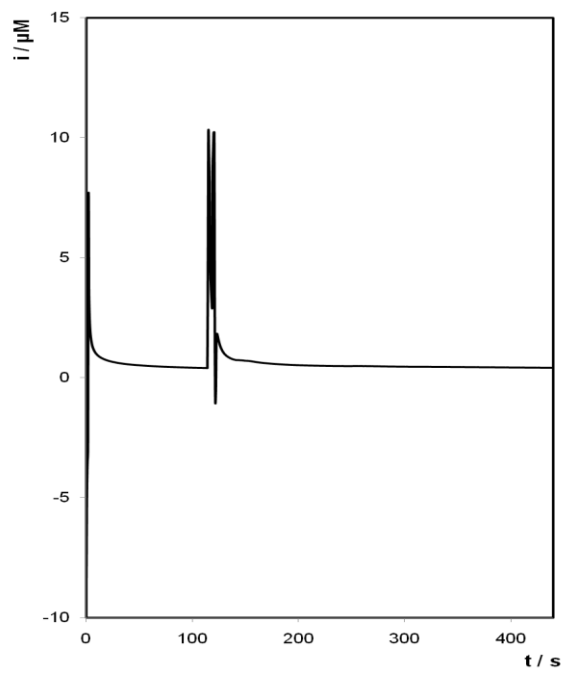
1 nM



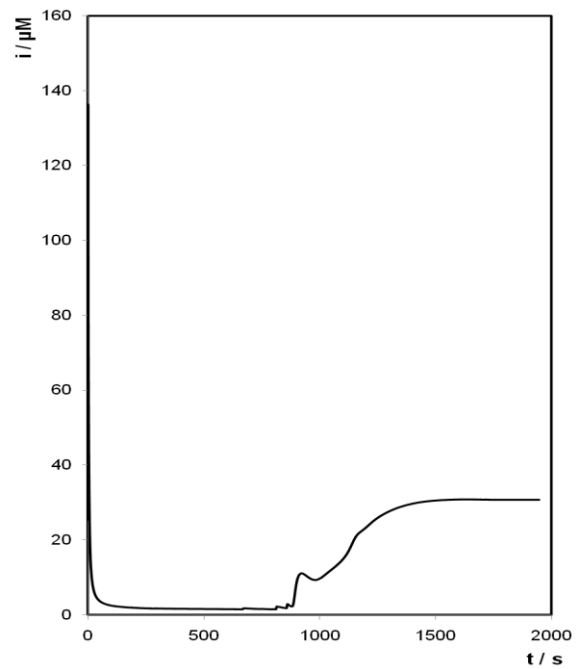
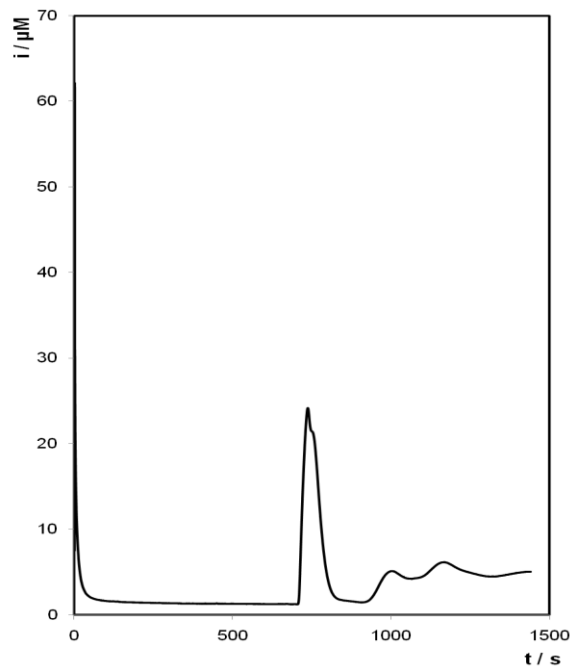
10 nM



100 nM



1 μ M

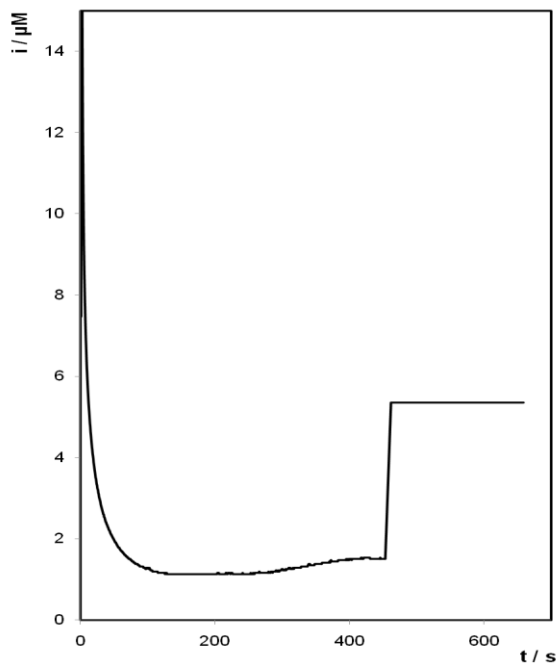
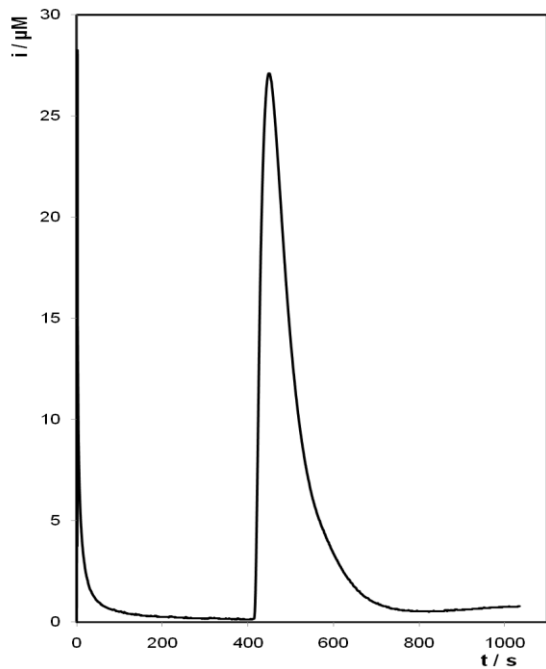




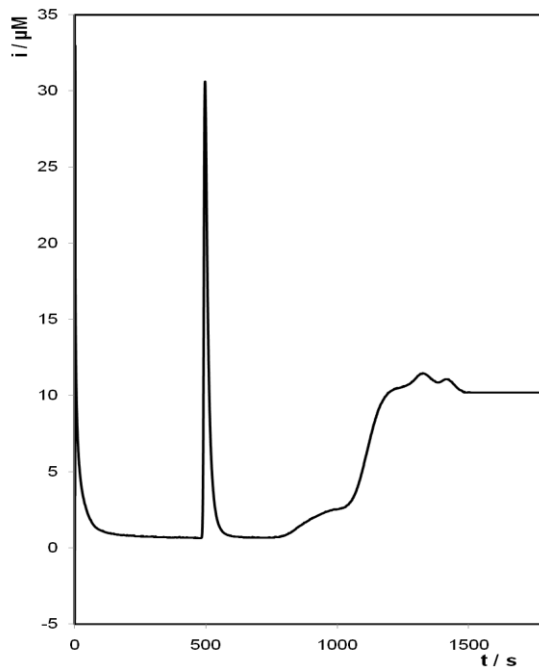
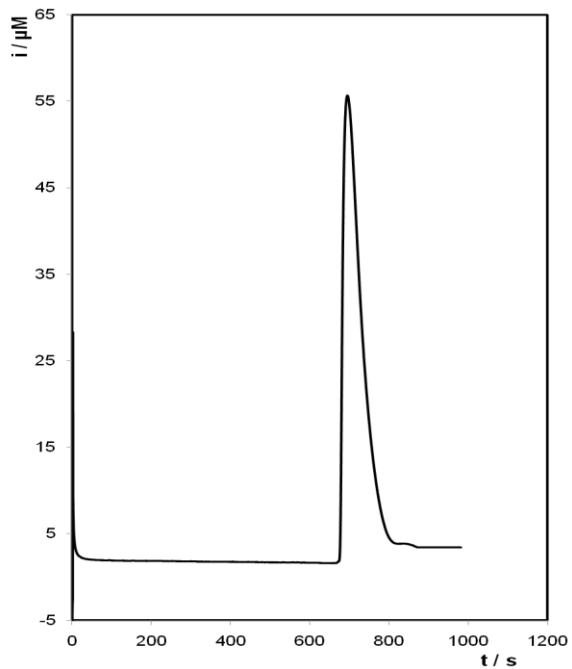
APPENDIX C

i-t curves for the detection of 150 pM to 1 μ M DNA after the electrochemical polymerisation of PEDOT with (column 1) and without (column 2) AuNPs

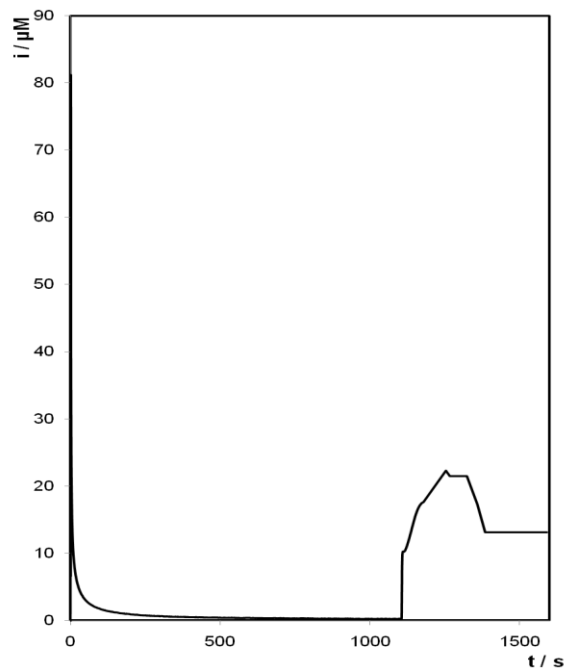
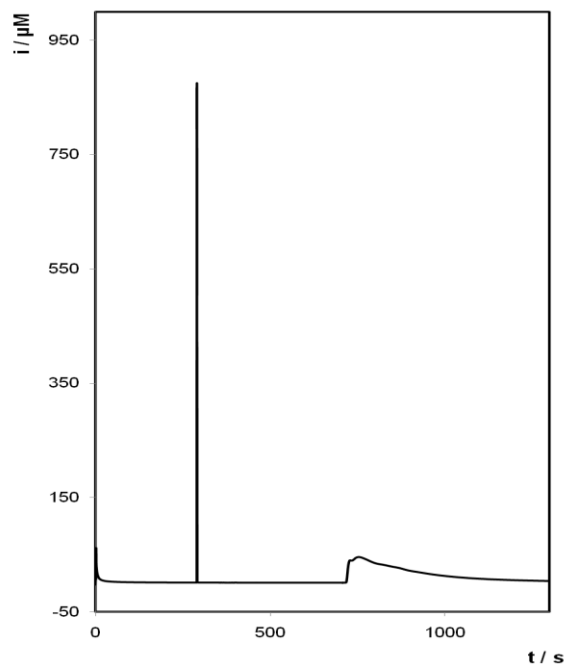
150 pM



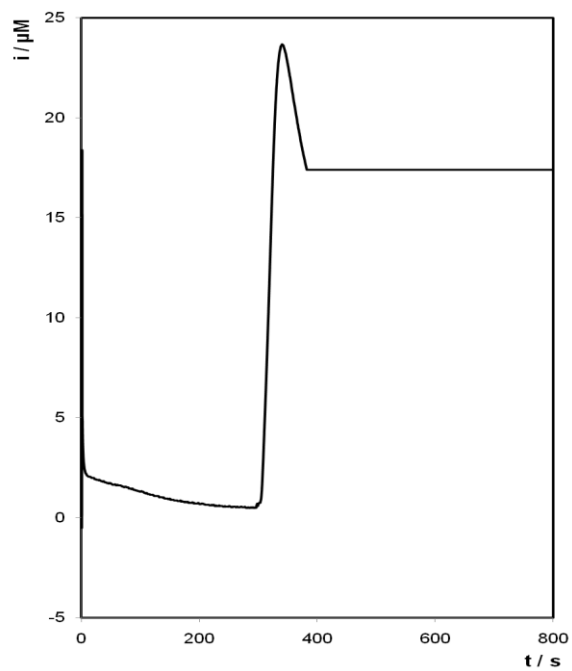
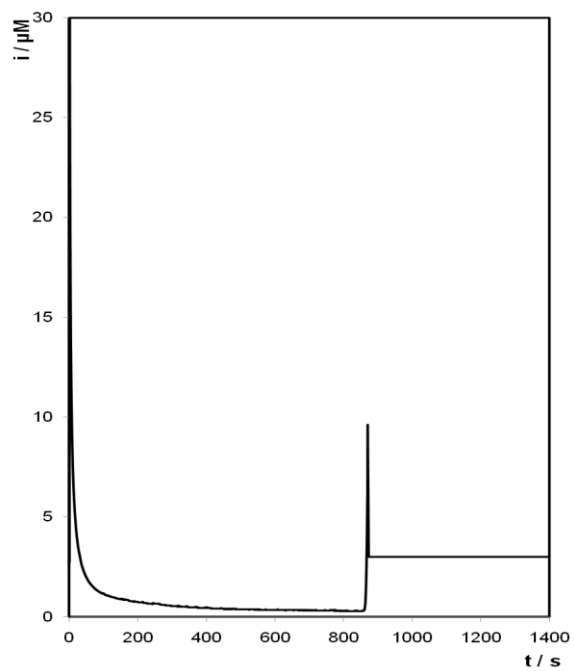
1nM



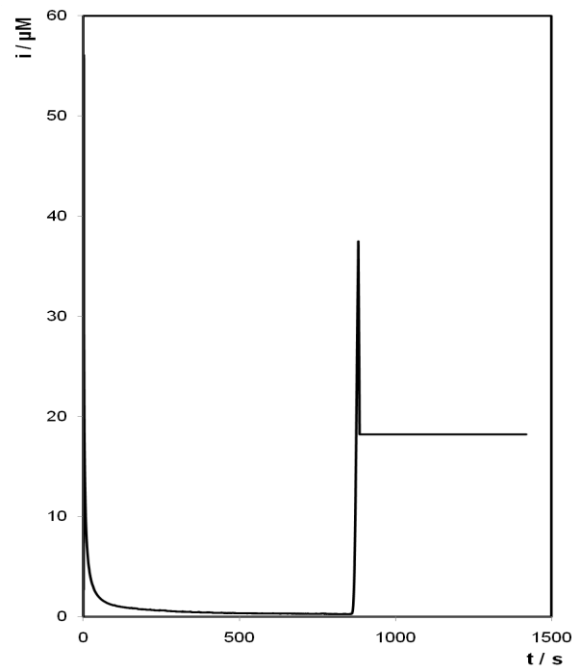
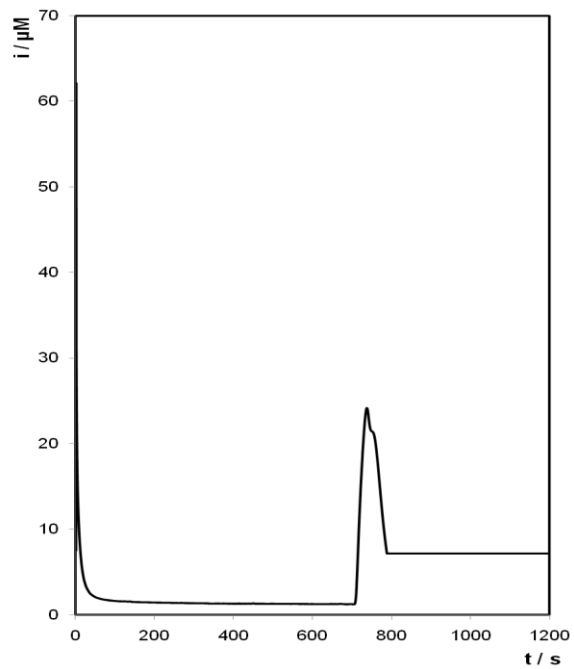
10 nM



100 nM

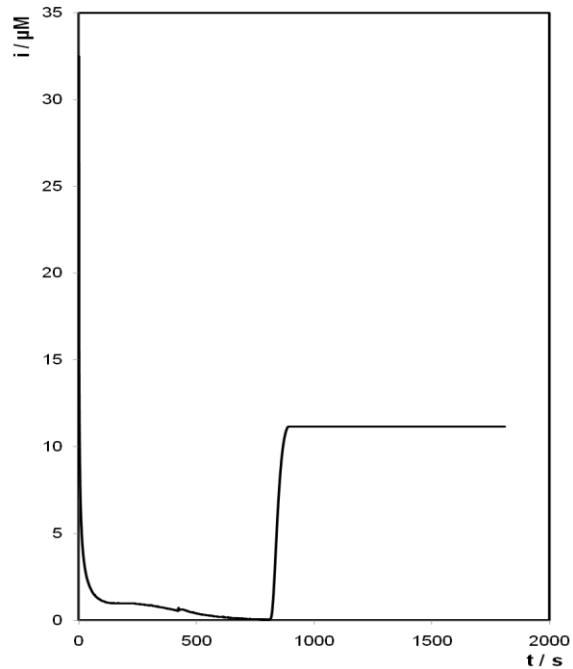
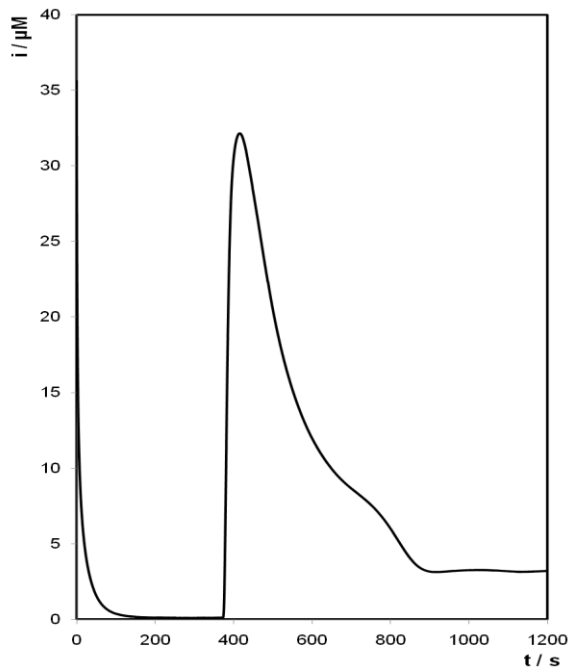


1 μ M

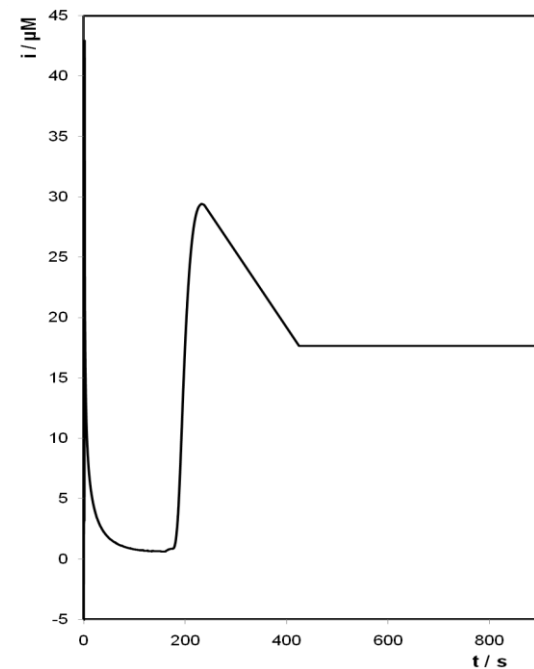
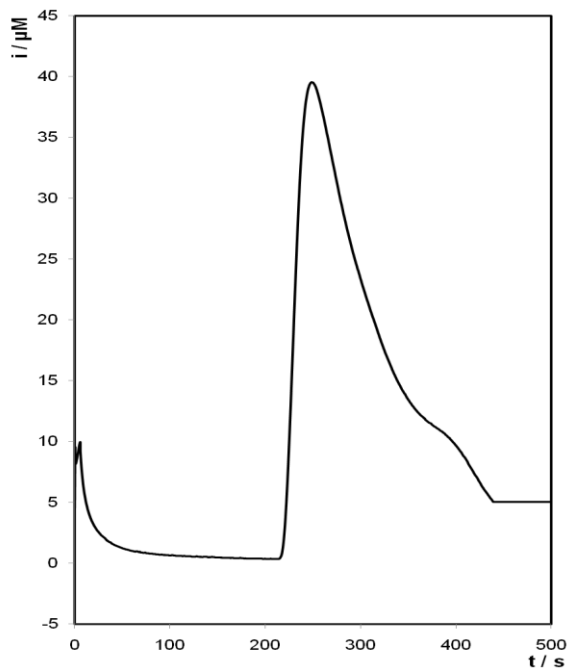


i-t curves for the detection of 150 pM to 1 μ M DNA after vapour polymerisation of PEDOT with (column 1) and without (column 2) AuNPs.

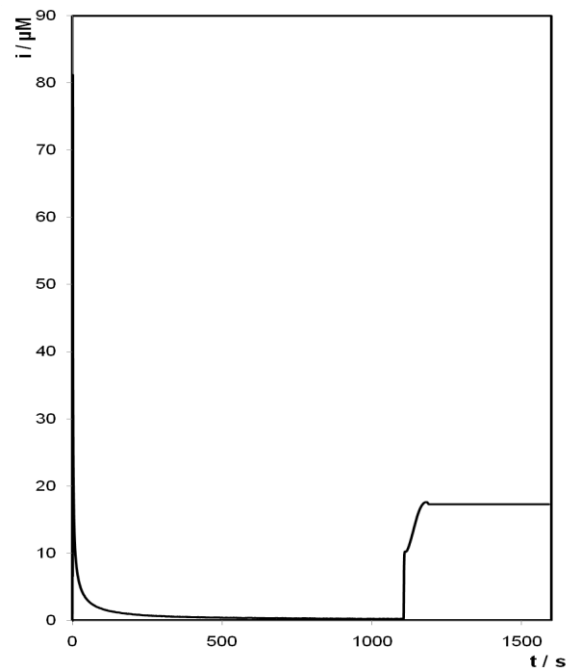
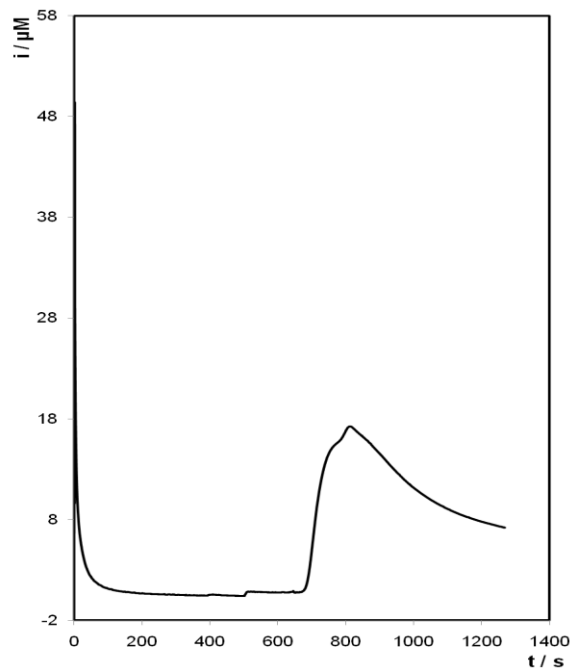
150 pM



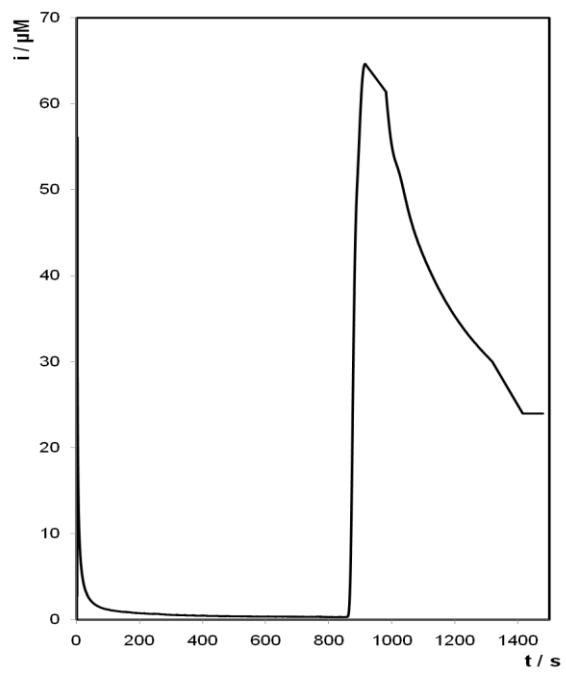
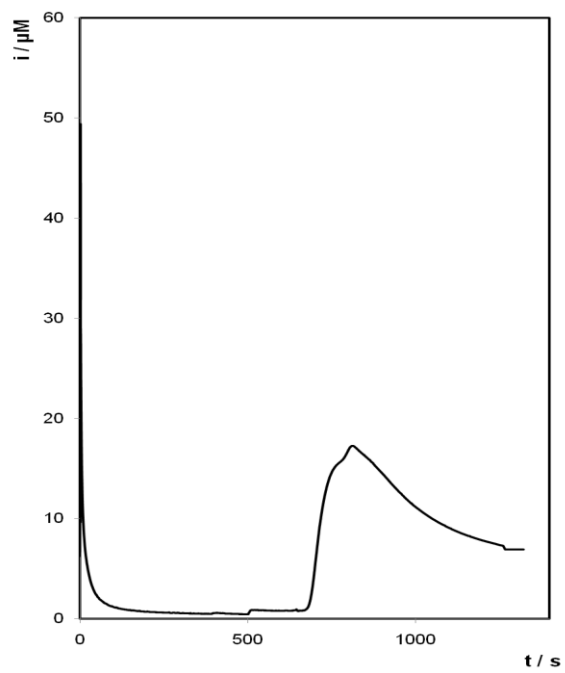
1 nM



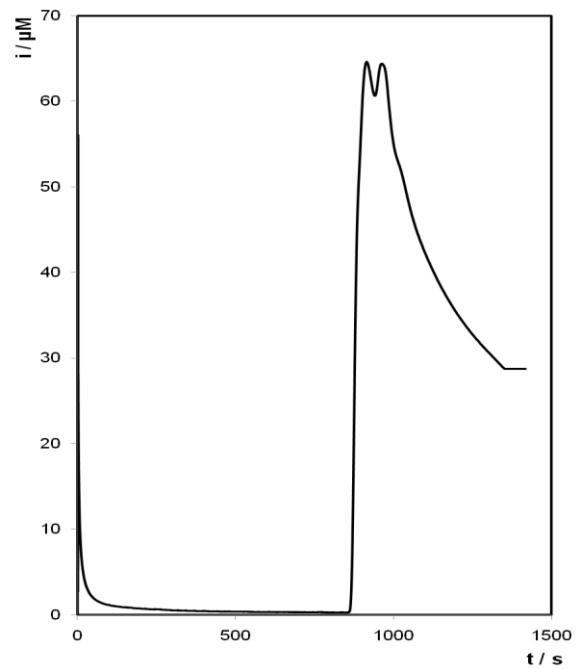
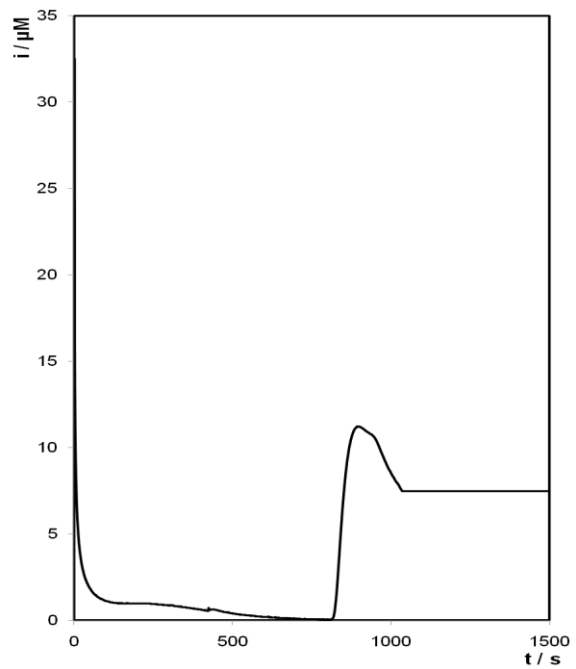
10 nM



100 nM

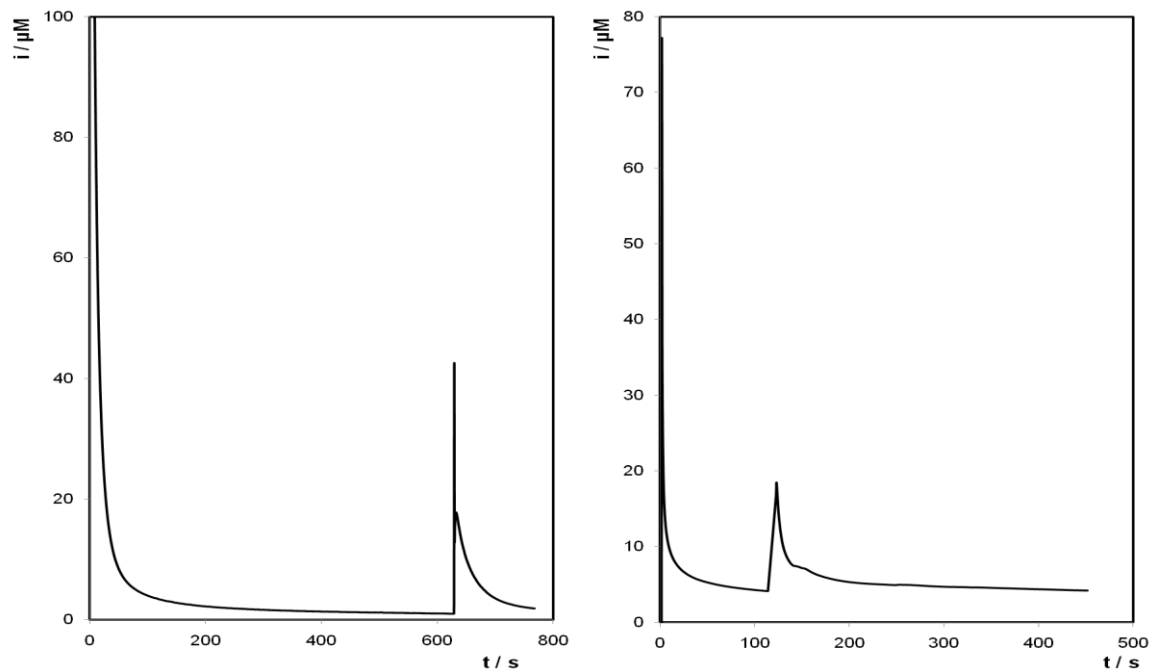


1 μ M

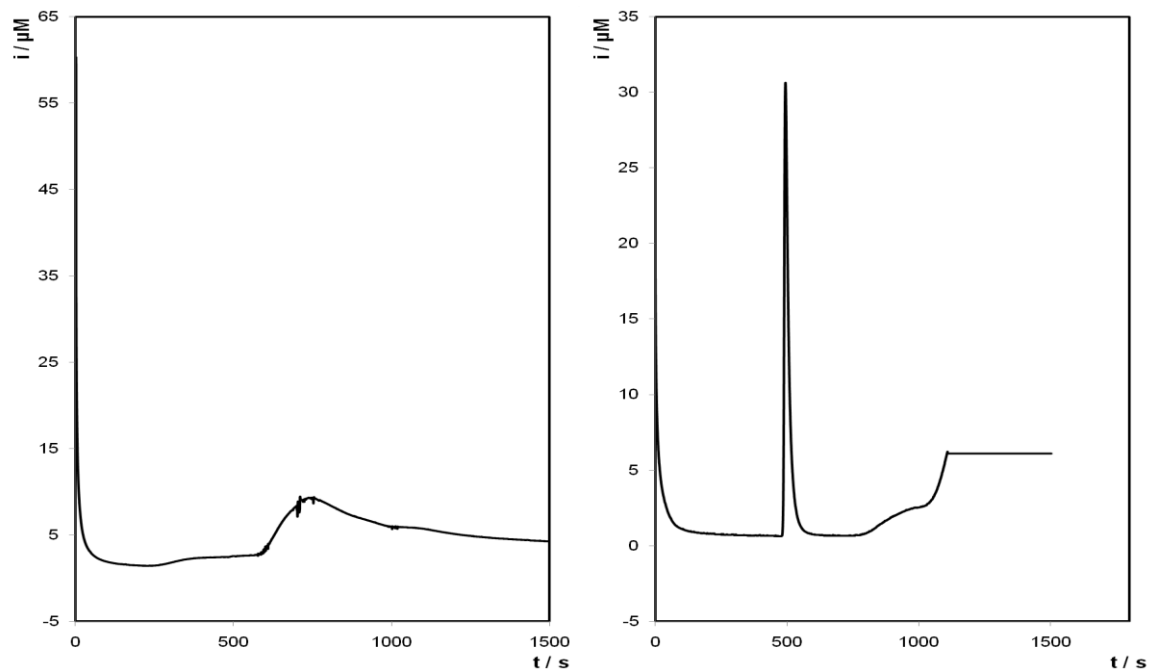


i-t curves for the detection of 150 pM to 1 μM DNA after the chemical polymerisation of PEDOT with (column 1) and without (column 2) AuNPs

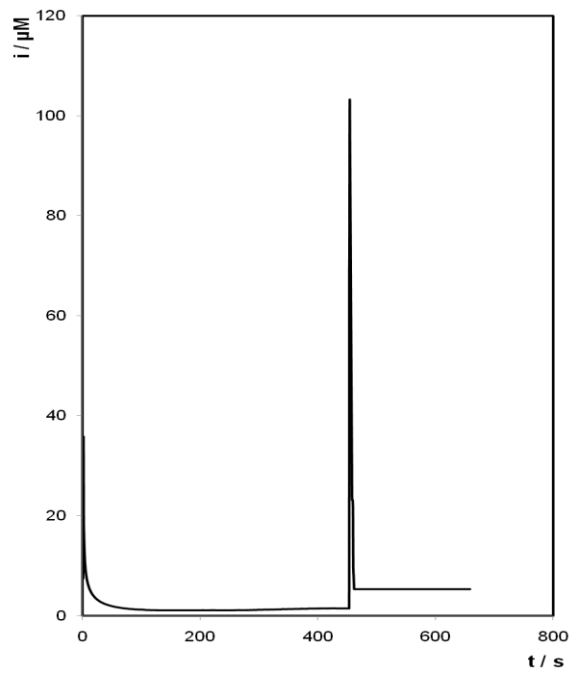
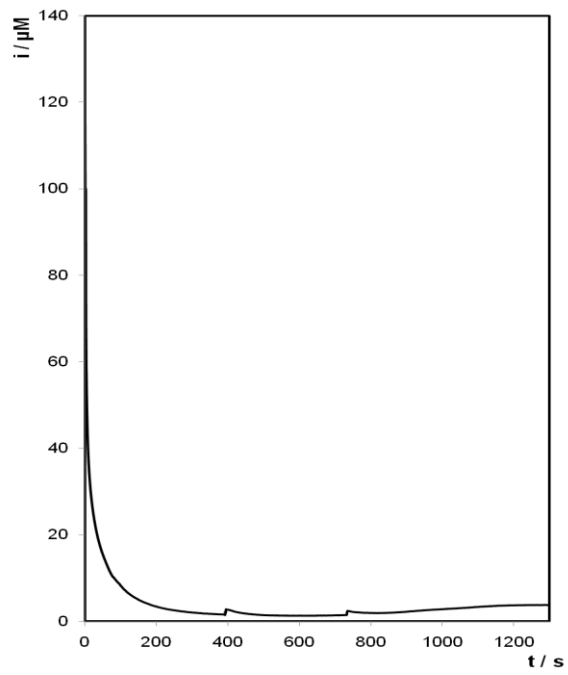
150 pM



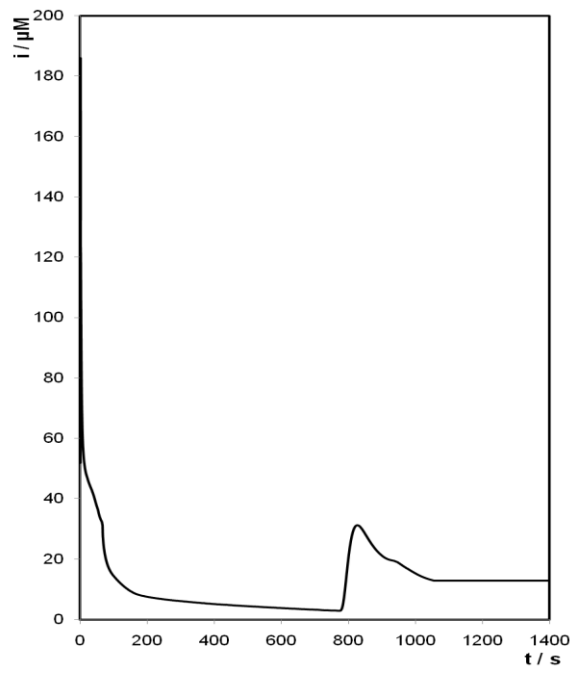
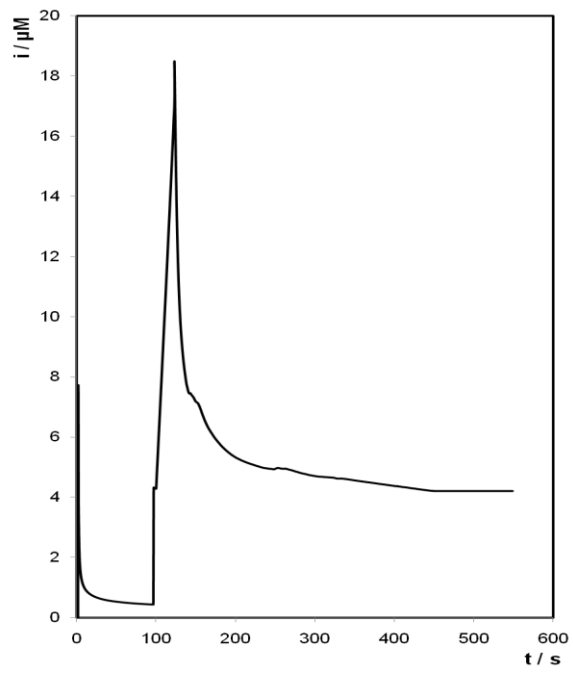
1 nM



10 nM



100 nM



1 μM

